# A THEORETICAL AND COMPUTATIONAL STUDY OF THE MECHANICS OF BIOMEMBRANES AT MULTIPLE SCALES

Alejandro Torres-Sánchez

Doctoral Thesis
Barcelona, May 2017

# A THEORETICAL AND COMPUTATIONAL STUDY OF THE MECHANICS OF BIOMEMBRANES AT MULTIPLE SCALES

Alejandro Torres-Sánchez




Doctoral Thesis
Advisor: Marino Arroyo
Barcelona, May 2017

Departament d'Enginyeria Civil i Ambiental
Programa de Doctorat de Matemàtica Aplicada

*A Laura y mis padres*


## Abstract

### A theoretical and computational study of the mechanics of biomembranes at multiple scales

Alejandro Torres-Sánchez

Lipid membranes are thin objects that form the main separation structure in cells. They have remarkable mechanical properties; while behaving as a solid shell against bending, they exhibit in-plane fluidity. These two aspects of their mechanics are not only interesting from a physical viewpoint, but also fundamental for their biological function. Indeed, the equilibrium shapes of different organelles in the cell rely on the bending elasticity of lipid membranes. On the other hand, the in-plane fluidity of the membrane is essential in functions such as cell motility, mechano-adaptation, or for the lateral diffusion of proteins and other membrane inclusions. The bending rigidity of membranes can be motivated from microscopic models that account for the stress distribution across the membrane thickness. In particular, the microscopic stress across the membrane is routinely computed from molecular dynamics simulations to investigate how different microscopic features, such as the addition of anesthetics or cholesterol, affect their effective mechanical response. The microscopic stress bridges the gap between the statistical mechanics of a set of point particles, the atoms in a molecular dynamics simulation, and continuum mechanics models. However, we lack an unambiguous definition of the microscopic stress, and different definitions of the microscopic stress suggest different connections between molecular and continuum models. In the first Part of this Thesis, we show that many of the existing definitions of the microscopic stress do not satisfy the most basic balance laws of continuum mechanics, and thus are not physically meaningful. This striking issue has motivated us to propose a new definition of the microscopic stress that complies with these fundamental balance laws. Furthermore, we provide a freely available implementation of our stress definition that can be computed from molecular dynamics simulations

(`mdstress.org`). Our definition of the stress along with our implementation provides a foundation for a meaningful analysis of molecular dynamics simulations from a continuum viewpoint. In addition to lipid membranes, we show the application of our methodology to other important systems, such as defective crystals or fibrous proteins. In the second part of the Thesis, we focus on the continuum modeling of lipid membranes. Because these membranes are continuously brought out-of-equilibrium by biological activity, it is important to go beyond curvature elasticity and describe the internal mechanisms associated with bilayer fluidity. We develop a three-dimensional and non-linear theory and a simulation methodology for the mechanics of lipid membranes, which have been lacking in the field. We base our approach on a general framework for the mechanics of dissipative systems, Onsager's variational principle, and on a careful formulation of the kinematics and balance principles for fluid surfaces. For the simulation of our models, we follow a finite element approach that, however, requires of unconventional dicretization methods due to the non-linear coupling between shape changes and tangent flows on fluid surfaces. Our formulation provides the basis for further investigations of the out-of-equilibrium chemo-mechanics of lipid membranes and other fluid surfaces, such as the cell cortex.

## Acknowledgments

I would like to start by thanking three people with a critical contribution to this work. First, I would like to express my deepest gratitude to my advisor, Marino Arroyo, for his guidance and support. He has always encouraged me to develop my ideas with criticism, but also with confidence, which has allowed me to grow not only as a scientist, but also as a person. I would also like to thank Juan M. Vanegas, whose knowledge and ideas were essential to develop the first Part of this Thesis. He taught me most of what I know about molecular dynamics, and at the same time, listened with enthusiasm to my crazy ideas of "pichón". Finally, I am deeply indebted to Daniel Millán, whose lessons, not only about finite elements and research, but also about life in general, have shaped the way I see the world in many aspects.

I would also like to thank the rest of the people in the group for creating such a enjoyable and exciting environment. In particular, I would like to thank Christian Peco, whose discussions about Catalonia's social movements along with a coffee and a good Spanish omelet were most diverting, to Behrooz Hashemian, with whom I shared many funny moments all around the world, to Dimitri Kaurin (this time I didn't messed up with your name, right?), whose particular political views along with coffee have been a scape valve during the writing process of this Thesis, to Ernest Latorre and his funny stories that can make you laugh in the worst days, to Nikhil Walani and his love for italian "prego" along with stimulating conversations about membrane physics, protein diffusion and Indian food and culture (what a mixture!), to Bin Li, and his funny faces when he thinks you are crazy or he doesn't understand you, to Flaviu Simon and Aditya Vasudevan, whose time with us was short but intensive and full of enjoyable moments, to Mohammad Rahimi, for his kindness and help in understanding dynamical processes in lipid membranes, and to Jing Yang, for his stimulating conversations about chinese culture. I would also like to thank other people in the lab (David, Onofre, Albert...) who make from day-to-day work an exciting experience.

¡Y qué sería de la vida si uno no pudiera echarse una risas con los amigos

cada día! A la gente del *Quark, Quark, Antiquark*, ¡gracias por estar siempre ahí!

Sin duda, esta tesis no habría sido posible sin el apoyo incondicional de mi familia, ¡gracias de corazón! En particular, quiero agradecer a Laura, cuyo amor llena mi vida de alegría e ilusión y crea una fuente continua de inspiración, ¡qué haría sin ti!?!? También quiero agradecer a mis padres, que me han inculcado el valor del trabajo, de la perseverancia, y siempre han alentado mis ambiciones. Esta tesis os pertenece más que a mí mismo. A mis suegros, por ser unos segundos padres para mí en Barcelona. Y a Arya, aunque sea incapaz de leer lo que escribo, porque siempre me recibe como si no hubiera otra persona en el mundo.

And finally, I would like to thank the funding sources that have directly or indirectly supported my research. In particular, I would like to thank the economic support of the Spanish Ministery of Economy (grant BES-2012-05489), the European Research Council (grants No. 240487 and 681434) and the computer resources, technical expertise and assistance provided by the Red Española de Supercomputación. I don't want to miss the opportunity to also thank the funding support of the Gayarre Council (grant No 251089).

# Contents

# List of Figures

# Chapter 1

# Introduction

## 1.1 Lipid bilayers

Biological membranes based on lipid bilayers are the most fundamental structure compartmentalizing cells. They define the plasma membrane, which encloses the cell itself, and also form the boundary of other organelles, such as the nucleus, mitochondria, the Golgi apparatus or the endoplasmic reticulum [6] (see Fig. 1.1). Lipid bilayers are mainly composed of lipid molecules. These molecules are amphiphilic, containing a hydrophilic ("water-attracted") head and a hydrophobic ("water-repelled") tail (see Fig. 1.2A). For that reason, lipids self-assemble in aqueous solution to form lipid bilayers, in which lipid tails face each other to avoid contact with water whereas lipid heads are exposed to water (see Fig. 1.2B). Often, lipid bilayers form closed surfaces, topologically equivalent to a sphere, called vesicles, although some organelles exhibit a greater degree of topological complexity. The lipid bilayer structure has the thickness of two lipids, usually ranging between 2 and 5 nm. On the other hand, lipid bilayers form structures with sizes that range from the 100 nm of a small vesicle to 100 µm of a large eukariotic cell. Due to this large difference between thickness and size, lipid bilayers are often modeled as continuous

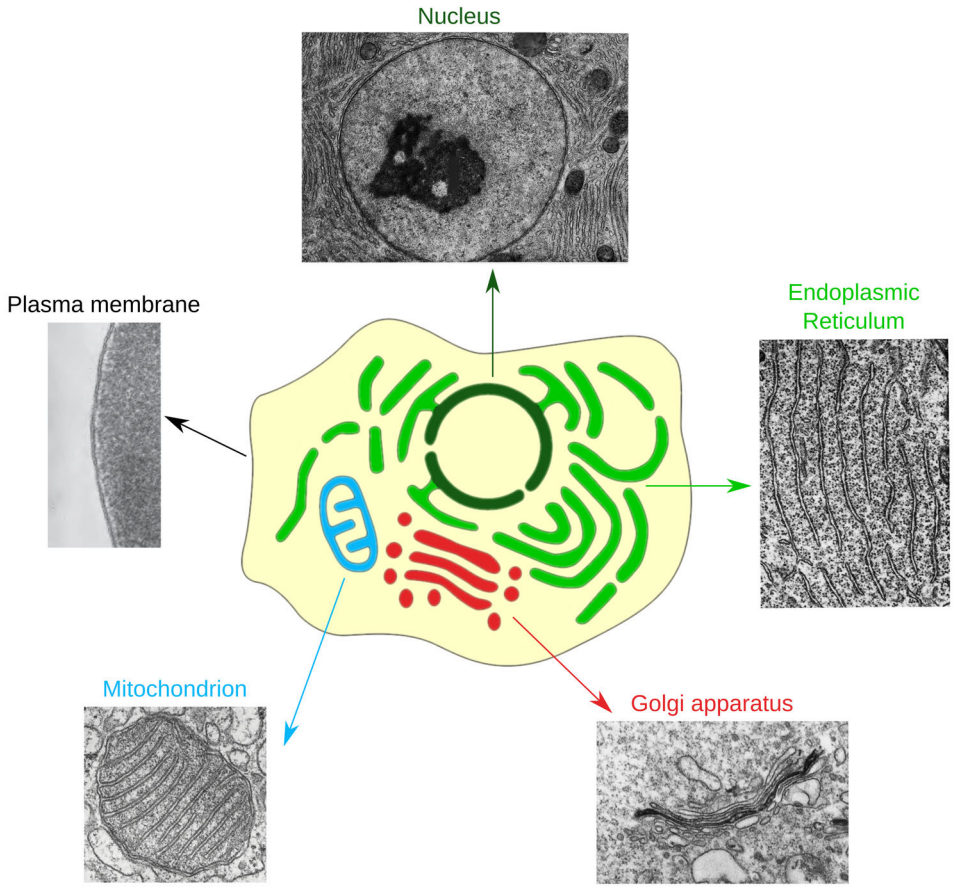


**Figure 1.1**: A schematic view of the cell and its different organelles (center) and transmission electron micrographs of some of them. Nucleus and Endoplasmic Reticulum: The Cell, 2nd Edition by Don W. Fawcett. Plasma membrane and Mithocondrion: Molecular biology of the cell, 6th edition by Bruce Alberts. Golgi Apparatus: Velasko et al., J. Cell Biol 122, 41.

surfaces.

As other thin shells, lipid bilayers exhibit an elastic resistance to bending [92]. However, opposite to solid shells, most lipid bilayers are fluid at physiological temperatures. Lipids on the membrane behave as molecules

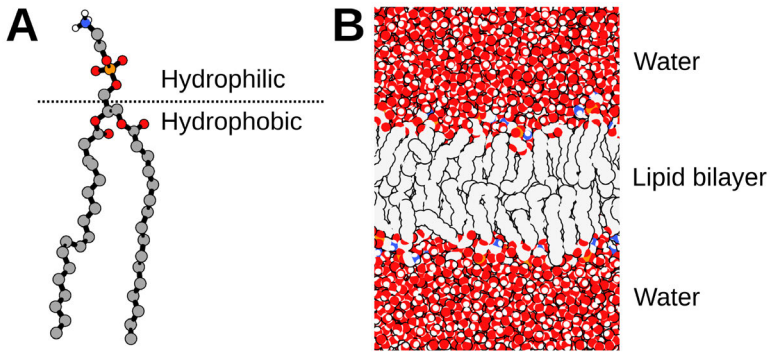


**Figure 1.2**: (A) Atomistic model of a lipid molecule formed by carbon (gray), oxygen (red), phosphorus (yellow), nitrogen (blue) and hydrogen (white) atoms (terminal hydrogens connected to the carbon atoms in the tail are not shown for simplicity). The head of the lipid molecule is hydrophilic while the tail is hydrophobic. (B) Side view of a lipid bilayer in water. Lipid heads face water whereas lipid tails face each other to avoid contact with water.

in a two-dimensional viscous fluid. Thus, lipid bilayers are a special kind of material, behaving as a solid shell against bending while presenting in-plane fluidity. This dual behavior is not only interesting from a physical or an engineering perspective, but is also essential for the biological function of membranes. On the one hand, lipid bilayers need to adopt various geometries, including vesicles, tubes, sheets or complex networks such as the endoplasmic reticulum, whose shape is governed by curvature elasticity [162]. On the other hand, these structures need to be dynamic to undergo different processes such as lipid transport [168, 151], diffusion of proteins [19], or cell motility [12, 198]. Furthermore, lipid bilayers dynamically respond to transient stimuli. For instance, they respond to chemical signals that alter their inner composition, such as pH differences [39], or interact with scaffolding proteins that adsorb, diffuse and curve the membrane [19].

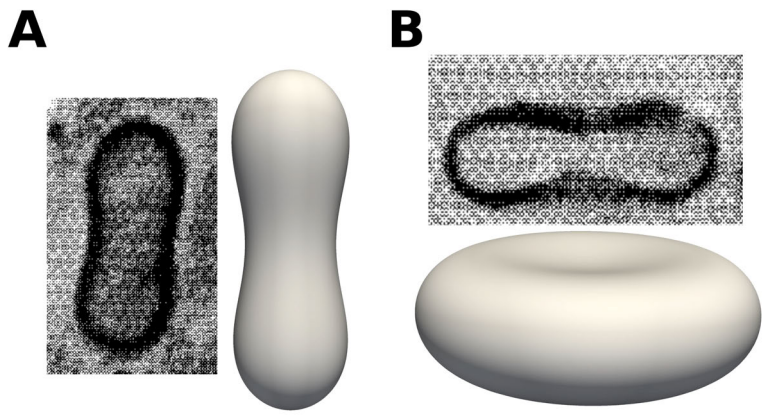


**Figure 1.3**: Comparison between microscopic images of vesicles [159] and solutions to the minimization of Helfrich energy for different values of enclosed volume and total area.

## 1.2 The Helfrich model

The curvature elasticity of lipid bilayers can be described to a surprising degree of accuracy by the Helfrich energy [70]

$$\mathcal{F}_{\mathrm{H}} = \int_{\Gamma} \left[ \frac{\kappa}{2}(H - H_0)^2 + \bar{\kappa} K \right] dS, \tag{1.1}$$

where $\Gamma$ represents the bilayer mid-surface, $H$ and $K$ are the mean and Gaussian curvatures of $\Gamma$, $H_0$ is the spontaneous curvature, and $\kappa$ and $\bar{\kappa}$ are the bending and Gaussian bending moduli. The first term in the integrand penalizes deviations of $H$ from the spontaneous curvature $H_0$. In general, for up-down symmetric bilayers with the same composition in the upper and lower monolayers and equal aqueous solution across the membrane, $H_0 = 0$. However, for asymmetric bilayers or bilayers containing scaffolding proteins, $H_0$ may be non-zero. Regarding the second term in the Helfrich energy, for a uniform $\bar{\kappa}$ and a closed vesicle, $\int_{\Gamma} \bar{\kappa} K dS$ is a topological invariant independent of the membrane shape (as a result of the Gauss-Bonnet theorem [40]). Reflecting the in-plane fluidity of the bilayer, the Helfrich energy is

independent of in-plane deformations of the surface; it only depends on the shape of $\Gamma$. Futhermore, this energy is scale-invariant. In general, it is assumed that the bilayer is inextensible, so that the area of $\Gamma$ is constant. Furthermore, cells and vesicles usually have a nearly constant volume because of the physiological osmotic strength; osmotic forces dominate all other forces. By minimizing the Helfrich energy at fixed volume and area, one can obtain different configurations that match experimental observations (see Fig. 1.3) [49]. The interplay of Helfrich energy with adhesion, or with thermal fluctuations, can explain a variety of experimental observations [70, 92, 80, 172].

## 1.3 Lateral stress profiles

In the Helfrich model, the lipid bilayer is seen as a surface with bending elasticity. The bending response of lipid bilayers strongly depends on the molecular structure of the bilayer. In fact, their bending elasticity can be understood in terms of the internal stress distribution, $\boldsymbol{\sigma}(\boldsymbol{x})$, across the bilayer thickness. To show it, let us consider a three-dimensional atomistic model of a fluid lipid bilayer and, for simplicity, let us examine a planar bilayer parallel to the $x-y$ plane (see Fig. 1.4). Since the bilayer is isotropic in the $x-y$ plane, $\boldsymbol{\sigma}(x,y,z) = \boldsymbol{\sigma}(z)$ and $\sigma^{xx} = \sigma^{yy}$. Furthermore, since the bilayer is fluid $\sigma^{ij} = 0$ for $i \neq j$. Conservation of linear momentum in the $z$ direction implies that $\sigma^{zz}$ is constant. Thus, the stress state of the bilayer in this configuration is simply characterized by the function $\sigma^{xx}(z)$ and the constant $\sigma^{zz}$, which is equal to the negative of the pressure in the fluid. In this configuration, the first two moments of the stress profile relate to the Helfrich model parameters as [177, 101, 75]

$$-\kappa H_0 = \int_{-t/2}^{t/2} [\sigma^{xx}(z) - \sigma^{zz}]\,(z - z_0)dz, \tag{1.2}$$

and

$$\bar{\kappa} = \int_{-t/2}^{t/2} [\sigma^{xx}(z) - \sigma^{zz}]\,(z - z_0)^2 dz, \tag{1.3}$$

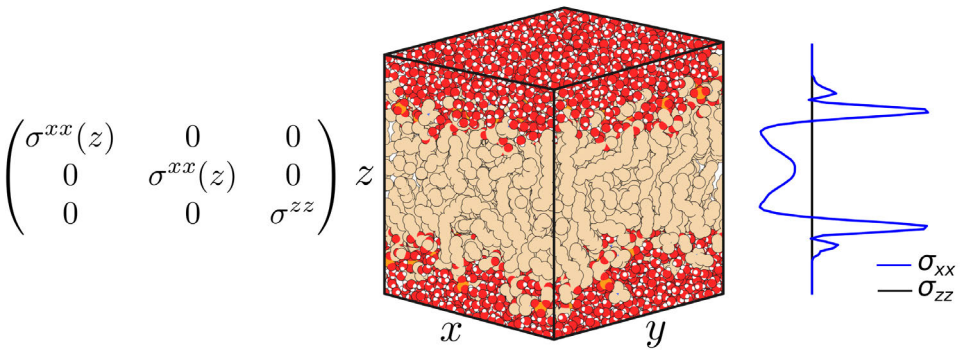


**Figure 1.4**: Stress tensor in a molecular simulation of a fluid lipid bilayer parallel to the $x - y$ plane at equilibrium.

where $z_0$ is the position of the neutral plane of the bilayer, $t$ is the bilayer thickness, and we have taken the mid-plane of the bilayer as $z = 0$. Unfortunately, these stress profiles cannot be measured experimentally. A convenient way to evaluate $\sigma^{xx}(z)$ and $\sigma^{zz}$ is through molecular simulations, where atoms are considered as point particles that interact through an interatomic potential and follow Newton's laws. By simulating patches of lipid bilayers with atomistic resolution, one can, for instance, evaluate $\bar{\kappa}$ for lipid bilayers with different chemical compositions. This is particularly useful, since $\bar{\kappa}$ is difficult to measure experimentally [75].

The applicability of the stress profiles computed from molecular simulations of lipid bilayers is not restricted to the evaluation of Eqs. (1.2) and (1.3); stress profiles are routinely used to evaluate the effect of electric fields [63, 28], of chemical composition [59, 90, 48, 85], or to measure the interaction with membrane inclusions such as proteins [188, 204, 14] or polymers [76].

To bridge the gap between molecular dynamics and a continuum stress field, a map between the statistical mechanics of molecular trajectories and the continuous stress field is required. This mapping, however, is not unique. In practice, different definitions of the microscopic stress suggest different continuum interpretations of the same system. Although this ambiguity is

widely appreciated theoretically, its practical consequences have been largely overlooked, partly because for systems with simple interactions the different definitions of the microscopic stress coincide. Motivated by this issue, in the first Part of this Thesis, we investigate the definition of the microscopic stress from molecular dynamics simulations.

## 1.4 Continuum modeling of the dynamics of lipid bilayers

While the Helfrich model allows us to predict the equilibrium shapes of lipid bilayers, it cannot describe the dynamic processes that lipid bilayers undergo, as they are continuously brought out of equilibrium by biological activity. The interfacial hydrodynamics of lipid membranes is crucial in processes such as vesicular trafficking [168, 151], cell motility and migration [12, 198], or in the mechano-adaptation of cells to stress [84]. Furthermore, membrane fluidity allows membrane proteins to diffuse [161]. Historically, the interfacial hydrodynamics of bilayer membranes was examined assuming a fixed membrane shape, starting with the seminal work of Saffman and Delbrück on planar lipid bilayers [152]. However, there is a rich interplay between the shape dynamics and the interfacial hydrodynamics of lipid membranes, which becomes apparent in processes such as tubulation [150, 89, 172], phase separation [15], budding and fission [171, 203], or pearling [54], to name a few. In the second Part of this thesis, we focus on a theoretical and computational framework for the elasto-hydrodynamics of lipid bilayers in a fully non-linear and three-dimensional setting.

## 1.5 Structure of the thesis

The Thesis is structured as follows. In the first Part, we examine the definition of the microscopic stress from molecular dynamics simulations. This work is a review of our recent contributions

- *Importance of Force Decomposition for Local Stress Calculations in Biomembrane Molecular Simulations*, J. M. Vanegas, A. Torres-Sánchez, and M. Arroyo, J. Chem. Theory Comput., 2014, 10 (2), 691.

- *Examining the Mechanical Equilibrium of Microscopic Stresses in Molecular Simulations*, A. Torres-Sánchez, J. M. Vanegas, and M. Arroyo, Phys. Rev. Lett., 2015, 114, 258102.

- *Geometric Derivation of the Microscopic Stress: A Covariant Central Force Decomposition*, A. Torres-Sánchez, J. M. Vanegas, and M. Arroyo, J. Mech. Phys. Solids, 2016, 93, 224.

We show that widely used implementations of the microscopic stress violate the most basic balance laws of continuum mechanics and are not suitable to interpret molecular dynamics simulations. To address this issue, we propose a new definition of the microscopic stress that satisfies the balance laws of continuum mechanics by construction, which leads to physically meaningful stress fields for general multibody potentials. We exemplify this stress definition in lipid bilayers, but also in fibrous proteins and crystalline structures such as a graphene sheet. For that purpose, we developed a freely-available library based on C++

- *MDStress library*, A. Torres-Sánchez, J. M. Vanegas and M. Arroyo, `mdstress.org`.

which can be used either as a standalone library or embedded in the GROMACS 4.5.5 molecular dynamics package [74]. This library includes our definition of the microscopic stress, along with previous definitions.

In the second part of this Thesis we focus on the continuum modeling and simulation of the dynamics of lipid bilayers. We first present a general framework for modeling dissipative systems, such as lipid bilayers, based on Onsager's variational principle. This theory was more extensively introduced in our recent publication

- *Onsager's Variational Principle in Soft Matter: Introduction and Application to the Dynamics of Adsorption of Proteins onto Fluid Membranes*, M. Arroyo, N. Walani, A. Torres-Sánchez and D. Kaurin. Chapter in the book "The role of mechanics in the study of lipid bilayers", Edited by D. Steigmann and published by CISM, 2017.

We then examine in detail the kinematics and transport theorems required to describe deformable fluid surfaces, which necessarily involve the formalism of differential geometry. Based on Onsager's variational principle and the differential geometry of fluid surfaces, we propose a three-dimensional and fully non-linear model for lipid bilayers extending that of [160], which we exercise numerically on different relevant examples to the mechanics of lipid membranes. This numerical approach is based on a finite-element formulation of the equations, which requires unconventional numerical methods. Finally, we show the application of the previous theoretical and computational framework to another important instance of fluid surface in the cell, the cell cortex.

In summary, the work of this Thesis has two complementary objectives. On the one hand, we have developed two general theoretical frameworks (the definition of the microscopic stress and the formulation of the elasto-hydrodynamics of fluid surfaces) and two computational tools (the MDStress library and a finite-element library for the continuum mechanics of lipid membranes). On the other hand, we have applied these theories and computer codes to understand the mechanics of lipid membranes at different scales. Apart from lipid membranes, we have also shown the potential of our theoretical and computational frameworks to understand other important systems, such as fibrous proteins, crystalline structures, or the cell cortex.

# Part I

# Theory and computation of the microscopic stress

# Chapter 2

# Introduction and review of basic concepts

## 2.1 Introduction and motivation

The increasing power of modern computers enables the atomistic simulation of material systems of growing size and complexity. However, it is difficult to interpret the physics of these systems from bare atomistic trajectories. In particular, there is a pressing need for coarse-grained measures of the effective mechanical behavior underlying molecular ensembles. Continuum mechanics has been successfully applied to understand the mechanics of a variety of systems at the nanoscale, such as carbon nanotubes [197, 8] or biomembranes [75, 172], and therefore it provides a natural framework to interpret molecular simulations of materials.

In particular, the stress $\boldsymbol{\sigma}(\boldsymbol{x})$ is a second-rank tensor field encoding the internal force distribution in a continuum system; when multiplied by a unit vector $\boldsymbol{n}$, it provides the forces per unit area in the material across a surface passing through $\boldsymbol{x}$ and perpendicular to $\boldsymbol{n}$. The continuum stress field of a system of point particles is defined through statistical mechanics in what is

called the microscopic stress. Today, the microscopic stress is increasingly used to recapitulate mechanical information contained in long molecular dynamics (MD) trajectories of non-uniform systems, or to connect molecular details with continuum physics at larger scales. Significant applications include defective bulk [88, 127] and two-dimensional crystals [194, 166], biomolecular assemblies such as lipid bilayers [91, 75, 191], membrane proteins [117, 188], and even isolated molecules [68].

The average (or virial) stress of a system of point particles, typically the average stress of a periodic simulation box, can be uniquely defined and given a precise thermodynamic interpretation [185, 178]. There are, however, multiple procedures to map a statistical mechanics ensemble of a molecular system into a microscopic stress field providing the local stress map in a heterogeneous system. The ambiguity in the microscopic stress is widely appreciated theoretically, but its practical consequences have been largely overlooked, partly because different definitions coincide for simple force-fields [191]. As molecular simulations model increasingly complex systems, the physical validity of the different definitions of the microscopic stress has not been systematically examined.

For example, let us consider a simple definition of the microscopic stress, the virial stress per atom (VSA) [179], reviewed in Section 2.5, which we denote by $\boldsymbol{\sigma}_{\mathrm{VSA}}$. This stress measure has been widely employed to analyze the mechanics of crystals from MD simulations, see [88, 127, 194, 166] for a selection of relevant works, and it is provided as a utility to compute the microscopic stress in the popular MD package LAMMPS [35]. To exercise this definition of the microscopic stress, we consider a graphene sheet with a Stone-Wales defect as a model of inhomogeneous two-dimensional crystal in thermodynamic equilibrium at a given temperature and volume (see Appendix B for details on simulation settings). The virial stress per atom assigns a stress tensor to each atom of the structure, see Fig. 2.1A for the trace of the stress at each atom in the vicinity of the defect. We can obtain a continuum stress field (Fig. 2.1B), which could be compared with stress fields obtained from

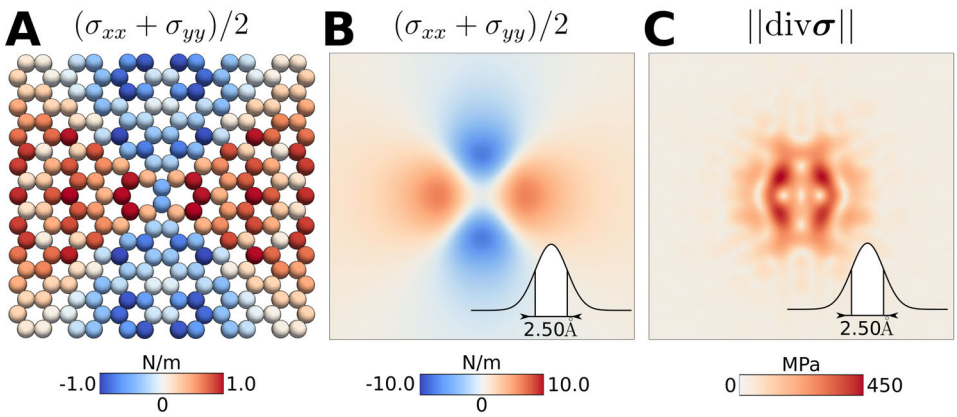


**Figure 2.1**: Virial stress per atom around a Stone-Wales defect in a graphene sheet. (A) Average structure of the crystal around the defect. Each atom is colored with the trace of the virial stress per atom. (B) Trace of $\bar{\boldsymbol{\sigma}}_{\mathrm{VSA}}$ with a Gaussian filter of standard deviation of 1.25Å. (C) Norm of the divergence of the virial stress per atom with the same Gaussian filter. The virial stress per atom is not self-equilibrated in the absence of forces and thus it violates conservation of linear momentum.

defect mechanics theory, by spatial averaging the discrete field as explained in Box 2.1. We denote the spatially-averaged stress by $\bar{\boldsymbol{\sigma}}_{\mathrm{VSA}}$. Since the graphene sheet is at thermodynamic equilibrium, we expect the resulting stress to be at mechanical equilibrium. In continuum mechanics, mechanical equilibrium implies that, in the absence of external forces, the divergence of the stress vanishes

$$\boxed{\mathrm{div}\boldsymbol{\sigma} = \mathbf{0}.} \tag{2.1}$$

However, we find that the divergence of $\bar{\boldsymbol{\sigma}}_{\mathrm{VSA}}$ is not zero in the vicinity of the defect (Fig. 2.1C), indicating that the virial stress per atom is out of equilibrium in that region. Let us note that, as explained in Box 2.1, the divergence of a spatially averaged stress field $\bar{\boldsymbol{\sigma}}$ coincides with the spatial average of the divergence of $\boldsymbol{\sigma}$, and therefore if $\mathrm{div}\bar{\boldsymbol{\sigma}}$ is not zero, both $\bar{\boldsymbol{\sigma}}$ and $\boldsymbol{\sigma}$ are not self-equilibrated. Thus, we conclude that *the virial stress per atom violates conservation of linear momentum from a continuum mechanics viewpoint*.

Let us now consider a different tool to compute the microscopic stress [97] based on GROMACS, another popular MD package [74], which has been widely employed to analyze the microscopic stress in fluids and in lipid bilayers (see for instance [91, 62, 167, 189, 202, 129, 113, 16, 116, 165, 123, 117, 202, 16]). This tool considers a special flavor of the Irving-Kirkwood-Noll (IKN) stress [77, 115], reviewed in Chapter 3, proposed by Goetz and Lipowsky [57], which we refer to as the IKN-GLD stress and denote it by $\boldsymbol{\sigma}_{\mathrm{GLD}}$. To analyze the stress produced by this tool, we examine a fluid DPPC (1,2-dipalmitoyl-sn-glycero-3-phosphocholine) lipid bilayer at equilibrium at a given temperature and pressure. We express the components of $\boldsymbol{\sigma}_{\mathrm{GLD}}$ in cartesian coordinates (see Fig. 2.2A). We note that, for a planar fluid lipid bilayer parallel to the $xy$-plane, we expect a stress with $\sigma^{xx} = \sigma^{yy}$ by symmetry and with $\sigma^{ij} = 0$ for $i \neq j$ since the fluid bilayer cannot sustain shear stress at equilibrium (see Fig. 2.2A).

Furthermore, due to the homogeneity in the $xy$-plane, the tensor components only depend on the coordinate $z$. Thus, balance of linear momentum Eq. (2.1) simplifies to $\partial\sigma^{zz}/\partial z = 0$, resulting in a constant $\sigma^{zz}$. However, from this tool we find that $\sigma^{zz}_{\mathrm{GLD}}$ is not constant (see Fig. 2.2B), indicating that the field $\boldsymbol{\sigma}_{\mathrm{GLD}}$ is out of equilibrium. This violation of conservation of linear momentum has sparkled some controversy [118, 16, 119, 1, 122]. Furthermore, the IKN-GLD stress exhibits non-vanishing off-diagonal components. Although these components could be non-zero for a lipid bilayer in the gel phase, where the lack of fluidity could explain the emergence of shear stress at equilibrium, they should satisfy that $\sigma^{xy} = \sigma^{yx}$, since balance of angular momentum is expressed in continuum mechanics by the symmetry of the stress tensor

$$\boxed{\boldsymbol{\sigma} = \boldsymbol{\sigma}^T.} \tag{2.2}$$

However, we find that $\sigma^{xy}_{\mathrm{GLD}} \neq \sigma^{yx}_{\mathrm{GLD}}$ indicating that the IKN-GLD stress violates balance of angular momentum. Thus, *the stress produced by this popular tool using IKN-GLD does not satisfy balance of linear momentum nor angular momentum.*

Being fundamental requirements of continuum mechanics, it is natural to demand that a microscopic stress definition satisfies balance of linear and angular momentum for a system in thermodynamic equilibrium. However,

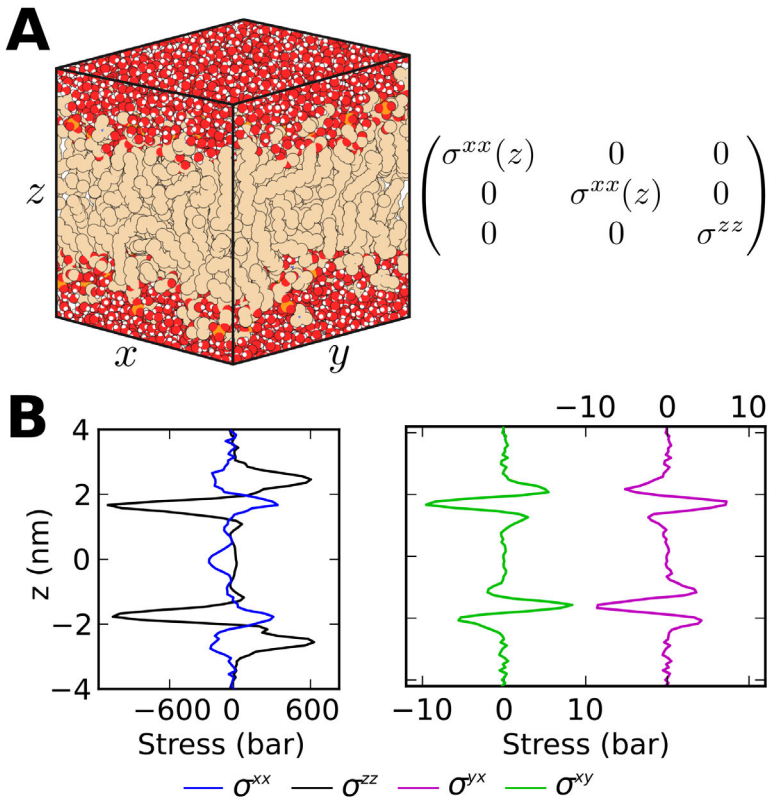


**Figure 2.2**: (A) Typical simulation box for a DPPC lipid bilayer with the bilayer midplane parallel to the $xy$-plane and periodic boundary conditions. Due to the isotropy of the bilayer, the components of the stress can only depend on $z$ and $\sigma^{yy}(z) = \sigma^{xx}(z)$. Since the lipid bilayer is fluid at the simulated temperature, the off-diagonal components of the stress, which stem from shear at equilibrium, must vanish. Furthermore, balance of linear momentum requires that $\sigma^{zz}$ is constant. (B) Components of the stress tensor calculated using a popular tool based on GROMACS [97] and on the IKN-GLD framework. We note that the $\sigma^{zz}$ obtained from this tool is not constant, which is inconsistent with balance of linear momentum. Furthermore, the off-diagonal components are not zero and $\sigma^{xy} \neq \sigma^{yx}$. While the off-diagonal components could be different from zero for a lipid bilayer in the gel phase, these should however satisfy $\sigma^{xy} = \sigma^{yx}$ from balance of angular momentum. Thus, the stress computed from this tool also violates balance of angular momentum.

from these examples we observe that some definitions of the microscopic stress found in the literature do not satisfy these balance laws. The issue is striking because these definitions have been widely employed to analyze molecular systems from a continuum mechanics viewpoint in different research areas, ranging from the analysis of inhomogeneous crystals to lipid bilayers. However, an examination of whether these definitions are consistent with the continuum notion of equilibrium, as we have done in Figs. 2.1 and 2.2, had not been reported before.

In view of the examples in this introduction, in this Part of the Thesis we examine why widely employed stress definitions do not satisfy balance laws of linear and angular momentum. We focus on the two definitions discussed in this introduction, the virial stress per atom and the IKN-GLD stress, since these are the most prominent microscopic stress measures in the literature. Other definitions of the microscopic stress, such as the method of planes by Heinz, Paul and Binder [69] or the Harasima stress [66], have been analyzed elsewhere [4, 182] with similar results: they do not satisfy mechanical equilibrium.

To solve this issue, we propose a new computational tool based on an alternative theory rooted in the IKN theory [4], the IKN-CFD stress, that computes stress tensors that satisfy balance of linear and angular momentum by construction. However, we show that the IKN-CFD stress is not completely satisfying, as it is not uniquely defined for multibody potentials, which are popular to model metals and proteins [37, 96]. To address this issue, we derive the microscopic stress from an alternative geometric route, based on the Doyle-Ericksen formula of continuum mechanics, that leads to a canonical stress of the form of IKN-CFD, which we call IKN-cCFD stress. Our definition of the stress, along with our implementation, provides a solid foot to analyze molecular systems from a continuum mechanics viewpoint. Furthermore, our new method to derive the microscopic stress is a significant contribution in its own, with potential ramifications discussed in Chapter 6.

Our procedure to compute the IKN-cCFD stress, along with other local stress definitions including the virial stress per atom, the IKN-GLD stress

and the IKN-CFD stress, has been made publicly available in our MDstress library (`mdstress.org`), which can be either used as a standalone library or embedded in the GROMACS 4.5.5 MD package [74]. Unless otherwise stated, we use this library to compute the different definitions of the stress in model systems throughout this chapter. The implementation details are given in Appendix A.

This work is an extensive review of our recent contributions [191, 182, 183] and is organized as follows. In the rest of this introductory chapter, we introduce basic concepts of statistical mechanics, the cluster form of the potential and the definition of the virial stress and the virial stress per atom. In Chapter 3 we introduce the Irving-Kirkwood-Noll approach, and the IKN-GLD and IKN-CFD definitions. In Chapter 4 we analyze different features of the IKN-CFD stress in lipid bilayers. Finally, in Chapter 5 we introduce our definition of the microscopic stress based on the Doyle-Ericksen formula, which extends the IKN-CFD definition to arbitrary multibody potentials.

## 2.2 A review of statistical mechanics concepts

Let us first review some thermodynamic and statistical-mechanics concepts that will be employed throughout this work. We refer the interested reader to [55, 178] for extensive reviews. We consider a system of $N$ point particles enclosed by a volume $\Omega$. Although different boundary conditions can be considered for $\Omega$, it is usual to consider periodic boundary conditions (PBC). The point-particles are characterized by their masses $\{m^\alpha\}_{\alpha=1}^N$, positions $\{\boldsymbol{r}^\alpha\}_{\alpha=1}^N$ $(\boldsymbol{r}^\alpha \in \Omega)$, and velocities $\{\boldsymbol{v}^\alpha\}_{\alpha=1}^N$ $\left(\boldsymbol{v}^\alpha \in \mathbb{R}^3\right)$. They interact through an interatomic potential $V(\boldsymbol{r}^1, \ldots, \boldsymbol{r}^N)$, from which the set of forces on the particles derive

$$\boldsymbol{F}^\alpha = -\partial_{\boldsymbol{r}^\alpha} V(\boldsymbol{r}^1, \ldots, \boldsymbol{r}^N), \quad \alpha = 1, \ldots, N, \tag{2.3}$$

where we write $\partial_{\boldsymbol{r}^\alpha}$ as a short form of $\frac{\partial}{\partial \boldsymbol{r}^\alpha}$. If the interatomic potential is invariant with respect to translations and rotations, then these forces satisfy

balance of linear momentum

$$\sum_{\alpha=1}^{N} \boldsymbol{F}^{\alpha} = \boldsymbol{0}, \tag{2.4}$$

and angular momentum

$$\sum_{\alpha=1}^{N} \boldsymbol{F}^{\alpha} \times \boldsymbol{r}^{\alpha} = \boldsymbol{0}, \tag{2.5}$$

where $\boldsymbol{a} \times \boldsymbol{b}$ stands for the vector product between vectors $\boldsymbol{a}$ and $\boldsymbol{b}$, in components $(\boldsymbol{a} \times \boldsymbol{b})^i = \varepsilon^{ijk} a_j b_k$, where $\varepsilon^{ijk}$ are the Levi-Civita symbols. The energy of this system is given by the Hamiltonian function

$$H(\boldsymbol{r}, \boldsymbol{p}) = \sum_{\alpha=1}^{N} \frac{||\boldsymbol{p}^{\alpha}||^2}{2m^{\alpha}} + V(\boldsymbol{r}), \tag{2.6}$$

where $\boldsymbol{r} = \left(\boldsymbol{r}^1, \ldots, \boldsymbol{r}^N\right)$ and $\boldsymbol{p} = \left(\boldsymbol{p}^1, \ldots, \boldsymbol{p}^N\right)$ collects the particle momenta $\boldsymbol{p}^{\alpha} = m^{\alpha} \boldsymbol{v}^{\alpha}$. The set of possible states $(\boldsymbol{r}, \boldsymbol{p})$ that are accessible to the system is $\Gamma = \Omega^N \times \mathbb{R}^{3N}$, which is referred to as the phase space. The time evolution of the positions and momenta follows Hamilton's equations

$$\dot{\boldsymbol{p}}^{\alpha} = -\partial_{\boldsymbol{r}^{\alpha}} H = \boldsymbol{F}^{\alpha}, \qquad \boldsymbol{v}^{\alpha} = \dot{\boldsymbol{r}}^{\alpha} = \partial_{\boldsymbol{p}^{\alpha}} H = \frac{\boldsymbol{p}^{\alpha}}{m^{\alpha}}, \tag{2.7}$$

where we write $\dot{a} = da/dt$. An ensemble of these systems is characterized by a probability distribution $f(\boldsymbol{r}, \boldsymbol{p}; t)$ over $\Gamma$. Conservation of probability along the trajectory of the ensemble leads to Liouville's equation

$$\begin{aligned} \dot{f} = 0 \Longrightarrow \partial_t f &= -\partial_{\boldsymbol{r}} f \cdot \dot{\boldsymbol{r}} - \partial_{\boldsymbol{p}} f \cdot \dot{\boldsymbol{p}} \\ &= \sum_{\alpha=1}^{N} \left[ -\partial_{\boldsymbol{r}^{\alpha}} f \cdot \frac{\boldsymbol{p}^{\alpha}}{m^{\alpha}} + \partial_{\boldsymbol{p}^{\alpha}} f \cdot \boldsymbol{F}^{\alpha} \right], \end{aligned} \tag{2.8}$$

where here we denoted by $\dot{f}$ the total or material time-derivative of $f$. At equilibrium, $\partial_t f = 0$ and we simply write $f(\boldsymbol{r}, \boldsymbol{p})$. For an ensemble at thermal equilibrium with a thermostat at temperature $T$, the equilibrium probability distribution follows the Boltzmann distribution

$$f_B(\boldsymbol{r}, \boldsymbol{p}) = \exp\left( -\frac{(H(\boldsymbol{r}, \boldsymbol{p}) - A(T, \Omega))}{k_B T} \right), \tag{2.9}$$

where $k_B$ is the Boltzmann constant and the normalizing factor $A(T, \Omega)$

$$A(T, \Omega) = -k_B T \log \left( \int_\Gamma \exp \left( -\frac{H(\boldsymbol{r}, \boldsymbol{p})}{k_B T} \right) d\boldsymbol{r} d\boldsymbol{p} \right), \tag{2.10}$$

is the free energy of the system. Given a quantity $a(\boldsymbol{r}, \boldsymbol{p}, t)$ we define the ensemble average of such quantity as

$$\langle a \rangle(t) = \int_\Gamma a(\boldsymbol{r}, \boldsymbol{p}, t) f(\boldsymbol{r}, \boldsymbol{p}, t) d\boldsymbol{r} d\boldsymbol{p}. \tag{2.11}$$

At equilibrium, for a quantity $a$ that does not depend on time explicitely, $\langle a \rangle$ is time-independent. Then, under the assumption of ergodicity, the ensemble average at equilibrium can be substituted by a time average for a single system in the ensemble

$$\langle a \rangle = \overline{a}, \tag{2.12}$$

where

$$\overline{a} = \lim_{T \to \infty} \left( \frac{1}{T} \int_0^T a(\boldsymbol{r}(t), \boldsymbol{p}(t)) dt \right). \tag{2.13}$$

In molecular dynamics (MD), we numerically integrate the time-evolution of a system of point particles following Eq. (2.7). Ensemble averages are numerically estimated from the discrete trajectory by approximating Eq. (2.13). To consider the effect of thermostats and barostats at a single system level, different numerical techniques can be employed to reproduce ensemble averages, such as the Nose-Hoover thermostat [46] or the Parrinello-Rahman barostat [128]. This allows us to reproduce through MD simulations the NVE (fixed number of particles, volume and energy), the NVT (fixed number of particles, volume and temperature) and NPT (fixed number of particles, pressure and temperature) equilibrium ensembles.

## 2.3 Cluster expansion of the potential

Usually, the interatomic potential $V(\boldsymbol{r}^1, \ldots, \boldsymbol{r}^N)$ in MD is written as the sum of multibody potentials in what is called the cluster expansion of the potential. The cluster expansion plays a key role in different definitions of the microscopic

stress, as it will become clear later. Any potential energy function, including those computed from first principles, can be expressed in a cluster form [51, 102]

$$V(\boldsymbol{r}^1, \ldots, \boldsymbol{r}^N) = \sum_{n=2}^{N} \sum_{I_n=1}^{M_n} V_{I_n}(\boldsymbol{r}^{I_n^1}, \boldsymbol{r}^{I_n^2}, \ldots, \boldsymbol{r}^{I_n^n}), \tag{2.14}$$

where each $V_{I_n}$ is a $n-$body potential, $M_n \leq \binom{N}{n}$ is the number $n-$body interactions amongst the $N$ particles, and $I_n^1, I_n^2, \ldots, I_n^n$ label the $n$ particles interacting through $V_{I_n}$. This cluster expansion can be made unique by requiring that the potentials $V_{I_n}(\boldsymbol{r}^{I_n^1}, \boldsymbol{r}^{I_n^2}, \ldots, \boldsymbol{r}^{I_n^n})$ vanish whenever any of the intervening particles is brought infinitely far away from the rest. If this were not true, then such a potential would not be a genuine $n-$body potential, but rather $n-1$ or lower [102]. With this definition, $V_{I_2}$ represents the interaction of two isolated atoms, $V_{I_3}$ is the excess of energy of an isolated triplet of atoms not accounted by their pair interactions, and in general $V_{I_n}$ represents the part of the interaction energy of $n$ particles minus the interaction energy from all their $n-1, n-2, \ldots,$ 2-body interactions. The cluster expansion isolates interactions between particles, which facilitates their physical interpretation, and eases the numerical computation of particle forces in MD codes. In biomolecular simulations, the interatomic potential usually involves 2-body potentials, such as bonds, Coulomb and van der Waals interactions, 3-body interactions, such as angle potentials, and 4-body interactions, such as torsional potentials. In protein simulations, some corrections to the potential are added through 5-body interactions [96]. In simulations of metals, such as those based on the embedded atom method [37], the energy function is not written in a cluster form, but the cluster form can be obtained sistematically [51, 102] and will involve higher order terms.

## 2.4 Virial stress

Given a unit vector $\boldsymbol{n}$, the virial stress $\boldsymbol{\Sigma}$ is a second-order tensor that encodes the average traction $\boldsymbol{t} = \boldsymbol{\Sigma} \cdot \boldsymbol{n}$ that a system of point particles in a volume $\Omega$ at

thermodynamic equilibrium exerts on an imaginary plane with unit normal $\boldsymbol{n}$ splitting $\Omega$ into two parts [185]. The virial stress admits a statistical mechanics representation that can be obtained from the change of free energy under an infinitesimal affine deformation [178]. More precisely, let us consider a linear deformation of $\Omega$, $\varphi : \Omega \to \mathbb{R}^3$, characterized by the deformation gradient $\boldsymbol{F}$, $x^i = \varphi^i(\boldsymbol{X}) = F^i{}_J X^J$. Denoting by $A(T, \boldsymbol{F})$ the free energy of the deformed system, then the virial stress can then be computed as

$$\boldsymbol{\Sigma} = \frac{1}{\det \boldsymbol{F}} \partial_{\boldsymbol{F}} A(T, \boldsymbol{F}) \boldsymbol{F}^T. \tag{2.15}$$

Exercising Eq. (2.15) on Eq. (2.10), we get the expression [178]

$$\begin{aligned} \boldsymbol{\Sigma} &= \boldsymbol{\Sigma}_{\mathrm{K}} + \boldsymbol{\Sigma}_{\mathrm{V}}, \\ \boldsymbol{\Sigma}_{\mathrm{K}} &= -\frac{1}{\Omega} \sum_{\alpha=1}^{N} \langle m^\alpha \boldsymbol{v}^\alpha \otimes \boldsymbol{v}^\alpha \rangle , \\ \boldsymbol{\Sigma}_{\mathrm{V}} &= -\frac{1}{\Omega} \sum_{\alpha=1}^{N} \langle \boldsymbol{F}^\alpha \otimes \boldsymbol{r}^\alpha \rangle , \end{aligned} \tag{2.16}$$

where $\boldsymbol{a} \otimes \boldsymbol{b}$ denotes the dyadic product of vectors $\boldsymbol{a}$ and $\boldsymbol{b}$. The kinetic stress $\boldsymbol{\Sigma}_{\mathrm{K}}$ can be interpreted as an ideal gas pressure generated by the vibration of the atoms, whereas the potential part of the stress $\boldsymbol{\Sigma}_{\mathrm{V}}$ characterizes the contributions generated by interatomic interactions. It is clear that $\boldsymbol{\Sigma}_{\mathrm{K}}$ is a symmetric tensor by construction; for $\boldsymbol{\Sigma}_V$ we have that

$$\epsilon^{ijk} \left(\Sigma_V\right)_{jk} = -\frac{1}{\Omega} \left\langle \sum_{\alpha=1}^{N} \epsilon^{ijk} F^\alpha_j r^\alpha_k \right\rangle = -\frac{1}{\Omega} \left( \left\langle \sum_{\alpha=1}^{N} \boldsymbol{F}^\alpha \times \boldsymbol{r}^\alpha \right\rangle \right)^i = 0, \tag{2.17}$$

where we have used the definition of cross product and conservation of angular momentum in Eq. (2.5). Since $\delta^{ip}\delta^{jq} - \delta^{iq}\delta^{jp} = \epsilon_k{}^{ij} \epsilon^{kpq}$ we find that the antisymmetric part of $\boldsymbol{\Sigma}_V$ vanishes. Indeed

$$\left(\Sigma_V\right)^{ij} - \left(\Sigma_V\right)^{ji} = \left(\delta^{ip}\delta^{jq} - \delta^{iq}\delta^{jp}\right) \left(\Sigma_V\right)_{pq} = \epsilon_k{}^{ij} \epsilon^{kpq} \left(\Sigma_V\right)_{pq} = 0, \tag{2.18}$$

where in the last step we have invoked Eq. (2.17). Therefore, the symmetry of $\boldsymbol{\Sigma}_V$, and thus of $\boldsymbol{\Sigma}$, is a consequence of conservation of angular momentum

for the set of point particles. In contrast with the definition of the possibly heterogeneous microscopic stress field, the virial stress is uniquely defined from a thermodynamic viewpoint. For thermodynamic consistency, any microscopic stress definition must satisfy that its average over $\Omega$ recovers the virial stress.

## 2.5 Virial stress per atom

The virial stress does not provide information regarding the distribution of tractions within the system, but rather the average tractions exerted by the system as a whole. For solids, where atoms stay relatively immobile, it is common to define a virial stress per atom by assigning atomic contributions to the total virial stress in Eq. (2.16) [179]. This definition of stress per atom is provided as a post-processing tool in the MD package LAMMPS [35] and has been widely employed to analyze the mechanics of crystals from MD simulations [88, 127, 194, 166]. In this method, the stress is distributed among the particles of the system such that

$$\Omega\boldsymbol{\Sigma} = \sum_{\alpha=1}^{N} \Omega^{\alpha}\boldsymbol{\sigma}^{\alpha}, \tag{2.19}$$

where $\boldsymbol{\sigma}^{\alpha}$ is the stress of particle $\alpha$ and $\Omega^{\alpha}$ is the volume of occupied by particle $\alpha$, which may be computed from a Voronoi tessellation. In particular, each atom carries a kinetic stress

$$\boldsymbol{\sigma}^{\alpha}_{\mathrm{K}} = -\frac{1}{\Omega^{\alpha}} \left\langle m^{\alpha}\boldsymbol{v}^{\alpha} \otimes \boldsymbol{v}^{\alpha} \right\rangle . \tag{2.20}$$

For the potential component, we consider the cluster expansion of the potential, see Section 2.3. In this method the potential part of the virial stress per atom is constructed by distributing the virial stress for each $V_{I_n}$ in the cluster expansion equally among the $n$ particles interacting through $V_{I_n}$. Mathematically,

$$\boldsymbol{\sigma}^{\alpha}_{\mathrm{V}} = \frac{1}{\Omega_{\alpha}} \sum_{I_n \in \mathcal{I}^{\alpha}} \frac{1}{n} \left\langle \sum_{\beta=1}^{n} \partial_{\boldsymbol{r}^{I_n^{\beta}}} V_{I_n} \otimes \boldsymbol{r}^{I_n^{\beta}} \right\rangle, \tag{2.21}$$

where $\mathcal{I}^\alpha$ collects the set of potential contributions involving particle $\alpha$. It is important to note that for each $V_{I_n}$ in the cluster expansion, the set of forces $-\partial_{\boldsymbol{r}^{I_n^\beta}} V_{I_n}$ are balanced

$$\sum_{\alpha=1}^{n} \partial_{\boldsymbol{r}^{I_n^\alpha}} V_{I_n} = \boldsymbol{0}, \qquad \sum_{\alpha=1}^{n} \partial_{\boldsymbol{r}^{I_n^\alpha}} V_{I_n} \times \boldsymbol{r}^{I_n^\alpha} = \boldsymbol{0}. \tag{2.22}$$

As a consequence, the stress at particle $\alpha$, $\boldsymbol{\sigma}^\alpha$, is symmetric by construction. To define a continuous stress that can be related to a continuum mechanics theory, we first spread each particle contribution in space using Diract delta distributions centered at the mean atomic positions

$$\boldsymbol{\sigma}_{\mathrm{VSA}}(\boldsymbol{x}) = \sum_{\alpha=1}^{N} \boldsymbol{\sigma}^\alpha \delta(\boldsymbol{x} - \langle \boldsymbol{r}^\alpha \rangle). \tag{2.23}$$

where VSA stands for Virial Stress per Atom. This stress, however, is a distribution-like measure rather than a continuous function. We can spatially average this measure with a weight function $w$ following the results in Box 2.1 to find

$$\bar{\boldsymbol{\sigma}}_{\mathrm{VSA}}(\boldsymbol{x}) = \sum_{\alpha=1}^{N} \boldsymbol{\sigma}^\alpha w(\boldsymbol{x} - \langle \boldsymbol{r}^\alpha \rangle). \tag{2.24}$$

Let us note that the averages of $\boldsymbol{\sigma}_{\mathrm{VSA}}$ and $\bar{\boldsymbol{\sigma}}_{\mathrm{VSA}}$ over $\Omega$ recover the virial stress

$$\boldsymbol{\Sigma} = \frac{1}{\Omega} \int_\Omega \boldsymbol{\sigma}_{\mathrm{VSA}}(\boldsymbol{x}) d\boldsymbol{x} = \frac{1}{\Omega} \int_\Omega \bar{\boldsymbol{\sigma}}_{\mathrm{VSA}}(\boldsymbol{x}) d\boldsymbol{x}. \tag{2.25}$$

As explained in Box 2.1, $\bar{\boldsymbol{\sigma}}_{\mathrm{VSA}}$ is symmetric due to the symmetry of $\boldsymbol{\sigma}^\alpha$ and, therefore, is a continuous stress satisfying the continuum statement of balance of angular momentum. However, it is not clear from the definition of $\boldsymbol{\sigma}_{\mathrm{VSA}}(\boldsymbol{x})$ whether it satisfies the continuum statement of balance of linear momentum in the absence of external forces, that is $\mathrm{div}\bar{\boldsymbol{\sigma}}_{\mathrm{VSA}}(\boldsymbol{x}) = \boldsymbol{0}$. In fact, the results on the graphene sheet with a Stone-Wales defect of Fig. 2.1 showed that $\mathrm{div}\bar{\boldsymbol{\sigma}}_{\mathrm{VSA}}(\boldsymbol{x}) \neq \boldsymbol{0}$. Thus, *VSA violates conservation of linear momentum.*

**Box 2.1:** Spatial averaging of microscopic stress fields and balance laws

The raw definitions of the microscopic stress may result in fields with highly localized features (even singular), see Fig. 3.1A for instance. This issue is especially severe in systems where atoms stay relatively immobile, such as crystals at low temperatures, and undermines the interpretation of the microscopic stress from a continuum mechanics viewpoint. Thus, it is often convenient to spatially average microscopic stresses. We define a spatially-averaged stress by

$$\bar{\boldsymbol{\sigma}}(\boldsymbol{x}) = \int_{\Omega} w(||\boldsymbol{x}-\boldsymbol{y}||)\boldsymbol{\sigma}(\boldsymbol{y})d\boldsymbol{y}, \tag{B1}$$

where $w(||\boldsymbol{x}-\boldsymbol{y}||)$ is a weighting function, with compact support, satisfying the normalization property

$$\int_{\Omega} w(||\boldsymbol{x}-\boldsymbol{y}||)d\boldsymbol{y} = 1. \tag{B2}$$

It is important to note that $\bar{\boldsymbol{\sigma}}$ inherits the equilibrium properties of $\boldsymbol{\sigma}$. By construction, it is clear that $\bar{\boldsymbol{\sigma}}$ is symmetric if $\boldsymbol{\sigma}$ is symmetric. Furthermore, the divergence of $\bar{\boldsymbol{\sigma}}$ coincides with the spatial average of $\mathrm{div}\boldsymbol{\sigma}$,

$$\begin{aligned}
\mathrm{div}\bar{\boldsymbol{\sigma}}(\boldsymbol{x}) &= \int_{\Omega} \sigma^{ij}(\boldsymbol{y})\partial_{x_j} w(||\boldsymbol{x}-\boldsymbol{y}||)d\boldsymbol{y} \\
&= \int_{\Omega} \sigma^{ij}(\boldsymbol{y})\left(-\partial_{y_j}\right) w(||\boldsymbol{x}-\boldsymbol{y}||)d\boldsymbol{y} \\
&= \int_{\Omega} \mathrm{div}\boldsymbol{\sigma}(\boldsymbol{y})w(||\boldsymbol{x}-\boldsymbol{y}||), d\boldsymbol{y}
\end{aligned} \tag{B3}$$

where we have used that $\partial_{x_j} w = -\partial_{y_j} w$, integration by parts, and that $w$ has a compact support. Thus, if $\mathrm{div}\boldsymbol{\sigma} = \mathbf{0}$ we get $\mathrm{div}\bar{\boldsymbol{\sigma}} = \mathbf{0}$.

# Chapter 3

# The Irving-Kirkwood-Noll approach

## 3.1 General framework

In the Irving-Kirkwood-Noll (IKN) approach, continuous fields are defined from general non-equilibrium ensemble averages of atomistic properties that are distributed in space [77, 115]. These fields are defined so that they satisfy the balance laws of continuum mechanics by construction. For instance, in this theory the continuum density field is defined as

$$\rho(\boldsymbol{x}) = \sum_{\alpha=1}^{N} \langle m^{\alpha} \delta(\boldsymbol{r}^{\alpha} - \boldsymbol{x}) \rangle \,, \tag{3.1}$$

where here the ensemble average is performed over a general non-equilibrium statistical-mechanics distribution $f(\boldsymbol{r}, \boldsymbol{p}; t)$. For each configuration in the ensemble, the mass of each particle $\alpha = 1, \ldots, N$ is assigned to the position $\boldsymbol{x} = \boldsymbol{r}^{\alpha}$ by means of the Dirac delta distribution. Because of the ensemble averaging, this leads to a quantity with units of mass per unit volume, defining a true density field. Invoking the equivalence between the macroscopic

momentum $\rho(\boldsymbol{x})\boldsymbol{v}(\boldsymbol{x})$ and the microscopic momentum $\sum_{\alpha=1}^{N}\langle m^\alpha \boldsymbol{v}^\alpha \delta(\boldsymbol{r}^\alpha - \boldsymbol{x})\rangle$, the continuum velocity field is defined as

$$\boldsymbol{v}(\boldsymbol{x}) = \frac{1}{\rho(\boldsymbol{x})}\sum_{\alpha=1}^{N}\langle m^\alpha \boldsymbol{v}^\alpha \delta(\boldsymbol{r}^\alpha - \boldsymbol{x})\rangle\,, \tag{3.2}$$

where $\boldsymbol{v}^\alpha$ is the velocity of particle $\alpha$. It is easy to show by a direct calculation invoking Liouville's Eq. (2.8) (see Box 3.1), that the fields defined in Eqs. (3.1) and (3.2) satisfy the continuity equation

$$\partial_t \rho + \mathrm{div}\,(\rho \boldsymbol{v}) = 0, \tag{3.3}$$

expressing balance of mass in continuum mechanics. In the absence of external forces, the continuum balance of linear momentum requires that

$$\mathrm{div}\boldsymbol{\sigma}(\boldsymbol{x}) = \partial_t\left[\rho(\boldsymbol{x})\boldsymbol{v}(\boldsymbol{x})\right] + \mathrm{div}\left[\rho(\boldsymbol{x})\boldsymbol{v}(\boldsymbol{x})\otimes\boldsymbol{v}(\boldsymbol{x})\right]. \tag{3.4}$$

The right hand side of this equation involves $\rho(\boldsymbol{x})$ and $\boldsymbol{v}(\boldsymbol{x})$, which we have already defined. The time-derivative of $\rho(\boldsymbol{x})\boldsymbol{v}(\boldsymbol{x})$ can be computed following Eq. (B6). Inserting the definitions of $\rho$ and $\boldsymbol{v}$ we find [4, 178]

$$\mathrm{div}\boldsymbol{\sigma}(\boldsymbol{x}) = -\mathrm{div}\left(\sum_{\alpha=1}^{N}\left\langle m^\alpha \boldsymbol{v}^\alpha_{\mathrm{rel}}\otimes\boldsymbol{v}^\alpha_{\mathrm{rel}}\delta(\boldsymbol{r}^\alpha - \boldsymbol{x})\right\rangle\right) + \sum_{\alpha=1}^{N}\langle \boldsymbol{F}^\alpha \delta(\boldsymbol{r}^\alpha - \boldsymbol{x})\rangle\,, \tag{3.5}$$

where $\boldsymbol{v}^\alpha_{\mathrm{rel}} = \boldsymbol{v}^\alpha - \boldsymbol{v}(\boldsymbol{r}^\alpha)$ is the relative velocity of particle $\alpha$ with respect to the continuum velocity at position $\boldsymbol{r}^\alpha$, $\boldsymbol{v}(\boldsymbol{r}^\alpha)$; in equilibrium $\boldsymbol{v}^\alpha_{\mathrm{rel}} = \boldsymbol{v}^\alpha$. As discussed next, it is possible to obtain a statistical-mechanics expression of the right-hand side of Eq. (3.5) as the divergence of a tensor. Therefore, this expression provides a connection between the statistical mechanics of the particle system and the continuum stress tensor. However, this equation clearly provides a non-unique definition of $\boldsymbol{\sigma}$ since given any stress field $\boldsymbol{\sigma}$ satisfying Eq. (3.5), we can add any divergence-free field $\boldsymbol{\omega}$, i.e. $\mathrm{div}\boldsymbol{\omega} = 0$, to $\boldsymbol{\sigma}$ with the resulting field $\boldsymbol{\sigma}+\boldsymbol{\omega}$ also satisfying this equation. Therefore, with this approach we may only hope to rationally obtain an unambiguous definition of the stress tensor making as few arbitrary choices as possible [156, 4]. It

**Box 3.1:** Computing rate of change of averages from Liouville's equation

An important point in the IKN theory is the use of Liouville's equation to compute rate of change of ensemble averages. Consider a general quantity $a(\boldsymbol{r}, \boldsymbol{p}, t)$ and its ensemble average $\langle a \rangle$ defined in Eq. (2.11). Then,

$$\frac{d}{dt}\langle a \rangle = \int_\Gamma \partial_t \left[ a f \right] d\boldsymbol{r} d\boldsymbol{p} = \langle \partial_t a \rangle + \int_\Gamma a \partial_t f \, d\boldsymbol{r} d\boldsymbol{p}. \tag{B4}$$

Using Liouville's Eq. (2.8), and integration by parts, the second term in the last equation can be rewritten as

$$\begin{aligned} \int_\Gamma a \partial_t f \, d\boldsymbol{r} d\boldsymbol{p} &= \sum_{\alpha=1}^{N} \int_\Gamma a \left[ -\partial_{\boldsymbol{r}^\alpha} f \cdot \frac{\boldsymbol{p}^\alpha}{m^\alpha} - \partial_{\boldsymbol{p}^\alpha} f \cdot \boldsymbol{F}^{\boldsymbol{\alpha}} \right] d\boldsymbol{r} d\boldsymbol{p} \\ &= \sum_{\alpha=1}^{N} \left\{ \int_\Gamma f \left[ \partial_{\boldsymbol{r}^\alpha} a \cdot \frac{\boldsymbol{p}^\alpha}{m^\alpha} + \partial_{\boldsymbol{p}^\alpha} a \cdot \boldsymbol{F}^\alpha \right] d\boldsymbol{r} d\boldsymbol{p} \right. \\ &\quad \left. + \int_\Gamma \left[ -\partial_{\boldsymbol{r}^\alpha} (a f) \cdot \frac{\boldsymbol{p}^\alpha}{m^\alpha} - \partial_{\boldsymbol{p}^\alpha} (a f) \cdot \boldsymbol{F}^\alpha \right] d\boldsymbol{r} d\boldsymbol{p} \right\}. \end{aligned} \tag{B5}$$

Assuming that the system is infinitely large and that the product $af$ decays appropriately at infinity, the second term in the previous equation vanishes, and we find

$$\boxed{\frac{d}{dt}\langle a \rangle = \langle \partial_t a \rangle + \sum_{\alpha=1}^{N} \left\langle \partial_{\boldsymbol{r}^\alpha} a \cdot \frac{\boldsymbol{p}^\alpha}{m^\alpha} + \partial_{\boldsymbol{p}^\alpha} a \cdot \boldsymbol{F}^\alpha \right\rangle.} \tag{B6}$$

For instance, given the density field $\rho$ defined in Eq. (3.1),

$$\begin{aligned} \partial_t \rho(\boldsymbol{x}) &= \partial_t \sum_{\alpha=1}^{N} \langle m^\alpha \delta(\boldsymbol{r}^\alpha - \boldsymbol{x}) \rangle = \sum_{\alpha=1}^{N} \langle \partial_{\boldsymbol{r}^\alpha} \delta(\boldsymbol{r}^\alpha - \boldsymbol{x}) \cdot \boldsymbol{p}^\alpha \rangle \\ &= -\partial_{\boldsymbol{x}} \left( \sum_{\alpha=1}^{N} \langle \delta(\boldsymbol{r}^\alpha - \boldsymbol{x}) \cdot \boldsymbol{p}^\alpha \rangle \right) = -\mathrm{div}(\rho(\boldsymbol{x}) \boldsymbol{v}(\boldsymbol{x})), \end{aligned} \tag{B7}$$

where we have used that $\partial_{\boldsymbol{r}^\alpha} \delta(\boldsymbol{r}^\alpha - \boldsymbol{x}) = -\partial_{\boldsymbol{x}} \delta(\boldsymbol{r}^\alpha - \boldsymbol{x})$. This proves Eq. (3.3).

is trivial to express the first term in the right-hand side of Eq. (3.5) as the divergence of the tensor

$$\boxed{\boldsymbol{\sigma}_{\mathrm{K}}(\boldsymbol{x}) = -\left\langle \sum_{\alpha=1}^{N} m^{\alpha} \boldsymbol{v}_{\mathrm{rel}}^{\alpha} \otimes \boldsymbol{v}_{\mathrm{rel}}^{\alpha} \delta(\boldsymbol{r}^{\alpha} - \boldsymbol{x}) \right\rangle.} \tag{3.6}$$

This is the kinetic part of the IKN stress, similar to the kinetic part of the virial stress per atom Eq. (2.20). Atomic vibrations generate sources of stress $-m^{\alpha}\boldsymbol{v}_{\mathrm{rel}}^{\alpha} \otimes \boldsymbol{v}_{\mathrm{rel}}^{\alpha}$ that are averaged in the ensemble. The second term in the right-hand side of Eq. (3.5) can be written as the divergence of a tensor by applicacion of Noll's lemma [115], a key technical ingredient in this theory, which leads to an expression of the form

$$\boxed{\boldsymbol{\sigma}_{\mathrm{V}}(\boldsymbol{x}) = \left\langle \sum_{\alpha,\beta>\alpha} \boldsymbol{f}^{\alpha\beta} \otimes \boldsymbol{r}^{\alpha\beta} B(\boldsymbol{r}^{\alpha}, \boldsymbol{r}^{\beta}; \boldsymbol{x}) \right\rangle.} \tag{3.7}$$

where $\boldsymbol{r}^{\alpha\beta} = \boldsymbol{r}^{\beta} - \boldsymbol{r}^{\alpha}$, $\boldsymbol{f}^{\alpha\beta}$ are the terms of a pairwise decomposition of the force acting on particle $\alpha$ (a force decomposition from now on),

$$\boldsymbol{F}^{\alpha} = \sum_{\beta=1}^{N} \boldsymbol{f}^{\alpha\beta}, \tag{3.8}$$

satisfying

$$\boxed{\boldsymbol{f}^{\alpha\beta} = -\boldsymbol{f}^{\beta\alpha},} \tag{3.9}$$

and

$$B(\boldsymbol{r}^{\alpha}, \boldsymbol{r}^{\beta}; \boldsymbol{x}) = \int_{0}^{1} \delta[(1-s)\boldsymbol{r}^{\alpha} + s\boldsymbol{r}^{\beta} - \boldsymbol{x}] ds, \tag{3.10}$$

is the so-called bond function. As a result of this derivation, *the IKN definition of the microscopic stress*

$$\boldsymbol{\sigma} = \boldsymbol{\sigma}_{K} + \boldsymbol{\sigma}_{V}, \tag{3.11}$$

*satisfies balance of linear momentum by construction.*

**Box 3.2:** A comment on extensions of the IKN theory

In this work we focus on the IKN theory as obtained by direct application of Noll's lemma, which leads to a bond function of the form Eq. (3.10). However, an alternative route to Noll's lemma was proposed by Schofield and Henderson [156]. In this theory the bond function takes the general form

$$B(\boldsymbol{r}^\alpha, \boldsymbol{r}^\beta; \boldsymbol{x}) = \int_0^1 \delta[\gamma_{\boldsymbol{r}^\alpha,\boldsymbol{r}^\beta}(s) - \boldsymbol{x}]ds, \tag{B8}$$

where $\gamma_{\boldsymbol{r}^\alpha,\boldsymbol{r}^\beta}(s)$ is any smooth curve joining the positions $\boldsymbol{r}^\alpha$ and $\boldsymbol{r}^\beta$. The choice of different $\gamma$ leads to different definitions of the stress, adding an extra freedom to that existing in the choice of force decomposition. For instance, a popular path for the analysis of lipid bilayers has been the Harasima contour [66], which is made by the union of two line segments, one parallel to the $(x$-$y)$-plane and another parallel to the $z$ direction. However, it has been recently shown that all these alternative paths lead to non-symmetric stresses [4] and are only meaningful for systems with internal structure. For that reason, we do not discuss them further in this work. Furthermore, in our derivation of the microscopic stress following the Doyle-Ericksen formula of continuum mechanics (see Chapter 5) we obtain the bond function Eq. (3.10) from an alternative method that does not rely on Noll's lemma.

Other extensions to the IKN theory for multibody potentials use the concept of center of mass to calculate tractions on virtual planes that split the particles in the potential into two groups. This is the case of the heuristic method proposed by Heinz, Paul and Binder [69]. However, we proved elsewhere [182] that this method does not satisfy balance of linear and angular momentum, and we do not discuss it further in this work.

The bond function spreads the contribution to the stress from the interaction between the pair $\alpha\beta$ along the line segment joining the particles [115]. An important feature that distinguishes the potential part of the IKN stress from the potential part of the virial stress per atom is the presence of line sources, as compared to point sources, where contributions from interactions are spread. It is important to note that *line sources appear naturally in the IKN expression as a requirement for balance of linear momentum through Noll's lemma.* Alternative extensions of the Irving-Kirkwood theory not relying on Noll's lemma have been proposed (see Box 3.2).

The force decomposition establishes the pairwise forces $\boldsymbol{f}^{\alpha\beta}$ between the particles that interact through an arbitrary multibody potential $V(\boldsymbol{r}^1, \dots, \boldsymbol{r}^N)$. An important fact of the IKN theory is that *the force decomposition is not unique in general, and different force decompositions lead to different definitions of the stress, all of which differ by divergence free tensors*[4]. In the original IKN theory, the potential was considered as a sum of 2-body interactions. In this situation, the force decomposition is trivially obtained as the sum of the individual forces from each 2-body potential,

$$\begin{aligned} \boldsymbol{f}^{\alpha\beta} &= -\sum_{I\in\mathcal{I}^\alpha\cap\mathcal{I}^\beta} \partial_{\boldsymbol{r}^\alpha} V_I(\boldsymbol{r}^\alpha, \boldsymbol{r}^\beta) = \sum_{I\in\mathcal{I}^\alpha\cap\mathcal{I}^\beta} \partial_{\boldsymbol{r}^\beta} V_I(\boldsymbol{r}^\alpha, \boldsymbol{r}^\beta) \\ &= -\sum_{I\in\mathcal{I}^\alpha\cap\mathcal{I}^\beta} \tilde{V}_I'(r^{\alpha\beta})\hat{\boldsymbol{r}}^{\alpha\beta}, \end{aligned} \tag{3.12}$$

where $\tilde{V}_I(r^{\alpha\beta}) = V_I(\boldsymbol{r}^\alpha, \boldsymbol{r}^\beta)$ is a representation of the pairwise interaction in terms of the interatomic distance $r^{\alpha\beta} = |\boldsymbol{r}^{\alpha\beta}|$, and $\hat{\boldsymbol{r}}^{\alpha\beta} = \boldsymbol{r}^{\alpha\beta}/r^{\alpha\beta}$. This representation always exists as a result of invariance with respect to rigid body motions. For general multibody potentials, the definition of a force decomposition is not so clear. In the next section we analyze an instance of the IKN stress based on a popular force decomposition for multibody interactions. Let us note that *in the IKN procedure the symmetry of the stress has not been explicitly enforced*. While the symmetry of $\boldsymbol{\sigma}_{\mathrm{K}}$ is clear by construction, the symmetry of $\boldsymbol{\sigma}_{\mathrm{V}}$ will in general depend on the force decomposition, as one can see from inspection of Eq. (3.7). We note that, for 2-body interactions, being

the pairwise forces in Eq. (3.12) parallel to $\boldsymbol{r}^{\alpha\beta}$, it is clear from Eq. (3.7) that the resulting stress is symmetric.

## 3.2 The IKN-GLD stress

A popular force decomposition within the IKN approach for the analysis of biomolecular simulations was proposed by Goetz and Lipowsky as [57]

$$\boxed{\boldsymbol{f}^{\alpha\beta}_{\mathrm{GLD}} = \sum_{n=2}^{N} \frac{1}{n} \sum_{I_n=1}^{M_n} \left( \partial_{\boldsymbol{r}^\beta} V_{I_n} - \partial_{\boldsymbol{r}^\alpha} V_{I_n} \right),} \tag{3.13}$$

where we have used again the cluster expansion of the interatomic potential. The stress resulting from the IKN procedure and the Goetz-Lipowksy decomposition is referred to as IKN-GLD stress and denoted by $\boldsymbol{\sigma}_{\mathrm{GLD}}$. It is clear by definition that $\boldsymbol{f}^{\alpha\beta}_{\mathrm{GLD}} = -\boldsymbol{f}^{\beta\alpha}_{\mathrm{GLD}}$ and

$$\sum_{\beta=1}^{N} \boldsymbol{f}^{\alpha\beta}_{\mathrm{GLD}} = \sum_{n=2}^{N} \frac{1}{n} \sum_{I_n=1}^{M_n} \sum_{\beta=1}^{N} \left( \partial_{\boldsymbol{r}^\beta} V_{I_n} - \partial_{\boldsymbol{r}^\alpha} V_{I_n} \right) = -\sum_{n=2}^{N} \sum_{I_n=1}^{M_n} \partial_{\boldsymbol{r}^\alpha} V_{I_n} = \boldsymbol{F}^\alpha, \tag{3.14}$$

where we have used balance of linear momentum within clusters Eq. (2.22). Thus, the GLD is a legitimate force decomposition. Furthermore, if $V_{I_n}(\boldsymbol{r}^\alpha, \boldsymbol{r}^\beta)$ is a genuine pairwise interaction, GLD recovers the pairwise term $\tilde{V}'_{I_n}(r^{\alpha\beta})\hat{\boldsymbol{r}}^{\alpha\beta}$. However, given the form of Eq. (3.13), it is not clear whether $\boldsymbol{\sigma}_{\mathrm{GLD}}$ is symmetric for multibody potentials. The IKN-GLD stress has been widely employed for the analysis of biomolecular assemblies such as lipid bilayers (see [91, 62, 167, 189, 202, 129, 113, 16, 116, 165, 123, 117, 202, 16] for a selection of relevant works), or membrane proteins [116] and therefore it is important to carefully analyze its features.

We start by revisiting the simulation of the graphene sheet with a Stone-Wales defect presented in Chapter 2. The trace of the IKN-GLD stress without filtering is shown in Fig. 3.1A. Although this is a continuous field by definition, it has marked concentrations at the interaction lines between atoms. To get a continuous stress that smears out this atomistic signature, we spatially average

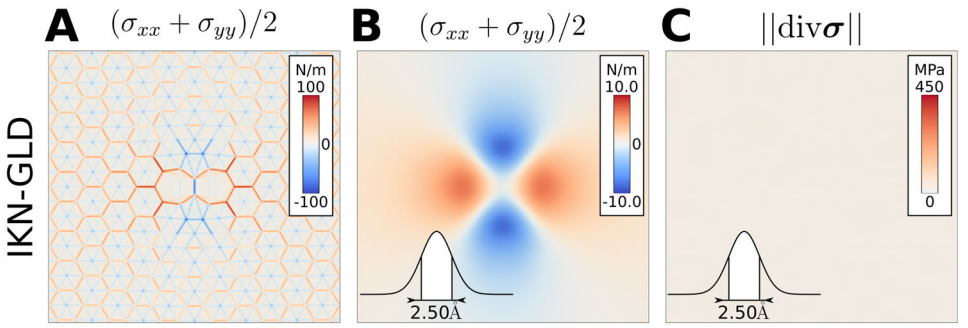


**Figure 3.1**: IKN-GLD stress around a Stone-Wales defect in a graphene sheet. (A) Trace of the raw IKN-GLD stress. As atoms remain almost stationary in the crystalline structure, the raw stress exhibits all interaction lines between carbon atoms. The color of these interaction lines indicate the magnitude and sense of the interatomic forces. (B) Trace of the IKN-GLD with a Gaussian filter of standard deviation of 1.25Å. The resulting continuous stress is very similar to that obtained from the virial stress per atom in Fig. 2.1. (C) Norm of the divergence of the IKN-GLD stress. The IKN-GLD stress is divergence-free as expected by mechanical equilibrium.

the resulting stress with a Gaussian filter to obtain $\bar{\boldsymbol{\sigma}}_{\mathrm{GLD}}$ as explained in Box 2.1. We plot the resulting stress in Fig. 3.1B. To see if this stress is self-equilibrated, we compute its divergence. In agreement with the IKN theory, $\mathrm{div}\boldsymbol{\sigma}_{\mathrm{GLD}}$, and thus $\mathrm{div}\bar{\boldsymbol{\sigma}}_{\mathrm{GLD}}$, vanish, as we demonstrate in Fig. 3.1C.

## 3.3 Constraints in the IKN theory and mechanical equilibrium

In the previous section we examined the definition of the IKN-GLD stress and showed that, in agreement with the general IKN theory, it has a vanishing divergence in a graphene sheet with a Stone-Wales defect at thermodynamic equilibrium, in contrast with the virial stress per atom. However, we showed in Chapter 2 that a popular implementation of the IKN-GLD stress leads to non-constant $\sigma^{zz}$ profiles in a lipid bilayer parallel to the $xy$-plane at equilibrium,

which constitutes a violation of balance of linear momentum (see Fig. 2.2B). This issue is striking because it is not coherent with the derivation of the IKN stress based on balance of linear momentum. In the literature, this issue has been reported in atomistic studies [16, 113, 189], while coarse-grained (CG) simulations generally show constant $\sigma^{zz}$ profiles. Apart from other structural differences, a key ingredient that differentiates CG from atomistic simulations is the use of bond constraints. Bonds in atomistic simulations are stiff, with short characteristic times. To increase the integration time-step and improve the computational efficiency, covalent bonds are often treated with rigid constraints. Common constraint algorithms include LINCS [73], SHAKE [52], and SETTLE [108]. On the other hand, CG simulations usually treat bonds with harmonic potentials, since these bonds are softer, with time-scales that can be more easily resolved. *The IKN theory does not deal with forces from constraints explicitly, and the contributions from constraints to the stress have usually been treated heuristically in MD codes.* For these reasons, the unphysical non-constant $\sigma^{zz}$ profiles have been related to the presence of bond constraints [118, 16, 119, 1, 122].

To analyze whether bond constraints are the reason of the non-constant $\sigma^{zz}$ profiles, we examine the stress from four different CG and atomistic models of a POPE (1-palmitoyl-2-oleoyl-sn-glycero-3-phosphoethanolamine) lipid bilayer in water, whose components are depicted in Fig. 3.2. In the atomistic POPE model (Fig. 3.2A), all atoms but terminal hydrogens of the structure are considered. For this lipid model, constraints are used to fix the bond lengths between atoms with the LINCS algorithm. The atomistic water model also uses the SETTLE algorithm to constraint the length between hydrogen and oxygen atoms. In the CG POPE model based on the MARTINI force field [98, 99] (Fig. 3.2B), a bead represents a point particle resulting from the coarse-graining of 4 atoms of the atomistic structure. In this model bonds are softer and are treated as harmonic bonds. We consider three types of CG water molecules. In the simplest CG MARTINI model, a water molecule is represented with a single bead. In the more complex big multipole water (BMW) model [195], water molecules are effectively represented as super-molecules with three

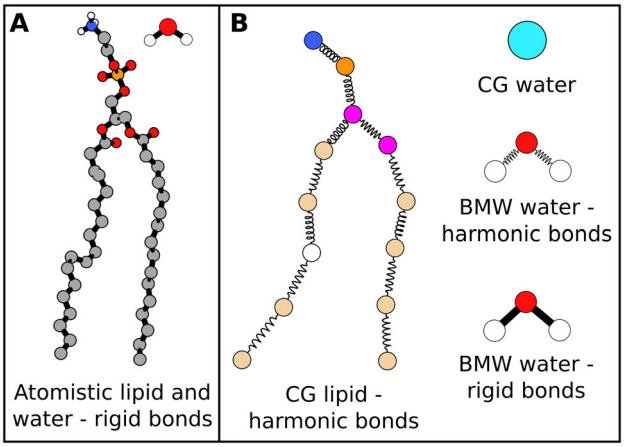


**Figure 3.2**: (A) Atomistic model for a POPE lipid and a water molecule. All bonds are treated with bond constraints. (B) Coarse-grained MARTINI models of POPE and water. In the model, the lipid is represented by beads that agglutinate the effect of 4 atoms. Bonds are treated with harmonic bonds. Water can be treated as a single bead, with a flexible BMW model or with a rigid BMW model.

beads following the underlying atomic structure. In this special kind of CG model, bonds between the three beads of the BMW water are usually modeled as rigid with bond constraints (CG-BMW-RW). It can also be treated as flexible with harmonic bonds (CG-BMW-FW). Details on the simulation settings and analysis can be found in Appendix B.

We analyze the stress in these models with a widely used implementation of the IKN-GLD theory [97], which we refer to as the reference implementation (Fig. 3.3). In Fig. 3.3A we compute $\sigma^{xx}$ and $\sigma^{zz}$ for CG POPE and observe a constant $\sigma^{zz}$ profile consistent with mechanical equilibrium. However, when we examine the CG-BMW-RW model (Fig. 3.3B), we observe a non-constant normal profile with large variations at the lipid-water interfaces. This unphysical non-constant profile is not present in the similar CG-BMW-FW model (Fig. 3.3C). Thus, this indicates that the presence of bond constraints in

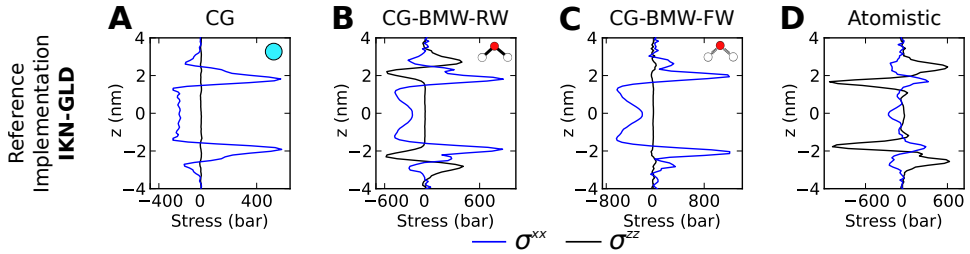


**Figure 3.3**: Stress profiles for different coarse-grained and atomistic models of a POPE lipid bilayer analyzed with the reference implementation. (A) MARTINI model, (B) MARTINI with rigid BMW water molecules, (C) MARTINI with flexible water molecules, (D) Atomistic model. Models with bond constraints show non-constant $\sigma^{zz}$ profiles violating balance of linear momentum.

water is the source for the non-constant $\sigma^{zz}$. For the atomistic model (Fig. 3.3D), we observe a very large non-constant $\sigma^{zz}$, whose signal is now also present at the lipid core, presumably due to LINCS constraints. Thus, it is clear that a proper treatment of constraints is required to avoid this unphysical results.

Here, we argue that *constraints admit a straightforward treatment within the IKN procedure* by noting that Liouville's equation Eq. (2.8) remains essentially unchanged in the presence of constraints [67]. Considering $Q$ constraints denoted by $C_q\left(\{\boldsymbol{r}^\alpha\}\right) = 0$, Liouville's equation governing the evolution of the probability distribution of the system takes the form

$$\partial_t f = \sum_\alpha \left[ -\boldsymbol{v}^\alpha \cdot \partial_{\boldsymbol{r}^\alpha} f + \frac{1}{m^\alpha} \underbrace{\left( \partial_{\boldsymbol{r}^\alpha} V + \sum_q \boldsymbol{F}_q^\alpha \right)}_{\boldsymbol{F}^\alpha} \cdot \partial_{\boldsymbol{v}^\alpha} f \right],$$

where $\boldsymbol{F}_q^\alpha = \lambda_q \partial C_q / \partial \boldsymbol{r}^\alpha$ are the constraint forces and $\lambda_q$ are the corresponding Lagrange multipliers provided by the constraint algorithms. Based on this, the IKN procedure outlined in Section 3.1 can be directly applied to the constrained system, where $\boldsymbol{F}^\alpha$ includes now the constraint forces. Note that a given particle may be subject to multiple constraints simultaneously, e.g. a carbon atom bonded to four other atoms. Following the common approach

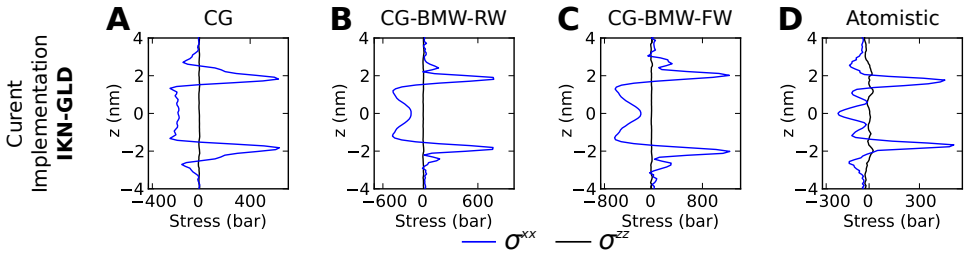


**Figure 3.4**: Stress profiles for different coarse-grained and atomistic models of a POPE lipid bilayer analyzed with the current implementation and IKN-GLD. (A) MARTINI model, (B) MARTINI with rigid BMW water molecules, (C) MARTINI with flexible water molecules, (D) Atomistic model. In this case, all models produce constant $\sigma^{zz}$ profiles.

of decomposing separately each additive contribution to $\boldsymbol{F}^{\alpha}$, and noting that a bond constraint $C_q = r^{\alpha\beta} - d = 0$ between particles $\alpha$ and $\beta$ depends only on their distance, the corresponding constraint forces admit a trivial decomposition $\boldsymbol{F}_q^{\alpha} = \boldsymbol{f}_q^{\alpha\beta} = \lambda_q \boldsymbol{r}^{\alpha\beta}/r^{\alpha\beta}$.

To show the effect of the proper treatment of bond constraints within the IKN formalism, we repeat the previous analysis of the POPE lipid bilayers with our implementation including constraint forces in the way we advocated in the previous paragraph (Fig. 3.4). We observe that in all models constant normal profiles are obtained in agreement with balance of linear momentum.

## 3.4 Unphysical torques in IKN-GLD

While the IKN-GLD stress with a proper treatment of bond constraints provides a stress consistent with balance of linear momentum, we observed in Chapter 2 that this stress definition can lead to non-symmetric stresses, which violate conservation of angular momentum. To examine this issue further, we revisit the stress components in the DPPC lipid bilayer (see Fig. 3.5A). We find that the off-diagonal components are in fact antisymmetric ($\sigma^{xy}_{\mathrm{GLD}} = -\sigma^{yx}_{\mathrm{GLD}}$) and

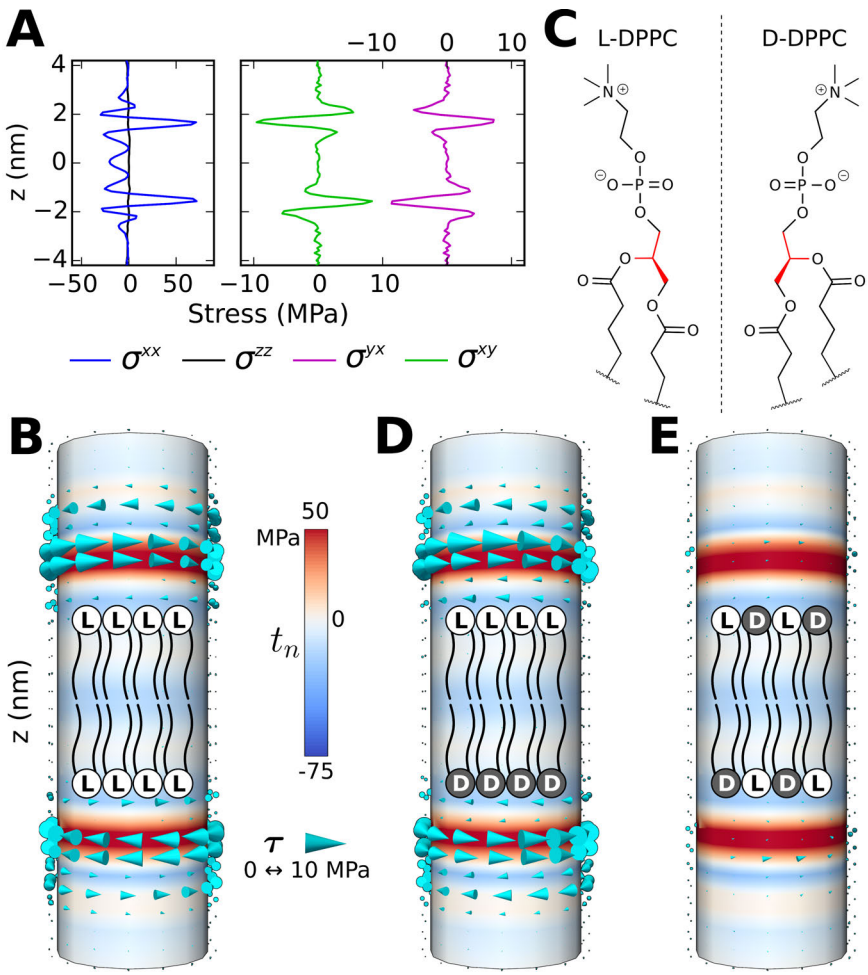


**Figure 3.5**: IKN-GLD leads to unphysical torques related to molecular chirality. (A) Different components of the stress for a DPPC lipid bilayer. Strikingly $\sigma_{xy} = -\sigma_{yx}$. (B) Tractions on the surface of an imaginary cylinder embedded in the lipid bilayer. Tractions are decomposed into a normal component to the cylinder $t_n \boldsymbol{n}$, depicted with a color map, and a tangential component $\boldsymbol{\tau}$, shown with arrows. The antisymmetric stress results in unphysical torques on the surface of the cylinder. (C) DPPC has a usual left-handed chirality. However there are two DPPC enantiomers, L-DPPC and D-DPPC. (D) Tractions on the cylinder when we change the L-DPPC lipids of the lower monolayer by D-DPPC lipids. Torques in the lower monolayer have now an opposite direction to that of the pure L-DPPC. (D) Tractions on the cylinder for a membrane composed of an homogeneous mixture of L-DPPC and D-DPPC. For this model, torques vanish.

of significant magnitude. To gain more physical intuition on this issue, we compute the tractions on the surface of a test cylinder with outer unit normal $\boldsymbol{n}$. The traction can be decomposed into a normal and a tangential component, $\boldsymbol{t} = t_n \boldsymbol{n} + \boldsymbol{\tau}$, which we represent as a color map and using arrows respectively (Fig. 3.5B). Focusing on the tangential traction, we note that $\boldsymbol{\tau}$ is parallel to the bilayer plane with sense and magnitude given by $\sigma^{xy} = -\sigma^{yx}$. It is also clear that the antisymmetry of the stress tensor introduces distributed torques of opposite sign in each leaflet of the bilayer, since $\sigma^{xy}(z) = -\sigma^{xy}(-z)$. We hypothesize that such behavior may be due to the internal structure of each lipid, since the headgroup portion of DPPC contains a chiral carbon. We test this hypothesis by comparing the stress tensors for three systems with different mixtures of the two DPPC enantiomers, L-DPPC and D-DPPC (related by a mirror symmetry), depicted in Fig. 3.5C. Consistent with this hypothesis, the torques induced in each monolayer according to GLD adopt the same sign for a system with one monolayer composed of solely L-DPPC and the second monolayer composed of solely D-DPPC (Fig. 3.5D). Mixing equal numbers of each chiral lipid in both monolayers results in nearly zero distributed torques (Fig. 3.5E). Thus, we conclude that *the off-diagonal components of the IKN-GLD stress tensor reflect the average chirality of the molecular composition.*

To physically interpret the GLD distributed torques, it is necessary to resort to an extended theory of continuum mechanics. In micropolar continuum theories, these torques can be balanced locally invoking a couple stress field $\boldsymbol{m}$. The statement of balance of angular momentum then becomes [156, 193, 111, 158],

$$\epsilon^{i}{}_{jk}\sigma^{jk} = \nabla_l m^{il}. \tag{3.15}$$

In our situation, however, there is no compelling physical justification for this field since the primary objects of our model are achiral point particles [158] and there is no apparent external source for $\boldsymbol{m}$. Thus, although the connection between the non-symmetry of the IKN-GLD stress and molecular chirality is very appealing, this example undermines its mechanical interpretation.

The microscopic stress tensor not only serves as a tool to explore the local distribution of forces, but it can also provide important material properties.

For instance, the Gaussian curvature elastic modulus of lipid bilayers can be computed as

$$\bar{\kappa} = \int (\sigma_{xx} - \sigma_{zz})\, z^2\, dz, \tag{3.16}$$

which is highly sensitive to the features of the stress profile, see [75] and references therein. Common estimates of $\bar{\kappa}$ suggest that it is in the order of the negative of the bending modulus $\sim 5 - 15 \cdot 10^{-20}$ J [101]. For the three bilayer systems with different chiralities in Fig. 3.5, we find $\bar{\kappa}_{\mathrm{GLD}} = (0.91, 0.57, 1.3) \cdot 10^{-20}$ J respectively, with the wrong sign–suggesting that a DPPC bilayer would be unstable [71]– and widely varying magnitudes. This exemplifies the lack of consistency of the IKN-GLD stress.

## 3.5 A central force decomposition: the IKN-CFD stress

We have previously examined two very popular definitions of the microscopic stress. The virial stress per atom gives a symmetric stress by construction, but violates conservation of linear momentum from a continuum viewpoint. The IKN approach introduces stresses that satisfy balance of linear momentum by construction and depend on the definition of a force decomposition. A popular force decomposition is the Goetz and Lipowsky decomposition, which leads to the IKN-GLD stress. However, the IKN-GLD stress is not symmetric in general; we have shown that in systems with chiral constituents, it leads to unphysical torques that cannot be rationalized with the theory of continuum mechanics of simple bodies. In this section we introduce a recent force decomposition, the central force decomposition, which leads to symmetric stresses by construction within the IKN theory [4, 178]. Thus, the resulting stress satisfies both balance of linear and angular momentum by construction in contrast with previous definitions.

It has been recently shown [4] that to obtain a symmetric stress from the IKN procedure, the force decomposition must satisfy the strong law of action and reaction:

$$\boxed{\boldsymbol{f}^{\alpha\beta} = -\boldsymbol{f}^{\beta\alpha}, \qquad \boldsymbol{f}^{\alpha\beta} = \varphi_{\alpha\beta}\hat{\boldsymbol{r}}^{\alpha\beta}.} \tag{3.17}$$

The first condition was previously required to invoke Noll's lemma (see Eq. (3.9)). The second condition ensures that the resulting stress is symmetric; since $\boldsymbol{f}^{\alpha\beta}$ is parallel to $\boldsymbol{r}^{\alpha\beta}$, the symmetry of the stress is apparent recalling Eq. (3.7). A force decomposition satisfying Eq. (3.17) is called a central force decomposition (CFD) [4, 178].

To define a CFD, let us express the potential energy of the system $V(\boldsymbol{r}^1, \dots, \boldsymbol{r}^N)$ in terms of the set of distances defined by particles $\boldsymbol{r}^1, \dots, \boldsymbol{r}^N$, which we denote by $\{r^{\alpha\beta}\}$. With such representation $\widetilde{V}(\{r^{\alpha\beta}\})$, which always exists as result of invariance with respect to rigid body transformations of classical potentials [178], we can define the corresponding CFD as

$$\boldsymbol{f}^{\alpha\beta}_{\text{CFD}} = \varphi_{\alpha\beta}\hat{\boldsymbol{r}}^{\alpha\beta}, \tag{3.18}$$

where

$$\varphi_{\alpha\beta} = \partial_{r^{\alpha\beta}}\widetilde{V}(\{r^{\alpha\beta}\}). \tag{3.19}$$

It is clear by definition that this definition satisfies Eq. (3.17), and

$$\begin{aligned}\boldsymbol{F}^{\alpha} &= -\partial_{\boldsymbol{r}^{\alpha}} V(\boldsymbol{r}) = -\sum_{\beta} \partial_{r^{\alpha\beta}}\widetilde{V}(\{r^{\alpha\beta}\})\partial_{\boldsymbol{r}^{\alpha}} r^{\alpha\beta} \\ &= \sum_{\beta} \partial_{r^{\alpha\beta}}\widetilde{V}(\{r^{\alpha\beta}\})\hat{\boldsymbol{r}}^{\alpha\beta} = \sum_{\beta} \boldsymbol{f}^{\alpha\beta}_{\text{CFD}},\end{aligned} \tag{3.20}$$

which shows that CFD is a genuine force decomposition. However, this CFD has an important limitation when $N > 4$. To show this, we first note that the $N(N-1)/2$ interatomic distances between $N$ particles $(r^{12}, \dots, r^{(N-1)N})$ cannot be arbitrarily chosen in the space $\mathcal{D} = \mathbb{R}_{+}^{N(N-1)/2}$. There are geometric conditions that guarantee that these distances can be realized by a system of $N$ particles in Euclidean space, which define the so-called shape space $\mathcal{S} \subset \mathcal{D}$. By noting that the dimension of $\mathcal{S}$ is equal to the number of degrees of freedom of a system of point particles removing the 6 degrees of freedom corresponding to rigid body motions, i.e. $\dim\mathcal{S} = 3N - 6$, it is clear that the dimension of $\mathcal{S}$ is smaller than $N(N-1)/2$ for $N > 4$. More rigorously, the geometric conditions that $(r^{12}, \dots, r^{(N-1)N})$ must satisfy in order to embeddable in Euclidean space

are expressed in terms of Caley-Menger determinants [178, 93, 134]

$$\begin{aligned}
\chi(r^{\alpha\beta}, r^{\alpha\gamma}, r^{\beta\gamma}) &\leq 0, \\
\chi(r^{\alpha\beta}, r^{\alpha\gamma}, r^{\alpha\delta}, \dots, r^{\gamma\delta}) &\leq 0, \\
\chi(r^{\alpha\beta}, r^{\alpha\gamma}, r^{\alpha\delta}, r^{\alpha\epsilon}, \dots, r^{\delta\epsilon}) &= 0, \\
\chi(r^{\alpha\beta}, r^{\alpha\gamma}, r^{\alpha\delta}, r^{\alpha\epsilon}, r^{\alpha\zeta}, \dots, r^{\epsilon\zeta}) &= 0, \\
\forall\ \alpha, \beta, \gamma, \delta, \epsilon, \zeta = 1, \dots, N,\ \alpha < \beta < \gamma < \delta < \epsilon < \zeta,&
\end{aligned} \tag{3.21}$$

where $\chi(r^{12}, \dots, r^{(N-1)N})$ is the Caley-Menger determinant given by

$$\chi(r^{12}, \dots, r^{(N-1)N}) = \begin{vmatrix} 0 & s^{12} & s^{13} & \dots & s^{1N} & 1 \\ s^{12} & 0 & s^{23} & \dots & s^{2N} & 1 \\ s^{13} & s^{23} & 0 & \dots & s^{3N} & 1 \\ \vdots & \vdots & \vdots & \ddots & \vdots & \vdots \\ s^{1N} & s^{2N} & s^{3N} & \dots & 0 & 1 \\ 1 & 1 & 1 & \dots & 1 & 0 \end{vmatrix}, \tag{3.22}$$

and $s^{\alpha\beta} = (r^{\alpha\beta})^2$. The first 2 equations in Eq. (3.21) are inequalities involving the distances between all clusters of 3 and 4 particles respectively, generalizing the triangle inequality, and restrict $\mathcal{S}$ to a subset of $\mathcal{D}$ but do not modify the intrinsic dimension of $\mathcal{S}$. Therefore, for a potentials involving up to 4 particles, there is no difficulty in taking the partial derivative in Eq. (3.19). However, the last two equations in Eq. (3.21), which restrict distances between clusters of 5 and 6 particles respectively, limit the intrinsic dimension of $\mathcal{S}$ to $3N - 6$. Therefore, when $N > 4$, the dimension of the manifold $\mathcal{S}$ is smaller than $N(N-1)/2$, and the differential calculus involved in Eq. (3.19) needs to be carefully considered [93, 134]. Indeed, for $N > 4$, $r^{\alpha\beta}$ cannot be arbitrary perturbed without leaving the shape space $\mathcal{S}$. Noting this fact, it has been argued that, to be able to take the partial derivative $\partial_{r^{\alpha\beta}} \widetilde{V}$ in Eq. (3.19), the potential needs to be extended to $\mathcal{D}$ [4, 178]. However, when $N > 4$, there exist infinitely many extensions of the potential onto $\mathcal{D}$, some of which can be obtained by combination of Caley-Menger determinants. For instance for

| Potential | Particles | Pairwise terms |
|---|---|---|
| Coulomb | 2 | 1 |
| Van der Waals | 2 | 1 |
| Angles | 3 | 3 |
| Dihedrals | 4 | 6 |
| Bond constraints | 2 | 1 |
| Harmonic bonds | 2 | 1 |

**Table 3.1**: Number of particles involved in the main MD potentials for biomolecular simulations.

a 5-body potential expressed by the function $\tilde{V}(r^{12}, \dots, r^{45})$ the alternative representation

$$\hat{V}(r^{12}, \dots, r^{45}) = \tilde{V}(r^{12}, \dots, r^{45}) + \chi(r^{12}, \dots, r^{45}), \tag{3.23}$$

coincides with $\tilde{V}$ on $\mathcal{S}$ but extends the potential differently on $\mathcal{D}$, and would produce a different force decomposition in Eq. (3.18). The lack of a rational procedure to fix this gauge freedom has been a source of criticism [111].

A natural way to alleviate the massive non-uniqueness associated with potential extensions is to perform the CFD independently on each of the terms of a multibody expansion of the potential energy. Within this formalism, the CFD can be written as

$$\boxed{\boldsymbol{f}^{\alpha\beta}_{\mathrm{CFD}} = \sum_{n=2}^{N} \sum_{I_n=1}^{M_n} \varphi^{I_n}_{\alpha\beta} \hat{\boldsymbol{r}}^{\alpha\beta},} \tag{3.24}$$

where

$$\varphi^{I_n}_{\alpha\beta} = \partial_{r^{\alpha\beta}} \widetilde{V}_{I_n}(\{r^{\alpha\beta}\}). \tag{3.25}$$

and $\widetilde{V}_{I_n}(\{r^{\alpha\beta}\})$ is the representation of the interatomic potential $V_{I_n}(\{\boldsymbol{r}^{\alpha}\})$ in terms of inter-particle distances. For interatomic potential that do not contain cluster potentials involving more than 4 particles, as it is the case for most force fields in MD simulations (see Table 3.1 for a table of the most relevant potentials in MD), this definition of CFD is unique. For higher order multibody

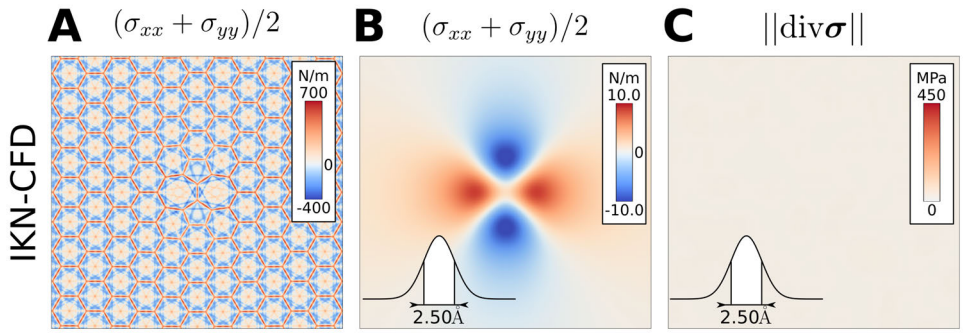


**Figure 3.6**: IKN-CFD stress around a Stone-Wales defect in a graphene sheet. (A) Trace of the raw IKN-GLD stress. (B) Trace of the IKN-CFD with a Gaussian filter of standard deviation of 1.25Å. (C) Norm of the divergence of the IKN-CFD stress, which vanishes as expected by mechanical equilibrium.

potentials, the issue is not resolved. In chapter 5 we revisit this problem and give a canonical CFD that extends Eq. (3.25) to arbitrary multibody potentials.

### Results

We now revisit previous experiments with the IKN-CFD definition. We start by examining the IKN-CFD stress around the Stone-Wales defect in the graphene sheet (Fig. 3.6). As for the IKN-GLD stress, the raw IKN-CFD stress shows concentrated stresses along interaction lines. However, the magnitude and direction of the pairwise forces is very different to the IKN-GLD case because of the different force decomposition (see Fig. 3.7 for the differences between CFD and GLD for a torsion potential). After a Gaussian filter, we obtain a distribution of the stress similar to that of the IKN-GLD stress, albeit with larger magnitudes. As for the IKN-GLD stress, the divergence of the IKN-CFD stress tensor vanishes in agreement with balance of linear momentum.

In the DPPC lipid bilayer the IKN-CFD stress is diagonal with $\sigma^{xy}$ =

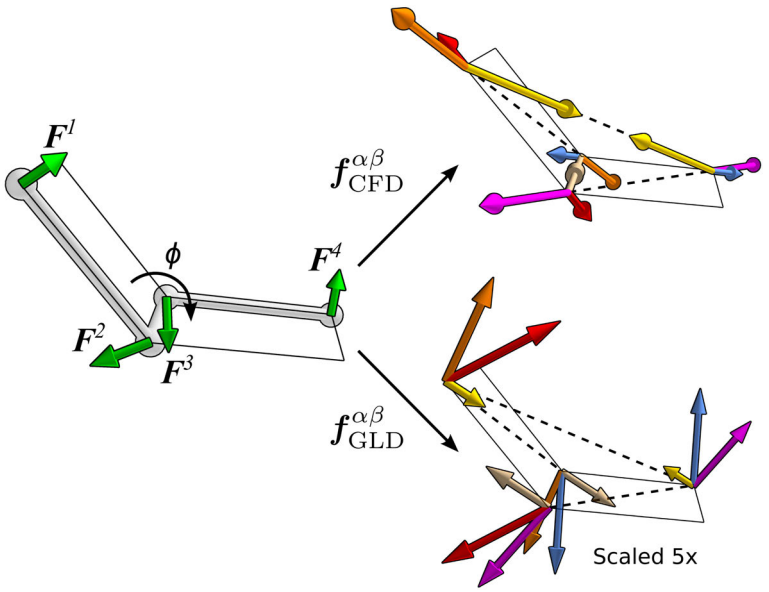


**Figure 3.7**: Pairwise forces obtained from different decompositions. Torsional potential acting on four atoms as determined by a dihedral angle $\phi$ (left). Net forces on each atom are displayed in green. The resulting decomposed forces in the case of CFD (top) and GLD (bottom, scaled 5x for visualization purposes) are shown on the right. There is a great difference both in the magnitude and direction of the resulting force pairs. While the CFD forces are always central (i.e. parallel to $\boldsymbol{r}^{\alpha\beta}$), the GLD pairs are not central, and much smaller than those of CFD.

$\sigma^{yx} = 0$ up to a noisy profile resulting from the finite sampling of the simulation (Fig. 3.6A) and with a constant normal profile, thanks to with our consistent treatment of constraints. Interestingly, the lateral stress $\sigma^{xx} = \sigma^{yy}$ has significant differences with respect to the IKN-GLD stress. Because the IKN-CFD stress is symmetric, we obtain vanishing lateral tractions on the surface of the imaginary cylinder (Fig. 3.6B). Computing the IKN-CFD stress for the different mixtures of DPPC enantiomers produces the same stress profiles (see Figure C.1). With this force decomposition, we compute again the Gaussian bending modulus using Eq. (3.16) for the three systems in Fig. 3.5,

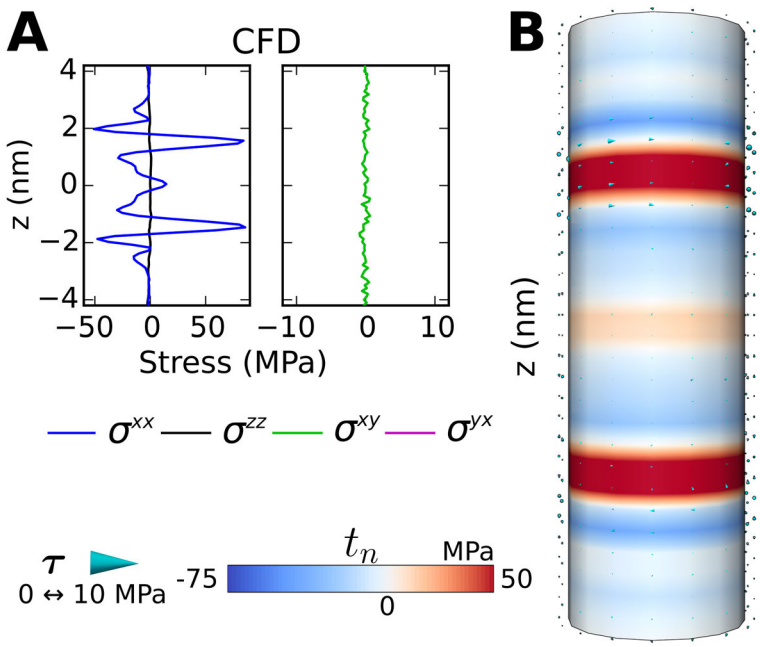


**Figure 3.8**: IKN-CFD stress is symmetric as expected by balance of angular momentum (A) Different components of the stress for a DPPC lipid bilayer. (B) Tractions on the surface of an imaginary cylinder embedded in the lipid bilayer. Tractions are decomposed into a normal component to the cylinder $t_n \boldsymbol{n}$, depicted with a color map, and a tangential component $\boldsymbol{\tau}$, shown with arrows.

finding $\bar{\kappa}_{\text{CFD}} = (-6.4, -6.7, -6.1) \cdot 10^{-20}$ J, in agreement with the common estimates of $\bar{\kappa}$, further supporting the physical validity of the IKN-CFD approach as compared with the IKN-GLD stress.

# Chapter 4

# Examining the microscopic stress in biomembranes

## 4.1 Individual contributions to the stress

Thanks to the mechanically consistent IKN-CFD microscopic stress definition and the proper treatment of constraints, all of which are implemented in our code, we examine here details about the features of the microscopic stress in lipid bilayers. For that, we re-examine the simulations of CG and atomistic POPE lipid bilayers introduced in Section 3.3 focusing on the IKN-CFD stress (see Fig. 4.1). We note that the stress profiles from CG simulations analyzed with IKN-CFD look similar to those of IKN-GLD, while those obtained from the atomistic membrane present significant differences in shape and magnitude (see also Fig. 3.4). This is because CG systems do not contain torsional potentials, for which the CFD and GLD differ greatly (see Fig. 3.7). The qualitative differences between profiles of CG systems and those from atomistic systems are also striking. To further investigate the nature of these stress profiles, we separate the kinetic and the different potential contributions (bonds, van der Waals, Coulomb, angle and dihedral potentials, etc.) for the

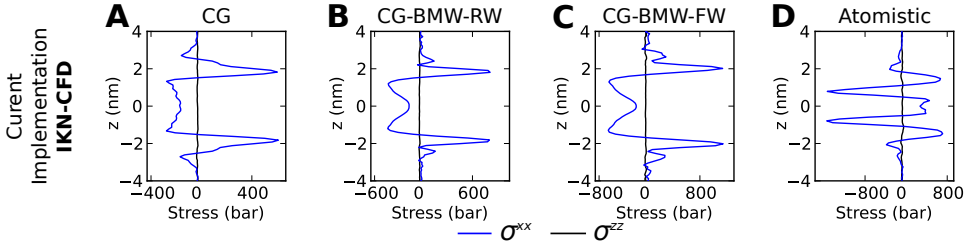


**Figure 4.1**: Stress profiles for different coarse-grained and atomistic models of a POPE lipid bilayer analyzed with the current implementation and IKN-CFD. (A) MARTINI model, (B) MARTINI with rigid BMW water molecules, (C) MARTINI with flexible water molecules, (D) Atomistic model.

coarse-grained (CG and CG-BMW-RW) and atomistic models of POPE, as shown in Fig. 4.2. Thermodynamic equilibrium in these models arises from the sum of various contributions and therefore it is expected that the partial stress profiles of each individual interaction may not exhibit similar behavior when compared across models, e.g. atomistic simulations include potentials that are not considered in the CG systems and change the equilibrium conditions. The treatment of water in the three models is one of the biggest factors influencing the behavior of the individual contributions to the stress.

We first focus on the CG model, which contains the least number of interaction potentials (Fig. 4.2A). We check that for this unconstrained system, the kinetic part of the stress locally satisfies the equipartition theorem and therefore $\sigma_{\mathrm{K}}^{xx}(z) = \sigma_{\mathrm{K}}^{zz}(z) = -\rho(z)k_BT$, where $\rho(z)$ is the particle density profile. The water beads in the CG model are not charged and therefore cannot reproduce the entropic or enthalpic behavior of real water, which are at the origin of the hydrophobic effect keeping the bilayer in place. This makes it necessary to include attractive van der Waals interactions at the lipid headgroups and in the water beads to preserve the integrity of the bilayer and the cohesion of fluid water. Therefore, van der Waals forces result in positive values in both $\sigma^{xx}$ and $\sigma^{zz}$. The lipid headgroups also present electrostatic interactions that lead to net cohesive stresses in this region. The

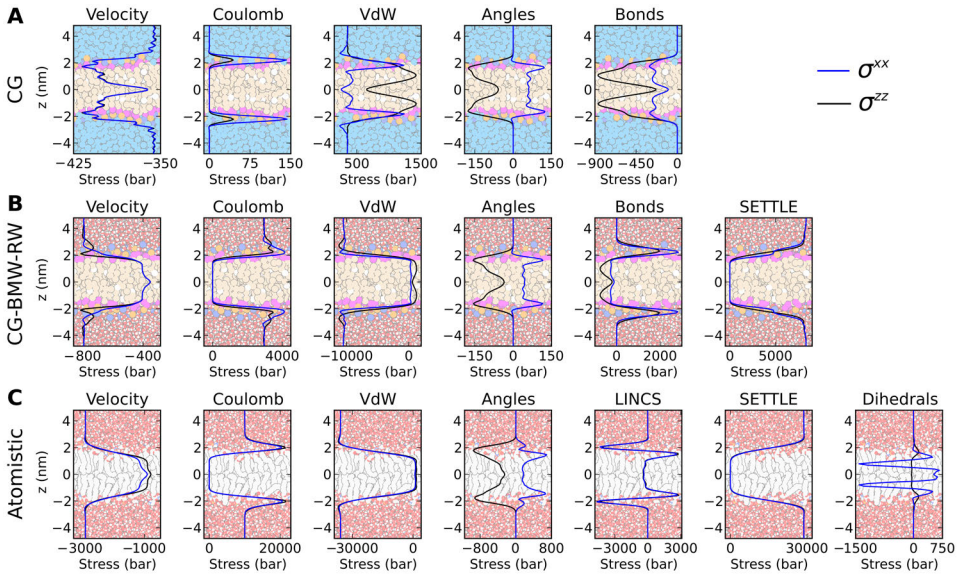


**Figure 4.2**: Individual contributions to the total stress of coarse-grained and atomistic membrane simulations. The lateral profile $\sigma^{xx}$ is represented by blue curves, while $\sigma^{zz}$ is plotted in black. The translucent image in the background of each plot depicts the lipid bilayer (tanned/grey atoms) and the water (light blue/red atoms) regions to guide the reader. (A) shows the contributions for the MARTINI CG POPE system, (B) shows those of the BMW-MARTINI (CG-BMW-RW) POPE with rigid water (SETTLE), and (C) shows the contributions of the atomistic POPE-PME with rigid lipid (LINCS) and water (SETTLE) bonds.

angle contribution presents a repulsive component in $\sigma^{zz}$ and an attractive component in $\sigma^{xx}$, which result from the vertical orientation of the lipids as well as from their packing within the membrane. The bonding contribution to both $\sigma^{xx}$ and $\sigma^{zz}$ is negative due to the reduction, on average, of bond lengths within the packed lipids.

In the more sophisticated CG-BMW-RW (Fig. 4.2B), the different water treatment introduces major changes in several partial profiles when compared to the CG model. These changes are located in the bulk water and at the lipid-water interface, since the two models are very similar in the hydrophobic

core. As expected, the kinetic contribution increases with the degrees of freedom in water. The Coulomb interactions between water molecules, which result in cohesive intermolecular forces due to the dipole-dipole interactions, completely changes the role of van der Waals forces. In this model, van der Waals forces in water mostly result in collisions that generate high repulsive stresses. On the other hand, the SETTLE constraints provide the intramolecular forces that keep the water structure fixed, resulting in cohesive stresses. At the lipid-water interphase, where the particle density is highest in the bilayer, the bond contribution presents an attractive stress to compensate for the higher rate of van der Waals collisions.

The individual contributions in the atomistic system (Fig. 4.2C) are qualitatively similar to those in the CG-BMW-RW model due to the analogous treatment of water, although the stress magnitudes are significantly different. Bonding forces, which are treated with LINCS constraints in this model, result in both attractive and repulsive stresses in the headgroup region. The negative peaks stem from the repulsive constraint forces that balance the attractive electrostatic interaction between the phosphate and ethanolamine groups. The CG and CG-BMW-RW models do not present this feature as these two charged groups are directly connected by a bond and therefore the electrostatic force is excluded.

## 4.2 Effect of unsaturations on stress profiles

In the atomistic model of POPE, the dihedral contributions to $\sigma^{xx}$ display large positive and negative values as shown in Fig. 4.2C (rightmost panel). In fact, as emphasized in Fig. 4.3A, this dihedral contribution nearly coincides with the total lateral stress profile within the hydrophobic core, and therefore the other contributions nearly balance each other in this region. As suggested by the excellent correlation between the location of the double bond and the large negative peaks in each leaflet of POPE, see Fig. 4.3A, we attribute this feature of the lateral stress profile to the dihedral potential that restraints the

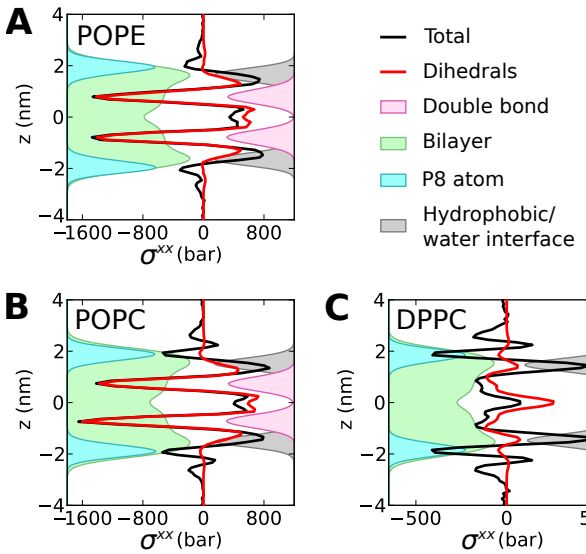


**Figure 4.3**: Dihedral contribution to the lateral stress profile $\sigma^{xx}$ (red curves) compared to the total $\sigma^{xx}$ profile (black curves), in atomistic POPE (A), POPC (B), and DPPC (C) bilayers. Density plots (filled areas, in arbitrary units) of particular lipid components are included for reference. The hydrophobic-water interface is identified from the overlap of water and lipid tail densities, $\rho_{\text{water}}(z) \cdot \rho_{\text{tails}}(z)$.

planar geometry of this *cis* double bond. The potentials used to restrain the geometry of a double bond are significantly stiffer compared to other dihedral interactions. We present a similar comparison of the dihedral contribution vs the total lateral profile for POPC, see Fig. 4.3B, differing from POPE in the headgroup but also exhibiting a double bond in the tails. Again, the contribution of dihedral forces overwhelmingly dominates the $\sigma^{xx}$ profile in the hydrophobic core. We compare this system with DPPC, see Fig. 4.3C, which differs from POPC in that it does not have double bonds. This system shows much smaller negative peaks in the hydrophobic core, and the total pressure profile does not closely follow the dihedral contribution, which is nevertheless significant. Comparison of Fig. 4.3B and C suggests that double

bonds in the lipid tails strongly affect the way stresses are distributed across the bilayer. This is consistent with experimental observations showing that the bending elasticity modulus of a fluid bilayer decreases with the number of unsaturations in the lipid tails, while the lateral area compressibility practically remains unchanged [143, 101]. The IKN-GLD stress does not capture the effect of double bonds in $\sigma^{xx}$, see Fig. 3.4D, and therefore misses the strong mechanical effect of dihedrals in the hydrophobic core predicted by IKN-CFD stress calculations. While the effects of the lipid unsaturations clearly dominate the stress profile differences between these systems, there are also smaller variations in the headgroup region. In all three systems shown in Fig. 4.3, there is a clear correlation between the large positive peak and the hydrophobic-water interface as expected from their unfavorable interaction, which induces a cohesive stress to minimize the exposure of the lipid tails to the water. In the headgroup region, the repulsion between the charged atoms (e.g. phosphorous, see cyan density plots in Fig. 4.3) results in a negative peak. In summary, *these results highlight the complex mechanical organization of lipid bilayers and the potential of the microscopic stress in connecting bilayer mechanics and lipid chemistry.*

# Chapter 5

# A covariant central force decomposition

In this chapter, we reexamine the derivation of the microscopic stress from an alternative route, not relying on the statement of balance of linear momentum, and thus fundamentally different from the IKN procedure. This new approach is based on a variational and geometric characterization of the stress in classical continuum mechanics called the Doyle-Ericksen formula. Following this new route, we obtain an expression that is equivalent to the IKN-CFD stress but that naturally extends CFD to arbitrary multibody potentials. While our derivation is performed at equilibrium, the emerging force decomposition can be naturally framed in the IKN theory, and thus our expression also applies to non-equilibrium situations.

## 5.1 Introduction

We define the microscopic stress as the statistical mechanics equivalent of the so-called Doyle-Ericksen formula in continuum mechanics [45, 100, 200, 199], in an approach similar in spirit to previous variational theories [20, 21, 107].

Suppose we have a continuous medium whose free energy is written as $A = \int_\Omega a dV$, with $a$ being the free energy density per unit of deformed volume. The Doyle-Ericksen formula expresses the Cauchy stress tensor of such system as

$$\sigma^{ij} = 2\,\frac{\partial a}{\partial g_{ij}}, \tag{5.1}$$

where $\boldsymbol{g}$ is the metric tensor of the ambient space. This formula is a consequence of requiring invariance of the statement of conservation of energy balance statement with respect to spatial diffeomorphisms, i.e. conservation of energy should hold in an arbitrary time-dependent curvilinear coordinate system.

For our discrete molecular system the notion of free energy density involved in the Doyle-Ericksen formula in Eq. (5.1) is unclear. Nevertheless, it is straightforward to modify the derivation of the Doyle-Ericksen formula in the continuum case to obtain a more general form not requiring the existence of such a density in terms of a functional derivative as

$$\sigma^{ij} = 2\,\frac{\delta A}{\delta g_{ij}}. \tag{5.2}$$

As we show next, this equation is pertinent to molecular systems because $A$ is indeed a functional of $\boldsymbol{g}$.

Being a fundamental covariance requirement of the theory of continuum mechanics, Eq. (5.2) is a legitimate starting point to define the microscopic stress, alternative to the continuum statement of linear momentum invoked by the more standard IKN approach, c.f. Eq. (3.5). To exercise this idea, we need to provide a statistical mechanics evaluation of the right-hand side of Eq. (5.2). In this case, the dependence on $\boldsymbol{g}$ emerges when the canonical free energy $A$, defined in Eq. (2.10), is expressed covariantly, i.e. for an arbitrary coordinate system, which then allows us to take the functional derivative.

## 5.2 The free energy in a general coordinate system

We analyze next the dependence of the free energy on the ambient metric. For that, we follow the passive approach of [45] and introduce an arbitrary change

of variables in space, characterized by the diffeomorphism $\xi(\boldsymbol{x})$ from $\Omega$ onto itself. This change of variables induces a canonical point transformation in phase space

$$\hat{\boldsymbol{r}}^\alpha = \xi(\boldsymbol{r}^\alpha), \tag{5.3}$$

$$\hat{\boldsymbol{p}}^\alpha = [D\xi(\boldsymbol{r}^\alpha)]^{-T}\,\boldsymbol{p}^\alpha \quad \text{or} \quad p_i^\alpha = D_i\xi^j(\boldsymbol{r}^\alpha)\;\hat{p}_j^\alpha, \tag{5.4}$$

for each particle. Note that momenta transform like co-vectors or one-forms. It immediately follows that $d\hat{\boldsymbol{r}} = [\det(D\xi)]^N\, d\boldsymbol{r}$ and $d\hat{\boldsymbol{p}} = [\det(D\xi)]^{-N}\, d\boldsymbol{p}$, and therefore this transformation leaves the phase volume element unchanged

$$d\hat{\boldsymbol{r}}\, d\hat{\boldsymbol{p}} = d\boldsymbol{r}\, d\boldsymbol{p}. \tag{5.5}$$

We consider a standard form for the kinetic energy in the initial coordinate system

$$K(\boldsymbol{r},\boldsymbol{p};\boldsymbol{g}_0) = \sum_{\alpha=1}^{N} \frac{1}{2m^\alpha} g_0^{ij}(\boldsymbol{r}^\alpha) p_i^\alpha p_j^\alpha, \tag{5.6}$$

where $\boldsymbol{g}_0$ the metric tensor associated to the initial coordinates $\{x^i\}$. In practice, this coordinate system is Cartesian and $g_0^{ij} = \delta^{ij}$. Inserting Eq. (5.4) into Eq. (5.6), we obtain

$$\begin{aligned} K(\boldsymbol{r},\boldsymbol{p};\boldsymbol{g}_0) &= \sum_{\alpha=1}^{N} \frac{1}{2m^\alpha} g_0^{ij}(\xi^{-1}(\hat{\boldsymbol{r}}^\alpha)) D_i\xi^k\; D_j\xi^l\; \hat{p}_k^\alpha\, \hat{p}_l^\alpha, \\ &= \sum_{\alpha=1}^{N} \frac{1}{2m^\alpha} g^{kl}(\hat{\boldsymbol{r}}^\alpha) \hat{p}_k^\alpha\, \hat{p}_l^\alpha = K(\hat{\boldsymbol{r}},\hat{\boldsymbol{p}};\boldsymbol{g}), \end{aligned} \tag{5.7}$$

where we have defined $\boldsymbol{g}$ as the push-forward by the mapping $\xi$ of the original metric tensor

$$\boldsymbol{g} = \xi_*\,\boldsymbol{g}_0 = D\xi^{-T}\left(\boldsymbol{g}_0 \circ \xi^{-1}\right) D\xi^{-1}. \tag{5.8}$$

It is easy to see that $\xi$ is an isometry between $(\Omega, \boldsymbol{g}_0)$ and $(\Omega, \boldsymbol{g})$, and therefore if $(g_0)_{ij} = \delta_{ij}$ is the standard Euclidean metric, then $\boldsymbol{g} = D\xi^{-T} D\xi^{-1}$ is the expression of the Euclidean metric in the coordinates given by $\xi$. In conclusion, the kinetic energy takes the same form in the original and in the new variables, provided the appropriate metric tensor is considered.

As for the potential energy, we consider for definiteness the cluster form of the potential in Eq. (2.14) and express each cluster potential in terms of particle distances

$$V = \sum_{n=2}^{N} \sum_{I_n=1}^{M_n} \widetilde{V}_{I_n}(\{r^{\alpha\beta}\}), \tag{5.9}$$

where $\widetilde{V}_{I_n}$ is any extension of the potential contribution $V_{I_n}$. To express $V$ covariantly, we note that irrespective of the coordinate system, i.e. for any metric tensor given as in Eq. (5.8), $r^{\alpha\beta}$ is the length of the geodesic curve joining points $\hat{\boldsymbol{r}}^{\alpha}$ and $\hat{\boldsymbol{r}}^{\beta}$, which we denote by $\boldsymbol{c}_{\boldsymbol{g}}(\lambda)$ for $\lambda \in [0,1]$, emphasizing its dependence on $\boldsymbol{g}$ [41]. Since here $\boldsymbol{g}$ is the expression of the standard Euclidean metric in a general coordinate system, there exists a single geodesic joining any two particles (the straight line of Euclidean space described in the general coordinate system). Thus, the distance between two particles can be written as

$$r^{\alpha\beta}(\hat{\boldsymbol{r}}^{\alpha}, \hat{\boldsymbol{r}}^{\beta}; \boldsymbol{g}) = \int_0^1 \sqrt{[g_s]_{ij}\,(\boldsymbol{c}_{\boldsymbol{g}}(\lambda))\;\partial_\lambda c^i_{\boldsymbol{g}}(\lambda)\,\partial_\lambda c^j_{\boldsymbol{g}}(\lambda)}\; d\lambda, \tag{5.10}$$

which clearly shows that $r^{\alpha\beta}$, and hence $V$, $H$, and $A$, are functionals of $\boldsymbol{g}$. Because $\xi$ is an isometry between $(\Omega, \boldsymbol{g}_0)$ and $(\Omega, \boldsymbol{g})$,

$$r^{\alpha\beta}(\hat{\boldsymbol{r}}^{\alpha}, \hat{\boldsymbol{r}}^{\beta}; \boldsymbol{g}) = r^{\alpha\beta}(\boldsymbol{r}^{\alpha}, \boldsymbol{r}^{\beta}; \boldsymbol{g}_0)$$

and $\boldsymbol{c}_{\boldsymbol{g}} = \xi \circ \boldsymbol{c}_{\boldsymbol{g}_0}$.

Thus, if we define

$$H(\boldsymbol{r}, \boldsymbol{p}; \boldsymbol{g}_0) = K(\boldsymbol{r}, \boldsymbol{p}; \boldsymbol{g}_0) + \sum_{n=2}^{N} \sum_{I_n=1}^{M_n} \widetilde{V}_{I_n}(\{r^{\alpha\beta}(\boldsymbol{r}^{\alpha}, \boldsymbol{r}^{\beta}; \boldsymbol{g}_0)\}) \tag{5.11}$$

and

$$H(\hat{\boldsymbol{r}}, \hat{\boldsymbol{p}}; \boldsymbol{g}) = K(\hat{\boldsymbol{r}}, \hat{\boldsymbol{p}}; \boldsymbol{g}) + \sum_{n=2}^{N} \sum_{I_n=1}^{M_n} \widetilde{V}_{I_n}(\{r^{\alpha\beta}(\hat{\boldsymbol{r}}^{\alpha}, \hat{\boldsymbol{r}}^{\beta}; \boldsymbol{g})\}), \tag{5.12}$$

we have shown that $H(\boldsymbol{r}, \boldsymbol{p}; \boldsymbol{g}_0) = H(\hat{\boldsymbol{r}}, \hat{\boldsymbol{p}}; \boldsymbol{g})$. Performing the change of variables given by Eqs. (5.3,5.4), this fact and Eq. (5.5) allow us to express the canonical free energy of the system as

$$A = -k_B T \log \int e^{-H(\boldsymbol{r}, \boldsymbol{p}; \boldsymbol{g}_0)/(k_B T)} d\boldsymbol{r} d\boldsymbol{p} \tag{5.13}$$

$$= -k_B T \log \int e^{-H(\hat{\boldsymbol{r}},\hat{\boldsymbol{p}};\boldsymbol{g})/(k_B T)} d\hat{\boldsymbol{r}} d\hat{\boldsymbol{p}}$$
$$= -k_B T \log \int e^{-H(\boldsymbol{r},\boldsymbol{p};\boldsymbol{g})/(k_B T)} d\boldsymbol{r} d\boldsymbol{p}, \tag{5.14}$$

where in the last step we have just changed the notation for the integration variables. Examining the first and last lines, we observe that although the free energy is a functional of the metric tensor $A[\boldsymbol{g}]$, it is independent of it as long as it is induced by a change of coordinates as in Eq. (5.8). We can also see that the diffeomorphism $\xi$ in this theory is just a tool to generate an admissible change of the ambient metric tensor, without moving or changing the coordinates of the particles themselves. We examine next the physical consequences of these facts.

## 5.3 Statistical mechanics representation of the microscopic stress and mechanical equilibrium

To compute the functional derivative in Eq. (5.2) we consider a family of changes of coordinates $\xi_s(\boldsymbol{x})$ from $\Omega$ onto itself, parametrized by $s$, and such that at $s = 0$, $\xi_0^i(\boldsymbol{x}) = x^i$ is the identity map. The mappings $\xi_s$ generate by push-forward admissible changes of the ambient metric tensor $\boldsymbol{g}_s$ as in Eq. (5.8), making the free energy $A$ effectively a function of $s$ alone, see Eq. (5.14).

Denoting by $\eta^i(\boldsymbol{x}) = \partial_s \xi_s^i(\boldsymbol{x})|_{s=0}$ the rate of change of the coordinate system at the identity, it follows that [41, 100]

$$\left.\frac{d}{ds}\right|_{s=0} (\boldsymbol{g}_s)_{ij} = \left[\mathcal{L}_{\boldsymbol{\eta}}(\boldsymbol{g}_0)\right]_{ij} = \frac{1}{2}\left[\nabla_i \eta_j + \nabla_j \eta_i\right], \tag{5.15}$$

where $\mathcal{L}_{\boldsymbol{\eta}}(\boldsymbol{g})$ is the Lie derivative of the metric along the vector field $\boldsymbol{\eta}$. Note the analogy with the rate of deformation tensor in continuum mechanics. Thus, the metric variation is characterized by $\boldsymbol{\eta}$ and the functional derivative of any functional depending on the metric tensor, $F[\boldsymbol{g}]$, is given by the relation

$$\left.\frac{d}{ds}\right|_{s=0} F[\boldsymbol{g}_s] = \int_\Omega \frac{\delta F}{\delta g_{ij}} \left[\mathcal{L}_{\boldsymbol{\eta}}(\boldsymbol{g}_0)\right]_{ij} d\Omega = \int_\Omega \frac{\delta F}{\delta g_{ij}} h_{ij}\, d\Omega, \tag{5.16}$$

where we have introduced the shorthand notation $\boldsymbol{h} = \mathcal{L}_{\boldsymbol{\eta}}(\boldsymbol{g}_0)$.

Recalling Doyle-Ericksen formula in Eq. (5.2), the form of the canonical free energy in Eq. (5.14), and Eq. (5.16), we have

$$\begin{aligned}\int_\Omega \frac{1}{2}\boldsymbol{\sigma} : \boldsymbol{h}\, d\Omega = \int_\Omega \frac{\delta A}{\delta \boldsymbol{g}} : \boldsymbol{h}\, d\Omega = \left.\frac{d}{ds}\right|_{s=0} A[\boldsymbol{g}_s] \\ = \int \left( \left.\frac{d}{ds}\right|_{s=0} H(\boldsymbol{r},\boldsymbol{p};\boldsymbol{g}_s) \right) e^{-(H(\boldsymbol{r},\boldsymbol{p};\boldsymbol{g}_0)-A[\boldsymbol{g}_0])/(k_B T)} d\boldsymbol{r}\, d\boldsymbol{p} \\ = \left\langle \left.\frac{d}{ds}\right|_{s=0} H(\boldsymbol{r},\boldsymbol{p};\boldsymbol{g}_s) \right\rangle = \left\langle \int_\Omega \frac{\delta H}{\delta \boldsymbol{g}} : \boldsymbol{h}\, d\Omega \right\rangle = \int_\Omega \left\langle \frac{\delta H}{\delta \boldsymbol{g}} \right\rangle : \boldsymbol{h}\, d\Omega.\end{aligned} \tag{5.17}$$

Thus, by defining the instantaneous microscopic stress tensor as

$$\boldsymbol{\sigma}_{\text{inst}} = 2\frac{\delta H}{\delta \boldsymbol{g}} = \underbrace{2\frac{\delta K}{\delta \boldsymbol{g}}}_{\boldsymbol{\sigma}_{K,\text{inst}}} + \underbrace{2\frac{\delta V}{\delta \boldsymbol{g}}}_{\boldsymbol{\sigma}_{V,\text{inst}}}, \tag{5.18}$$

we can represent the microscopic stress tensor as $\boldsymbol{\sigma} = \boldsymbol{\sigma}_K + \boldsymbol{\sigma}_V$, where the kinetic and potential contributions are the ensemble averages $\boldsymbol{\sigma}_K = \langle \boldsymbol{\sigma}_{K,\text{inst}} \rangle$ and $\boldsymbol{\sigma}_V = \langle \boldsymbol{\sigma}_{V,\text{inst}} \rangle$.

This definition of the stress tensor obviously satisfies balance of angular momentum because it is symmetric by construction. Furthermore, comparing Eqs. (5.13,5.14) and recalling Eq. (5.15), it is clear that

$$0 = \left.\frac{d}{ds}\right|_{s=0} A[\boldsymbol{g}_s] = \int_\Omega \frac{1}{2}\boldsymbol{\sigma} : \nabla \boldsymbol{\eta}\, d\Omega, \tag{5.19}$$

which should hold for any infinitesimal change of coordinates $\boldsymbol{\eta}$. This is the weak form of balance of linear momentum for the microscopic stress.

## 5.4 Uniqueness of the variational definition of the stress tensor

We emphasize that here we consider a system evolving in standard Euclidean space but described by a general set of curvilinear coordinates. For this reason, when computing the functional derivative of $A$ we only consider

metric changes characterized by Eq. (5.15), which are not the most general metric variations (i.e. merely symmetric tensor fields). As we discuss next, this fact is related to the fundamental non-uniqueness of the microscopic stress tensor, also present in the proposed formalism despite previous claims [107, 149]. Indeed, let $\mathcal{L}_2$ be the completion of the Hilbert space of symmetric tensors with the scalar product

$$(\boldsymbol{\alpha}, \boldsymbol{\beta}) = \int_\Omega \alpha^{ij}\beta_{ij} d\Omega. \tag{5.20}$$

This space admits the orthogonal decomposition $\mathcal{L}_2 = \mathcal{L}_2^{\parallel} \oplus \mathcal{L}_2^{\perp}$, where

$$\mathcal{L}_2^{\parallel} = \left\{ \boldsymbol{h} \mid h_{ij} = \frac{1}{2}\left[\nabla_i \eta_j + \nabla_j \eta_i\right] \right\}, \tag{5.21}$$

are the metric variations induced by diffeomorphisms and

$$\mathcal{L}_2^{\perp} = \{\boldsymbol{\omega} \mid \nabla \cdot \boldsymbol{\omega} = \mathbf{0}\}, \tag{5.22}$$

are perpendicular to them [23]. For infinitely large domains and smooth decaying tensors, $\mathcal{L}_2^{\parallel} \cap \mathcal{L}_2^{\perp}$ only contains the zero tensor. Therefore, given any tensor $\boldsymbol{\sigma}$, it can be uniquely decomposed into a parallel part $\boldsymbol{\sigma}^{\parallel} \in \mathcal{L}_2^{\parallel}$ and a normal part $\boldsymbol{\sigma}^{\perp} \in \mathcal{L}_2^{\perp}$. On the other hand, for bounded domains $\mathcal{L}_2^{\parallel} \cap \mathcal{L}_2^{\perp}$ may contain elements different from zero. That is, there may be tensors of the form in Eq. (5.21) with zero divergence. To define a unique decomposition of tensors into a parallel and a normal parts, boundary conditions are required, as explained in [2, 3]. Here we do not discuss this issue further in this work. As a direct consequence of this decomposition, the functional derivative $\delta A/\delta \boldsymbol{g}$ in Eq. (5.17) cannot be uniquely identified since we can add to it any field in $\mathcal{L}_2^{\perp}$ without altering the variation of $A$. Physically, adding a self-equilibrated stress field does not perform work against an infinitesimal metric variation in $\mathcal{L}_2^{\parallel}$.

Considering general variations of the metric would remove this indeterminacy, but such variations would bring the system out of the shape space, where interatomic potentials are not intrinsically defined. In other words, metric variations not induced by changes of coordinates would result in pairwise

distances that cannot be embedded in Euclidean space, and thus it would not make physical sense to evaluate $\widetilde{V}(\{r^{\alpha\beta}\})$ at these pairwise distances. Despite this fundamental indeterminacy also present in the IKN procedure, we show next that the method presented here provides a rational and unambiguous definition of the stress, and leads to a unique central force decomposition irrespective of the number of particles intervening in the potential.

We also see from this discussion that, since $\boldsymbol{\sigma}$ satisfies Eq. (5.19), $\boldsymbol{\sigma} \in \mathcal{L}_2^{\perp}$. In other words, $\boldsymbol{\sigma}$ satisfies the strong form of the balance of linear momentum $\mathrm{div}\boldsymbol{\sigma} = 0$.

## 5.5 Kinetic part of the microscopic stress

We focus now on the kinetic contribution to the stress tensor

$$\boldsymbol{\sigma}_K = 2\left\langle \frac{\delta K}{\delta \boldsymbol{g}} \right\rangle. \tag{5.23}$$

As previously discussed,

$$K(\boldsymbol{r}, \boldsymbol{p}; \boldsymbol{g}_s) = \sum_{\alpha=1}^{N} \frac{1}{2m^\alpha} g_s^{ij}(\boldsymbol{r}^\alpha) p_i^\alpha p_j^\alpha, \tag{5.24}$$

which can be formally expressed as a functional depending on $\boldsymbol{g}(\boldsymbol{x})$ using Dirac distributions $\delta(\boldsymbol{r}^\alpha - \boldsymbol{x})$,

$$K(\boldsymbol{r}, \boldsymbol{p}; \boldsymbol{g}_s) = \sum_{\alpha=1}^{N} \frac{1}{2m^\alpha} \int_\Omega g_s^{ij}(\boldsymbol{x}) p_i^\alpha p_j^\alpha \delta(\boldsymbol{x} - \boldsymbol{r}^\alpha)\, d\Omega. \tag{5.25}$$

The variation produced by a change of metric $\boldsymbol{h} = \mathcal{L}_{\boldsymbol{\eta}}(\boldsymbol{g})$ is

$$\left.\frac{d}{ds}\right|_{s=0} K(\boldsymbol{r}, \boldsymbol{p}; \boldsymbol{g}_s) = -\sum_{\alpha=1}^{N} \frac{1}{2m^\alpha} \int_\Omega h^{kl}(\boldsymbol{x}) p_k^\alpha p_l^\alpha \delta(\boldsymbol{x} - \boldsymbol{r}^\alpha)\, d\Omega, \tag{5.26}$$

where we have used the identity

$$\left.\frac{d}{ds}\right|_{s=0} g_s^{ij}(\boldsymbol{x}) = -g_0^{ik}(\boldsymbol{x}) h_{kl}(\boldsymbol{x}) g_0^{lj}(\boldsymbol{x}) = -h^{ij}(\boldsymbol{x}), \tag{5.27}$$

which follows from differentiating with respect to $s$ the relation $g_s^{ij}\,(g_s)_{jk} = \delta^i_k$. Recalling Eq. (5.16), it is clear that Eq. (5.26) allows us to identify the functional derivative as

$$\frac{\delta K}{\delta g_{ij}}(\boldsymbol{x}) = -\sum_{\alpha=1}^{N} \frac{1}{2m^\alpha} g_0^{ki}(\boldsymbol{x}) g_0^{jl}(\boldsymbol{x}) p_k^\alpha p_l^\alpha \delta(\boldsymbol{x} - \boldsymbol{r}^\alpha). \tag{5.28}$$

Noting that $m^\alpha v^{\alpha i} = g_0^{ik}(\boldsymbol{r}^\alpha) p_k^\alpha$ and taking the ensemble average, we reach the classical Irving-Kirkwood result

$$\sigma_K^{ij}(\boldsymbol{x}) = -\sum_{\alpha=1}^{N} m^\alpha \left\langle v^{\alpha i} v^{\alpha j} \delta(\boldsymbol{x} - \boldsymbol{r}^\alpha) \right\rangle. \tag{5.29}$$

We discuss next the uniqueness of the kinetic stress. Because the kinetic energy can be written as the integral of a kinetic energy density

$$K = \int_\Omega k(\boldsymbol{x}; \boldsymbol{g}_s(\boldsymbol{x})) d\Omega, \tag{5.30}$$

which depends locally on the metric tensor,

$$k(\boldsymbol{x}; \boldsymbol{g}_s(\boldsymbol{x})) = \sum_{\alpha=1}^{N} \frac{1}{2m^\alpha} g_s^{ij}(\boldsymbol{x}) p_i^\alpha p_j^\alpha \delta(\boldsymbol{x} - \boldsymbol{r}^\alpha), \tag{5.31}$$

then the functional derivative can be localized to the partial derivative and

$$\boldsymbol{\sigma}_K(\boldsymbol{x}) = 2 \left\langle \frac{\partial k}{\partial \boldsymbol{g}}(\boldsymbol{x}) \right\rangle. \tag{5.32}$$

This formula leads directly to Eq. (5.29) and is devoid of ambiguity. The key observation in this argument is the existence of a local energy density.

## 5.6 Potential part of the microscopic stress

We focus now on the potential contribution to the stress tensor

$$\boldsymbol{\sigma}_V = 2 \left\langle \frac{\delta V}{\delta \boldsymbol{g}} \right\rangle. \tag{5.33}$$

Unfortunately, the potential energy cannot be naturally expressed as the integral of a potential energy density, i.e. there is no canonical notion of how to localize in space the potential energy of a set of discrete interacting particles [5]. However, the cluster expansion in Eq. (2.14) provides a systematic way to localize as much as possible the potential interactions. By computing variations for each cluster potential $V_{I_n}$ independently, we partially localize these variations because they are only affected by changes of metric that alter the distances between the particles involved, but are independent of changes of metric that alter other regions of space.

The significance of Eq. (5.14) is that we can compute variations of $A$ (or of $V$) by keeping the particle positions fixed and just changing the background metric $\boldsymbol{g}_s$ as given by Eqs. (5.8,5.15). Therefore, we can write the inter-particle distances as

$$r^{\alpha\beta}(s) = \int_0^1 \sqrt{[g_s]_{ij}\,(\boldsymbol{c}(\lambda,s))\;\partial_\lambda c^i(\lambda,s)\,\partial_\lambda c^j(\lambda,s)}\;d\lambda, \tag{5.34}$$

where now the curve $\boldsymbol{c}(\lambda,s)$ is the geodesic relative to $\boldsymbol{g}_s$ joining two particles with fixed coordinates, and consequently we can write the potential energy as

$$V(s) = \sum_{n=2}^{N}\sum_{I_n=1}^{M_n} \widetilde{V}_{I_n} \circ R_{I_n}(s), \tag{5.35}$$

where $R_{I_n}$ maps the parameter $s$ to the sets of distances $\{r^{\alpha\beta}\}$ involved in the potential contribution $\widetilde{V}_{I_n}$ measured with metric tensor $\boldsymbol{g}_s$. Because we only consider metric tensors defined as in Eq. (5.8), the distances produced by $R_{I_n}$ lie on the shape space $\mathcal{S}_{I_n}$, i.e. the range of $R_{I_n} : \mathbb{R}_+ \longrightarrow \mathcal{S}_{I_n}$ is precisely the domain of $\widetilde{V}_{I_n} : \mathcal{S}_{I_n} \longrightarrow \mathbb{R}$. For this reason, potential extensions are not necessary in the present framework.

To identify $\delta V/\delta \boldsymbol{g}$ in Eq. (5.33), we need to evaluate the derivative of $V$ with respect to $s$. A crucial observation is that the chain rule applied to Eq. (5.35) naturally involves the tangent map of $\widetilde{V}_{I_n}$, which being $\widetilde{V}_{I_n}$ a scalar function is homeomorphic to the covariant derivative of $\widetilde{V}_{I_n}$ along $\mathcal{S}_{I_n}$. Thus, we obtain

$$\left.\frac{d}{ds}\right|_{s=0} V = \sum_{n=2}^{N}\sum_{I_n=1}^{M_n}\sum_{\alpha,\beta>\alpha} \varphi^{\mathcal{S}_{I_n}}_{\alpha\beta}\left.\frac{d}{ds}\right|_{s=0} r^{\alpha\beta}(s) \tag{5.36}$$

where, in contrast to Eq. (3.19), here

$$\varphi_{\alpha\beta}^{\mathcal{S}_{I_n}} = \left(\nabla_{\mathcal{S}_{I_n}} \widetilde{V}_{I_n}\right)_{\alpha\beta} \tag{5.37}$$

stands for the $\alpha\beta$ component of the covariant derivative of the potential along the shape space $\mathcal{S}_{I_n}$ expressed in the canonical basis of the space of pairwise distances $\mathcal{D}_{I_n}$. Because the coordinates $\{r^{\alpha\beta}\}$ do not parametrize $\mathcal{S}_{I_n}$ but rather its embedding space $\mathcal{D}_{I_n}$, the covariant derivative can be understood as the projection onto $\mathcal{S}_{I_n}$ of the gradient of a potential extension in $\mathcal{D}_{I_n}$. The result is however independent of the extension.

Further elaborating on Eq. (5.36), we have

$$\left.\frac{d}{ds}\right|_{s=0} V = \sum_{n=2}^{N} \sum_{I_n=1}^{M_n} \sum_{\alpha,\beta>\alpha} \varphi_{\alpha\beta}^{\mathcal{S}_{I_n}} \int_\Omega \frac{\delta r^{\alpha\beta}}{\delta g_{ij}} h_{ij}\, d\Omega \tag{5.38}$$

$$= \int_\Omega \sum_{n=2}^{N} \sum_{I_n=1}^{M_n} \sum_{\alpha,\beta>\alpha} \varphi_{\alpha\beta}^{\mathcal{S}_{I_n}} \frac{\delta r^{\alpha\beta}}{\delta g_{ij}} h_{ij}\, d\Omega, \tag{5.39}$$

which recalling Eq. (5.18) leads to

$$\sigma_{V,\text{inst}}^{ij}(\boldsymbol{x}) = 2 \sum_{n=2}^{N} \sum_{I_n=1}^{M_n} \sum_{\alpha,\beta>\alpha} \varphi_{\alpha\beta}^{\mathcal{S}_{I_n}} \frac{\delta r^{\alpha\beta}}{\delta g_{ij}}(\boldsymbol{x}). \tag{5.40}$$

To evaluate this expression, we use Eq. (5.34) carefully considering the dependence on $s$ to compute

$$\left.\frac{d}{ds}\right|_{s=0} r^{\alpha\beta} = \int_\Omega \frac{\delta r^{\alpha\beta}}{\delta g_{ij}} h_{ij}\, d\Omega \tag{5.41}$$

$$= \int_0^1 \frac{1}{2\,|\partial_\lambda \boldsymbol{c}_0|_{\boldsymbol{g}_0}} \left\{ h_{ij} \partial_\lambda c_0^i \partial_\lambda c_0^j + D_s g_{ij} \partial_\lambda c_0^i \partial_\lambda c_0^j + 2 g_{ij} D_s \partial_\lambda c_0^i\, \partial_\lambda c_0^j \right\} d\lambda,$$

where $\boldsymbol{c}_0(\lambda) = \boldsymbol{c}(\lambda, 0)$ and $D_s$ denotes the covariant differentiation along the vector field $\partial_s \boldsymbol{c}(\lambda, 0)$ [41]. Here, the variation of the length does not involve boundary terms because the end points of the geodesic do not depend on $s$. The second term of the integrand vanishes because the covariant derivative

of the metric tensor is zero. To treat the last term, we first use the fact that $D_s\partial_\lambda \boldsymbol{c} = D_\lambda \partial_s \boldsymbol{c}$ [41]. Then, it is easily seen that it vanishes. Indeed,

$$\int_0^1 \frac{1}{|\partial_\lambda \boldsymbol{c}_0|_{\boldsymbol{g}_0}} g_{ij} D_\lambda W^i \, \partial_\lambda c_0^j \, d\lambda \tag{5.42}$$

is the variation of the length of $\boldsymbol{c}_0$ with respect to a variation of this curve along the vector field $\boldsymbol{W}$. Because $\boldsymbol{c}_0$ is a geodesic, this expression vanishes for all $\boldsymbol{W}$ vanishing at the ends of the curve, in particular $\partial_s \boldsymbol{c}$.

Thus, retaining only the first term we can express the variation of bond lengths in terms of an integral over the whole space by resorting to a Dirac distribution

$$\left.\frac{d}{ds}\right|_{s=0} r^{\alpha\beta}(s) = \int_\Omega \int_0^1 \delta(\boldsymbol{c}_0(\lambda) - \boldsymbol{x}) \frac{h_{ij}(\boldsymbol{x}) \partial_\lambda c_0^i \partial_\lambda c_0^j}{2\sqrt{[g_0]_{kl}(\boldsymbol{x}) \partial_\lambda c_0^k \partial_\lambda c_0^l}} \, d\lambda d\Omega, \tag{5.43}$$

which allows us to identify the functional derivative as

$$\frac{\delta r^{\alpha\beta}}{\delta g_{ij}}(\boldsymbol{x}) = \int_0^1 \delta(\boldsymbol{c}_0(\lambda) - \boldsymbol{x}) \frac{\partial_\lambda c_0^i \partial_\lambda c_0^j}{2\sqrt{[g_0]_{kl}(\boldsymbol{x}) \partial_\lambda c_0^k \partial_\lambda c_0^l}} \, d\lambda. \tag{5.44}$$

Considering Cartesian coordinates ($[g_0]_{ij} = \delta_{ij}$) and parametrizing the straight line as $\boldsymbol{c}_0(\lambda) = (1-\lambda)\boldsymbol{r}^\alpha + \lambda \boldsymbol{r}^\beta$, this expression simplifies to

$$\frac{\delta r^{\alpha\beta}}{\delta \boldsymbol{g}}(\boldsymbol{x}) = \frac{1}{2} \frac{\boldsymbol{r}^{\alpha\beta} \otimes \boldsymbol{r}^{\alpha\beta}}{r^{\alpha\beta}} \underbrace{\int_0^1 \delta\left[(1-\lambda)\boldsymbol{r}^\alpha + \lambda \boldsymbol{r}^\beta - \boldsymbol{x}\right] d\lambda}_{B(\boldsymbol{r}^\alpha, \boldsymbol{r}^\beta; \boldsymbol{x})} . \tag{5.45}$$

Recalling Eq. (5.40), we obtain an expression for the potential part of the stress tensor

$$\begin{aligned} \boldsymbol{\sigma}_V(\boldsymbol{x}) &= \sum_{n=2}^{N} \sum_{I_n=1}^{M_n} \sum_{\alpha,\beta>\alpha} \left\langle \varphi_{\alpha\beta}^{\mathcal{S}_{I_n}} \frac{\boldsymbol{r}^{\alpha\beta} \otimes \boldsymbol{r}^{\alpha\beta}}{r^{\alpha\beta}} B(\boldsymbol{r}^\alpha, \boldsymbol{r}^\beta; \boldsymbol{x}) \right\rangle \\ &= \left\langle \sum_{\alpha,\beta>\alpha} \boldsymbol{f}^{\alpha\beta} \otimes \boldsymbol{r}^{\alpha\beta} B(\boldsymbol{r}^\alpha, \boldsymbol{r}^\beta; \boldsymbol{x}) \right\rangle, \end{aligned} \tag{5.46}$$

which, remarkably, is the Irving-Kirkwood result with a force decomposition

$$\boxed{\boldsymbol{f}^{\alpha\beta} = \sum_{n=2}^{N} \sum_{I_n=1}^{M_n} \varphi_{\alpha\beta}^{\mathcal{S}_{I_n}} \hat{\boldsymbol{r}}^{\alpha\beta}.} \tag{5.47}$$

This last expression should be understood as a sum over all potential contributions that involve particles $\alpha$ and $\beta$. This covariant central force decomposition (cCFD) is a close analog of the usual CFD in Eq. (3.18), which replaces the partial differentiation of $\widetilde{V}_{I_n}$ by a covariant differentiation along the shape spaces $\mathcal{S}_{I_n}$. Since $\mathcal{S}_{I_n}$ is an open subset of $\mathcal{D}_{I_n}$ for $n \leq 4$, cCFD and CFD coincide in this case. However, when $n > 5$, our definition resolves the ambiguity of the usual CFD. Strikingly, this alternative derivation of the IKN theory does not requite Noll's lemma but results in the same bond function, see Eq. (3.10).

## 5.7 Evaluating the covariant derivative of the potential along the shape space

Practically, the evaluation of $(\nabla_{\mathcal{S}_{I_n}} \widetilde{V}_{I_n})_{\alpha\beta}$ can be performed by first computing the gradient of an extension of the potential in the distance space $\mathcal{D}_{I_n}$, $\nabla_{\mathcal{D}_{I_n}} \widetilde{V}_{I_n}$, and then projecting the result onto the tangent of the shape space $\mathcal{S}_{I_n}$.

The calculation of $\nabla_{\mathcal{D}_{I_n}} \widetilde{V}_{I_n}$, see Eq. (3.25), for an arbitrary extension can be

performed by solving the following linear system of equations

$$\underbrace{\begin{pmatrix} \hat{x}^{12} & \dots & \hat{x}^{1n} & 0 & \dots & 0 & \dots & 0 \\ \hat{y}^{12} & \dots & \hat{y}^{1n} & 0 & \dots & 0 & \dots & 0 \\ \hat{z}^{12} & \dots & \hat{z}^{1n} & 0 & \dots & 0 & \dots & 0 \\ -\hat{x}^{12} & \dots & 0 & \hat{x}^{23} & \dots & \hat{x}^{2n} & \dots & 0 \\ -\hat{y}^{12} & \dots & 0 & \hat{y}^{23} & \dots & \hat{y}^{2n} & \dots & 0 \\ -\hat{z}^{12} & \dots & 0 & \hat{z}^{23} & \dots & \hat{z}^{2n} & \dots & 0 \\ \vdots & \ddots & \vdots & \vdots & \ddots & \vdots & \ddots & \vdots \\ 0 & \dots & -\hat{z}^{1n} & 0 & \dots & -\hat{z}^{2n} & \dots & \hat{z}^{(n-1),n} \end{pmatrix}}_{\mathbf{D},\ \dim = P \times S} \underbrace{\begin{pmatrix} \varphi^{12}_{I_n} \\ \vdots \\ \varphi^{1n}_{I_n} \\ \varphi^{23}_{I_n} \\ \vdots \\ \varphi^{2n}_{I_n} \\ \vdots \\ \varphi^{(n-1),n}_{I_n} \end{pmatrix}}_{\boldsymbol{\varphi},\ \dim = S} = \underbrace{\begin{pmatrix} F^1_{I_n,x} \\ F^1_{I_n,y} \\ F^1_{I_n,z} \\ F^2_{I_n,x} \\ F^2_{I_n,y} \\ F^2_{I_n,z} \\ \vdots \\ F^n_{I_n,z} \end{pmatrix}}_{\mathbf{F},\ \dim = P}, \tag{5.48}$$

which reflects the fact that $\boldsymbol{F}^{\alpha}_{I_n} = -\partial_{\boldsymbol{r}^{\alpha}} V_{I_n} = \sum_{\beta} \varphi^{I_n}_{\alpha\beta} \hat{\boldsymbol{r}}^{\alpha\beta}$. Here, $P = 3n$, $S = n(n-1)/2$, and the rank of $\mathbf{D}$ is $R = 3n - 6$ (the number of degrees of freedom of a set of $n$ particles satisfying balance of linear and angular momentum). A particular solution of this system can be obtained, for instance, by minimizing the norm of the solution $\boldsymbol{\varphi}$.

We now note that the normal space to the shape space $\mathcal{S}_{I_n}$ is precisely the kernel of $\mathbf{D}$, i.e. it is the vector space spanned by the solutions of

$$\mathbf{D}\mathbf{X} = \mathbf{0}. \tag{5.49}$$

Any component of the force decomposition on this space does not alter the net forces on the particles, as can be checked by comparing Eqs. (5.48) and (5.49). The solution to this problem can be computed through a QR decomposition. Let $\mathbf{D}^T$ be the transpose of $\mathbf{D}$. Its QR decomposition exists and has the general form

$$\mathbf{D}^T\mathbf{P} = \mathbf{Q}\mathbf{R} = \begin{pmatrix} \mathbf{Q}_1 & \mathbf{Q}_2 \end{pmatrix} \begin{pmatrix} \mathbf{R}_1 & \mathbf{R}_2 \\ \mathbf{0} & \mathbf{0} \end{pmatrix} \tag{5.50}$$

where $\mathbf{Q}$ is an orthogonal matrix of dimension $S \times S$, $\mathbf{Q}_1$ is a $S \times R$ matrix with orthonormal columns (this is uniquely defined), $\mathbf{Q}_2$ is a $S \times (S - R)$ matrix with orthonormal columns, $\mathbf{R}_1$ is a $R \times R$ upper triangular and invertible matrix,

$\mathbf{R}_2$ is a $R \times (P - R)$ matrix, $\mathbf{P}$ is a $P \times P$ pivoting matrix. Then we can rewrite Eq. (5.49) as

$$\mathbf{D}\mathbf{X} = \mathbf{P}\mathbf{R}^T\mathbf{Q}^T\mathbf{X} = \mathbf{P}\begin{pmatrix}\mathbf{R}_1^T & \mathbf{0}\\ \mathbf{R}_2^T & \mathbf{0}\end{pmatrix}\begin{pmatrix}\mathbf{Q}_1^T\\ \mathbf{Q}_2^T\end{pmatrix}\mathbf{X} = \mathbf{0}. \tag{5.51}$$

Taking into account that $\mathbf{Q}$ is an orthogonal matrix, its columns form an orthonormal basis of $\mathbb{R}^S$. We can then define the two components of $\mathbf{X}$ on the subspaces spanned by the columns of $\mathbf{Q}_1$ and $\mathbf{Q}_2$, $\mathbf{X}_1 = \mathbf{Q}_1^T\mathbf{X}$, $\mathbf{X}_2 = \mathbf{Q}_2^T\mathbf{X}$. Inserting this decomposition in Eq. (5.51) we obtain the equivalent system

$$\begin{pmatrix}\mathbf{R}_1^T\mathbf{X}_1\\ \mathbf{R}_2^T\mathbf{X}_1\end{pmatrix} = \mathbf{0}. \tag{5.52}$$

Since $\mathbf{R}_1^T$ is invertible, this results in $\mathbf{X}_1 = \mathbf{0}$, while the component $\mathbf{X}_2$ is completely free. In other words, the kernel of $\mathbf{D}$ is the subspace formed by the column vectors of $\mathbf{Q}_2$. Therefore, given a CFD $\boldsymbol{\varphi}$, its projection onto the shape space is simply

$$\boldsymbol{\varphi}_{\mathcal{S}_{I_n}} = \mathbf{Q}_1\mathbf{Q}_1^T\boldsymbol{\varphi}. \tag{5.53}$$

An alternative method to compute the cCFD involves Caley-Menger determinants. As illustration, let us examine the simplest example of the cCFD for a 5-body potential following this methodology. In this case, $\mathcal{D}_{I_n} = \mathbb{R}_+^{10}$ while $\mathcal{S}_{I_n}$ is a hypersurface with dimension $(3 \cdot 5 - 6) = 9$, where 6 stands for the rigid body degrees of freedom. It can be shown [178] that $\mathcal{S}_{I_n}$ can be locally characterized by the equation

$$\chi(r^{12}, \ldots, r^{45}) = 0. \tag{5.54}$$

The normal to $\mathcal{S}_{I_n}$ can then be computed as

$$\begin{aligned}\boldsymbol{n}_{\mathcal{S}_{I_n}} &= \left[\left(\nabla_{\mathcal{D}_{I_n}}\chi\right)_{\alpha\beta}\right] = \left(\partial_{r^{12}}\chi, \ldots, \partial_{r^{45}}\chi\right),\\ \widehat{\boldsymbol{n}}_{\mathcal{S}_{I_n}} &= \frac{\boldsymbol{n}_{\mathcal{S}_{I_n}}}{||\boldsymbol{n}_{\mathcal{S}_{I_n}}||}.\end{aligned} \tag{5.55}$$

Thus, we can evaluate the covariant derivative of the potential along $\mathcal{S}_{I_n}$ by projecting the derivative of an extension of the potential onto the tangent space

using the normal, i.e.

$$\begin{aligned}\left(\nabla_{\mathcal{S}_{I_n}}\widetilde{V}_{I_n}\right)_{\alpha\beta} &= \partial_{r^{\alpha\beta}}\widetilde{V}_{I_n} - \left(\nabla_{\mathcal{D}_{I_n}}\widetilde{V}_{I_n}\cdot\widehat{\boldsymbol{n}}_{\mathcal{S}_{I_n}}\right)\left(\widehat{n}_{\mathcal{S}_{I_n}}\right)_{\alpha\beta} = \\ &= \partial_{r^{\alpha\beta}}\widetilde{V}_{I_n} - \frac{\left(\widehat{n}_{\mathcal{S}_{I_n}}\right)_{\alpha\beta}}{||\boldsymbol{n}_{\mathcal{S}_{I_n}}||^2}\left(\partial_{r^{12}}\widetilde{V}_I,\ldots,\partial_{r^{45}}\widetilde{V}_I\right)\begin{pmatrix}\partial_{r^{12}}\chi\\ \vdots\\ \partial_{r^{45}}\chi\end{pmatrix}.\end{aligned} \tag{5.56}$$

This is equivalent to the QR method presented before (the normal in Eq. (5.55) is the generator of the null space of **D**). To exercise this formula, we consider the following 5-body potential

$$\begin{aligned}\widetilde{V}_{I_n}(r^{12},\ldots,r^{45}) = \big(&s^{12}+3s^{13}+s^{14}+2s^{15}+5s^{23}+2s^{24}\\ &+5s^{25}+s^{34}+s^{35}+4s^{45}\big)^{1/2}.\end{aligned} \tag{5.57}$$

We want to evaluate the force decomposition Eq. (5.47) at positions

$$\begin{aligned}&\boldsymbol{r}^1=(0,0,0), \quad \boldsymbol{r}^2=(1,0,0),\\ &\boldsymbol{r}^3=(1,0,1), \quad \boldsymbol{r}^4=(0,1,-2),\\ &\boldsymbol{r}^5=(-2,1,3).\end{aligned} \tag{5.58}$$

The normal vector to $\mathcal{S}_{I_n}$ at this configuration is

$$[\boldsymbol{n}_{S_{I_n}}] = \begin{pmatrix}-0.234\\ 0.236\\ 0.075\\ -0.125\\ -0.585\\ -0.287\\ 0.510\\ 0.277\\ -0.313\\ -0.090\end{pmatrix} \tag{5.59}$$

and the gradient of the potential, if we consider its trivial extension to $\mathcal{D}_{I_n}$, is

$$\left[\varphi^{I_n}_{\alpha\beta}\right] = \left[\left(\nabla_{\mathcal{D}_{I_n}} \widetilde{V}_{I_n}\right)_{\alpha\beta}\right] = \begin{pmatrix} 0.058 \\ 0.248 \\ 0.131 \\ 0.437 \\ 0.292 \\ 0.286 \\ 1.273 \\ 0.194 \\ 0.219 \\ 1.258 \end{pmatrix}. \tag{5.60}$$

Therefore, we obtain the covariant derivative

$$\left[\varphi^{\mathcal{S}_{I_n}}_{\alpha\beta}\right] = \left[\left(\nabla_{\mathcal{S}_{I_n}} \widetilde{V}_{I_n}\right)_{\alpha\beta}\right] = \begin{pmatrix} 0.121 \\ 0.184 \\ 0.111 \\ 0.471 \\ 0.449 \\ 0.363 \\ 1.136 \\ 0.119 \\ 0.303 \\ 1.283 \end{pmatrix}. \tag{5.61}$$

Eq. (5.60) is used in the standard CFD, while Eq. (5.61) appears in the cCFD. The two arrays are significantly different. If we now take another extension of the potential to the distance space, summing for instance the Caley-Menger determinant in Eq. (5.54) to the potential $\widetilde{V}_{I_n}$ (which does not affect the potential

along $\mathcal{S}_{I_n}$ as the Caley-Menger determinant is 0 on it), we obtain

$$\left[\varphi^{I_n}_{\alpha\beta}\right] = \left[\left(\nabla_{\mathcal{D}_{I_n}} \widetilde{V}_{I_n}\right)_{\alpha\beta}\right] = \begin{pmatrix} -447.942 \\ 452.796 \\ 143.239 \\ -239.0289 \\ -1119.708 \\ -548.399 \\ 977.667 \\ 530.854 \\ -598.447 \\ -171.067 \end{pmatrix}, \tag{5.62}$$

while the cCDF result

$$\left[\varphi^{\mathcal{S}_{I_n}}_{\alpha\beta}\right] = \left[\left(\nabla_{\mathcal{S}_{I_n}} \widetilde{V}_{I_n}\right)_{\alpha\beta}\right] = \begin{pmatrix} 0.121 \\ 0.184 \\ 0.111 \\ 0.471 \\ 0.449 \\ 0.363 \\ 1.136 \\ 0.119 \\ 0.303 \\ 1.283 \end{pmatrix}, \tag{5.63}$$

is independent of the representation of the potential in terms of distances between particles. Thus, this example shows that, while CFD is extension-dependent, cCFD is uniquely defined as the covariant derivative of the potential along the shape space $\mathcal{S}_{I_n}$.

## 5.8 Numerical results

In this section we exercise the theory described previously on a coiled-coil structural protein. This protein is composed of two identical $\alpha$-helical chains

that wrap around each other to form a super-helix (see Fig. 5.1A). The inner core of this coiled-coil is composed of intercalating hydrophobic amino acids, and is surrounded by opposing negatively and positively charged amino acids. We consider an infinitely long protein, modeled with periodic boundary conditions. The interatomic potential is taken from a widely used protein force-field (CHARMM22/CMAP), which comprises 2- (bonds, Coulomb and van der Waals interactions), 3- (angle potentials), 4- (torsional potentials) and 5-body (cross-term energy correction map, CMAP) interactions. The system is simulated in a NVT ensemble, with a fixed simulation box and the temperature held constant at 298 K. See Appendix B for more details on the simulation settings.

As previously mentioned, 2-, 3- and 4-body interactions are straightforward to decompose in a CFD: once the net forces $\boldsymbol{F}^\alpha$ are computed, the system of equations in Eq. (5.48) admits a unique solution for the pairwise terms $\boldsymbol{f}^{\alpha\beta}$. In this case both CFD and cCFD give the same results. In contrast, Eq. (5.48) for 5-body interactions such as CMAP admits infinitely many solutions. The CMAP interaction [96] is a backbone correction that depends on two dihedral angles, $\phi$ and $\psi$. In the $\phi\psi$-plane, values of the potential are given on a grid, which are then interpolated. Since dihedral angles can be expressed in terms of distances, we can give a natural extension of the potential $V_{\text{CMAP}}\left(\phi\left(\left\{r^{\alpha\beta}\right\}\right), \psi\left(\left\{r^{\alpha\beta}\right\}\right)\right)$, where $\phi$ depends on the distances between the first four particles, while $\psi$ depends on the distances between the last four particles. A natural CFD follows

$$\varphi_{\alpha\beta} = \frac{\partial V_{\text{CMAP}}(\phi,\psi)}{\partial\phi}\frac{\partial\phi}{\partial r^{\alpha\beta}} + \frac{\partial V_{\text{CMAP}}(\phi,\psi)}{\partial\psi}\frac{\partial\psi}{\partial r^{\alpha\beta}}. \tag{5.64}$$

With the terminology of [4], this CFD corresponds to a particular extension of the CMAP potential. This CFD, or any other CFD, can then be projected onto $\mathcal{S}_{I_n}$ to obtain the cCFD. However, as described in Section 5.7, a solution to Eq. (5.48) can be found without introducing an extension by minimizing the norm of $\boldsymbol{\varphi}$. This latter method has two major advantages. First, it is less intrusive with respect to the MD code. This is because it only requires the net forces acting on the particles, which are directly provided by the MD

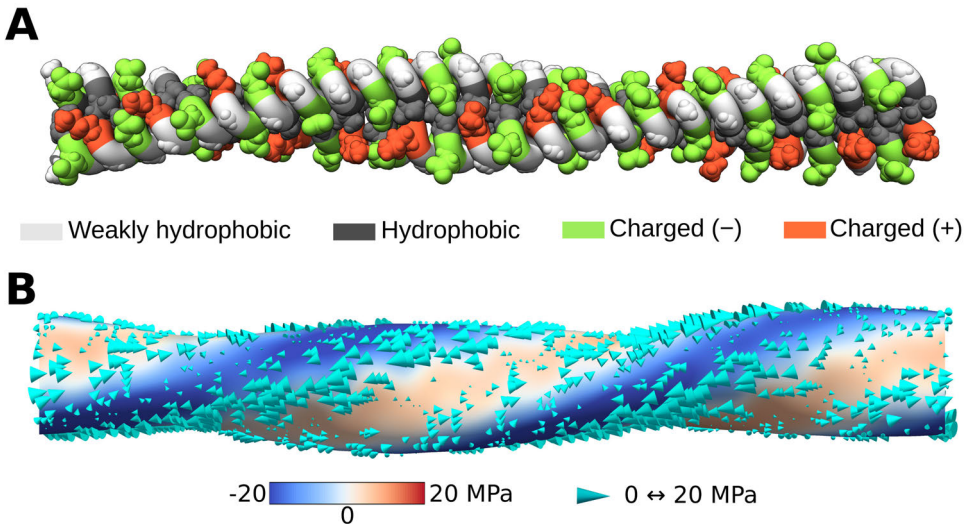


**Figure 5.1**: Structure of the coiled-coil protein (A) and total traction $\boldsymbol{t} = \boldsymbol{\sigma} \cdot \boldsymbol{n}$ on the coiled-coil (B). The total traction is split into the normal traction $t_n = \boldsymbol{t} \cdot \boldsymbol{n}$, which is represented as a color map, and the lateral traction $\boldsymbol{\tau}$, which we plot with arrows.

code, rather than the partial derivatives in Eq. (5.64), which would require modifying the CMAP routine. Second, this method is completely general for any n-body potential, and does not rely on its specific functional form.

To analyze the microscopic stress in the coiled-coil protein, we plot the traction $\boldsymbol{t}$ on the external surface of the protein. This surface is determined from a level set of the mass density of the protein. We then separate the normal traction, $t_n = \boldsymbol{t} \cdot \boldsymbol{n}$, which we represent as a color map, and the tangential traction, $\boldsymbol{\tau} = \boldsymbol{t} - t_n \boldsymbol{n}$, which we represent with arrows. Both the density and the stress are ensemble averaged and smoothed by means of a Gaussian filter.

In Fig. 5.1B we plot the traction for a Gaussian filter of standard deviation 0.4 nm. From this Figure we can extract two major conclusions. First, we observe that the zippered interface between the two coils produces outward tractions (red), while the periphery of the protein is dominated by inward tractions (blue). Regarding $\boldsymbol{\tau}$, we observe that tractions are larger at the

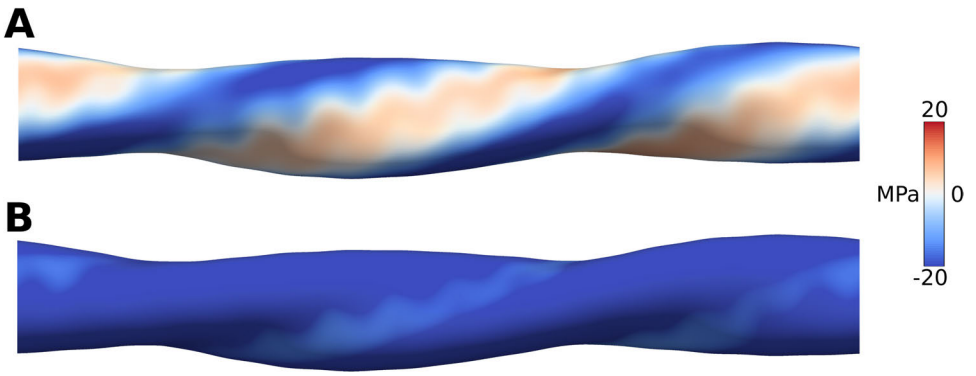


**Figure 5.2**: Normal traction on the surface of the coiled-coil protein for the total stress (A) and for the stress without the contribution from the CMAP interaction (B).

periphery of the protein with opposite regions where arrows go leftwards and rightwards respectively. The total force and torque obtained as surface integrals of the traction are negligible since the cCDF stress is in mechanical equilibrium.

Since the CMAP interaction is a higher-body correction that complicates the calculation of the microscopic stress, one may be tempted to simply ignore it in the analysis of the MD trajectory. To examine this, we plot the normal traction on the protein surface considering all interactions and following the cCFD proposed here (Fig. 5.2A) and the traction obtained ignoring the CMAP contributions to the microscopic stress Fig. 5.2B. The figure clearly shows that the CMAP contribution is very significant and cannot be ignored, since otherwise the normal traction is only inwards indicating that the protein would collapse. This highlights the importance of properly dealing with higher-order interactions, as cCFD does.

We now examine the differences between cCFD and different CFDs when analyzing the CMAP potential in the coiled-coil (Fig. 5.3). We first we compare cCFD (A) with CFD in Eq. (5.64) (B) and see small, yet not negligible, differences (C). To highlight the effect of the extension on the resulting CFD, we examine

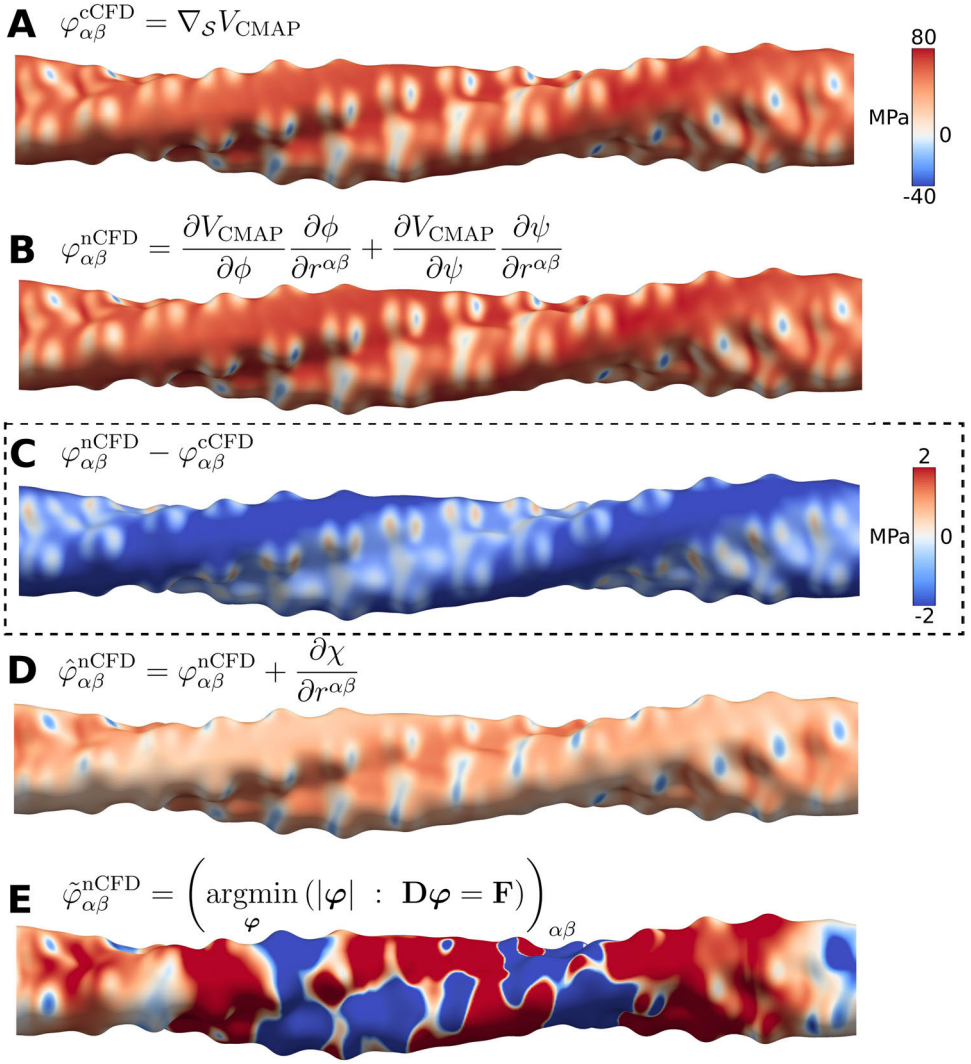


**Figure 5.3**: Comparison of the CMAP contribution to the stress from different central force decompositions for a Gaussian filter of 0.2 nm. (A) cCFD, (B) CFD from the specific potential extension in Eq. (5.64), (C) Difference between A and B, (D) CFD obtained from the alternative representation $V_{\mathrm{CMAP}} + k\chi$, where $\chi$ is the Caley-Menger determinant from Eq. (5.54) and $k = 10^6$ nm$^{-5}$, and (E) CFD obtained from Eq. (5.48) by finding the solution minimizing the norm of $\boldsymbol{\varphi}$.

an alternative extension of the potential of the form $V_{\text{CMAP}} + k\chi$, where $\chi$ is the Caley-Menger determinant defined in Eq. (5.54) (D). We see that in this case, due to the effect of the Caley-Menger determinant, contributions of the resulting CFD along the normal to $\mathcal{S}$ distort the stress field, leading to tractions that differ from those of cCFD largely. We finally compute the CFD obtained from the solution to Eq. (5.48) that minimizes the norm of the CFD (D). This CFD, which does not have a clear physical justification, results in a very non-homogeneous stress, which lacks of a meaningful interpretation. It is remarkable that cCFD is obtained from this CFD by projecting onto $\mathcal{S}$. Thus, selecting the extension of the potential for a CFD is a delicate subject and can lead to very different stresses, some of which do not have a clear physical interpretation. On the other hand, cCFD is independent of the extension of the potential and provides physically meaningful stresses.

We next use this example to examine the interpretation of the microscopic stress in such a nanoscale mechanical system. For this, we represent in Fig. 5.4 the structure and stress field with different levels of resolution as given by the standard deviation of the Gaussian filter. For a Gaussian filter of standard deviation of 0.1 nm for both the stress and the density (A) we observe highly localized tractions, which correlate with interaction sites and molecular features. In particular, we observe high tractions in the zippered region of the protein. As we broaden the spacial extent of the filter (0.2 nm in B and C, 0.4 nm in D), we progressively smoothen geometric and stress features, lower the magnitudes of the tractions, and loose atomistic details. In D, we still observe two intercalated helical bands of inward and outward tractions that relate to hydrophobic and hydrophilic regions of the protein. We represent in C the stress on one of the individual coils, showing the confinement at the coil-coil interface due to the hydrophobic effect. In summary, this example illustrates how the microscopic stress can provide insights about the interplay between chemistry and mechanics, and how it can provide a continuum-like picture of a nanoscale system.

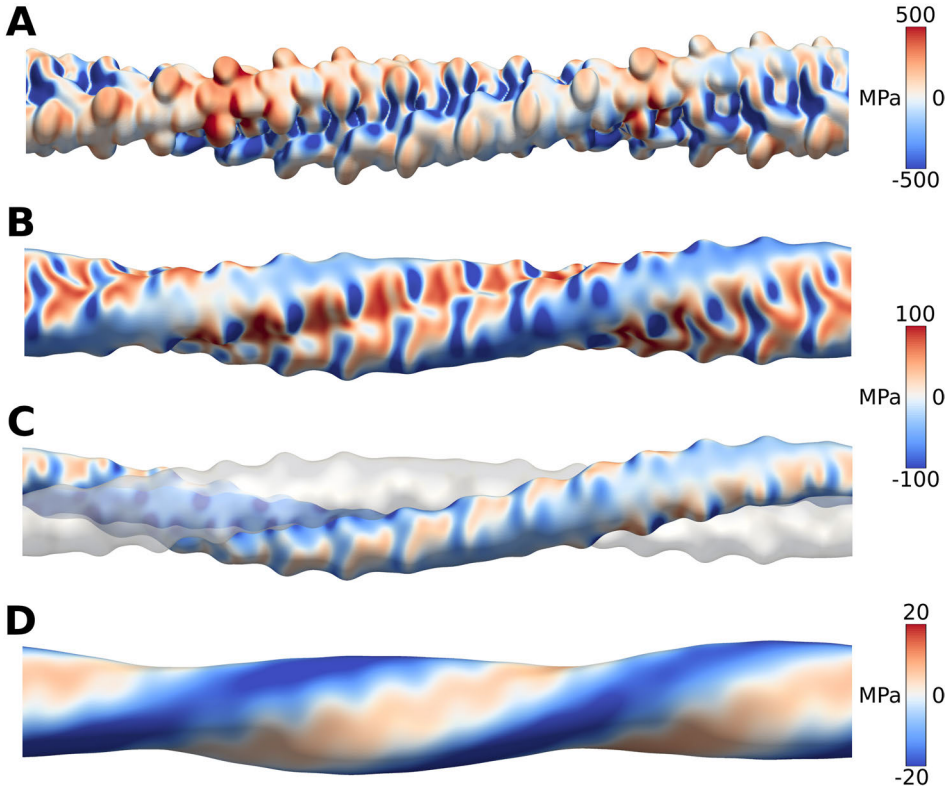


**Figure 5.4**: Normal traction $t_n = \boldsymbol{t} \cdot \boldsymbol{n}$ on the coiled-coil surface for increasing smoothness from Gaussian filters with standard deviations (A) 0.1 nm (B,C) 0.2 nm (D) 0.4 nm. In (C) we plot the traction on the surface of a single coil.

# Chapter 6

# Summary and discussion

In this work we have examined the definition of the microscopic stress in molecular systems. We have shown that existing definitions of the microscopic stress are unsatisfactory, either because they violate the balance laws of linear or angular momentum for a continuum medium or because they are not well-defined for general multibody potentials. We have provided a new definition of the microscopic stress, the IKN-cCFD stress, that satisfies the balance laws by construction and is uniquely defined for arbitrary multibody potentials. More precisely,

- We have shown in a model system, a graphene sheet with a Stone-Wales defect, that the virial stress per atom, a widely employed microscopic stress for the analysis of crystalline materials, violates conservation of linear momentum.

- In contrast, we have introduced the Irving-Kirkwood-Noll (IKN) theory, which leads by construction to stress fields satisfying balance of linear momentum. This definition of the stress depends on the choice of a force decomposition of atomic forces.

- A popular force decomposition for the analysis of lipid bilayers and other biomolecular simulations was proposed by Goetz and Lipowsky, and the stress resulting from the IKN procedure with this decomposition is called the IKN-GLD stress. The IKN-GLD stress violates conservation of angular momentum, as we have shown in a DPPC lipid bilayer. In particular, we have found that this decomposition introduces torques related to molecular chirality, which, however, do not have a clear physical meaning.

- We have shown that the unphysical non-constant $\sigma^{zz}$ profiles in lipid bilayers obtained with a popular implementation of the IKN-GLD stress were a result of an inconsistent treatment of bond constraints, solving a long-standing controversy. We have proven that contributions to the stress from bond constraints can be included naturally in the IKN theory by noting that they do not disturb the form of Liouville's equation, a key ingredient in this theory. We have tested our approach in various coarse-grained and atomistic bilayers containing different types of constraints.

- We have reviewed a recent definition of the IKN stress, the IKN-CFD stress, which provides a stress satisfying balance of linear and angular momentum by construction. This stress is well defined for interatomic potentials involving interactions with less than five particles, which comprises most interatomic potentials used in biomolecular simulations.

- We have used the IKN-CFD stress to examine the complex internal features of lateral stress in lipid bilayers, where we have found the strong effect of unsaturations that was hidden in the commonly-employed IKN-GLD definition.

- However, the CFD is not uniquely defined for potentials involving 5- or higher-multibody potentials, which appear in some models of proteins and metals. To address this issue, we have proposed a covariant CFD (cCFD) that extends CFD to higher multibody potentials based on a covariant definition of the stress within continuum mechanics, the

Doyle-Ericksen formula. We have shown that, in contrast with the CFD, the cCFD provides meaningful stresses regardless of the extension of the potential one uses to evaluate it, which we have exemplified in a coiled-coil protein. This theory provides the basis for a meaningful computation of the microscopic stress from MD simulations.

- We have provided a freely available implementation of the IKN-cCFD stress that can be employed within the GROMACS MD simulation package or as a standalone library. It also provides the virial stress per atom, and the IKN-GLD and the IKN-CFD stresses for comparison.

The new derivation of the microscopic stress is an important theoretical contribution in itself. Our variational and geometric method can be extended in various ways. For instance, by considering the second variation of the free energy with respect to the metric tensor, one should be able to obtain expressions for the fourth order tensor of elastic moduli. Implemented in a computer code, this would allow us to compute a fundamental mechanical property, the elasticity tensor, from an equilibrium MD simulation. This would open new avenues in the connection between chemistry and nanoscale mechanics with potential impact in materials design. Furthermore, the definition of the microscopic stress based on the Doyle-Ericksen formula is in principle applicable to electronic structure models of materials, thereby opening a new potential connection between quantum mechanics and mechanics of materials.

# Part II

# Three-dimensional modeling and simulation of lipid bilayers and other fluid surfaces

# Chapter 7

# Introduction and motivation

Lipid bilayers are unique soft materials, operating in general in the low Reynolds limit. While their shape is predominantly dominated by curvature elasticity as in a solid shell [92], their in-plane behavior is that of a largely inextensible viscous fluid with Newtonian rheology [39]. These two behaviors, however, are tightly coupled through the membrane geometry. Indeed, shape transformations necessarily induce lipid flows that bring material from one part of the membrane to another [47]. On the other hand, fluid flows in the presence of curvature generate out-of-plane forces, which further curve the membrane and elicit elastic forces [140]. This mechanical duality provides structural stability and adaptability, allowing membranes to build relatively stable structures that can nevertheless undergo dynamic shape transformations. The ability of lipid membranes to flow and remodel is critical for the cell function; it is required in vesicular trafficking [168, 151], cell motility and migration [12, 198], mechano-adaptation of cells to stretch and osmotic stress [84], and it allows membrane proteins to diffuse [161], to name a few. Complementary to observations in cells, controlled experimental studies with artificial bilayers highlight this mechanical duality during tubulation [150, 89, 172], phase separation [15], budding and fission [171, 203], or pearling [54].

Thus, lipid membranes are interfacial viscous fluids with bending elasticity. The interplay between viscosity and elasticity determines their relaxation dynamics after they are brought out-of-equilibrium by biological activity. Viscous and elastic forces also determine the magnitude of the forces, or the power, required to remodel biological membranes, or the way membrane proteins diffuse. For these reasons, it is important to develop theoretical models that predict and quantify the out-of-equilbrium behavior of lipid membranes. Molecular dynamics (MD) simulations, either atomistic or coarse-grained, are a major modeling tool for bilayers, capturing chemical specificity and equilibrium properties, see Chapter 2. However, this approach faces severe limitations in the accessible time and length-scales. For instance, the time-step of a fully atomistic simulation is in the order of few femtoseconds, whereas the time-scales of relevant processes in membranes reach the millisecond; similarly, the typical length of a MD box is in the order of tens of nanometers, whereas membranes in vesicles and cells reach sizes of tens of micrometers. Furthermore, consideration of hydrodynamic effects in MD simulations is still a subject in development [192, 38]. In view of this, a continuum model capturing the elasto-hydrodynamics of lipid bilayers is required.

The two essential mechanical features of lipid membranes, their elasticity and interfacial hydrodynamics, have usually been examined separately. The mechanical equilibrium of lipid bilayers can be understood to a large extent with the classical bending model of Helfrich [70, 92, 80, 172]. For that reason, modeling and simulation of lipid bilayers at scales beyond tens of nanometers have mainly focused on this model, e.g. to investigate the different equilibrium configurations of closed vesicles under geometric constraints, such as fixed surface area or fixed enclosed volume [173, 30, 186, 49, 142, 155]. Beyond the Helfrich model, and subsequent refinements such as the Area Difference Elasticity model [159], more general models are required to describe the dynamical transformations that bilayers undergo, which should capture the interfacial dissipative mechanisms that dominate at sub-cellular scales.

The interfacial hydrodynamics of bilayer membranes was first examined separately from membrane deformation, i.e. assuming fixed membrane shape.

These studies focused on the mobility of membrane inclusions, such as proteins, starting with the seminal work of Saffman and Delbrück on planar lipid bilayers [152]. Subsequent studies have considered the effect of fluid boundaries [175] or the (fixed) shape of the fluid membrane [86, 72, 163]. Interfacial flows of vesicles induced by shear bulk flows were also considered at fixed vesicle shape [164]. Following the seminal work of Scriven on the hydrodynamics of insoluble fluid films [157, 9], who presented a mathematical framework coupling changes in geometry and interfacial hydrodynamics, [18] examined the interfacial flow of vesicles in a shear flow allowing for infinitesimal shape deformations. More recently, a geometrically non-linear model for an inextensible viscous interfacial fluid with bending rigidity was examined, formulated geometrically, and exercised under the assumption of axisymmetry [10, 11]. Along these lines, there is an increasing interest in the community of applied and computational mathematics to develop numerical methods to solve the three-dimensional equations governing inextensible viscous interfaces with curvature elasticity [114, 148, 146, 17]. This model provides a first approximation to the dynamical behavior of lipid membranes and is interesting in itself. It is often overlooked, however, that by ignoring the bilayer architecture this model fails to capture many important phenomena.

Seifert and Langer developed a continuum model explicitly accounting for the bilayer architecture and capturing the major energetic driving forces and dissipative drag forces involved in the dynamics of lipid membranes [160]. The elastic forces in this theory appear in response to bending of the membrane, as in the basic Helfrich model, and to monolayer stretching (see Fig. 7.1). As viscous effects, the in-plane Newtonian rheology of the lipid bilayer [39] is included through shear and dilatation dissipations, and the frictional coupling between the two monolayers opposing inter-monolayer slippage is also included. This model provided predictions about the relaxation dynamics of membrane fluctuations. Importantly, the material parameters of this model can be experimentally measured [39]. This work, along with [47], highlighted the role of inter-monolayer friction as a “hidden” but significant

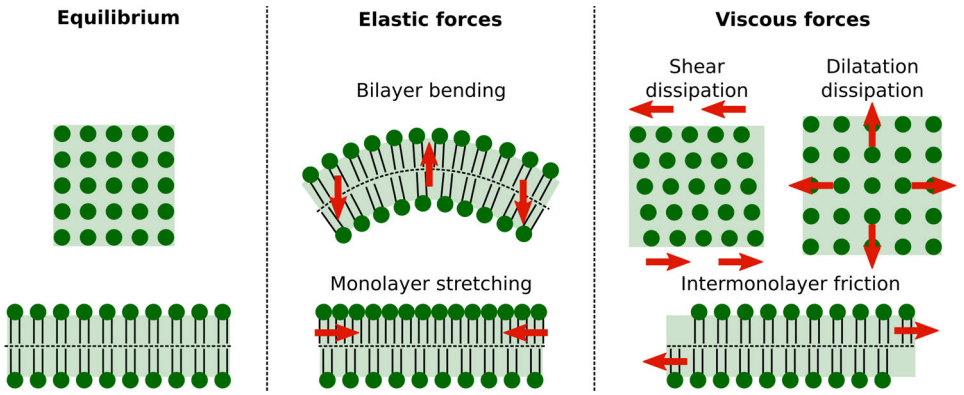


**Figure 7.1**: In a basic model incorporating elasticity and hydrodynamics [160], a lipid bilayer stores energy due to bending and monolayer stretching and dissipates energy through shear, dilatation and inter-monolayer friction.

dissipative effect. To make the mathematically complex governing equations of this theory tractable, they were linearized about a planar state in this and most subsequent works [53]. This approximation, however, hides much of the interaction between shape dynamics and interfacial hydrodynamics, which is mediated by membrane curvature. This was demonstrated by the linearization of the theory about spherical or cylindrical configurations [138] and by simulations based on a fully non-linear version of this theory, albeit axisymmetric [139], which further demonstrated the geometry-dependent subtle interplay between all the ingredients in Fig. 7.1 at multiple scales.

Seifert and Langer's (SL) model is conceptually simple, captures sufficient physics to describe a plethora of dynamical phenomena, and can be the basis for more sophisticated dynamical models including for instance lipid tilt near molecular inclusions [64, 65] or the physicochemical interaction of lipids with scaffolding or integral proteins [27, 13]. Yet, a three-dimensional fully non-linear formulation of this model is lacking. The original reference and most subsequent works considered a linearized theory. Furthermore, these equations were derived through a procedure based on the interfacial stress tensor, which is difficult to generalize.

The main objective of this Part of the Thesis is to systematically derive a nonlinear SL theory for the dynamics of bilayer membranes in three dimensions. One key aspect of this theory is that it provides a transparent modeling framework to augment the SL model with additional physics, such as the adsorption and mechanical action of curving proteins. The cornerstone in this theory is Onsager's variational principle, which as we show here and elsewhere [13] provides a unified framework for the dissipative dynamics of soft-matter systems. In this framework, the dynamics result from the interplay between energetic driving forces and dissipative drag forces, each of them deriving from potentials that are the sum of individual contributions for each physical mechanism. In fact, the dissipative dynamics emerge from a minimization principle, in which the free energy is identified as a Lyapunov functional. Complex models coupling different physics can be assembled by just adding more terms to the energy and dissipation potentials, and encoding in them the interactions between the different physical mechanisms. Thus, this framework provides a transparent and thermodynamically consistent method to generate complex models. Onsager's variational principle is applicable to capillarity, elasticity, low Reynolds number hydrodynamics, reaction-diffusion systems, and, as hinted in Chapter 13, provides a natural framework to model biological activity, e.g. through the action of molecular motors.

In addition to coupling different physical ingredients, modeling lipid bilayers inevitably requires the tools and language of differential geometry to describe a fluid surface evolving in Euclidean space. As a result, the kinematics and balance laws exhibit a strong dependence on geometry. For instance, the classical rate-of-deformation tensor couples interfacial flows with shape changes in the presence of curvature and introduces a dependence on geometry in the statement of balance of mass. Furthermore, the bilayer nature of this evolving interface challenges classical Lagrangian or Eulerian descriptions of deforming bodies. Indeed, two material particles, belonging to each of the two monolayers, occupy the same location at the mid-surface of the membrane, and therefore it is not possible to resort to a single Lagrangian parametrization. On the other hand, since we need to track the position of the interface, the

meaning of an Eulerian description is unclear. Arbitrary Lagrangian-Eulerian formulations, well established for bulk media [44], appear as a natural choice but such a formulation for a deforming surface needs careful consideration. Thus, a proper geometric formulation of continuum mechanics is essential for a general theory for lipid bilayers based on the SL model.

Finally, in addition to the multi-physics and geometric aspects of the theory, the three-dimensional simulation of lipid bilayers requires unconventional numerical methods since the resulting equations (1) involve higher-order derivatives of the parametrization, (2) lead to a mixed system of elliptic and hyperbolic partial differential equations and (3) are stiff and difficult to integrate in time [139]. Indeed, membrane shape enters into the energy and dissipation expressions through curvature, which involves second-order derivatives of the parametrization. From a finite element method (FEM) perspective, this implies that the basis functions used to represent the parametrization need to be in $H^2$ (square-integrable functions whose first- and second-order derivatives are also square-integrable), which poses a challenge to usual finite element approaches. Here, we propose a discretization based on subdivision surfaces, which has already been used to study the equilibrium shapes of lipid bilayers [49] and in engineering applications in thin shell theory [34, 33, 105]. While the Galerkin FEM deals naturally with elliptic equations, hyperbolic systems such as the continuity equation modeling lipid transport require special treatment [44]. Regarding time integration, we show that the functional being minimized in Onsager's principle can be time-discretized, yielding variational integrators that inherit qualitative features of the time-continuous system, in particular the existence of a Lyapunov function and therefore a notion of non-linear stability.

As we show in Chapter 13, the theoretical and computational tools developed for the description and simulation of lipid bilayers can be readily applied to other instances of fluid surfaces in biology. In particular, we show the direct application of our methodology to describe and simulate the cell cortex, an important structure that regulates many mechanical functions of animal cells [6].

The work is structured as follows. In Chapter 8 we introduce Onsager's variational principle by way of elementary mechanical models. We show how it can be applied to incompressible and compressible viscous fluids, as a prelude to the SL model. We also discuss how to derive variational time-integrators. In Chapter 9, we develop the mathematical background to describe fluid surfaces as continuous media. We examine the Lagrangian, Eulerian or arbitrary Lagrangian-Eulerian parametrizations of the surface, along with other key concepts such as the rate-of-deformation tensor or the Reynolds transport theorem. In Chapter 10 we combine the results of the previous two chapters to derive a general three-dimensional and non-linear formulation of the SL theory for lipid bilayers. In Chapter 11, we develop a computational approach for the time- and space-discretization of the problem, including the finite-element formulation of the mechanical problem and the stabilized formulation for the transport equations. In Chapters 12 and 13, we show some examples of application of our methodology for lipid membranes and the cell cortex respectively. Finally, we conclude with a summary and conclusions of the work.

# Chapter 8

# Onsager's variational principle

Variational principles underly many mechanical and thermodynamic theories. These principles provide a systematic procedure to generate governing equations, and provide an additional mathematical structure that highlights qualitative properties of the solutions not apparent from the Euler-Lagrange equations. For instance, the principle of minimum potential energy provides information about the stability of equilibria, not accessible from the mere equilibrium equations. Hamilton's principle for the inertial mechanics of particles and continua characterizes variationally trajectories otherwise satisfying "$F = mA$". This variational principle provides a natural framework to understand Noether's theorem and to derive variational time-integrators [87].

Towards an analogous framework to model soft-matter and biological systems, we introduce here Onsager's variational principle [120, 121], in a terminology introduced by [42, 43]. This variational framework describes the dynamics of dissipative systems and is an extension of the principle of least energy dissipation, first introduced by Rayleigh [144] [58]. Onsager's relations are generally invoked in the context of linear irreversible thermodynamics [135]. However, non-linearity is essential in many soft matter systems. For instance, lipid bilayers undergo very large deformations that elicit elastic

geometric non-linearity. The Helfrich model introduced in Chapter 1 is highly non-linear. Importantly, as noted by [42], Onsager's relations emerge from a more general variational principle applicable in fully non-linear settings. This fact was exploited to derive the geometrically non-linear equations for an inextensible interfacial fluid with bending rigidity coupled to a bulk viscous fluid [10], or to derive the governing equations for a phase-field model of membranes coupled to a bulk viscous fluid [130]. This formalism assumes that inertial forces are negligible (see [125] for an extension), but otherwise encompasses the classes of problems encountered in soft matter and biological physics, tightly coupling chemistry, hydrodynamics and non-linear solid mechanics.

Besides soft matter physics, variational principles of the Onsager type were introduced in solid mechanics, in particular invoking time-incremental discretized principles to generate algorithms [124] or to develop mathematical analysis [103, 104]. Along similar lines, Otto et al. [78, 126] identified a variational formulation for diffusion equations as gradient flows of entropy functionals, providing mathematical and physical insight and highlighting the importance of adequately parametrizing the *processes* that modify the state of the system. This led to a further formalization of Onsager's variational principle by Peletier [131] introducing the so-called process operators, which were independently used by Doi [42] to model viscoelastic fluids and by Rahimi and Arroyo [139] to derive the equations of a non-linear dynamical model for lipid bilayers. More recently, the gradient structure of reaction-diffusion systems has been identified [103], allowing us to couple such problems with other phenomena through Onsager's principle. For example, [13] describes the reaction-diffusion-elasticity problem associated to the adsorption of curving molecules onto lipid bilayers using Onsager's principle.

Here, we provide an introduction to Onsager's principle, focusing on elementary models and on viscous compressible and incompressible fluids in Euclidean space. These models provide a gentle introduction to the topic and serve as a prelude to the derivation of the equations for a lipid bilayer based on the ingredients presented in Chapter 7. We want to emphasize

two main ideas. First, this principle leads to a systematic way to derive the governing equations for complex systems starting from elementary energetic and dissipative ingredients. The potentials for these mechanisms act as building blocks of the theory. Second, the variational approach results in a natural time-discretization that can be employed to develop variational time-integrators for computational purposes. Furthermore, this approach does not rely on the formulation of the strong form of the problem and can be readily discretized with finite elements.

## 8.1 Simple one-dimensional examples

We consider a spring of elastic constant $k$ coupled in parallel with a dashpot of drag coefficient $\eta$ and under the action of a force $F$ (see Fig. 8.1A). It may seem an overkill to invoke Onsager's principle to describe such an elementary model. However, we shall see that the treatment of more complex systems follows the same rationale, and therefore this and subsequent examples provide a simple physical picture to understand the essential ideas.

The state of the system is characterized by the displacement of the spring with respect to its natural elongation, $x$. The force generated by the spring is

$$F_{\text{cons}} = -kx, \tag{8.1}$$

where the label "cons" identifies that this force is conservative. The system is also experiencing a viscous force opposing its motion

$$F_{\text{visc}} = -\mu v, \tag{8.2}$$

where $v = \dot{x}$. If the drag is sufficiently large, inertia can be neglected. Then, balance of forces reads

$$F_{\text{cons}} + F_{\text{visc}} + F = 0, \tag{8.3}$$

leading to

$$\eta\dot{x} + kx = F. \tag{8.4}$$

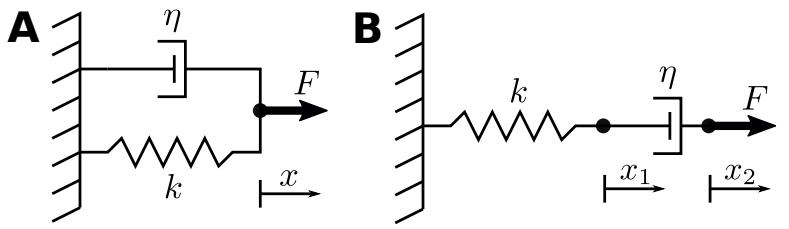


**Figure 8.1**: Diagrams of two elementary mechanical systems. (A) A spring with constant $k$ is in parallel with a dashpot with drag coefficient $\eta$ and a force $F$ is applied. The system is characterized by the displacement of the point of application of the force from its equilibrium position, $x$. (B) The spring is now in series with the dashpot and the force is applied to the dashpot; the system in this case is characterized by $x_1$, the displacement of the spring relative to its equilibrium position, and $x_2$, the relative displacement of the dashpot with respect to the spring.

This is an ordinary differential equation that can be easily integrated in time to obtain $x(t)$ given an initial condition. But let us focus on the structure of this equation rather than on its solution; this equation follows from a variational principle. Indeed, on the one hand, the spring and external forces derive from a potential, which includes the stored elastic energy in the spring and the potential for the external force

$$F_{\text{cons}} + F = -\frac{d\mathcal{F}}{dx} \quad \text{where} \quad \mathcal{F}(x) = \frac{k}{2}x^2 - Fx. \tag{8.5}$$

On the other hand, the viscous force also derives from a potential, usually referred to as the dissipation potential or as the Rayleigh dissipation function, depending on $v$

$$F_{\text{visc}} = -\frac{\partial \mathcal{D}}{\partial v} \quad \text{where} \quad \mathcal{D}(v) = \frac{\eta}{2}v^2. \tag{8.6}$$

The rate of change of the energy can be written, using the chain rule, as

$$\frac{d}{dt}\left[\mathcal{F}(x(t))\right] = \frac{d\mathcal{F}}{dx}(x(t))\,\dot{x}(t) = (kx - F)\,v, \tag{8.7}$$

and therefore $\dot{\mathcal{F}}$ depends on the state of the system $x$ and on the rate of change of the state $v$. Now, let us define the function

$$\mathcal{R}(x, v) = \dot{\mathcal{F}}(x, v) + \mathcal{D}(v) = (kx - F)\, v + \frac{1}{2}\eta v^2. \tag{8.8}$$

It is clear that the governing equation for this system (8.4) follows from $0 = \partial\mathcal{R}/\partial v$. Furthermore, because $\eta > 0$, $\mathcal{R}$ is a convex function of $v$. Thus, we conclude that the governing equation follows from the variational principle

$$\boxed{v = \underset{w}{\operatorname{argmin}}\, \mathcal{R}(x, w).} \tag{8.9}$$

This is Onsager's variational principle and the function $\mathcal{R}(x, v)$ is called the *Rayleighian* of the system. The minimization is performed over the rate of change of the state of the system, $v$, rather than on the state of the system, $x$, in contrast with the classical equilibrium principle of minimum potential energy. *This is a genuinely dynamical principle establishing a competition between the energy release rate and dissipation*. Focusing on linear response theory, Onsager showed that this principle holds for general irreversible processes, where *the key assumptions are that (i) dissipation dominates over inertia and (ii) viscous forces are derived from a dissipation potential*. This principle, however, is still valid if $\mathcal{F}$ or $\mathcal{D}$ are general non-harmonic potentials for the spring or for the dashpot.

Before showing the application of Onsager's variational principle to continuous systems, we consider another discrete example consisting of a spring in series with a dashpot loaded with a force (see Fig. 8.1B). The system is characterized by the displacement of the spring from its equilibrium position, $x_1$, and by the displacement of the dashpot with respect to the spring, $x_2$. We denote the rate of change of these coordinates by $v_i = dx_i/dt$. Let us proceed directly following Onsager's variational principle. The energy of this system is just the energy stored by the spring and the potential energy of the load, whose application point is displaced by $x_1 + x_2$

$$\mathcal{F}(x_1, x_2) = \frac{k}{2}x_1^2 - F(x_1 + x_2). \tag{8.10}$$

The rate of change of the energy is

$$\dot{\mathcal{F}}(x_1; v_1, v_2) = kx_1v_1 - F(v_1 + v_2), \tag{8.11}$$

which here happens not to depend on $x_2$. On the other hand, the dissipation potential can be written in terms of $v_2$ only

$$\mathcal{D}(v_2) = \frac{\eta}{2} v_2^2. \tag{8.12}$$

Thus, the Rayleighian is

$$\mathcal{R}(x_1; v_1, v_2) = k x_1 v_1 - F(v_1 + v_2) + \frac{\eta}{2} v_2^2 \tag{8.13}$$

and Onsager's variational principle states that

$$v_1, v_2 = \underset{w_1, w_2}{\operatorname{argmin}} \, \mathcal{R}(x_1; w_1, w_2). \tag{8.14}$$

The stationarity necessary conditions for the minimizer, $0 = \partial \mathcal{R} / \partial v_i$, lead to

$$F = k x_1 = \eta v_2, \tag{8.15}$$

which coincides with the result obtained from direct force balance for this system.

## 8.2 Incompressible Stokes flow

To show the application of Onsager's variational framework to continuous systems, let us now consider the derivation of the equations governing an incompressible Newtonian fluid in three-dimensional space, the classical Stokes equations. We consider the fluid in a fixed volume $\Omega$ with boundary $\partial\Omega$. The motion of material particles in the fluid is characterized by a velocity field $\boldsymbol{v}(\boldsymbol{x})$. The field $\boldsymbol{v}(\boldsymbol{x})$ is the continuous equivalent to $v$ in the previous example; these variables characterize the rates of the different processes by which the system is changing its state and are usually referred to as *process variables*. The dissipation potential characterizes the energy dissipated by these processes and therefore depends on the process variables, and possibly on the state of the system. For this problem, the dissipation potential encodes the energy dissipated in the viscous fluid by shear

$$\mathcal{D}_S[\boldsymbol{v}] = \mu \int_\Omega ||\boldsymbol{d}||^2 \, dV, \tag{8.16}$$

where $\boldsymbol{d}$ is the rate-of-deformation tensor in the bulk, $\boldsymbol{d} = \frac{1}{2}\left(\nabla \boldsymbol{v} + (\nabla \boldsymbol{v})^T\right)$, $||\boldsymbol{d}|| = \sqrt{d^{\alpha\beta} d_{\alpha\beta}}$, $[\cdot]$ stands for a functional dependence, and $\mu$ is the shear viscosity of the fluid. We split $\partial\Omega$ into two subdomains, the Dirichlet boundary $\partial_D\Omega$, where a velocity field $\boldsymbol{u}(\boldsymbol{x})$ is imposed, and the Neumann boundary $\partial_N\Omega$ , where a traction $\boldsymbol{t}(\boldsymbol{x})$ is applied. The traction at the Neumann boundary is generating a power

$$\mathcal{P}_N[\boldsymbol{v}] = -\int_{\partial_N\Omega} \boldsymbol{t} \cdot \boldsymbol{v} dS. \tag{8.17}$$

In this problem there is no energetic ingredient, and therefore the system is oblivious to any variable encoding the state of the system. Thus the Rayleghian accounting for internal dissipation and power supply through boundary traction is simply

$$\mathcal{R}[\boldsymbol{v}] = \mathcal{D}_S[\boldsymbol{v}] + \mathcal{P}_N[\boldsymbol{v}] = \mu \int_\Omega ||\boldsymbol{d}||^2 \, dV - \int_{\partial_N\Omega} \boldsymbol{t} \cdot \boldsymbol{v} dS. \tag{8.18}$$

Onsager's principle states that the system evolves in such a way that the Rayleghian is minimized with respect to $\boldsymbol{v}$

$$\boldsymbol{v} = \underset{\boldsymbol{w}}{\operatorname{argmin}}\, \mathcal{R}[\boldsymbol{w}]. \tag{8.19}$$

However, it is important to realize that the velocity field is subjected to constraints. First, it should satisfy the Dirichlet boundary conditions. Furthermore, since the fluid is incompressible, it should satisfy $\nabla \cdot \boldsymbol{v} = 0$ in $\Omega$. The variational principle allows us to easily incorporate constraints, for instance using a field of Lagrange multipliers, $p$, and forming the Lagrangian

$$\begin{aligned} \mathcal{L}[\boldsymbol{v}, p] &= \mathcal{R}[\boldsymbol{v}] - \int_\Omega p \, \nabla \cdot \boldsymbol{v} \, dV \\ &= \mu \int_\Omega ||\boldsymbol{d}||^2 \, dV - \int_{\Gamma_N} \boldsymbol{t} \cdot \boldsymbol{v} dS - \int_\Omega p \, \nabla \cdot \boldsymbol{v} \, dV, \end{aligned} \tag{8.20}$$

Now, the constrained Onsager's principle can be stated as a saddle problem

$$\boldsymbol{v}, p = \underset{q}{\operatorname{argmax}}\, \underset{\boldsymbol{w}}{\operatorname{argmin}} \left\{\mathcal{L}[\boldsymbol{w}, q]\right\}. \tag{8.21}$$

Variations of the velocity field $\delta\boldsymbol{v}(\boldsymbol{x})$ consistent with Dirichlet boundary conditions, i.e. $\delta\boldsymbol{v}(\boldsymbol{x}) = \boldsymbol{0}$ at $\partial_D\Omega$, lead to the stationarity condition

$$2\mu \int_\Omega \boldsymbol{d} : \nabla\delta\boldsymbol{v}\, dV - \int_{\partial_N\Omega} \boldsymbol{t}\cdot\delta\boldsymbol{v}\, dS - \int_\Omega p\, \mathrm{div}\delta\boldsymbol{v}\, dV = 0, \tag{8.22}$$

where $\boldsymbol{a} : \boldsymbol{b} = a^{\alpha\beta}b_{\alpha\beta}$. Variations with respect to $p$ lead to

$$\int_\Omega \delta p\, \mathrm{div}\boldsymbol{v}\, dV = 0. \tag{8.23}$$

Eqs. (8.22) and (8.23) are the weak form of the problem. The strong form follows after integration by parts and taking into account the arbitrariness in $\delta\boldsymbol{v}$ and $\delta p$ (see Box 8.1),

$$\begin{aligned} \mathrm{div}\boldsymbol{\sigma} &= \boldsymbol{0} && \text{in } \Omega, \\ \mathrm{div}\boldsymbol{v} &= 0 && \text{in } \Omega, \\ \boldsymbol{v} &= \boldsymbol{u} && \text{on } \partial_D\Omega, \\ \boldsymbol{\sigma}\cdot\boldsymbol{n} &= \boldsymbol{t} && \text{on } \partial_N\Omega, \end{aligned} \tag{8.24}$$

where $\boldsymbol{\sigma} = 2\mu\boldsymbol{d} - p\boldsymbol{I}$ is the stress tensor of the Newtonian fluid and $\boldsymbol{I}$ is the $3\times 3$ identity tensor. Thus, the equations characterizing an incompressible Newtonian fluid in $\Omega$, with $p$ playing the role of the pressure, can be obtained from Onsager's variational principle.

## 8.3 Compressible Stokes flow

As a final exercise, we consider a compressible Newtonian fluid in the low Reynolds number limit. This example illustrates the interplay between energy release rate and dissipation in a continuous and open system. In this case, we consider the same dissipation mechanisms as for the incompressible Stokes flow. However, as the fluid is compressible, we need to track its density $\rho$, and find an equation of state that characterizes how the free energy depends on $\rho$. We model the free energy associated to changes in density with a quadratic

**Box 8.1:** From the weak to the strong form

We want to show for the simple example of a Stokes flow on $\Omega$ how the strong form of the problem is derived from the weak form. First, we note that using the product rule of differentiation we can rewrite

$$\begin{aligned} \boldsymbol{d} : \nabla\delta\boldsymbol{v} &= \mathrm{div}(\delta\boldsymbol{v}\cdot\boldsymbol{d}) - \mathrm{div}\boldsymbol{d}\cdot\delta\boldsymbol{v}, \\ p\mathrm{div}\delta\boldsymbol{v} &= \mathrm{div}(p\delta\boldsymbol{v}) - \nabla p\cdot\delta\boldsymbol{v}. \end{aligned} \tag{B9}$$

Using these expressions we can reformulate Eq. (8.22) as

$$-\int_\Omega [2\mu\mathrm{div}\boldsymbol{d} + \nabla p]\cdot\delta\boldsymbol{v}\, dV + \int_{\partial_N\Omega} [(2\mu\boldsymbol{d} + p\boldsymbol{I})\cdot\boldsymbol{n} - \boldsymbol{t}]\cdot\delta\boldsymbol{v}\, dS = 0, \tag{B10}$$

where we have used the divergence theorem and that $\delta\boldsymbol{v} = \boldsymbol{0}$ on $\partial_D\Omega$. Since $\delta\boldsymbol{v}$ can vary independently at any point in $\Omega$ and $\partial_N\Omega$, the terms inside $[\cdot]$ need to vanish everywhere on the domains of integration, which leads to

$$\begin{aligned} \mathrm{div}\boldsymbol{\sigma} &= \boldsymbol{0} \qquad \text{in } \Omega, \\ \boldsymbol{\sigma}\cdot\boldsymbol{n} &= \boldsymbol{t} \quad \text{on } \partial_N\Omega, \end{aligned} \tag{B11}$$

with $\boldsymbol{\sigma} = 2\mu\boldsymbol{d} - p\boldsymbol{I}$. Furthermore, as $\delta p$ can also vary independently on $\Omega$, from Eq. (8.23) we get the incompressibility constraint

$$\mathrm{div}\boldsymbol{v} = 0 \qquad \text{in } \Omega, \tag{B12}$$

Together with the Dirichlet boundary conditions, this leads to Eq. (8.24).

potential

$$\mathcal{F}[\rho] = \int_\Omega \frac{k}{2}\left(\frac{\rho}{\rho_0} - 1\right)^2 dV, \tag{8.25}$$

where $\rho(\boldsymbol{x}, t)$ is the density of fluid, $\rho_0$ is the equilibrium density and $k$ is the bulk elastic modulus of the material. In this case, $\rho$ is a *state variable*; $\mathcal{F}$ depends on the configuration of the system through state variables, such as $x$ in the simple one-dimensional example or $\rho$ in this example. As before, we consider the fluid in a fixed (or Eulerian) domain $\Omega$. The rate of change of the

free energy in $\Omega$ is

$$\dot{\mathcal{F}}[\rho;\partial_t\rho] = \frac{d}{dt}\int_\Omega \frac{k}{2}\left(\frac{\rho}{\rho_0}-1\right)^2 dV = \int_\Omega \partial_t\left[\frac{k}{2}\left(\frac{\rho}{\rho_0}-1\right)^2\right] dV$$
$$= \int_\Omega k\left(\frac{\rho}{\rho_0}-1\right)\frac{\partial_t\rho}{\rho_0} dV. \tag{8.26}$$

We note, however, that the rate of change of the free energy for the material contained in $\Omega$ differs from $\dot{\mathcal{F}}$ since $\Omega$ is not a material domain. To calculate the rate of change of the free energy for the material in $\Omega$, let us consider a material domain evolving with the fluid, $\Omega_t$, such that $\Omega_0 = \Omega$. Then, we can define the free energy in $\Omega_t$ as

$$\bar{\mathcal{F}}\left[\rho,\Omega_t\right] = \int_{\Omega_t}\frac{k}{2}\left(\frac{\rho}{\rho_0}-1\right)^2 dV, \tag{8.27}$$

where we have written the explicit dependence of $\bar{\mathcal{F}}$ on $\Omega_t$ because $\Omega_t$ is time-dependent. At $t = 0$, $\mathcal{F} = \bar{\mathcal{F}}$, but they will evolve differently. More precisely, applying Reynolds transport theorem, we find that at $t = 0$

$$\dot{\bar{\mathcal{F}}}[\rho;\partial_t\rho;\boldsymbol{v}] = \int_\Omega k\left(\frac{\rho}{\rho_0}-1\right)\frac{\partial_t\rho}{\rho_0}dV + \int_{\partial\Omega}\frac{k}{2}\left(\frac{\rho}{\rho_0}-1\right)^2 \boldsymbol{v}\cdot\boldsymbol{n}dS. \tag{8.28}$$

For simplicity in the notation, we call $\dot{\bar{\mathcal{F}}}[\rho,\Omega_t]$ the *material time derivative* of the functional $\mathcal{F}$ and denote it by $D_t\mathcal{F}[\rho;\partial_t\rho,\boldsymbol{v}]$. We have the relation

$$D_t\mathcal{F}[\rho;\partial_t\rho,\boldsymbol{v}] = \dot{\mathcal{F}}[\rho;\partial_t\rho] + \mathcal{P}_T[\rho;\boldsymbol{v}], \tag{8.29}$$

where we have defined

$$\mathcal{P}_T[\rho;\boldsymbol{v}] = \int_{\partial\Omega}\frac{k}{2}\left(\frac{\rho}{\rho_0}-1\right)^2\boldsymbol{v}\cdot\boldsymbol{n}dS, \tag{8.30}$$

which can be interpreted as the power supply by the transport of material in or out of $\Omega$. A more detailed discussion about different time-derivatives for integrals on surfaces is given in Chapter 9. The relevant rate of change of $\mathcal{F}$ for Onsager's principle is $D_t\mathcal{F}[\rho;\partial_t\rho,\boldsymbol{v}]$, since tractions in the boundary are exerted on material particles.

To be able to exercise Onsager's principle, we need to express the rate of change of $\mathcal{F}$ only in terms of the process variable $\boldsymbol{v}$, which appears in the dissipation functional Eq. (8.16). However, $\dot{\mathcal{F}}$ depends on $\partial_t \rho$. To relate $\partial_t \rho$ with $\boldsymbol{v}$ we need an extra relation, which in this case is mass conservation

$$\partial_t \rho + \text{div}\,(\rho \boldsymbol{v}) = 0. \tag{8.31}$$

This equation has to be supplemented with a boundary condition for $\rho$ at the in-flow boundary

$$\rho(\boldsymbol{x}) = c(\boldsymbol{x}) \quad \text{on } \partial_I \Omega, \tag{8.32}$$

where $\partial_I \Omega = \{\boldsymbol{x} \in \partial\Omega \,:\, \boldsymbol{v}(\boldsymbol{x}) \cdot \boldsymbol{n}(\boldsymbol{x}) < 0)\}$ and $c(\boldsymbol{x})$ is given. This allows us to define a *process operator* $P$, such that

$$\partial_t \rho = P(\rho; \boldsymbol{v}) = -\text{div}(\rho \boldsymbol{v}). \tag{8.33}$$

Process operators relate the rate of change of the state variables, such as $\partial_t \rho$, with the process variables, such as $\boldsymbol{v}$. In the simple one-dimensional example, we just had $\dot{x} = v$, and $P(v) = v$. Substituting Eq. (8.33) in Eq. (8.28) and simplifying the terms in Eq. (8.28), we obtain

$$D_t \mathcal{F}[\rho; \boldsymbol{v}] = \int_\Omega \frac{k}{2} \left[1 - \left(\frac{\rho}{\rho_0}\right)^2\right] \text{div} \boldsymbol{v} dV, \tag{8.34}$$

Now, the Rayleighian of the system can be written as the sum of Eqs. (8.16), (8.17) and (8.34)

$$\begin{aligned} \mathcal{R}[\rho; \boldsymbol{v}] &= D_t \mathcal{F}[\rho; \boldsymbol{v}] + \mathcal{D}_S[\boldsymbol{v}] + \mathcal{P}_N[\boldsymbol{v}] \\ &= \int_\Omega \frac{k}{2} \left[1 - \left(\frac{\rho}{\rho_0}\right)^2\right] \text{div} \boldsymbol{v} dV + \mu \int_\Omega ||\boldsymbol{d}||^2 \, dV - \int_{\partial_N \Omega} \boldsymbol{t} \cdot \boldsymbol{v} dS. \end{aligned} \tag{8.35}$$

According to Onsager's variational principle, the dynamics of the system follows from

$$\boldsymbol{v} = \underset{\boldsymbol{w}}{\text{argmin}}\, \mathcal{R}[\rho, \boldsymbol{w}]. \tag{8.36}$$

Variations of the velocity $\delta\boldsymbol{v}$ consistent with Dirichlet boundary conditions result in the stationarity condition

$$\int_\Omega \frac{k}{2}\left[1-\left(\frac{\rho}{\rho_0}\right)^2\right]\mathrm{div}\delta\boldsymbol{v}dV + 2\mu\int_\Omega \boldsymbol{d}:\nabla\delta\boldsymbol{v}\,dV - \int_{\partial_N\Omega}\boldsymbol{t}\cdot\delta\boldsymbol{v}dS = 0, \quad (8.37)$$

which, proceeding similarly as in Box 8.1, leads to the strong form

$$\begin{aligned} \mathrm{div}\boldsymbol{\sigma} &= \boldsymbol{0} && \text{in } \Omega, \\ \partial_t\rho + \mathrm{div}\,(\rho\boldsymbol{v}) &= 0 && \text{in } \Omega, \\ \boldsymbol{v} &= \boldsymbol{u} && \text{on } \partial_D\Omega, \\ \boldsymbol{\sigma}\cdot\boldsymbol{n} &= \boldsymbol{t} && \text{on } \partial_N\Omega, \\ \rho &= c && \text{on } \partial_I\Omega, \end{aligned} \quad (8.38)$$

where $\boldsymbol{\sigma} = 2\mu\boldsymbol{d} - p\boldsymbol{I}$ has the same form as before and $p$ is given by the equation of state

$$p = \frac{k}{2}\left[\left(\frac{\rho}{\rho_0}\right)^2 - 1\right]. \quad (8.39)$$

Finally, let us note that in Eq. (8.38) we have a system coupling an elliptic PDE, requiring mechanical equilibrium, and a hyperbolic PDE, modeling mass conservation and subjected to in-flow Dirichlet boundary conditions.

## 8.4 General statement of Onsager's principle

The previous example has shown that the rate of change of the energy and the dissipation potential may be expressed in terms of different descriptions of the rate of change of the system. $\dot{\mathcal{F}}$ was a functional of $\partial_t\rho$ while $\mathcal{D}$ was a functional of $\boldsymbol{v}$. To place the rate of change of the energy and the dissipation potential on an equal footing in the Rayleighian, we needed a relation between these two quantities (the continuity equation), termed *process operator* in the terminology of [131]. We follow this reference in this Section to formalize an abstract statement of Onsager's principle. The objective of this formal exercise is to conceptualize the procedure and guide our formulation of more complex

problems. It remains a nontrivial task, however, to map a particular physical model into this formalism.

In the examples examined previously, we have seen that the main ingredients in Onsager's modeling framework are (1) the state variables, such as $x$ or $\rho$, which identify the state of the system, (2) the free energy $\mathcal{F}$, which depends on the state variables, (3) the process variables, such as $v$ or $\boldsymbol{v}$, which describe how the system changes its state and generates dissipation, (4) the process operator $P$, which relates the rate of change of the state variables and the process variables, (5) the dissipation potential $\mathcal{D}$, measuring the energy dissipated by the process variables, and possibly (6) potentials accounting for the externally supplied power $\mathcal{P}$ and (7) constraints such as the incompressibility condition. Constraints may be formulated on the state or on the process variables, but the former can always be linearized and expressed as constraints on the process variables. Collecting all these ingredients, we can abstractly state Onsager's variational principle as follows.

Let us describe a dissipative system through some state variables $X(t)$ evolving in a suitable space (possibly a non-linear manifold), a free energy $\mathcal{F}(X)$, some process variables $V$ (living in a vector bundle and therefore with a clear notion of 0), a dissipation potential $\mathcal{D}(X;V)$, and a potential for the external power supply $\mathcal{P}(X;V)$. Suppose also that the process variables are linearly constrained by $0 = \mathbb{C}(X)V$ during the time-evolution of the system. $\mathcal{F}$ is often a non-linear function of $X$, $\mathcal{D}$ may be a non-linear function of $X$ but is generally quadratic in $V$, and $\mathcal{P}$ is generally linear in $V$. However, $\mathcal{D}$ does not need to be quadratic in $V$ in Onsager's formalism as described here. As motivated below, *the thermodynamic requirements we will need on $\mathcal{D}$ are (1) that it is nonnegative, (2) that $\mathcal{D}(X,0) = 0$ and (3) that it is a convex function of $V$*. We will also assume here that the dissipation potential is differentiable. This is not necessarily the case, for instance in rate-independent dissipative processes such as dry friction, which can nevertheless be framed in Onsager's principle. The differentiability assumption is justified here because soft and biological matter is generally wet and rate-dependent.

To form the Rayleighian, we need to evaluate the rate of change of the

energy, which can be obtained by the chain rule

$$\dot{\mathcal{F}}(X;\partial_t X) = \frac{d}{dt}\left[\mathcal{F}(X(t))\right] = D\mathcal{F}(X)\,\partial_t X, \tag{8.40}$$

where $D\mathcal{F}(X)$ denotes the derivative of the free energy. The situation is slightly more complicated when considering free energy integrals over non-material domains (open systems). In these cases, the rate of change of the free energy that is relevant for Onsager's principle is $D_t\mathcal{F}$, the material time-derivative of the free energy, which differs from $\dot{\mathcal{F}}$ by a term in the boundary parametrizing the flow of energy to/from the domain. This is the case in the example in Section 8.3. This, however, does not complicate the application of Onsager's principle in any way since the term in the boundary can be included in the power function $\mathcal{P}$.

In general, the process variable $V$ ($\boldsymbol{v}$ in the previous example) will not be simply the time-derivative of the state variable $\partial_t X$ ($\partial_t \rho$ in the previous example), although this was the case in the examples of Section 8.1. To relate these two descriptions of the evolution of the state of the system, we need a process operator, which we consider here to be linear

$$\partial_t X = P(X)V. \tag{8.41}$$

This operator will often be either trivial, i.e. $\partial_t X = V$, or a statement of conservation of mass. Importantly, as noted by [126, 131], $V$ often contains redundant information to describe $\partial_t X$, which is however required to properly model dissipation. This is the case in the previous example, where $\partial_t \rho$ is a scalar field but $\boldsymbol{v}$ is a vector field.

The process operator allows us to express the rate of change of the system in terms of the process variable $V$, and thus form the Rayleighian as

$$\boxed{\mathcal{R}(X;V) = D\mathcal{F}(X)\,P(X)V + \mathcal{D}(X;V) + \mathcal{P}(X;V).} \tag{8.42}$$

Onsager's variational principle then states that the system evolves such that

$$\boxed{V = \underset{W}{\operatorname{argmin}}\,\mathcal{R}(X;W),} \tag{8.43}$$

subject to the constraints on $W$

$$\mathbb{C}(X)W = 0. \tag{8.44}$$

The constrained dynamics can be equivalently characterized as stationary (saddle) points of the Lagrangian

$$\mathcal{L}(X; V, \Lambda) = D\mathcal{F}(X)\ P(X)V + \mathcal{D}(X; V) + \mathcal{P}(X; V) + \Lambda \cdot \mathbb{C}(X)\ V, \tag{8.45}$$

where $\Lambda$ are the Lagrange multipliers. Once $V$ is obtained from this variational principle, we can then integrate $\partial_t X$ in time recalling Eq. (8.41).

Let us now formally examine an important qualitative property of the resulting dissipative dynamics. For this, we consider a "homogeneous" system with $\mathcal{P}(X; V) = 0$. The stationarity condition $0 = \delta_\Lambda \mathcal{L}$ simply leads to $0 = \mathbb{C}(X)V$. The stationarity condition $0 = \delta_V \mathcal{L}$ results in the Euler-Lagrange equations

$$0 = D_X\mathcal{F}(X)\ P(X) + D_V\mathcal{D}(X; V) + \Lambda \cdot \mathbb{C}(X). \tag{8.46}$$

Multiplying this equation by the actual $V$ along the dissipative dynamics and rearranging terms, we obtain

$$\underbrace{D_X\mathcal{F}(X)\ P(X)V}_{\dot{\mathcal{F}}} = -D_V\mathcal{D}(X; V)V - \Lambda \cdot \underbrace{\mathbb{C}(X)V}_{0}, \tag{8.47}$$

and since $\mathcal{D}$ is convex and differentiable in $V$ and we have required that $\mathcal{D}(X; 0) = 0$, we conclude that

$$0 = \mathcal{D}(X; 0) \geq \mathcal{D}(X; V) + D_V\mathcal{D}(X; V)(0 - V). \tag{8.48}$$

Since we have required $\mathcal{D}(X; V) \geq 0$, we conclude from this equation that

$$0 \geq -\mathcal{D}(X; V) \geq -D_V\mathcal{D}(X; V)V. \tag{8.49}$$

This equation, together with Eq. (8.47), show that during the dynamics

$$\boxed{\dot{\mathcal{F}} = -D_V\mathcal{D}(X; V)V \leq 0,} \tag{8.50}$$

and $D_V \mathcal{D}(X;V)V$ is the rate of dissipation. For quadratic dissipation potentials, it is easily checked that $D_V \mathcal{D}(X;V)V = 2\mathcal{D}(X;V)$. Therefore, *the free energy $\mathcal{F}$ is a Lyapunov function of the dynamics*. This also shows that *Onsager's principle complies with the second law of thermodynamics by construction, as long as $\mathcal{D}$ satisfies a set of minimal requirements*. Finally, we note that this notion of stability is fully non-linear and does not assume a quadratic form for the dissipation or free energy potentials.

## 8.5 Time discretization: A variational time-integrator

To discretize in time the governing equations obtained from Onsager's variational principle, the most common approach is to discretize Eq. (8.46), a system of ODEs or PDEs. However, the variational principle for the dynamics offers an alternative option: discretizing in time the variational principle itself, see Eq. (8.43). Time-integrators based on the discretization of a variational principle are usually referred to as *variational time-integrators*, and have been widely employed, for instance, for the discretization of Hamilton's principle in conservative systems, in molecular dynamics [55] or in continuum mechanics [87], and in the context of dissipative systems [124, 130]. Variational time-integrators inherit qualitative properties of the associated time-continuous problem. For instance, in the case of time-integrators based on Hamilton's principle, Noether's theorem ensures that symmetries in the discrete action result in conserved currents as in the original continuous theory. Here, we propose a first order variational time-integrator for Onsager's principle that inherits that $\mathcal{F}$ is a Lyapunov functional of the dynamics. This feature provides stability to the resulting discrete dynamics by construction. To describe this variational time-integrator, let us consider a time discretization characterized by the time grid $(t^1, \dots, t^N)$ and let us start with the simple case in which $\partial_t X = V$. We will consider here the simplest low order version of implicit variational time-integrator based on Onsager's principle, and leave the investigation of higher-order schemes to future work. We approximate $V^n = V(t^n)$

with a simple backward difference

$$V^{n+1} \approx \frac{X^{n+1} - X^n}{\Delta t^n}, \tag{8.51}$$

where $X^n = X(t^n)$ and $\Delta t^n = t^{n+1} - t^n$. The dissipation potential and the power can now be approximated as

$$\begin{aligned} \mathcal{D}(X; V) &\approx \mathcal{D}\left(X^n; \frac{X^{n+1} - X^n}{\Delta t^n}\right), \\ \mathcal{P}(X; V) &\approx \mathcal{P}\left(X^n; \frac{X^{n+1} - X^n}{\Delta t^n}\right). \end{aligned} \tag{8.52}$$

To discretize the Rayleighian, we also need to discretize the rate of change of the free energy. Rather than resorting to an expression like $\dot{\mathcal{F}} \approx D\mathcal{F} \cdot \left(X^{n+1} - X^n\right)/\Delta t^n$, we consider

$$\dot{\mathcal{F}}(X, \partial_t X) \approx \frac{\mathcal{F}\left(X^{n+1}\right) - \mathcal{F}\left(X^n\right)}{\Delta t^n}, \tag{8.53}$$

or a similar higher-order finite difference. This approach ensures that $\mathcal{F}$ is a Lyapunov functional of the dynamics, as we prove below, and retains the full non-linearity of $\mathcal{F}$ in the formulation. Using the previous expressions we define the discrete Rayleighian as

$$\boxed{\begin{aligned} \mathcal{R}\left(X^n; X^{n+1}\right) = \frac{\mathcal{F}\left(X^{n+1}\right)}{\Delta t^n} &+ \mathcal{D}\left(X^n; \frac{X^{n+1} - X^n}{\Delta t^n}\right) \\ &+ \mathcal{P}\left(X^n; \frac{X^{n+1} - X^n}{\Delta t^n}\right), \end{aligned}} \tag{8.54}$$

where we have ignored the constant term $\mathcal{F}(X^n)/\Delta t$ since it is irrelevant from the viewpoint of the variational principle. Then, Eq. (8.43) is approximated by

$$\boxed{X^{n+1} = \underset{X}{\operatorname{argmin}}\, \mathcal{R}\left(X^n; X\right).} \tag{8.55}$$

Thus, the dynamical problem arising from our variational time discretization can be interpreted as an energy minimization problem for $\mathcal{F}$, which is usually

a non-linear function of $X^{n+1}$, with the addition of a convex –and in many occasions quadratic– function of $X^{n+1}$, $\mathcal{D}$, subject to the external forces represented in $\mathcal{P}$. The weight of $\mathcal{F}$ relative to $\mathcal{D}$ and $\mathcal{P}$ is controlled by $\Delta t^n$, which can be decreased to ease the solvability of the problem by increasing the influence of the convex functional $\mathcal{D}$, or increased to allow the system to reach equilibrium faster. Let us now prove that the free energy is a Lyapunov functional of the dynamics, for which we consider a homogeneous problem with $\mathcal{P}(X;V)=0$. We evaluate the Rayleighians

$$\begin{aligned}\mathcal{R}\left(X^n;X^{n+1}\right) &= \frac{\mathcal{F}\left(X^{n+1}\right)}{\Delta t^n} + \mathcal{D}\left(X^n;\frac{X^{n+1}-X^n}{\Delta t^n}\right),\\ \mathcal{R}\left(X^n;X^n\right) &= \frac{\mathcal{F}\left(X^n\right)}{\Delta t^n} + \mathcal{D}\left(X^n;0\right) = \frac{\mathcal{F}\left(X^n\right)}{\Delta t^n},\end{aligned} \tag{8.56}$$

where we have used that $\mathcal{D}\left(X^n;0\right)=0$. Since $X^{n+1}$ minimizes $\mathcal{R}$, it is clear that $\mathcal{R}\left(X^n;X^{n+1}\right)-\mathcal{R}\left(X^n;X^n\right)\leq 0$. Then,

$$\begin{aligned}0 &\geq \mathcal{R}\left(X^n;X^{n+1}\right)-\mathcal{R}\left(X^n;X^n\right)\\ &= \frac{\mathcal{F}\left(X^{n+1}\right)-\mathcal{F}\left(X^n\right)}{\Delta t^n} + \mathcal{D}\left(X^n;\frac{X^{n+1}-X^n}{\Delta t^n}\right)\\ &\geq \frac{\mathcal{F}\left(X^{n+1}\right)-\mathcal{F}\left(X^n\right)}{\Delta t^n},\end{aligned} \tag{8.57}$$

where we have used that $\mathcal{D}\left(X^n;\frac{X^{n+1}-X^n}{\Delta t^n}\right)$ is positive. Therefore, we obtain

$$\boxed{\mathcal{F}\left(X^{n+1}\right)\leq\mathcal{F}\left(X^n\right).} \tag{8.58}$$

which shows that $\mathcal{F}$ *is a Lyapunov functional of the discrete dynamics*. We note here that a key point is that $\dot{\mathcal{F}}$ has been discretized in terms of the difference $\mathcal{F}(X^{n+1})-\mathcal{F}(X^n)$. Thus, the time-step is not limited by stability, but rather by the accuracy and by the solvability of the non-linear optimization problem in Eq. (8.55) (which becomes "easier" or "more convex" for small $\Delta t^n$). This is particularly important in stiff problems, such as those involving the Helfrich curvature energy.

There are some cases in which $\partial_t X \neq V$ and the previous discretization cannot be carried out explicitly. For those cases, we keep $V^{n+1}$ as the variable of the discrete problem and consider a simple forward Euler approximation for the process operator

$$\partial_t X \approx \frac{X^{n+1} - X^n}{\Delta t^n} = P\left(X^n; V^{n+1}\right) \Longrightarrow X^{n+1} = X^n + \Delta t^n P\left(X^n; V^{n+1}\right). \quad (8.59)$$

We can then rewrite Eq. (8.53) as

$$\dot{\mathcal{F}} \approx \frac{\mathcal{F}\left(X^{n+1}\right) - \mathcal{F}(X^n)}{\Delta t^n} = \frac{\mathcal{F}\left(X^n + \Delta t P\left(X^n; V^{n+1}\right)\right) - \mathcal{F}(X^n)}{\Delta t^n}. \quad (8.60)$$

This approximation still retains the non-linearity of $\mathcal{F}$ as is thus implicit in this sense. We can now define the Rayleghian as

$$\boxed{\begin{aligned}\mathcal{R}(X^n; V^{n+1}) = &\frac{\mathcal{F}\left(X^n + \Delta t^n P(X^n; V^{n+1})\right)}{\Delta t^n} \\ &+ \mathcal{D}(X^n; V^{n+1}) + \mathcal{P}(X^n; V^{n+1}),\end{aligned}} \quad (8.61)$$

and solve

$$\boxed{V^{n+1} = \underset{V}{\operatorname{argmin}}\, \mathcal{R}(X^n; V).} \quad (8.62)$$

Finally, we can recover the rate of change of the state variables by solving Eq. (8.59). It is easily shown that with this discretization $\mathcal{F}$ is also a Lyapunov function of the dynamics. For systems with only some of the variables satisfying $\partial_t X = V$, we can use a formulation mixing the two approaches presented here independently.

### Example: compressible Stokes flow

Let us show the application of this time-integrator for the simple compressible Stokes flow of Section 8.3. In this example, the process operator is not trivial. The discrete Rayleighian takes the form:

$$\mathcal{R}^n[\rho^n; \boldsymbol{v}] = \frac{\mathcal{F}\left[\rho^n + \Delta t^n\, P\left(\rho, \boldsymbol{v}\right)\right]}{\Delta t^n} + \mathcal{D}_S\left[\boldsymbol{v}\right] + \mathcal{P}_N\left[\boldsymbol{v}\right] + \mathcal{P}_T\left[\boldsymbol{v}\right]$$

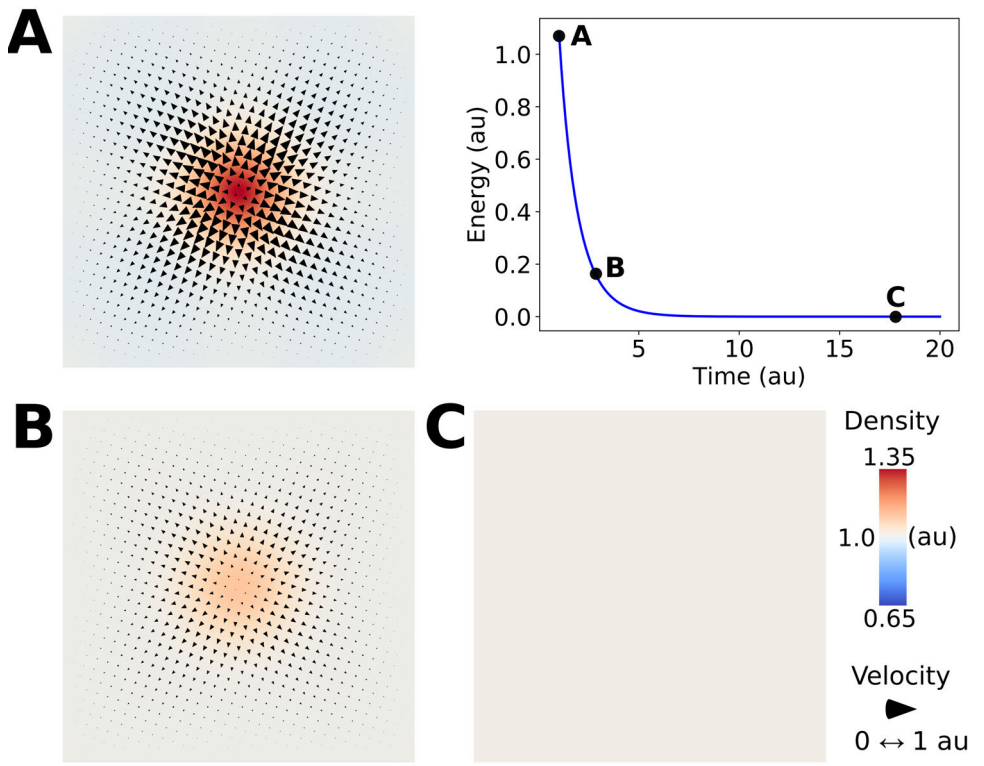


**Figure 8.2**: Time-evolution of a compressible visco-elastic fluid in the presence of an original disturbance. The free enegy is a Lyapunov functional of the dynamics. The sub-plots (A-C) show the density state (color map) along with the velocity profile (arrows).

$$= \int_\Omega \frac{k}{2}\left(\frac{\rho^n - \Delta t^n \operatorname{div}(\rho^n \boldsymbol{v})}{\rho_0} - 1\right)^2 dV + \mu \int_\Omega ||\boldsymbol{d}||^2 \, dV$$
$$- \int_{\partial_N \Omega} \boldsymbol{t}\cdot\boldsymbol{v} dS + \int_{\partial\Omega} \frac{k}{2}\left(\frac{\rho^n}{\rho_0} - 1\right)^2 \boldsymbol{v}\cdot\boldsymbol{n} dS. \tag{8.63}$$

Let us note that $\frac{\mathcal{F}[\rho^n + \Delta t^n P(\rho, \boldsymbol{v}^{n+1})] - \mathcal{F}[\rho^n]}{\Delta t^n}$ approximates $\dot{\mathcal{F}}$ and not $D_t\mathcal{F}$ and for that reason we need to write the transport power explicitly. Then,

$$\boldsymbol{v}^{n+1} = \underset{\boldsymbol{v}}{\operatorname{argmin}}\, \mathcal{R}^n[\rho^n; \boldsymbol{v}]. \tag{8.64}$$

and

$$\rho^{n+1} = \rho^n - \Delta t^n \operatorname{div}\left(\rho^n \boldsymbol{v}^{n+1}\right). \tag{8.65}$$

This time-discretization of the system of differential equations leads to an elliptic problem for $\boldsymbol{v}^{n+1}$, the mechanical problem in Eq. (8.64), and a simple algebraic equation for $\rho^{n+1}$ in Eq. (8.65). In Fig, 8.2 we show a simple example of the time-evolution of the compressible Stokes flow following the discrete dynamics in Eqs. (8.64) and (8.65). Initially, the system is prepared out of equilibrium with a given density profile (of the form of a Gaussian centered at the origin). The system is then allowed to equilibrate following the dissipative dynamics. Homogeneous Dirichlet boundary conditions are considered for the flow at the boundary of the square. The different snapshots show the density and velocity profiles at different instants during the evolution. As expected, the free energy monotonically decreases. For the spatial discretization, we have followed an approach similar to the one discussed in Chapter 11.

# Chapter 9

# Mathematical description of fluid surfaces

In this chapter, we focus on the representation of fluid surfaces as a two-dimensional continuum moving in Euclidean space. One way to represent this kind of material is through a Lagrangian parametrization of the surface, $\phi(\boldsymbol{\xi}, t)$, in which a material particle is identified with a point $\boldsymbol{\xi}^*$ in parametric domain and $\phi(\boldsymbol{\xi}^*, t)$ follows its trajectory in time. However, Lagrangian parametrizations present two major drawbacks for the description of fluid surfaces, and lipid bilayers in particular. First, due to the fluid nature of the interface, Lagrangian parametrizations suffer from very large distortions that are difficult to accommodate with conventional discretization schemes. Second, a single Lagrangian parametrization cannot track simultaneously all material particles in a multicomponent material. For example, in a lipid bilayer, two material particles, representing lipid molecules from each monolayer, occupy the same position on the surface; a single Lagrangian parametrization cannot track the time-evolution of both simultaneously because they can slip relative to each other.

It follows from arguments of material symmetry that for elastic fluid

surfaces the free energy only depends on $\phi$ through the density field and the mean and Gaussian curvatures, $H$ and $K$ respectively, which only depend on the shape of the surface [173]. Thus, one can separate the description of the density field, viewed as a scalar field that is advected by flows on the surface, from the parametrization of the surface, now seen as a mathematical tool employed to characterize the surface shape and independent of in-plane deformations. This leads to arbitrary Lagrangian-Eulerian (ALE) parametrizations that are better suited for the description of fluid surfaces. Although ALE formulations are common for the numerical treatment of fluids in the bulk [44], special consideration is required to treat fluid surfaces. In this chapter, we examine the definition of Lagrangian, Eulerian and ALE parametrizations of material surfaces and establish their relations. Associated with the flow generated by these parametrizations, we define the Lagrangian, Eulerian and ALE time-derivatives of fields on the surface. We then introduce the right Cauchy deformation tensor and the rate-of-deformation tensor, which characterizes the rate at which lengths, angles and areas transform on the time-evolving surface. Using the results obtained from previous Sections, we examine time-derivatives of integrals on time-evolving surfaces, and derive the form of Reynolds transport theorem and conservation of mass for the Lagrangian, Eulerian and ALE descriptions. Throughout the chapter, we make extensive use of the differential geometry of surfaces, including the definition of the metric tensor or first fundamental form $\boldsymbol{g}$, the curvature tensor or second fundamental form $\boldsymbol{k}$, covariant differentiation $\nabla$, and Lie derivation $L_{\boldsymbol{v}}$, along with the definition of maps, push-forwards and pull-backs. We briefly review these concepts in Appendix D. We refer to [40, 41] for extensive reviews on the differential geometry of surfaces and manifolds in general.

## 9.1 Lagrangian, Eulerian and ALE parametrizations

In this section, we consider the parametrization of a two-dimensional continuum $\Gamma_t$ moving in $\mathbb{R}^3$. We assume the existence of a Lagrangian parametrization of $\Gamma_t$, $\boldsymbol{\phi} : \bar{\Gamma} \times \mathcal{I} \ni (\boldsymbol{\xi}, t) \mapsto \boldsymbol{x} \in \Gamma_t$, where $\bar{\Gamma} \subset \mathbb{R}^2$, $\Gamma_t \subset \mathbb{R}^3$ and $\mathcal{I} \subset \mathbb{R}$, so that

a point $\boldsymbol{\xi} = (\xi_1, \xi_2) \in \bar{\Gamma}$ identifies a material particle and the curve obtained by fixing $\boldsymbol{\xi}$, $\boldsymbol{\phi}_{\boldsymbol{\xi}}(t) = \boldsymbol{\phi}(\boldsymbol{\xi}, t)$, its trajectory in $\mathbb{R}^3$ (see Fig. 9.1). We focus on a specific chart, although the arguments presented in this section can be trivially extended to surfaces represented with an atlas of charts. For systems with multiple components, where material particles of the different components coexist at the same point $\boldsymbol{x} \in \Gamma_t$, a single Lagrangian parametrization of $\Gamma_t$ does not exist. This is the case of a lipid bilayer, where a point $\boldsymbol{x} \in \Gamma_t$ has simultaneously attached two material particles belonging to each monolayer. Nevertheless, we can always define a Lagrangian parametrization for each of the components of the system independently so that the results in this and following Sections can be applied to each component (monolayer) separately. The velocity resulting from the Lagrangian parametrization is called the material velocity

$$\bar{\boldsymbol{V}}(\boldsymbol{\xi}, t) = \frac{d}{dt}\boldsymbol{\phi}_{\boldsymbol{\xi}}(t) = \partial_t \boldsymbol{\phi}(\boldsymbol{\xi}, t)\,. \tag{9.1}$$

The spatial velocity $\boldsymbol{V}$ on $\Gamma_t$ is obtained by composition with $\boldsymbol{\phi}^{-1}$

$$\boldsymbol{V}(\boldsymbol{x}, t) = \bar{\boldsymbol{V}} \circ \boldsymbol{\phi}^{-1}(\boldsymbol{x}, t). \tag{9.2}$$

We note that $\boldsymbol{\phi}^{-1}(\boldsymbol{x}, t)$ refers to the inverse of the mapping $\boldsymbol{\phi}_t(\boldsymbol{\xi}) = \boldsymbol{\phi}(\boldsymbol{\xi}, t)$ obtained by fixing time $t$. In general, $\boldsymbol{V}$ has a tangential and a normal component to $\Gamma_t$

$$\boldsymbol{V} = \boldsymbol{v} + v_n \boldsymbol{n}, \tag{9.3}$$

where $\boldsymbol{n}$ is the unit normal to the surface. The normal velocity $v_n$ characterizes shape changes of $\Gamma_t$ while $\boldsymbol{v}$ represents the flow of material tangent to $\Gamma_t$. In the remainder of this work we denote by upper-case letters vectors with tangential and normal components to $\Gamma_t$ and by lower-case letters vectors that are tangent to $\Gamma_t$; the only exception to this rule is the normal $\boldsymbol{n}$. We now introduce an alternative parametrization of the surface $\boldsymbol{\psi} : \tilde{\Gamma} \times \mathcal{I} \ni (\boldsymbol{\xi}, t) \mapsto \boldsymbol{x} \in \Gamma_t$, where $\tilde{\Gamma} \subset \mathbb{R}^2$. The curves of constant $\boldsymbol{\xi}$, $\boldsymbol{\psi}_{\boldsymbol{\xi}}(t) = \boldsymbol{\psi}(\boldsymbol{\xi}, t)$ do not follow trajectories of material particles in general. The velocity fields associated with

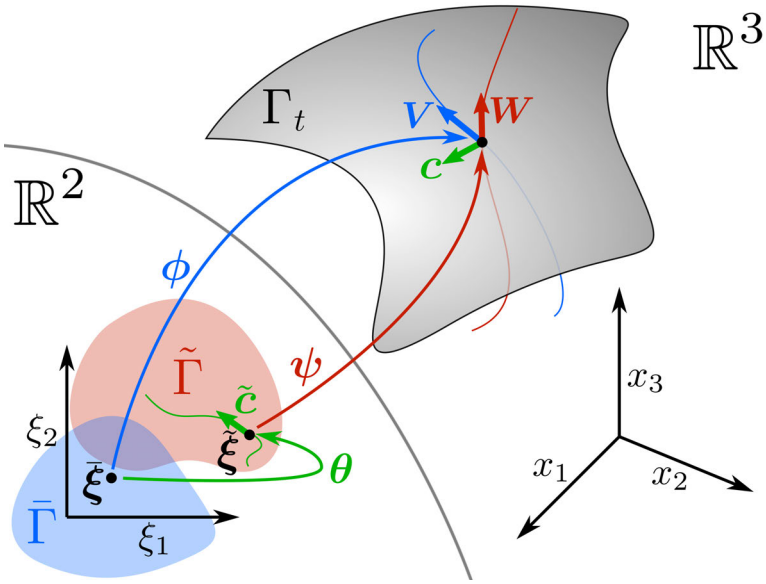


**Figure 9.1**: A Lagrangian parametrization $\phi(\xi, t)$ maps a domain $\bar{\Gamma} \subset \mathbb{R}^2$ onto a time-evolving surface $\Gamma_t$. Fixing a point $\bar{\xi}$ in $\bar{\Gamma}$, the curve in $\mathbb{R}^3$ generated by $\phi$ follows the time evolution of a material particle (blue). The velocity of this particle at time $t$ is given by $\boldsymbol{V}$. An alternative parametrization $\psi(\xi, t)$ maps the parametric domain $\tilde{\Gamma}$ onto $\Gamma_t$. The composition $\boldsymbol{\theta} = \psi^{-1} \circ \phi$ characterize the position of material particles in $\tilde{\Gamma}$. The curve in $\tilde{\Gamma}$ generated by the mapping $\boldsymbol{\theta}$ for $\bar{\xi}$ fixed (green) indicates how the parametric position of a material particle evolves with time in $\tilde{\Gamma}$. At time $t$ this curve has a velocity $\tilde{c}$. The curve constructed from the map $\psi$ by fixing $\tilde{\xi} = \boldsymbol{\theta}(\bar{\xi}, t)$ (red) does not follow the time-evolution of any material particle in general. At time $t$ this curve has a velocity $\boldsymbol{W}$. The velocities $\boldsymbol{V}$ and $\boldsymbol{W}$ are related by $\boldsymbol{V} = \boldsymbol{W} + \boldsymbol{c}$, where $\boldsymbol{c}$ is the push-forward of $\tilde{c}$ through $\psi$.

this parametrization are

$$\begin{aligned} \tilde{\boldsymbol{W}}(\xi, t) &= \frac{d}{dt}\psi_{\xi}(t) = \partial_t \psi(\xi, t), \\ \boldsymbol{W}(\boldsymbol{x}, t) &= \tilde{\boldsymbol{W}} \circ \psi^{-1}(\boldsymbol{x}, t) = \boldsymbol{w} + w_n \boldsymbol{n}. \end{aligned} \tag{9.4}$$

We can construct a map relating both parametrizations $\boldsymbol{\theta} = \psi^{-1} \circ \phi : \bar{\Gamma} \times \mathcal{I} \ni (\xi, t) \mapsto \xi \in \tilde{\Gamma}$. The curves of constant $\xi$, $\boldsymbol{\theta}_{\xi}(t) = \boldsymbol{\theta}(\xi, t)$, track the parametric

positions of material particles evolving in $\tilde{\Gamma}$, and have a velocity

$$\begin{aligned} \bar{\boldsymbol{c}}(\boldsymbol{\xi}, t) &= \frac{d}{dt}\boldsymbol{\theta}_{\boldsymbol{\xi}}(t) = \partial_t \boldsymbol{\theta}(\boldsymbol{\xi}, t). \\ \tilde{\boldsymbol{c}}(\boldsymbol{\xi}, t) &= \bar{\boldsymbol{c}} \circ \boldsymbol{\theta}^{-1}(\boldsymbol{\xi}), \end{aligned} \tag{9.5}$$

To physically interpret $\tilde{\boldsymbol{c}}$, we note that its push-forward by $\boldsymbol{\psi}$ is a field on $\Gamma_t$ that represents the relative velocity of material particles with respect to the parametrization given by $\boldsymbol{\psi}$. Indeed,

$$\boldsymbol{c} = \boldsymbol{\psi}_* \tilde{\boldsymbol{c}} = [D\boldsymbol{\psi}\tilde{\boldsymbol{c}}] \circ \boldsymbol{\psi}^{-1}, \tag{9.6}$$

where $\boldsymbol{\psi}_*$ denotes the push-forward, and $D\boldsymbol{\psi}$ stands for the derivative of $\boldsymbol{\psi}$, which is a linear mapping $D\boldsymbol{\psi} : T_{\boldsymbol{\xi}}\tilde{\Gamma} \to T_{\boldsymbol{x}}\Gamma$ from the tangent space of $\tilde{\Gamma}$ at $\boldsymbol{\xi}$, $T_{\boldsymbol{\xi}}\tilde{\Gamma}$, to the tangent space of $\Gamma$ at $\boldsymbol{x} = \boldsymbol{\psi}(\boldsymbol{\xi})$, $T_{\boldsymbol{x}}\Gamma$. Using the chain rule and previous definitions

$$\begin{aligned} \boldsymbol{V} &= \partial_t \boldsymbol{\phi} \circ \boldsymbol{\phi}^{-1} \\ &= \partial_t \left( \boldsymbol{\psi} \circ \boldsymbol{\psi}^{-1} \circ \boldsymbol{\phi} \right) \circ \boldsymbol{\phi}^{-1} \\ &= \partial_t \left( \boldsymbol{\psi} \circ \boldsymbol{\theta} \right) \circ \boldsymbol{\phi}^{-1} \\ &= \partial_t \boldsymbol{\psi} \circ \boldsymbol{\theta} \circ \boldsymbol{\phi}^{-1} + \left[ (D\boldsymbol{\psi}) \circ \boldsymbol{\theta} \circ \boldsymbol{\phi}^{-1} \right] \left[ \partial_t \boldsymbol{\theta} \circ \boldsymbol{\phi}^{-1} \right] \\ &= \partial_t \boldsymbol{\psi} \circ \boldsymbol{\psi}^{-1} + \left[ (D\boldsymbol{\psi}) \circ \boldsymbol{\psi}^{-1} \right] \left[ \bar{\boldsymbol{c}} \circ \boldsymbol{\phi}^{-1} \right] \\ &= \boldsymbol{W} + \left[ (D\boldsymbol{\psi}) \circ \boldsymbol{\psi}^{-1} \right] \left[ \tilde{\boldsymbol{c}} \circ \boldsymbol{\theta} \circ \boldsymbol{\phi}^{-1} \right] \\ &= \boldsymbol{W} + \left[ (D\boldsymbol{\psi}) \circ \boldsymbol{\psi}^{-1} \right] \left[ \tilde{\boldsymbol{c}} \circ \boldsymbol{\psi}^{-1} \right] \\ &= \boldsymbol{W} + \left[ (D\boldsymbol{\psi})\, \tilde{\boldsymbol{c}} \right] \circ \boldsymbol{\psi}^{-1} \\ &= \boldsymbol{W} + \boldsymbol{\psi}_* \tilde{\boldsymbol{c}} \\ &= \boldsymbol{W} + \boldsymbol{c}. \end{aligned} \tag{9.7}$$

Since $\boldsymbol{c}$ is the push-forward with respect to $\boldsymbol{\psi}$, then it is tangent to $\Gamma_t$. Comparing Eqs. (9.3) and (9.4), we conclude that

$$v_n = w_n, \tag{9.8}$$

and

$$\boldsymbol{v} = \boldsymbol{w} + \boldsymbol{c}. \tag{9.9}$$

This reflects that, since both parametrizations describe the same shape, their normal velocities, characterizing shape changes, must coincide. With this restriction in mind, we can now introduce the notion of Eulerian parametrization in the context of a time-evolving surface. We say that a parametrization $\boldsymbol{\chi}$ is Eulerian if its velocity field is always perpendicular to the surface

$$\partial_t \boldsymbol{\chi} \circ \boldsymbol{\chi}^{-1} = v_n \boldsymbol{n}. \tag{9.10}$$

In summary, the parametrization $\boldsymbol{\phi}$ is a Lagrangian parametrization that tracks the evolution of material particles as they move with and along $\Gamma_t$. On the other hand, $\boldsymbol{\chi}$ is an Eulerian parametrization whose velocity is always perpendicular to $\Gamma_t$ regardless of the tangential flows of material. These parametrizations are special cases of a general parametrization $\boldsymbol{\psi}$, which may present tangential movements not consistent with the velocity of material particles. This kind of parametrization is referred to as an arbitrary Lagrangian-Eulerian (ALE) parametrization.

We introduce here some notation. The pull-back of a tensor $\boldsymbol{t}$ on $\Gamma_t$ onto the material, Eulerian and ALE parametric domains are denoted by

$$\bar{\boldsymbol{t}} = \boldsymbol{\phi}^* \boldsymbol{t}, \qquad \hat{\boldsymbol{t}} = \boldsymbol{\chi}^* \boldsymbol{t}, \qquad \tilde{\boldsymbol{t}} = \boldsymbol{\psi}^* \boldsymbol{t}, \tag{9.11}$$

where $\boldsymbol{\phi}^*$ denotes the pull-back through $\boldsymbol{\phi}$. In the basis of the tangent bundle to $\Gamma_t$ given by the vector fields $\left\{\boldsymbol{e}_1 = \partial_1 \boldsymbol{\phi} \circ \boldsymbol{\phi}^{-1}, \boldsymbol{e}_2 = \partial_2 \boldsymbol{\phi} \circ \boldsymbol{\phi}^{-1}\right\}$, the so-called convected basis of $\boldsymbol{\phi}$, the components of $\boldsymbol{t}$ equal those of $\bar{\boldsymbol{t}}$ in the orthonormal basis $\{\boldsymbol{i}_1, \boldsymbol{i}_2\}$ of $\bar{\Gamma}$ given by the pair of normalized vectors perpendicular to the lines of constant $\xi_2$ and $\xi_1$. Equivalently, this holds for tensors expressed in the convected basis given by the Eulerian and ALE parametrizations.

## 9.2 Material, Eulerian and ALE time derivatives

We introduce next the concept of time-derivative of fields on $\Gamma_t$. Let us focus for simplicity on a scalar field $f(\boldsymbol{x}, t)$. We first note that the operator $\partial_t$ acting on $f(\boldsymbol{x}, t)$, with the usual meaning of taking the time-derivative at $\boldsymbol{x}$ fixed, is not well defined since $\boldsymbol{x}$ cannot be held fixed in a time-evolving surface in general

[31]. The idea of time-derivative can be more easily rationalized with the use of a parametrization. Let us first consider the Lagrangian parametrization $\phi$. Fixing a point $\boldsymbol{\xi} \in \bar{\Gamma}$, we can compute how $f(\boldsymbol{x}, t)$ changes along the curve $\phi_{\boldsymbol{\xi}}(t)$. We define the *material time derivative* of the scalar $f$ as

$$D_t f(\boldsymbol{x}, t) \equiv \left. \frac{d}{dt} f\left(\phi_{\boldsymbol{\xi}}(t), t\right) \right|_{\boldsymbol{\xi}=\phi^{-1}(\boldsymbol{x})} . \tag{9.12}$$

We note that $f\left(\phi_{\boldsymbol{\xi}}(t), t\right)$ is a function of $t$ only and therefore the right-hand side of the previous expression is univocally defined. By noting that the pull-back of $f$ onto $\bar{\Gamma}$ is $\bar{f} = \phi_* f = f \circ \phi$, we can rewrite the previous expression as

$$\begin{aligned} D_t f(\boldsymbol{x}, t) = & \left. \frac{d}{dt} \bar{f}\left(\boldsymbol{\xi}, t\right) \right|_{\boldsymbol{\xi}=\phi^{-1}(\boldsymbol{x})} \\ & = \partial_t \bar{f} \circ \phi^{-1}(\boldsymbol{x}) = \partial_t \left(f \circ \phi\right) \circ \phi^{-1}(\boldsymbol{x}) = \phi_* \partial_t \left(\phi^* f\right)(\boldsymbol{x}), \end{aligned} \tag{9.13}$$

where $\partial_t \bar{f}$ has the usual meaning of taking the partial derivative of $\bar{f}$ at fixed $\boldsymbol{\xi}$. This is nothing but the *Lie-derivative* of $f$ along the flow generated by $\boldsymbol{V}$, usually denoted by $L_{\boldsymbol{V}} f$, which is an extension to non-tangential vector fields of the usual definition of Lie-derivative (see Appendix D.6). Thus, the material time-derivative of $f$ is the push-forward of the time-derivative of the pull-back of $f$ by the Lagrangian parametrization $\phi$

$$D_t f = L_{\boldsymbol{V}} f = \phi_* \partial_t \left(\phi^* f\right) . \tag{9.14}$$

We can equivalently define the *ALE time-derivative* of $f$

$$\tilde{\partial}_t f \equiv L_{\boldsymbol{W}} f = \psi_* \partial_t \left(\psi^* f\right) , \tag{9.15}$$

and the *Eulerian time derivative*

$$\partial_t f \equiv L_{v_n \boldsymbol{n}} \boldsymbol{t} = \chi_* \partial_t \left(\chi^* f\right) . \tag{9.16}$$

In this context the meaning of the symbol $\partial_t$ is clear; it measures the rate of change of $f$ along the flow normal to $\Gamma_t$. If the shape of $\Gamma_t$ remains stationary,

then $\partial_t$ recovers the usual meaning of taking the derivative with respect to time at fixed $\boldsymbol{x}$. We note that $\partial_t$ retains the usual meaning when applied to fields on parametric domains, e.g. $\partial_t \bar{f} = \lim_{\Delta t \to 0} \frac{\bar{f}(\boldsymbol{\xi}, t+\Delta t) - \bar{f}(\boldsymbol{\xi}, t)}{\Delta t}$, and should not be confused with the definition Eq. (9.16) for fields on $\Gamma_t$. The operators $D_t$, $\tilde{\partial}_t$ and $\partial_t$ are related. For instance, using previous definitions in Eq. (9.11) and the chain rule,

$$\begin{aligned} D_t f &= \partial_t \bar{f} \circ \boldsymbol{\phi}^{-1} = \partial_t \left( \tilde{f} \circ \boldsymbol{\theta} \right) \circ \boldsymbol{\phi}^{-1} \\ &= \partial_t \tilde{f} \circ \boldsymbol{\theta} \circ \boldsymbol{\phi}^{-1} + \left[ D\tilde{f} \circ \boldsymbol{\theta} \circ \boldsymbol{\phi}^{-1} \right] \left[ \partial_t \boldsymbol{\theta} \circ \boldsymbol{\phi}^{-1} \right] \\ &= L_{\boldsymbol{W}} f + \left[ D\tilde{f} \circ \boldsymbol{\psi}^{-1} \right] \left[ \bar{\boldsymbol{c}} \circ \boldsymbol{\phi}^{-1} \right] \\ &= L_{\boldsymbol{W}} f + \left[ D\tilde{f} \circ \boldsymbol{\psi}^{-1} \right] \left[ \tilde{\boldsymbol{c}} \circ \boldsymbol{\theta} \circ \boldsymbol{\phi}^{-1} \right] \\ &= L_{\boldsymbol{W}} f + \left[ D\tilde{f} \circ \boldsymbol{\psi}^{-1} \right] \left[ \tilde{\boldsymbol{c}} \circ \boldsymbol{\psi}^{-1} \right] \\ &= L_{\boldsymbol{W}} f + \left[ D\tilde{f} \tilde{\boldsymbol{c}} \right] \circ \boldsymbol{\psi}^{-1}. \end{aligned} \tag{9.17}$$

Here we identify $\left[ D\tilde{f}\tilde{\boldsymbol{c}} \right] \circ \boldsymbol{\psi}^{-1}$ as the pull-back of $\nabla f(\boldsymbol{c})$, where $\nabla f$ is the covariant derivative of $f$, i.e. a linear form that, applied to a vector $\boldsymbol{c}$, computes the directional derivative of $f$ along $\boldsymbol{c}$ (see Appendix D). Thus, we can rewrite the previous equation as

$$\begin{aligned} D_t f &= L_{\boldsymbol{W}} f + \nabla f(\boldsymbol{c}) \\ &= \tilde{\partial}_t f + \nabla f(\boldsymbol{c}), \end{aligned} \tag{9.18}$$

which can also be expressed as

$$D_t f = \tilde{\partial}_t f + \mathbf{grad} f \cdot (\boldsymbol{c}). \tag{9.19}$$

where $\mathbf{grad} f$ is the gradient of $f$, defined as $\mathbf{grad} f = (\nabla f)^\sharp$, in components $(\mathbf{grad} f)^a = g^{ab} \nabla_b f$. Equivalently one can derive the relations

$$\begin{aligned} D_t f &= \partial_t f + \mathbf{grad} f \cdot \boldsymbol{v}, \\ \tilde{\partial}_t f &= \partial_t f + \mathbf{grad} f \cdot \boldsymbol{w}. \end{aligned} \tag{9.20}$$

## 9.3 Deformation and rate-of-deformation tensors

An important tensor on $\Gamma_t$ is the first fundamental form or metric tensor $\boldsymbol{g}$. The metric tensor induces a scalar product on the tangent space of $\Gamma_t$ that allows

us to measure lengths, angles and areas on $\Gamma_t$. Given two tangent vectors to $\Gamma_t$, $\boldsymbol{v}$ and $\boldsymbol{w}$, the scalar product is defined by

$$\boldsymbol{v} \cdot \boldsymbol{w} = \boldsymbol{g}(\boldsymbol{v}, \boldsymbol{w}) = g_{ab} v^a w^b. \tag{9.21}$$

where the notation $\boldsymbol{g}(\cdot, \cdot)$ denotes that $\boldsymbol{g}$ is a bilinear form. For surfaces in $\mathbb{R}^3$, the metric tensor is defined so that the scalar product on $\Gamma_t$ coincides with the scalar product $\langle \cdot, \cdot \rangle$ in $\mathbb{R}^3$, $\boldsymbol{v} \cdot \boldsymbol{w} = \langle \boldsymbol{v}, \boldsymbol{w} \rangle$ for all $\boldsymbol{v}$ and $\boldsymbol{w}$ tangent to $\Gamma_t$. Then, given a basis $\{\boldsymbol{e}_1, \boldsymbol{e}_2\}$ of $T\Gamma_t$, the tangent bundle of $\Gamma_t$, the components of the metric tensor in this basis are $g_{ab} = \langle \boldsymbol{e}_a, \boldsymbol{e}_b \rangle$. Let us consider two curves in the parametric domain $\bar{\Gamma}$, given by $\bar{\boldsymbol{\alpha}}(\lambda) : [-1, 1] \to \bar{\Gamma}$ and $\bar{\boldsymbol{\beta}}(\lambda) : [-1, 1] \to \bar{\Gamma}$, that cross at $\lambda = 0$, and the image of these curves by $\boldsymbol{\phi}$, $\boldsymbol{\alpha}(\lambda, t) = \boldsymbol{\phi}(\bar{\boldsymbol{\alpha}}(\lambda), t)$ and $\boldsymbol{\beta}(\lambda, t) = \boldsymbol{\phi}(\bar{\boldsymbol{\beta}}(\lambda), t)$ (see Fig. 9.2). The length of $\boldsymbol{\alpha}$ (and equivalently of $\boldsymbol{\beta}$) is given by the functional

$$l[\boldsymbol{\alpha}](t) = \int_{-1}^{1} ||\partial_\lambda \boldsymbol{\alpha}|| d\lambda. \tag{9.22}$$

where $||\boldsymbol{v}|| = \sqrt{\boldsymbol{v} \cdot \boldsymbol{v}}$ is the norm of $\boldsymbol{v}$. The angle $\theta(t)$ between curves $\boldsymbol{\alpha}$ and $\boldsymbol{\beta}$ is given by

$$\cos\theta(t) = \left[ \frac{\partial_\lambda \boldsymbol{\alpha} \cdot \partial_\lambda \boldsymbol{\beta}}{||\partial_\lambda \boldsymbol{\alpha}|| ||\partial_\lambda \boldsymbol{\beta}||} \right]_{\lambda=0} \tag{9.23}$$

The time-evolution of the lengths of material curves and the angles between them measures how the material deforms. It is interesting to note that the pull-back of $\boldsymbol{g}$, $\bar{\boldsymbol{g}} = \boldsymbol{\phi}^* \boldsymbol{g}$, induces a time-dependent scalar product on $\bar{\Gamma}$ that allows us to compute products of deformed vectors from their time-independent description on $\bar{\Gamma}$. For instance,

$$\begin{aligned}
(\partial_\lambda \boldsymbol{\alpha} \cdot \partial_\lambda \boldsymbol{\beta})_{\lambda=0} &= [(\boldsymbol{g} \circ \boldsymbol{\alpha})(\partial_\lambda \boldsymbol{\alpha}, \partial_\lambda \boldsymbol{\beta})]_{\lambda=0} \\
&= \left[ (\boldsymbol{g} \circ \boldsymbol{\phi} \circ \bar{\boldsymbol{\alpha}}) \left( (D\boldsymbol{\phi} \circ \bar{\boldsymbol{\alpha}}) \bar{\boldsymbol{\alpha}}', (D\boldsymbol{\phi} \circ \bar{\boldsymbol{\alpha}}) \bar{\boldsymbol{\beta}}' \right) \right]_{\lambda=0} \\
&= \left[ \left\{ \left[ D\boldsymbol{\phi}^T (\boldsymbol{g} \circ \boldsymbol{\phi}) D\boldsymbol{\phi} \right] \circ \bar{\boldsymbol{\alpha}} \right\} \left( \bar{\boldsymbol{\alpha}}', \bar{\boldsymbol{\beta}}' \right) \right]_{\lambda=0} \\
&= \left[ (\bar{\boldsymbol{g}} \circ \bar{\boldsymbol{\alpha}}) \left( \bar{\boldsymbol{\alpha}}', \bar{\boldsymbol{\beta}}' \right) \right]_{\lambda=0},
\end{aligned} \tag{9.24}$$

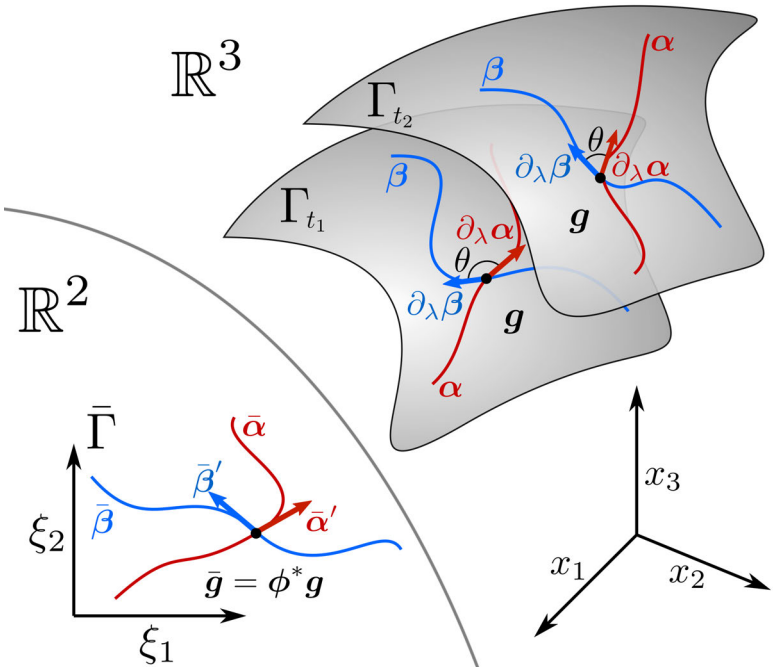


**Figure 9.2**: The material curves $\bar{\boldsymbol{\alpha}}$ and $\bar{\boldsymbol{\beta}}$ are mapped onto $\Gamma_t$ to curves $\boldsymbol{\alpha}$ and $\boldsymbol{\beta}$ through the Lagrangian parametrization $\boldsymbol{\phi}$. As $\Gamma_t$ deforms, the length of material curves and the angle between them changes. Through the action of the pull-back, we can induce a metric on $\bar{\Gamma}$, $\bar{\boldsymbol{g}} = \boldsymbol{\phi}^* \boldsymbol{g}$, the right Cauchy-Green deformation tensor, that allows us to compute scalar products such as $\partial_\lambda \boldsymbol{\alpha} \cdot \partial_\lambda \boldsymbol{\beta}$ from $\bar{\boldsymbol{g}}(\bar{\boldsymbol{\alpha}}', \bar{\boldsymbol{\beta}}')$. Thus, the deformation of $\Gamma_t$ is encoded on $\bar{\Gamma}$ by $\bar{\boldsymbol{g}}$.

where we have used that $\bar{\boldsymbol{g}} = \boldsymbol{\phi}^* \boldsymbol{g} = D\boldsymbol{\phi}^T \, (\boldsymbol{g} \circ \boldsymbol{\phi}) \, D\boldsymbol{\phi}$. In components

$$
\begin{aligned}
(\partial_\lambda \alpha^a \partial_\lambda \beta_a)_{\lambda=0} &= \left[ (g_{ab} \circ \boldsymbol{\alpha}) \, \partial_\lambda \alpha^a \partial_\lambda \beta^b \right]_{\lambda=0} \\
&= \left[ (g_{ab} \circ \boldsymbol{\phi} \circ \bar{\boldsymbol{\alpha}}) \, (D\phi^a_c \circ \bar{\boldsymbol{\alpha}}) \, \frac{d}{d\lambda} \bar{\alpha}^c \left( D\phi^b_d \circ \bar{\boldsymbol{\alpha}} \right) \frac{d}{d\lambda} \bar{\beta}^d \right]_{\lambda=0} \\
&= \left[ \left\{ \left[ (g_{ab} \circ \boldsymbol{\phi}) \, (D\boldsymbol{\phi})^a_c \, (D\boldsymbol{\phi})^b_d \right] \circ \bar{\boldsymbol{\alpha}} \right\} \frac{d}{d\lambda} \bar{\alpha}^c \frac{d}{d\lambda} \bar{\beta}^d \right]_{\lambda=0} \\
&= \left[ (\bar{g}_{ab} \circ \bar{\boldsymbol{\alpha}}) \, \frac{d}{d\lambda} \bar{\alpha}^a \frac{d}{d\lambda} \bar{\beta}^b \right]_{\lambda=0} .
\end{aligned}
\tag{9.25}
$$

Equivalently,

$$||\partial_\lambda \boldsymbol{\alpha}|| = \sqrt{(\bar{\boldsymbol{g}} \circ \bar{\boldsymbol{\alpha}})\,(\bar{\boldsymbol{\alpha}}', \bar{\boldsymbol{\alpha}}')}. \tag{9.26}$$

Thus, scalar products, lengths and angles of material curves on $\Gamma_t$, such as $\boldsymbol{\alpha}$ and $\boldsymbol{\beta}$, can be measured on $\bar{\Gamma}$ , from the time-independent $\bar{\boldsymbol{\alpha}}$ and $\bar{\boldsymbol{\beta}}$, with the time-dependent scalar product induced by $\bar{\boldsymbol{g}}$. It is clear from Eqs. (9.24) and (9.26) that the time-dependence of these measures of local deformation is completely encoded in $\bar{\boldsymbol{g}}$. We conclude that the tensor $\bar{\boldsymbol{g}}$ characterizes the deformation of $\Gamma_t$; in continuum mechanics this tensor is referred to as the (right Cauchy-Green) *deformation tensor* and is generally denoted by $\boldsymbol{C}$. The rate of change of this tensor is

$$\bar{\boldsymbol{d}} = \frac{1}{2}\partial_t \bar{\boldsymbol{g}}, \tag{9.27}$$

where the 1/2 is introduced here to follow the usual convention. The push-forward of this tensor to $\Gamma_t$ by $\phi$ defines the so-called *rate-of-deformation tensor*,

$$\boldsymbol{d} = \frac{1}{2}\phi_* \partial_t \bar{\boldsymbol{g}} = \frac{1}{2}\phi_* \partial_t \left(\phi^* \boldsymbol{g}\right) = \frac{1}{2} L_{\boldsymbol{v}} \boldsymbol{g}, \tag{9.28}$$

where we recognize again the Lie derivative, this time applied to the metric tensor. The rate of change of the scalar product can then be written as

$$\begin{aligned} \frac{d}{dt}\left(\partial_\lambda \boldsymbol{\alpha} \cdot \partial_\lambda \boldsymbol{\beta}\right)\Big|_{\lambda=0} &= \left[\frac{d}{dt}\left(\bar{\boldsymbol{g}} \circ \bar{\boldsymbol{\alpha}}\right)\left(\bar{\boldsymbol{\alpha}}', \bar{\boldsymbol{\beta}}'\right)\right]_{\lambda=0} \\ &= \left[\left(\partial_t \bar{\boldsymbol{g}} \circ \bar{\boldsymbol{\alpha}}\right)\left(\bar{\boldsymbol{\alpha}}', \bar{\boldsymbol{\beta}}'\right)\right]_{\lambda=0} \\ &= \left[\phi_*\left(\partial_t \bar{\boldsymbol{g}} \circ \bar{\boldsymbol{\alpha}}\right)\left(\phi_* \bar{\boldsymbol{\alpha}}', \phi_* \bar{\boldsymbol{\beta}}'\right)\right]_{\lambda=0} \\ &= 2\left[\left(\boldsymbol{d} \circ \boldsymbol{\alpha}\right)\left(\partial_\lambda \boldsymbol{\alpha}, \partial_\lambda \boldsymbol{\beta}\right)\right]_{\lambda=0}, \end{aligned} \tag{9.29}$$

and the rate of change of the norm

$$\begin{aligned} \left[\frac{d}{dt}\left|\partial_\lambda \boldsymbol{\alpha}\right|\right] &= \frac{1}{2\left|\partial_\lambda \boldsymbol{\alpha}\right|}\frac{d}{dt}\left(\bar{\boldsymbol{g}} \circ \bar{\boldsymbol{\alpha}}\right)\left(\bar{\boldsymbol{\alpha}}', \bar{\boldsymbol{\alpha}}'\right) \\ &= \frac{1}{\left|\partial_\lambda \boldsymbol{\alpha}\right|}\left(\boldsymbol{d} \circ \boldsymbol{\alpha}\right)\left(\partial_\lambda \boldsymbol{\alpha}, \partial_\lambda \boldsymbol{\alpha}\right). \end{aligned} \tag{9.30}$$

Thus, the rate of change of the deformation of $\Gamma_t$ is encoded in $\boldsymbol{d}$. To obtain the form of this tensor in terms of $\boldsymbol{V}$, let us consider the components of $\bar{\boldsymbol{g}}$

$$[\bar{\boldsymbol{g}}]_{ab}(\boldsymbol{\xi}) = g_{ab} \circ \boldsymbol{\phi}(\boldsymbol{\xi}) = \langle \boldsymbol{e}_a, \boldsymbol{e}_b \rangle \circ \boldsymbol{\phi}(\boldsymbol{\xi}) \tag{9.31}$$

where $\boldsymbol{e}_a = \partial_a \boldsymbol{\phi} \circ \boldsymbol{\phi}^{-1}$. Then, since pull-backs and push-forward do not have an effect in convected coordinates, we have

$$\begin{aligned}
[L_{\boldsymbol{V}} \boldsymbol{g}]_{ab} &= \partial_t \bar{g}_{ab} \circ \boldsymbol{\phi}^{-1} \\
&= \left[ \langle \partial_t \partial_a \boldsymbol{\phi} \circ \boldsymbol{\phi}^{-1}, \boldsymbol{e}_b \rangle + \langle \boldsymbol{e}_a, \partial_t \partial_b \boldsymbol{\phi} \circ \boldsymbol{\phi}^{-1} \rangle \right] \\
&= \left[ \left\langle \partial_a \left[ (\boldsymbol{v} + v_n \boldsymbol{n}) \circ \boldsymbol{\phi} \right] \circ \boldsymbol{\phi}^{-1}, \boldsymbol{e}_b \right\rangle + \left\langle \boldsymbol{e}_a, \partial_a \left[ (\boldsymbol{v} + v_n \boldsymbol{n}) \circ \boldsymbol{\phi} \right] \circ \boldsymbol{\phi}^{-1} \right\rangle \right] \\
&= \nabla_a v_b + \nabla_b v_a - 2 v_n k_{ab},
\end{aligned} \tag{9.32}$$

where we have used the conmutativity of partial derivatives, the definition of covariant derivative $\nabla_a v_b = \langle \partial_a (\boldsymbol{v} \circ \boldsymbol{\phi}) \circ \boldsymbol{\phi}^{-1}, \boldsymbol{e}_b \rangle$, the orthogonality of $\boldsymbol{n}$ to the tangent space of $\Gamma_t$ $\langle \boldsymbol{e}_a, \boldsymbol{n} \rangle = 0$, and the definition of the curvature tensor $k_{ab} = \langle \partial_b (\boldsymbol{n} \circ \boldsymbol{\phi}) \circ \boldsymbol{\phi}^{-1}, \boldsymbol{e}_a \rangle$. Therefore, the expression of the rate-of-deformation tensor for a surface moving in Euclidean space is given by [100]

$$\boldsymbol{d} = \frac{1}{2} \left[ \nabla \boldsymbol{v}^\flat + \left( \nabla \boldsymbol{v}^\flat \right)^T \right] - v_n \boldsymbol{k}, \tag{9.33}$$

or in indicial notation

$$d_{ab} = \frac{1}{2} \left[ \nabla_a v_b + \nabla_b v_a \right] - v_n k_{ab}. \tag{9.34}$$

From this expression, it is clear that $\Gamma_t$ deforms through tangential flows, which contribute to the rate-of-deformation tensor with the usual term $\frac{1}{2} \left[ \nabla \boldsymbol{v}^\flat + \left( \nabla \boldsymbol{v}^\flat \right)^T \right]$, but also through the change in shape of $\Gamma_t$, which contributes with the term $-v_n \boldsymbol{k}$. This relation illustrates the coupling between tangential flows and shape changes in the presence of curvature.

## 9.4 Reynolds transport theorem and conservation of mass

In this section we extend the concept of Lagrangian, Eulerian and ALE time-derivatives of integrals on $\Gamma_t$. These are useful for computing the rate of

change of the free energy in Onsager's variational principle for non-material domains, or to derive conservation of mass. Consider a subset $\Xi \subset \Gamma_t$, a scalar field $f : \Gamma_t \to \mathbb{R}$, and define

$$I = \int_{\Xi} f dS. \tag{9.35}$$

To compute this integral, we can pull-back $f dS$ onto $\bar{\Gamma}$

$$I = \int_{\bar{\Xi}} \bar{f} \bar{J} d\boldsymbol{\xi}. \tag{9.36}$$

where $\bar{\Xi} = \boldsymbol{\phi}^{-1}(\Xi)$, $\bar{J} = \sqrt{\bar{g}}$, $\bar{g} = \det(\bar{\boldsymbol{g}}) = \det\left(D\boldsymbol{\phi}^T \cdot D\boldsymbol{\phi}\right)$ and $d\boldsymbol{\xi} = d\xi_1 d\xi_2$. We define the material time derivative of $I$ as

$$D_t I = \frac{d}{dt} \int_{\bar{\Xi}} \bar{f} \bar{J} d\boldsymbol{\xi}. \tag{9.37}$$

This characterizes the change of the integral $I$ when the domain $\Xi$ is a material subset of $\Gamma_t$, i.e. it evolves following the flow generated by $\boldsymbol{\phi}$ (see Fig. 9.3). Developing the definition we have

$$\begin{aligned} D_t I = \frac{d}{dt} \int_{\bar{\Xi}} \bar{f} \bar{J} d\boldsymbol{\xi} = \\ = \int_{\bar{\Xi}} \partial_t \left(\bar{f} \bar{J}\right) d\boldsymbol{\xi} = \int_{\bar{\Xi}} \left(\partial_t \bar{f} \bar{J} + \bar{f} \partial_t \bar{J}\right) d\boldsymbol{\xi}. \end{aligned} \tag{9.38}$$

The rate of change of $\bar{J} = \sqrt{\bar{g}}$ can be written in terms of $\boldsymbol{d}$ by noting that $\partial_t J = \frac{1}{2J} \partial_t \bar{g}$ and using Jacobi's formula $\partial_t \bar{g} = \bar{g} \bar{\boldsymbol{g}}^{-1} : (\partial_t \bar{\boldsymbol{g}}) = \bar{g} \left[\boldsymbol{g}^{-1} : (L_{\boldsymbol{V}} \boldsymbol{g}) \circ \boldsymbol{\phi}\right] = 2\bar{g} \left[\mathrm{tr}\boldsymbol{d} \circ \boldsymbol{\phi}\right]$, where $\mathrm{tr}\boldsymbol{d} = d^a{}_a = g^{ab} d_{ab}$ is the trace of the tensor $\boldsymbol{d}$. Thus, we have

$$\partial_t \bar{J} = \bar{J} \left(\mathrm{tr}\boldsymbol{d} \circ \boldsymbol{\phi}\right) = \bar{J} \left[\left(\mathrm{div}\boldsymbol{v} - v_n H\right) \circ \boldsymbol{\phi}\right], \tag{9.39}$$

where we have used Eq. (9.33), and $\mathrm{div}\boldsymbol{v} = \nabla_a v^a$ is the surface divergence of the tangential vector field $\boldsymbol{v}$. Then,

$$\begin{aligned} D_t I = \int_{\Xi} D_t f dS + \int_{\bar{\Xi}} \bar{f} \bar{J} \left[\left(\mathrm{div}\boldsymbol{v} - v_n H\right) \circ \boldsymbol{\phi}\right] d\boldsymbol{\xi} = \\ = \int_{\Xi} \left[D_t f + f \left(\mathrm{div}\boldsymbol{v} - v_n H\right)\right] dS. \end{aligned} \tag{9.40}$$

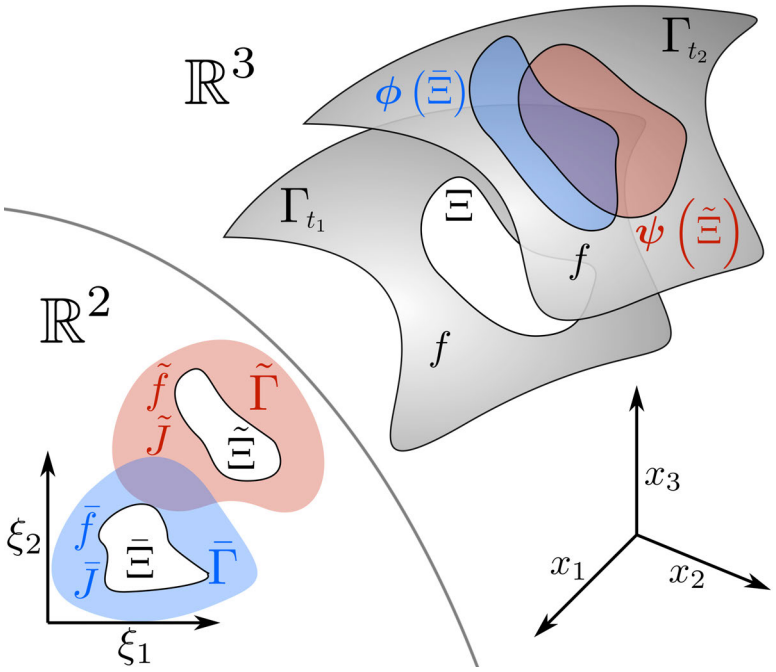


**Figure 9.3**: Given a domain $\Xi$ on $\Gamma_{t_1}$ and a scalar function $f$, we can compute the integral of $f$ on $\Xi$, $I = \int_\Xi f dS$, on $\bar{\Gamma}$ by pulling back the domain onto $\bar{\Gamma}$, $\bar{\Xi} = \phi^{-1}(\Xi)$, the function $\bar{f} = \phi^* f$ and using the Jacobian $\bar{J} = \sqrt{\bar{g}}$, $I = \int_{\bar{\Xi}} \bar{f}\bar{J} d\boldsymbol{\xi}$ (blue). The same can be done for the ALE parametrization (red). As $t$ evolves, the domain $\Xi$ evolves differently following the Lagrangian parametrization, $\boldsymbol{\phi}\left(\tilde{\Xi}\right)$, or the ALE parametrization, $\boldsymbol{\psi}\left(\tilde{\Xi}\right)$, and therefore the rate of change of $I$ on $\bar{\Gamma}$, $D_t I$, and on $\tilde{\Gamma}$, $\tilde{\partial}_t I$, is different. These are the material and ALE time-derivatives of $I$.

Using Eqs. (9.17) and (9.20) and the divergence theorem for surfaces (see Appendix D.7), we can rewrite the previous equation in different ways

$$D_t I = \int_\Xi \left[\partial_t f + \mathrm{div}\left(f\boldsymbol{v}\right) - f v_n H\right] dS, \tag{9.41}$$

$$= \int_\Xi \left[\partial_t f - f v_n H\right] dS + \int_{\partial\Xi} f\boldsymbol{v}\cdot\boldsymbol{\nu} dl, \tag{9.42}$$

$$= \int_\Xi \left[\tilde{\partial}_t f + \mathrm{div}\left(f\boldsymbol{c}\right) + f\left(\mathrm{div}\boldsymbol{w} - v_n H\right)\right] dS, \tag{9.43}$$

$$= \int_{\Xi} \left[ \tilde{\partial}_t f + f \left( \mathrm{div} \boldsymbol{w} - v_n H \right) \right] dS + \int_{\partial \Xi} f \boldsymbol{c} \cdot \boldsymbol{\nu} dl, \tag{9.44}$$

where $\partial\Xi$ indicates the boundary curve of $\Xi$ and $\boldsymbol{\nu}$ the outer normal to $\partial\Xi$ and tangent to $\Xi$. Eqs. (9.40)-(9.44) are the equivalent to Reynold's transport theorem for material domains terms of the material, Eulerian and ALE time-derivative of $f$. As for scalar fields, we can extend the notion of material time-derivative of an integral relative to other parametrizations. In particular, we can consider the parametric domain $\tilde{\Xi} = \psi^{-1}(\Xi)$, and the time-derivative

$$\tilde{\partial}_t I = \frac{d}{dt} \int_{\tilde{\Xi}} \tilde{f} \tilde{J} d\boldsymbol{\xi}, \tag{9.45}$$

where $\tilde{J} = \det \tilde{\boldsymbol{g}}$. This time-derivative characterizes the change of $I$ when it follows the flow generated by the ALE parametrization. One can easily prove that

$$D_t I = \tilde{\partial}_t I + \int_{\partial \Xi} f \boldsymbol{c} \cdot \boldsymbol{\nu} dl. \tag{9.46}$$

For an Eulerian parametrization, one equivalently finds

$$D_t I = \partial_t I + \int_{\partial \Xi} f \boldsymbol{v} \cdot \boldsymbol{\nu} dl. \tag{9.47}$$

From the previous expressions, it is clear that for a closed surface $D_t I = \tilde{\partial}_t I = \partial_t I$.

If $f = \rho$, the mass density, conservation of mass for every material subdomain $\Gamma_t$ requires that

$$D_t \int_{\Xi} \rho dS = \int_{\Xi} r dS, \tag{9.48}$$

where $r$ is the rate of creation of mass per unit area, which may for instance result from the exchange of material with the bulk. Since this must hold for every subdomain $\Xi$, localization leads to the Lagrangian, Eulerian and ALE forms of local conservation of mass

$$\begin{aligned} 0 &= D_t \rho + \rho \left( \mathrm{div} \boldsymbol{v} - v_n H \right) - r, \\ &= \partial_t \rho + \mathrm{div}(\rho \boldsymbol{v}) - \rho v_n H - r, \\ &= \tilde{\partial}_t \rho + \mathrm{div}(\rho \boldsymbol{c}) + \rho \left( \mathrm{div} \boldsymbol{w} - v_n H \right) - r. \end{aligned} \tag{9.49}$$

For inextensible fluid surfaces in the absence of mass exchange, balance of mass reduces to $D_t \rho = 0$, leading to the condition

$$\mathrm{div}\boldsymbol{v} - v_n H = 0. \tag{9.50}$$

It is then clear that for an inextensible surface with curvature, any shape change must be accompanied by a tangent flow to fulfill the inextensibility constraint, providing a clear example of the coupling between tangent flows and shape changes in the presence of curvature.

## 9.5 Characterization of elastic fluid surfaces: monolayers and bilayers

In previous Sections we have examined the definition of different parametrizations of a fluid surface $\Gamma_t$. Now, let us consider, without specific mention to any specific model, the basic ingredients needed for the characterization of a fluid surface from the viewpoint of Onsager's variational principle. For concreteness, we consider that $\Gamma_t$ is either a simple mono-component visco-elastic fluid or a bilayer model composed of two monolayers. These examples are relevant for modeling lipid bilayers. A summary of the different descriptions for these systems is presented in table 9.1.

Let us start with the monolayer. One way to describe $\Gamma_t$ is through a Lagrangian parametrization $\phi$. Since the Lagrangian parametrization encodes the deformation mapping of $\Gamma_t$, the free energy associated with $\Gamma_t$ can be entirely written in terms of $\phi$, $\mathcal{F}[\phi]$. Furthermore, since the velocity of the material particles is given by $\bar{\boldsymbol{V}} = \partial_t \phi$, we are in the simple situation in which $\dot{X} = V$ and we can characterize the dissipation potential as $\mathcal{D}\left[\phi; \bar{\boldsymbol{V}}\right]$. From the viewpoint of Onsager's variational principle, it is clear that the number of (continuous) degrees of freedom for this problem is 3, the components of $\bar{\boldsymbol{V}}$. As a major drawback, $\phi$ will in general develop large distortions due to the fluid nature of the monolayer that may require substantial remeshing.

Let us now consider a bilayer; in this case we can to consider $\phi^+$, a Lagrangian parametrization for one of the layers, and $\phi^-$ a Lagrangian

parametrization for the other layer. Associated with these Lagrangian parametrizations, we have the velocity fields $\bar{\boldsymbol{V}}^+$ and $\bar{\boldsymbol{V}}^-$ (6 degrees of freedom). However, since both layers move together coherently, it is clear that $v_n^+ = v_n^-$, which imposes a constraint in the formulation. Thus, the degrees of freedom of the system are only 5. However, imposing the constraint $v_n^+ = v_n^-$ would in general require introducing a Lagrange multiplier field $\lambda_n$, and constructing a Lagrangian with the term

$$-\int_{\Gamma_t} \lambda_n (v_n^+ - v_n^-) dS. \tag{9.51}$$

This approach (1) increases the number of effective degrees of freedom to 7 and (2) may lead to problems related to the consistency between discrete functional spaces for $\boldsymbol{V}^\pm$ and $\lambda_n$ used in a numerical implementation of the problem. In conclusion, Lagrangian descriptions present two major drawbacks: (1) they lead to large distortions and (2) they require constraints for bilayer models.

Let us now go back to the monolayer. As mentioned in the introduction to this Chapter, due to material symmetries in a fluid surface, $F[\boldsymbol{\phi}]$ can be written entirely as $F[\rho, H, K]$, where $\rho = \rho^{\text{ref}}/J$ is the density of the fluid, and $H$ and $K$ and are the mean and Gaussian curvatures, which only depend on the shape of $\Gamma_t$ but not on in-plane deformations [173]. In other words, due to the fluid nature of the surface, in-plane deformations contained in $\boldsymbol{\phi}$ only enter the free energy through $\rho$. This suggests using an alternative approach to Lagrangian parametrizations that separates in-plane deformations from the shape of $\Gamma_t$. Thus, we describe the surface $\Gamma_t$ by an Eulerian or ALE parametrization $\boldsymbol{\psi}$; $H$ and $K$ can be expressed in terms of $\boldsymbol{\psi}$. On $\Gamma_t$ we consider a time-evolving density field $\rho$. This leads to the set of state variables $\{\rho, \boldsymbol{\psi}\}$. To characterize the rate of change of the shape we consider $\tilde{\boldsymbol{W}} = \partial_t \boldsymbol{\psi}$. Along with $\tilde{\boldsymbol{W}}$, we also need to consider the tangential flow of material, which is characterized by the vector field $\boldsymbol{v}$. Recalling balance of mass, it is clear that $\tilde{\partial}_t \rho$ is related to both $\tilde{\boldsymbol{W}}$ and $\boldsymbol{v}$ through the process operator

$$\tilde{\partial}_t \rho = \text{div}(\rho \boldsymbol{c}) + \rho \left(\text{div}\boldsymbol{w} - v_n H\right), \tag{9.52}$$

| Model | Type | $X$ | $V$ | DOF | Essential DOF | Drawbacks |
|---|---|---|---|---|---|---|
| Monolayer | Lagrangian | $\phi$ | $\bar{\boldsymbol{V}}$ | 3 | 3 | Distortions |
| | ALE | $\{\psi, \rho\}$ | $\{\tilde{\boldsymbol{W}}, \boldsymbol{v}\}$ | 5 | | ↑DOF, Non-trivial PO* |
| | ALE Offset | $\{h, \rho\}$ | $\{\partial_t h, \boldsymbol{v}\}$ | 3 | | Non-trivial PO* |
| Bilayer | Lagrangian | $\{\phi^+, \phi^-\}$ | $\{\bar{\boldsymbol{V}}^+, \bar{\boldsymbol{V}}^-\}$ | 6 (7)** | 5 | Distortions, constraints |
| | ALE | $\{\psi, \rho^+, \rho^-\}$ | $\{\tilde{\boldsymbol{W}}, \boldsymbol{v}^+, \boldsymbol{v}^-\}$ | 7 | | ↑DOF, Non-trivial PO* |
| | ALE Offset | $\{h, \rho^+, \rho^-\}$ | $\{\partial_t h, \boldsymbol{v}^+, \boldsymbol{v}^-\}$ | 5 | | Non-trivial PO* |

*: PO stands for process operator.

**: There are 6 degrees of freedom and a constraint, which in general will involve a Lagrange multiplier field and lead to 7 DOF.

**Table 9.1**: State variables, process variables, degrees of freedom and drawbacks for different Lagrangian and ALE characterizations of monolayer and bilayer models.

where we have assumed that there is no production of material for simplicity. Thus, $\tilde{\boldsymbol{W}}$ and $\boldsymbol{v}$ form the set of process variables $\{\tilde{\boldsymbol{W}}, \boldsymbol{v}\}$. With this approach, we have been able to separate the flow of material from the change in shape of the surface. Of course $\tilde{\boldsymbol{W}}$ contains redundant information to describe the shape changes, but these extra degrees of freedom can be chosen to avoid large distortions generated by the fluid nature of the surface. For this reason, in this work we focus on ALE parametrizations for the description of fluid surfaces. However, this approach has three major drawbacks that we need to take into account. First, it leads to a system with 5 degrees of freedom as opposed to the 3 that we found for a Lagrangian approach. For a bilayer model, the same analysis leads to the state variables $\{\psi, \rho^+, \rho^-\}$ and the set of process variables $\{\tilde{\boldsymbol{W}}, \boldsymbol{v}^+, \boldsymbol{v}^-\}$, which has as many as 7 degrees of freedom. Thus, there is a severe increase in the number of degrees of freedom. Second, the tangent fields $\boldsymbol{v}$, which in a Lagrangian parametrization are simply the projection of $\boldsymbol{V}$ onto the tangent bundle of $\Gamma_t$, are now degrees of freedom in their own and independent of $\tilde{\boldsymbol{W}}$. The interpolation of tangent vector fields in general curvilinear coordinates and with multiple charts is a delicate issue, as we describe in Chapter 11. Third, since $\rho$ is now a state variable and not a by-product of $\phi$, we need to consider explicitly a non-trivial process operator, Eq. (9.52), which needs to be solved together with the minimization of the Rayleighian. In the next Section we describe an ALE parametrization based on an offset that solves the problem of the excess of degrees of freedom in the parametrization. Then, we introduce the Hodge decomposition of vector fields, which allows us to characterize $\boldsymbol{v}$ in terms of scalar potentials $\alpha$ and $\beta$, which can be easily interpolated and do not increase the number of degrees of freedom in the formulation. One cannot, however, avoid taking into account the process operator in Onsager's framework as discussed in Chapter 8.

### An ALE parametrization based on an offset

We define next an ALE parametrization that reduces the degrees of freedom required to describe $\psi$ from 3 to 1. Let us consider the state of the surface at a

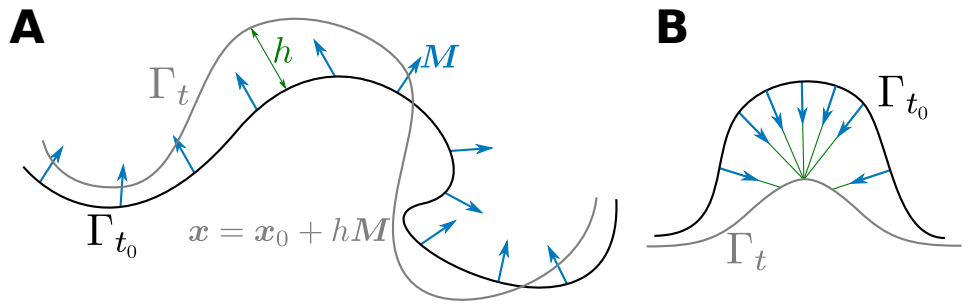


**Figure 9.4**: Surface parametrization in terms of an offset. (A) The field of directors $\boldsymbol{M}$ represents the direction in which the point $\boldsymbol{x}_0 \in \Gamma_{t_0}$ can evolve. The height function $h$, which may be negative, represents the distance of the point parametrized $\boldsymbol{x}$ on $\Gamma_t$ to $\Gamma_{t_0}$ in the direction of $\boldsymbol{M}$. (B) In this example $\Gamma_t$ lies at the limit of the tubular neighborhood to $\Gamma_{t_0}$ for the set of directors.

given time $t_0$, $\Gamma_{t_0}$, and a parametrization of this surface $\boldsymbol{\psi}_0(\boldsymbol{\xi})$. We consider a vector field $\boldsymbol{M}(\boldsymbol{\xi})$, representing a field of directors sitting on $\Gamma_{t_0}$, with non-zero normal component but possibly not normal to $\Gamma_{t_0}$. Then, we define a parametrization of $\Gamma_t$ at time $t > t_0$ in terms of the offset of a point $\boldsymbol{x} = \boldsymbol{\psi}_0(\boldsymbol{\xi})$ along $\boldsymbol{M}(\boldsymbol{\xi})$,

$$\boldsymbol{\psi}(\boldsymbol{\xi}, t) = \boldsymbol{\psi}_0(\boldsymbol{\xi}) + h(\boldsymbol{\xi}, t)\boldsymbol{M}(\boldsymbol{\xi}), \tag{9.53}$$

see Fig. 9.4A. Thus, the field that characterizes the time-evolution of the parametrization is $h$, a simple scalar field on $\tilde{\Gamma}$. However, not all surfaces can be parametrized in terms of Eq. (9.53); those that can lie in what is called the *tubular neighborhood* of $\Gamma_{t_0}$, defined as $\mathcal{T}_{\boldsymbol{M}}(\Gamma_{t_0}) = \{\Gamma \ : \ \exists$ a scalar field $h \in \bar{\Gamma} : \forall\, \boldsymbol{x} \in \Gamma \ \exists\, \boldsymbol{\xi} \in \tilde{\Gamma} : \boldsymbol{\psi}_0(\boldsymbol{\xi}) + h(\boldsymbol{\xi})\boldsymbol{M}(\boldsymbol{\xi})\}$. For some interval $I = (t_0, t_0 + \epsilon)$, the deformed surface $\Gamma_t$ will lie in the tubular neighborhood of $\Gamma_{t_0}$ if the time-evolution is smooth. However, after some time, $\Gamma_t$ may get out of the tubular neighborhood of $\Gamma_{t_0}$ (see Fig. 9.4B for an example). A simple solution to this issue is then to update the reference configuration $\Gamma_{t_0}$. This kind of parametrization was proposed by [142], with $\boldsymbol{M}$ being the field of normals to $\Gamma_{t_0}$, and generalizes the classical Monge parametrization, where $\Gamma_{t_0}$ is a plane,

$\boldsymbol{M}$ is the (constant) normal to $\Gamma_{t_0}$ and $h$ is simply the height of the surface $\Gamma_t$ with respect to the plane [40]. We finally note that for this kind of surface parametrization we have,

$$\boldsymbol{W}(\boldsymbol{x}, t) = (\partial_t h\, \boldsymbol{M}) \circ \boldsymbol{\psi}^{-1}(\boldsymbol{x}, t). \tag{9.54}$$

where since $h$ is a scalar field on $\tilde{\Gamma}$, $\partial_t h$ retains its usual meaning of taking the time-derivative at fixed $\boldsymbol{\xi}$. In general, this field will have non-zero normal and tangential components. Thus, with this offset parametrization of the surface we recover a formulation for both the bilayer and the monolayer that are optimal from the point of view of the number of degrees of freedom, see Table 9.1.

### Velocity potentials: Hodge decomposition

It is sometimes useful to describe tangent vectors to $\Gamma_t$ with vector potentials. Given a vector field $\boldsymbol{V} \in \mathbb{R}^3$, it is well-known that $\boldsymbol{V}$ admits a decomposition in terms of the gradient of a function $\Phi$ and the curl of a vector potential $\boldsymbol{A}$ in what is called the Helmholtz decomposition,

$$\boldsymbol{V} = \mathbf{GRAD}\Phi + \mathbf{CURL}\boldsymbol{A}, \tag{9.55}$$

where **GRAD** and **CURL** stand for the gradient and curl in $\mathbb{R}^3$. For a vector field tangent to a plane embedded in $\mathbb{R}^3$, this can be simplified to

$$\boldsymbol{V} = \mathbf{GRAD}\Phi + \mathbf{CURL}\,(\Psi \boldsymbol{n})\,, \tag{9.56}$$

where $\boldsymbol{n}$ is the normal to the plane and $\Psi$ is a scalar function. Therefore, for a plane embedded in $\mathbb{R}^3$, a vector field can be represented in terms of two scalar fields, $\Phi$ and $\Psi$. This property can be generalized to arbitrary surfaces in terms of their intrinsic differential geometry, i.e. not relying on their embedding in $\mathbb{R}^3$, as a special case of the Hodge decomposition for $n$-forms [41]. A vector field $\boldsymbol{v}$ tangent to a surface $\Gamma$ can be decomposed as

$$\boldsymbol{v} = \mathbf{grad}\alpha + \mathbf{curl}\beta, \tag{9.57}$$

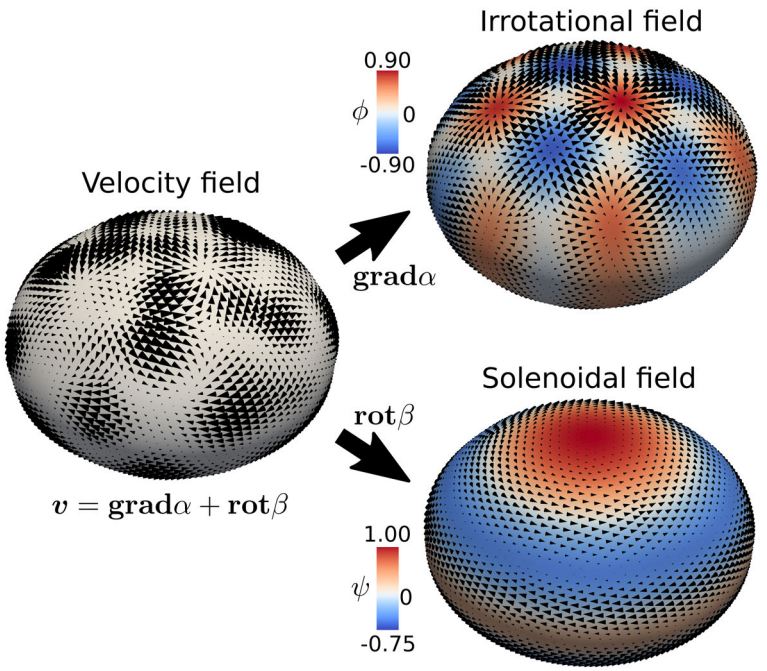


**Figure 9.5**: A vector field on a surface can be decomposed in a solenoidal and a irrotational fields.

where $\alpha$ and $\beta$ are scalar fields on $\Gamma$ and we have introduced the operator $(\mathbf{curl}\beta)^a = \epsilon^{ab}\nabla_b\beta$, where $\boldsymbol{\epsilon}$ is the antisymmetric tensor (see Appendix D). This decomposition will be useful later for the discretization of vector fields tangent to $\Gamma$. This decomposition is unique for simply connected closed surfaces, i.e. closed surfaces with genus equal to 0 (see Fig. 9.5 for an example on an ellipsoid). Equivalently, the decomposition is unique for simply connected surfaces with boundary $\partial\Omega$ with either of the following boundary conditions [25]

$$\nabla\alpha \wedge \boldsymbol{\nu}^\flat = 0 \quad \text{at } \partial\Gamma, \tag{9.58}$$

where $\boldsymbol{\nu}$ is the boundary normal tangent to $\Omega$, $\boldsymbol{\nu}^\flat$ its associated 1-form, and $\wedge$ indicates the external product of 1-forms (in components $\boldsymbol{\alpha} \wedge \boldsymbol{\beta} = \epsilon^{ab}\alpha_a\beta_b dS$),

or

$$\mathbf{curl}\beta \cdot \boldsymbol{\nu} = 0 \quad \text{at } \partial\Gamma. \tag{9.59}$$

In the absence of shape changes, from Eq. (9.50) it is clear that an inextensible flow satisfies $\mathrm{div}\boldsymbol{v} = 0$. In this case, $\boldsymbol{v}$ can be represented in terms of a stream function $\beta$, $\boldsymbol{v} = \mathbf{curl}\beta$. This approach has been recently employed to describe flows in lipid bilayers with fixed shapes [109, 163, 146]. However, we note that for inextensible surfaces that are deforming in space, both $\alpha$ and $\beta$ need be considered. In this case, it follows from Eq. (9.50) that $\alpha$ and $v_n$ satisfy the constraint

$$\Delta\alpha = v_n H, \tag{9.60}$$

where $\Delta\alpha = \mathrm{div}\,\mathbf{grad}\alpha$ and we have used the fact that $\mathrm{div}\boldsymbol{v} = \mathrm{div}\,\mathbf{grad}\alpha + \mathrm{div}\,\mathbf{curl}\alpha = \mathrm{div}\,\mathbf{grad}\alpha = \Delta\alpha$.

# Chapter 10

# A model for the mechanics of lipid bilayers

## 10.1 Introduction

Using Onsager's variational principle and the description of fluid surfaces, we can now address the three-dimensional and non-linear variational formulation of the mechanics of a lipid bilayer following the Seifert-Langer (SL) model sketched in Chapter 7, which has not been developed before. This model is driven by curvature and stretching elasticity and is dragged by in-plane shear and dilatation viscosity, and by inter-monolayer friction (see Fig. 7.1).

Let us start by identifying the state variables of this system. We characterize the state of a lipid bilayer at a given time $t$ by the position of its mid-surface $\Gamma_t$ and two density fields, $\rho^+(\boldsymbol{x}, t)$ and $\rho^-(\boldsymbol{x}, t)$, which represent the lipid densities of the upper (+) and lower (-) monolayers per unit area of the mid-surface $\Gamma_t$ (see Fig. 10.1). The shape and position of $\Gamma_t$ is characterized by an ALE parametrization of the form discussed in Section 9.5, $\boldsymbol{\psi}(\boldsymbol{\xi}, t) = \boldsymbol{\psi}_0(\boldsymbol{\xi}) + h(\boldsymbol{\xi}, t)\boldsymbol{M}(\boldsymbol{\xi})$, so that the surface $\Gamma_t$ is given by the scalar field $h$ on

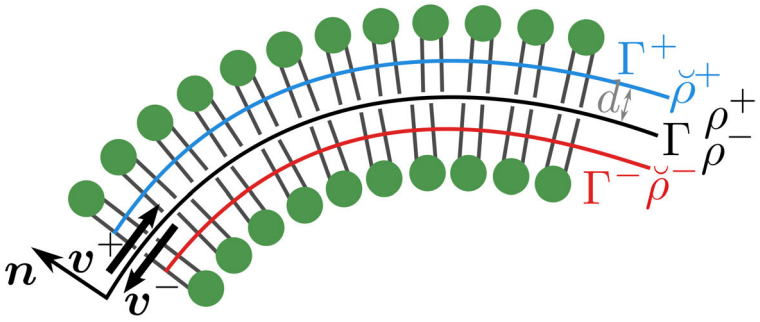


**Figure 10.1**: Sketch of relevant fields in the SL model. The densities at the monolayer midsurfaces $\breve{\rho}^\pm$ are projected onto the bilayer midsurface leading to the scalar fields $\rho^\pm : \Gamma_t \to \mathbb{R}$. The velocity fields $\boldsymbol{v}^\pm$ identify the velocity of the material particles at $\Gamma_t$.

$\tilde{\Gamma}$. All fields depending on the shape of $\Gamma_t$, such as $H$, $K$ or $dS$, ultimately depend on $\psi$ and therefore on $h$. Thus, the scalar fields $h$ and $\rho^\pm$ are the state variables of the lipid bilayer.

The process variables characterizing the rate of change of the material are $\partial_t h$, which provides the information about shape changes, and the two tangential velocity fields of the fluid, $\boldsymbol{v}^+$ and $\boldsymbol{v}^-$, which represent the flow of material particles along $\Gamma_t$. The rate of change of $\rho^\pm$ is related to these fields through mass conservation, which in the ALE formulation reads (see Eq. (9.49))

$$\tilde{\partial}_t \rho^\pm + \mathrm{div}(\rho^\pm \boldsymbol{c}^\pm) + \rho^\pm \left(\mathrm{div}\boldsymbol{w} - v_n H\right) = 0, \tag{10.1}$$

where $\boldsymbol{c}^\pm = \boldsymbol{v}^\pm - \boldsymbol{w}$. Thus, we define the process operator $P$ as

$$\tilde{\partial}_t \rho^\pm = P\left(h, \rho^\pm; \partial_t h, \boldsymbol{v}^\pm\right) = -\mathrm{div}(\rho^\pm \boldsymbol{c}^\pm) - \rho^\pm \left(\mathrm{div}\boldsymbol{w} - v_n H\right). \tag{10.2}$$

where

$$v_n = \partial_t h \left\langle \boldsymbol{M}, \boldsymbol{n} \right\rangle, \tag{10.3}$$

and

$$\boldsymbol{w} = \boldsymbol{W} - v_n \boldsymbol{n}. \tag{10.4}$$

For simplicity, we consider the formulation for a closed membrane first and extend the results for a patch of membrane with boundary in Section 10.5.

## 10.2 Energy

The energy stored by the membrane due to the curvature of each monolayer is represented by the classical Helfrich model

$$\mathcal{F}_H[h] = \int_{\Gamma_t} \left[ \frac{\kappa}{2}(H - H_0)^2 + \bar{\kappa} K \right] dS, \tag{10.5}$$

where $\kappa$ is the bending modulus, $\bar{\kappa}$ the Gaussian bending modulus, and $H_0$ the spontaneous curvature of the bilayer. In this approximation, this energy does not depend on the lipid densities. Apart from the bending energy, monolayers also store energy due to stretching. To characterize the stretching energy, let us first note that the density fields at the neutral surface of each monolayer, $\breve{\rho}^+$ and $\breve{\rho}^-$, are related to $\rho^+$ and $\rho^-$ through (see Fig. 10.1)

$$\breve{\rho}^{\pm} = \rho^{\pm} \left( 1 \pm dH + O(d^2 K) \right) \tag{10.6}$$

where $d$ ($\approx 1$ nm) is the distance between the mid-surface and the neutral surface of each monolayer, usually close to the polar-apolar interface [101]. Following [160, 139] we define a simple quadratic elastic energy for each monolayer, equivalent to the energy considered for the compressible Stokes problem in Section 8.3,

$$\mathcal{F}_S[h, \rho^{\pm}] = \int_{\Gamma_t} \frac{k_S}{2} \left( \frac{\breve{\rho}^{\pm}}{\rho_0} - 1 \right)^2 dS = \int_{\Gamma_t} \frac{k_S}{2} \left[ \frac{\rho^{\pm}}{\rho_0}(1 \pm dH) - 1 \right]^2 dS, \tag{10.7}$$

where $k_S$ is the stretching modulus of each monolayer. Here and throughout the text, whenever $\pm$ appears in a functional we imply a summation on $+$ and $-$ unless otherwise noted. Although the energy was initially modeled with a quadratic potential depending on $\breve{\rho}^{\pm}$, the resulting expression in terms of $\rho^{\pm}$ is a non-linear function of the shape of $\Gamma_t$ due to the coupling with $H$. The total energy is

$$\mathcal{F}[h, \rho^{\pm}] = \mathcal{F}_H[h] + \mathcal{F}_S[h, \rho^{\pm}]. \tag{10.8}$$

Associated with the free energy $\mathcal{F}$, we define the free energy density for each monolayer

$$f^{\pm}(h,\rho^{\pm}) = \frac{1}{2}\left[\frac{\kappa}{2}(H-H_0)^2 + \bar{\kappa}K\right] + \frac{k_S}{2}\left[\frac{\rho^{\pm}}{\rho_0}(1 \pm dH) - 1\right]^2, \tag{10.9}$$

where we have split the Helfrich energy equally amongst the two monolayers.

## 10.3 Dissipation

We take into account three main dissipation mechanisms in the bilayer. First we consider the dissipation due to shear, similar to the examples in the bulk in Chapter 8,

$$\mathcal{D}_S\left[h;\partial_t h,\boldsymbol{v}^{\pm}\right] = \int_{\Gamma_t} \mu||\boldsymbol{d}^{\pm}||^2 dS, \tag{10.10}$$

where $\mu$ is the shear viscosity and

$$\boldsymbol{d}^{\pm} = \frac{1}{2}\left\{\nabla\left(\boldsymbol{v}^{\pm}\right)^{\flat} + \left[\nabla\left(\boldsymbol{v}^{\pm}\right)^{\flat}\right]^T\right\} - v_n\boldsymbol{k}, \tag{10.11}$$

is the rate-of-deformation tensor for each monolayer (see Eq. (9.33)). We note that, since $\boldsymbol{d}^{\pm}$ contains the term $v_n\boldsymbol{k}$, $\mathcal{D}_S$ also accounts for the rate-of-deformation induced by shape changes of $\Gamma_t$. Additionally, we consider a dilatational dissipation

$$\mathcal{D}_D\left[h;\partial_t h,\boldsymbol{v}^{\pm}\right] = \frac{1}{2}\int_{\Gamma_t} \lambda\left(\mathrm{tr}\boldsymbol{d}^{\pm}\right)^2 dS, \tag{10.12}$$

where $\lambda$ is the dilatational viscosity. Finally, we consider the inter-monolayer friction caused by the slippage of fluid from one monolayer on the other,

$$\mathcal{D}_I\left[h;\partial_t h,\boldsymbol{v}^{\pm}\right] = \int_{\Gamma_t} b_I||\boldsymbol{v}^{+} - \boldsymbol{v}^{-}||^2 dS, \tag{10.13}$$

where $b_I$ is the inter-monolayer viscosity. Thus, the total dissipation is

$$\mathcal{D}\left[h;\partial_t h,\boldsymbol{v}^{\pm}\right] = \mathcal{D}_S\left[h;\partial_t h,\boldsymbol{v}^{\pm}\right] + \mathcal{D}_D\left[h;\partial_t h,\boldsymbol{v}^{\pm}\right] + \mathcal{D}_I\left[h;\partial_t h,\boldsymbol{v}^{\pm}\right]. \tag{10.14}$$

Interestingly, all the material parameters in this theory ($\kappa, k_S, d, \lambda, \mu, b_I$) can be measured experimentally [39].

## 10.4 Governing equations

Now that we have identified the energies and dissipations of our system, we can write the Rayleighian as

$$\mathcal{R}\left[h;\partial_t h,\boldsymbol{v}^{\pm}\right]=\tilde{\partial}_t\mathcal{F}\left[h;\partial_t h,\boldsymbol{v}^{\pm}\right]+\mathcal{D}\left[h;\partial_t h,\boldsymbol{v}^{\pm}\right]. \tag{10.15}$$

and Onsager's variational principle reduces to

$$\{\partial_t h,\boldsymbol{v}^{\pm}\}=\underset{\{\partial_t h,\boldsymbol{v}^{\pm}\}}{\operatorname{argmin}}\,\mathcal{R}\left[h;\partial_t h,\boldsymbol{v}^{\pm}\right] \tag{10.16}$$

Note that, for a closed surface, $\tilde{\partial}_t\mathcal{F}=D_t\mathcal{F}$ (see Section 9.4). The strong form that follows from this principle involves the shape equation and the different viscous stresses on the bilayer. The expression for small deviations from a plane was originally given by [160], where $h$ identifies the height with respect to the plane following a classical Monge parametrization. Although the derivation of the strong form is interesting in itself, it is not required for our computational purposes, and we leave for future work. If we represent the velocities $\boldsymbol{v}^{\pm}$ through velocity potentials

$$\boldsymbol{v}^{\pm}=\mathbf{grad}\alpha^{\pm}+\mathbf{curl}\beta^{\pm}, \tag{10.17}$$

we can rewrite the Rayleighian in terms of $\alpha^{\pm}$ and $\beta^{\pm}$ and define

$$\begin{aligned}\mathcal{R}\left[h,\rho^{\pm};\partial_t h,\alpha^{\pm},\beta^{\pm}\right]=&\tilde{\partial}_t\mathcal{F}\left[h,\rho^{\pm};\partial_t h,\alpha^{\pm},\beta^{\pm}\right]\\&+\mathcal{D}\left[h,\rho^{\pm};\partial_t h,\alpha^{\pm},\beta^{\pm}\right].\end{aligned} \tag{10.18}$$

Then, we need to solve

$$\begin{aligned}\{\partial_t h,\alpha^{\pm},\beta^{\pm}\}=&\underset{\{\partial_t h,\alpha^{\pm},\beta^{\pm}\}}{\operatorname{argmin}}\,\mathcal{R}\left[h,\rho^{\pm};\partial_t h,\alpha^{\pm},\beta^{\pm}\right],\\\tilde{\partial}_t\rho^{\pm}=&P\left(h,\rho^{\pm};\partial_t h,\alpha^{\pm},\beta^{\pm}\right),\end{aligned} \tag{10.19}$$

where we have rewritten the process operator in terms of the velocity potentials. Again, this is a system of mixed elliptic and hyperbolic PDEs. Before dealing with the numerical treatment of the problem in Chapter 11, we examine the statement of the problem for open patches.

## 10.5 Open patch: Boundary conditions

Let us now consider a patch of membrane. In this case $\Gamma_t$ is a surface with boundary, which we denote by $\partial\Gamma_t$. Here, we do not consider membranes with a physical boundary; the boundary delimits the region of study of an otherwise larger membrane. We consider that this patch of surface follows the flow generated by the parametrization $\psi$, which is not Eulerian nor Lagrangian. Thus, the boundary $\partial\Gamma_t$ is mapped by $\psi$ from a boundary $\partial\tilde{\Gamma}$ that stays stationary in parametric space. The field $\partial_t h$ admits two kinds of Dirichlet boundary conditions at $\partial\tilde{\Gamma}$ since $\mathcal{R}$ depends on second order derivatives of $\partial_t h$ with respect to parametric coordinates. Thus, we have the Dirichlet boundary conditions

$$\begin{aligned} \partial_t h &= o \qquad \text{at } \partial_{D_h}\tilde{\Gamma}, \\ \tilde{\nabla}_{\tilde{\boldsymbol{\nu}}}\partial_t h &= \theta \qquad \text{at } \partial_{D_{h'}}\tilde{\Gamma}, \end{aligned} \tag{10.20}$$

where $\tilde{\boldsymbol{\nu}}$ is the outer normal to $\partial\tilde{\Gamma}$ and $\tilde{\nabla}$ denotes the gradient on $\tilde{\Gamma}$. We note that in general $\partial_{D_h}\tilde{\Gamma} \cap \partial_{D_{h'}}\tilde{\Gamma} \neq \emptyset$. For the velocity fields $\boldsymbol{v}^{\pm}$, we have a Dirichlet boundary condition

$$\boldsymbol{v}^{\pm} = \boldsymbol{u}^{\pm} \qquad \text{at } \partial_{D_{\boldsymbol{v}^{\pm}}}\Gamma_t, \tag{10.21}$$

with $\boldsymbol{u}^{\pm}$ given. If we write the velocity in terms of vector potentials, this Dirichlet boundary condition becomes

$$\mathbf{grad}\alpha^{\pm} + \mathbf{curl}\beta^{\pm} = \boldsymbol{u}^{\pm} \quad \text{at } \partial_{D_{\boldsymbol{v}^{\pm}}}\Gamma_t. \tag{10.22}$$

We also need one of the boundary conditions

$$\mathbf{grad}\alpha^{\pm} \wedge \boldsymbol{\nu} = 0 \quad \text{at } \partial\Gamma_t, \tag{10.23}$$

$$\mathbf{curl}\beta^{\pm} \cdot \boldsymbol{\nu} = 0 \quad \text{at } \partial\Gamma_t, \tag{10.24}$$

for a unique Hodge decomposition of $\boldsymbol{v}^{\pm}$. We choose (10.23) over (10.24) since, for a stationary shape in the inextensible limit, these conditions lead to $\alpha^{\pm} = 0$. The action of an external traction $\boldsymbol{T}^{\pm} = \boldsymbol{t}^{\pm} + t_n\boldsymbol{n}$ and a bending moment $\boldsymbol{\omega}$ generate a power at the boundary [174]

$$\mathcal{P}_N[h, \partial_t h, \alpha^{\pm}, \beta^{\pm}] = -\int_{\partial\Gamma_t} \left[\langle \boldsymbol{T}^{\pm}, \boldsymbol{V}^{\pm}\rangle + \boldsymbol{\omega} \cdot D_t^{\pm}\boldsymbol{n}\right] dl \tag{10.25}$$

where $\boldsymbol{T}^{\pm} = \boldsymbol{t}^{\pm} + t_n \boldsymbol{n}$ is the traction exerted on the boundary, $\boldsymbol{\omega}$ is the bending moment and $D_t^{\pm}$ is the material time-derivative in the upper and lower monolayers respectively. We write the power generated by tractions and moments at the whole boundary $\partial\Gamma_t$ for notational convenience. Taking into account that $D_t^{\pm}\boldsymbol{n} = -\mathbf{grad} v_n - \boldsymbol{k}^{\sharp} \cdot \boldsymbol{v}^{\pm}$.

$$\begin{aligned} \mathcal{P}_N[h, \partial_t h, \alpha^{\pm}, \beta^{\pm}] &= -\int_{\partial\Gamma_t} \left[ \boldsymbol{t}^{\pm} \cdot \boldsymbol{v}^{\pm} + t_n v_n + \boldsymbol{\omega} \cdot \left( -\mathbf{grad} v_n - \boldsymbol{k}^{\sharp} \cdot \boldsymbol{v}^{\pm} \right) \right] dl \\ &= \int_{\partial\Gamma_t} \left( \boldsymbol{k}^{\sharp} \cdot \boldsymbol{\omega} - \boldsymbol{t}^{\pm} \right) \cdot \boldsymbol{v}^{\pm} dl + \int_{\partial\Gamma_t} \left( \boldsymbol{\omega} \cdot \mathbf{grad} v_n - t_n v_n \right) dl \end{aligned} \tag{10.26}$$

Furthermore, since now the patch is open and follows the ALE description, we need to consider the power generated by the transport of material across $\partial\Gamma_t$

$$\mathcal{P}_T[h, \partial_t h, \alpha^{\pm}, \beta^{\pm}] = \int_{\partial\Gamma_t} f^{\pm} \boldsymbol{c}^{\pm} \cdot \boldsymbol{\nu} dl, \tag{10.27}$$

where $f^{\pm}$ is the free energy density, see Eq. (10.9). Finally, balance of mass has to be complemented with an in-flow condition for $\rho^{\pm}$

$$\rho^{\pm}(\boldsymbol{x}) = c^{\pm}(\boldsymbol{x}) \quad \text{on } \partial_I \Gamma_t, \tag{10.28}$$

where $\partial_I \Gamma_t = \{\boldsymbol{x} \in \partial\Gamma_t \ : \ \boldsymbol{v}(\boldsymbol{x}) \cdot \boldsymbol{\nu}(\boldsymbol{x}) < 0)\}$ and $c^{\pm}(\boldsymbol{x})$ is given. Altogether, we obtain the Rayleighian

$$\mathcal{R} = \tilde{\partial}_t \mathcal{F} + \mathcal{D} + \mathcal{P}_N + \mathcal{P}_T. \tag{10.29}$$

The constraints applied to the process variables from Dirichlet boundary conditions are Eqs. (10.20), (10.23), (10.24) and the constraint associated to the process operator is Eq. (10.28).

# Chapter 11

# A computational framework for the simulation of lipid bilayers

## 11.1 Time discretization

For the time-discretization of Eq. (10.19) we consider the idea described in Section 8.5. We have two kinds of state variables, $h$, whose time-derivative $\partial_t h$ is a process variable, and $\rho^\pm$, for which we have the process operator $\tilde{\partial}_t \rho^\pm = P(h, \rho^\pm; \partial_t h, \alpha^\pm, \beta^\pm)$. We discretize the time-evolution of the system in a general non-uniform grid $(t^1, \dots, t^N)$ so that $t^{n+1} - t^n = \Delta t^n$ for $n = 0, \dots, N-1$. We discretize variables in time using the same convention, for any field $a$ evolving in time $a^n = a(t^n)$. The discrete Rayleighian is

$$\mathcal{R}^n \left[ h^n, (\rho^\pm)^n ; h, \alpha^\pm, \beta^\pm \right] = \frac{\mathcal{F}\left[ h, (\rho^\pm)^n + \Delta t \, P\left( h, (\rho^\pm)^n ; \frac{h-h^n}{\Delta t}, \alpha^\pm, \beta^\pm \right) \right]}{\Delta t^n} \tag{11.1}$$

$$+ \mathcal{D}\left[ h^n; \frac{h-h^n}{\Delta t^n}, \alpha^\pm, \beta^\pm \right] + \mathcal{P}_N \left[ h^n; \frac{h-h^n}{\Delta t^n}, \alpha^\pm, \beta^\pm \right] + \mathcal{P}_T \left[ h^n; \frac{h-h^n}{\Delta t^n}, \alpha^\pm, \beta^\pm \right].$$

The discrete time-evolution of $h$ and the velocity potentials $\alpha^{\pm}$ and $\beta^{\pm}$ can be obtained by applying Onsager's principle

$$\left\{h^{n+1}, (\alpha^{\pm})^{n+1}, (\beta^{\pm})^{n+1}\right\} = \underset{\{h,\alpha^{\pm},\beta^{\pm}\}}{\operatorname{argmin}} \mathcal{R}^n \left[h^n, (\rho^{\pm})^n; h, \alpha^{\pm}, \beta^{\pm}\right] \tag{11.2}$$

To obtain the discrete time-evolution $\rho^{\pm}$, we apply the process operator

$$(\rho^{\pm})^{n+1} = (\tilde{\rho}^{\pm})^n + \Delta t^n \, P\left(h^{n+1}, (\rho^{\pm})^n; \frac{h^{n+1} - h^n}{\Delta t^n}, (\alpha^{\pm})^{n+1}, (\beta^{\pm})^{n+1}\right) \tag{11.3}$$

Thus, the time-evolution of the system is given by an interative and staggered process in which given the fields $(\rho^{\pm})^n$ and $h^n$ at time $t^n$, one can solve Eq. (11.2) to obtain $(\alpha^{\pm})^{n+1}$, $(\beta^{\pm})^{n+1}$, and $h^{n+1}$, which can then be used to solve for $\rho^{n+1}$ using Eq. (11.3). This shows that the system of differential equations has been transformed through time discretization into (1) an elliptic problem from Onsager's principle, which solves $h^{n+1}$ along with $(\alpha^{\pm})^{n+1}$ and $(\beta^{\pm})^{n+1}$, and (2) an algebraic problem for $(\rho^{\pm})^{n+1}$ from mass conservation.

## 11.2 Spatial discretization

In this Section we examine the spatial discretization of $\Gamma_t$ and the different fields defined on it. For simplicity, let us start by examining the spatial discretization of a generic surface $\Gamma$. We first note that, for the discretization of the Rayleighian later on, we need that the curvature tensor $\boldsymbol{k}$ be square-integrable on $\Gamma$. For that reason, the parametrization of $\Gamma$ must be in $H^2$, i.e. it must be a square-integrable function with its its first- and second-order derivatives being square-integrable functions too; we call such a surface a $H^2$ surface. The problem of discretizing a $H^2$ surface may be addressed resorting to different numerical frameworks, such as higher-order B-splines [133] or max-ent approximants [106]. Another versatile technique to discretize smooth surfaces based on meshes with arbitrary connectivity is *subdivision surfaces*. Here we focus on *Loop subdivision surfaces* based on triangular meshes [94, 170, 26, 33], which we discuss in Appendix E. To define the discretization

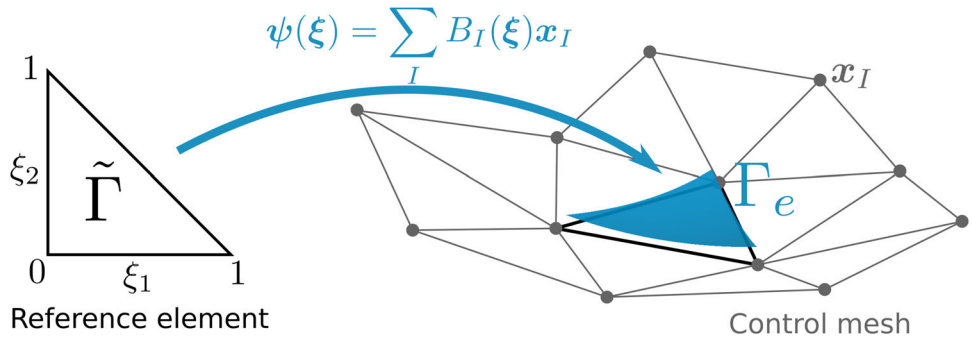


**Figure 11.1**: In subdivision surfaces, a control mesh is used to parametrize the surface $\Gamma$. For each triangle in the control mesh, $E$, the mapping Eq. (11.4), depending on the control points of the first ring of neighbors to $E$, $\boldsymbol{x}_I$ with $I \in \langle E \rangle^1$, define the surface $\Gamma^E$ (blue). The union of $\Gamma^E$ for each $E$ in the control mesh forms the $H^2$ surface $\Gamma$.

of $\Gamma$ with subdivision surfaces, we consider a control mesh made of triangles $E = 1, \ldots, N_e$ whose edges join the set of control points $I = 1, \ldots, N_n$ with positions $\{\boldsymbol{x}_I\}_{I=1}^{N_n}$. For each triangle in the mesh, we define the parametrization $\boldsymbol{\psi}^E(\boldsymbol{\xi}) : \tilde{\Gamma} \to \mathbb{R}^3$, with $\tilde{\Gamma}$ the reference triangle (see Fig. 11.1), by

$$\boldsymbol{\psi}^E(\boldsymbol{\xi}) = \sum_{I \in \langle E \rangle^1} B_I^E(\boldsymbol{\xi}) \boldsymbol{x}_I, \tag{11.4}$$

where $B_I^E$ represents the *subdivision surface basis function* associated to node $I$ at element $E$ and $\langle E \rangle^1$ identifies the set of control points whose basis functions do not vanish on $E$, which are those contained in the first ring of nodes surrounding $E$ –including the nodes forming the element and all first neighbors to them. We denote by $\Gamma^E = \boldsymbol{\psi}^E\left(\tilde{\Gamma}\right)$ the curved triangle obtained by the local parametrization in Eq. (11.4). It can be shown that these curved triangles are disjoint and that their union defines a $C^2$-continuous surface almost everywhere, except at a finite number of points where it is $C^1$. These points coincide with the image by $\boldsymbol{\psi}$ of irregular nodes in the mesh, which are those with a valence different from 6. There, the surface is continuous with continuous derivative but presents a discontinuity in the second derivative.

For the parametrization of the surface $\Gamma_{t_0}$, we write

$$\boldsymbol{\psi}_0^E(\boldsymbol{\xi}) = \sum_{I \in \langle E \rangle^1} B_I^E(\boldsymbol{\xi}) \boldsymbol{x}_{0I}. \tag{11.5}$$

Thus, the control mesh in our scheme is given by the position of the control points $\{\boldsymbol{x}_{0I}\}_{I=1}^{N_n}$. In $\tilde{\Gamma}$ we also define the fields

$$h^E(\boldsymbol{\xi}) = \sum_{I \in \langle E \rangle^1} B_I^E(\boldsymbol{\xi}) h_I, \tag{11.6}$$

$$\boldsymbol{M}^E(\boldsymbol{\xi}) = \sum_{I \in \langle E \rangle^1} B_I^E(\boldsymbol{\xi}) \boldsymbol{M}_I, \tag{11.7}$$

and then the parametrization of the deformed surface $\Gamma_t$ reads

$$\boldsymbol{\psi}^E(\boldsymbol{\xi}) = \sum_{I \in \langle E \rangle^1} B_I^E(\boldsymbol{\xi}) \boldsymbol{x}_{0I} + \left( \sum_{J \in \langle E \rangle^1} B_J^E(\boldsymbol{\xi}) h_J \right) \left( \sum_{K \in \langle E \rangle^1} B_K^E(\boldsymbol{\xi}) \boldsymbol{M}_K \right). \tag{11.8}$$

We note that, given that $\boldsymbol{\psi}_0$, $h$ and $\boldsymbol{M}$ are in $H^2$, $\boldsymbol{\psi}$ is also in $H^2$. We can define in $\tilde{\Gamma}$ other kinds of basis functions. In particular, we consider the set of linear basis functions $N_I(\boldsymbol{\xi})$ with $I \in \langle E \rangle^0$, the zeroth-ring of nodes of the element, defined by

$$N_{E_1} = (1 - \xi_1, 1 - \xi_2) \quad N_{E_2} = (\xi_1, 0), \quad N_{E_3} = (0, \xi_2), \tag{11.9}$$

where $E_1, E_2$ and $E_3$ denote the labels of the three nodes forming the element $E$. We can then discretize fields on $\Gamma_t$ also with $N_I$ if they only need to be in $H^1$ (that is, square-integrable functions with a square-integrable derivative). This is the case of the density field, since the Rayleighian and the process operator only depend on $\rho^{\pm}$ through its value and its first-order derivatives,

$$\left(\rho^{\pm}\right)^E(\boldsymbol{\xi}) = \sum_{I \in \langle E \rangle^0} N_I^E(\boldsymbol{\xi}) \rho_I^{\pm}. \tag{11.10}$$

We note that here all integrals and equations are computed in parametric space $\tilde{\Gamma}$. For notational simplicity, we use the same symbol to denote $\rho$ and $\tilde{\rho} = \rho \circ \boldsymbol{\psi}$, since there is no danger of confusion between different parametrizations; the

parametrization is fixed to be of the form Eq. (11.8), and this diffeomorphism identifies points in $\Gamma_t^E$ with points in $\tilde{\Gamma}$ univocally. Following the discretization of $\rho^{\pm}$, we could be tempted to discretize the components of $\boldsymbol{v}$ as

$$\left((v^{\pm})^a\right)^E(\boldsymbol{\xi}) = \sum_{I\in\langle E\rangle^0} N_I^E(\boldsymbol{\xi})\,(v^{\pm})_I^a\,. \tag{11.11}$$

since the Rayleighian only depends on $\boldsymbol{v}^{\pm}$ through its value and its first-order derivatives. However, we note that since

$$(\boldsymbol{v}^{\pm})^E = \left((v^{\pm})^a\right)^E \boldsymbol{e}_a^E = \left((v^{\pm})^a\right)^E \partial_a \boldsymbol{\psi}^E, \tag{11.12}$$

and since $\partial_a \boldsymbol{\psi}^E$ is discontinuous across elements due to the jump in the definition of local coordinates, for $\boldsymbol{v}$ to be continuous $v^a$ must be discontinuous across elements. This cannot be achieved with the set $N_I^E$, which always produces a continuous function. One possible solution is to increase the number of degrees of freedom of the problem and discretize the three components of $\boldsymbol{v}^{\pm}$ in the global basis of Euclidean space

$$\boldsymbol{v}^{\pm} = (v^{\pm})^{\alpha}\,\boldsymbol{i}_{\alpha}. \tag{11.13}$$

Being the basis vectors $\boldsymbol{i}_{\alpha}$ constant, $v^{\alpha}$ is continuous and we could use

$$\left((v^{\pm})^{\alpha}\right)^E(\boldsymbol{\xi}) = \sum_{I\in\langle E\rangle^0} N_I^E(\boldsymbol{\xi})\,(v^{\pm})_I^{\alpha}\,. \tag{11.14}$$

However, since $(v^{\pm})^1, (v^{\pm})^2, (v^{\pm})^3$ are not independent –as they must be tangent to $\Gamma$–, one would need to introduce the additional contraint $(\boldsymbol{v}^{\pm})^E\cdot\boldsymbol{n} = 0$. A more convenient option is to recall the Hodge decomposition of $\boldsymbol{v}^{\pm}$ in Eq. (10.17) and discretize the scalar fields $\alpha^{\pm}$ and $\beta^{\pm}$. We note that $\alpha^{\pm}$ and $\beta^{\pm}$ need to be in $H^2$ for $\boldsymbol{d}^{\pm}$ to be well-defined. This is not a problem for our formulation, since subdivision basis functions are smooth enough. Thus, we consider the following discretization for the velocity potentials

$$(\alpha^{\pm})^E(\boldsymbol{\xi}) = \sum_{I\in\langle E\rangle^1} B_I^E(\boldsymbol{\xi})\alpha_I^{\pm}, \tag{11.15}$$

$$(\beta^{\pm})^{E}(\boldsymbol{\xi}) = \sum_{I \in \langle E \rangle^{1}} B_I^E(\boldsymbol{\xi}) \beta_I^{\pm}. \tag{11.16}$$

Now that we have introduced the spatial discretization of the different fields on $\Gamma_t$ we can tackle the mechanical and transport problems.

## 11.3 Finite element formulation of force balance

To obtain the equations that govern the discrete time-evolution of the control values of the different fields, we first calculate the discretized functionals in the Rayleighian. In this Section we omit the summation on $E$ for notational simplicity. The discretized Helfrich energy is

$$\mathcal{F}_H(\{h_I\}) = \int_{\tilde{\Gamma}} \left[ \frac{\kappa}{2} \left( H(\{h_I\}) - H_0 \right)^2 + \bar{\kappa} K(\{h_I\}) \right] J(\{h_I\})\, d\boldsymbol{\xi}, \tag{11.17}$$

where we have written the explicit dependence of the different quantities on the control values of the unknowns, $\left\{h_I, \alpha_I^{\pm}, \beta_I^{\pm}\right\}$, and omit the dependence on the rest of fields for simplicity. The discretized stretching energy, can be written as

$$\mathcal{F}_S\left(\left\{h_I, \alpha_I^{\pm}, \beta_I^{\pm}\right\}\right) = \int_{\tilde{\Gamma}} \frac{k_S}{2} \left[ \frac{(\rho^{\pm})^n + \Delta t^n\, P\left(\left\{h_I, \alpha_I^{\pm}, \beta_I^{\pm}\right\}\right)}{\rho_0} \times \left(1 \pm dH(\{h_I\})\right) - 1 \right]^2 J(\{h_I\})\, d\boldsymbol{\xi}, \tag{11.18}$$

and the discretized dissipation potentials as

$$\mathcal{D}_S\left(\left\{h_I, \alpha_I^{\pm}, \beta_I^{\pm}\right\}\right) = \mu \int_{\tilde{\Gamma}} \left\| \boldsymbol{d}^{\pm}\left(\left\{h_I, \alpha_I^{\pm}, \beta_I^{\pm}\right\}\right) \right\|^2 J^n d\boldsymbol{\xi}, \tag{11.19}$$

$$\mathcal{D}_D\left(\left\{h_I, \alpha_I^{\pm}, \beta_I^{\pm}\right\}\right) = \frac{\lambda}{2} \int_{\tilde{\Gamma}} \left( \operatorname{tr} \boldsymbol{d}^{\pm}\left(\left\{h_I, \alpha_I^{\pm}, \beta_I^{\pm}\right\}\right) \right)^2 J^n d\boldsymbol{\xi}, \tag{11.20}$$

$$\mathcal{D}_I\left(\left\{h_I, \alpha_I^{\pm}, \beta_I^{\pm}\right\}\right) = \frac{b_I}{2} \int_{\tilde{\Gamma}} \left\| \boldsymbol{v}^{-}\left(\left\{\alpha_I^{+}, \beta_I^{+}\right\}\right) - \boldsymbol{v}^{-}\left(\left\{\alpha_I^{-}, \beta_I^{-}\right\}\right) \right\|^2 J^n d\boldsymbol{\xi}, \tag{11.21}$$

For the power generated by tractions at the boundary, we consider the collection of edges $l = 1, \ldots, N_l$ indentifying the boundary of the control mesh. These edges lie at elements where basis functions can be calculated. Defining the variable $\lambda$ at each edge that goes from 0 to 1 linearly along the edge in $\tilde{\Gamma}$, we can then write

$$\mathcal{P}_N\left(\left\{h_I, \alpha_I^{\pm}, \beta_I^{\pm}\right\}\right) = \sum_{l=1}^{N_l}\left[\int_0^1 \left(\boldsymbol{k}^{\sharp}\boldsymbol{\omega} - \boldsymbol{t}^{\pm}\right)\cdot \boldsymbol{v}^{\pm}\left(\left\{\alpha_I^{\pm}, \beta_I^{\pm}\right\}\right)||\nabla_\lambda \psi^n||d\lambda\right.$$
$$\left. + \int_0^1 \left(\boldsymbol{\omega}\cdot \mathbf{grad} v_n\left(\{h_I\}\right) - t_n\left(\{h_I\}\right) v_n\left(\{h_I\}\right)\right)||\nabla_\lambda \psi^n||d\lambda\right], \quad (11.22)$$

where we have used that the length element is $dl = ||\nabla_\lambda \psi^n||d\lambda$, $\nabla_\lambda \psi = \partial_a \psi \lambda^a$ and $\boldsymbol{\lambda}$ is the vector joining the two nodes in the edge $l_e$ in $\tilde{\Gamma}$. Equivalently,

$$\mathcal{P}_T\left(\left\{h_I, \alpha_I^{\pm}, \beta_I^{\pm}\right\}\right) = \sum_{l=1}^{N_l}\int_0^1 f^{\pm}\left(\left\{h_I, \alpha_I^{\pm}, \beta_I^{\pm}\right\}\right)\times \quad (11.23)$$
$$\boldsymbol{c}^{\pm}\left(\left\{h_I, \alpha_I^{\pm}, \beta_I^{\pm}\right\}\right)\cdot\boldsymbol{\nu}||\nabla_\lambda \psi^n||d\lambda,$$

For the numeric integration of Eqs. (11.17)-(11.23) we use Gauss quadrature in the reference element $\tilde{\Gamma}$, although other integration schemes specially suited for subdivision surfaces have been recently proposed [81]. We define the array with the unknowns per node for the mechanical problem as

$$\mathsf{u} = \begin{pmatrix} \mathsf{u}_1 \\ \vdots \\ \mathsf{u}_{N_n} \end{pmatrix}, \quad (11.24)$$

where

$$\mathsf{u}_I = \begin{pmatrix} h_I \\ \alpha_I^+ \\ \beta_I^+ \\ \alpha_I^- \\ \beta_I^- \end{pmatrix}. \quad (11.25)$$

Then, extremizing the discrete Rayleighian amounts to solving the equation on $\mathsf{u}$

$$\mathsf{f}(\mathsf{u}) = \frac{1}{\Delta t^n}\mathsf{h}(\mathsf{u}) + \mathsf{d}(\mathsf{u}) + \mathsf{p} = 0, \tag{11.26}$$

where

$$\mathsf{h}_I(\mathsf{u}) = \begin{pmatrix} \partial_{h_I}\mathcal{F} \\ \partial_{\alpha_I^+}\mathcal{F} \\ \partial_{\beta_I^+}\mathcal{F} \\ \partial_{\alpha_I^-}\mathcal{F} \\ \partial_{\beta_I^-}\mathcal{F} \end{pmatrix}, \qquad \mathsf{d}_I(\mathsf{u}) = \begin{pmatrix} \partial_{h_I}\mathcal{D} \\ \partial_{\alpha_I^+}\mathcal{D} \\ \partial_{\beta_I^+}\mathcal{D} \\ \partial_{\alpha_I^-}\mathcal{D} \\ \partial_{\beta_I^-}\mathcal{D} \end{pmatrix}, \qquad \mathsf{p}_I = \begin{pmatrix} \partial_{h_I}\mathcal{P} \\ \partial_{\alpha_I^+}\mathcal{P} \\ \partial_{\beta_I^+}\mathcal{P} \\ \partial_{\alpha_I^-}\mathcal{P} \\ \partial_{\beta_I^-}\mathcal{P} \end{pmatrix}. \tag{11.27}$$

and $\mathsf{p}$ is independent of $\mathsf{u}$. This is a non-linear system of equations emanating from an optimization problem in $\mathsf{u}$. To solve it, we can resort to a variety of optimization solvers. Here, we employ Newton's method. To use this method, we compute the hessian of the Rayleighian, which takes the form

$$\mathsf{K}(\mathsf{u}) = \frac{1}{\Delta t^n}\mathsf{H}(\mathsf{u}) + \mathsf{D}, \tag{11.28}$$

with

$$\mathsf{H}_{IJ}(\mathsf{u}) = \begin{pmatrix} \partial_{h_I}\partial_{h_J}\mathcal{F} & \partial_{h_I}\partial_{\alpha_J^+}\mathcal{F} & \partial_{h_I}\partial_{\beta_J^+}\mathcal{F} & \partial_{h_I}\partial_{\alpha_J^-}\mathcal{F} & \partial_{h_I}\partial_{\beta_J^-}\mathcal{F} \\ \partial_{\alpha_I^+}\partial_{h_J}\mathcal{F} & \partial_{\alpha_I^+}\partial_{\alpha_J^+}\mathcal{F} & \partial_{\alpha_I^+}\partial_{\beta_J^+}\mathcal{F} & \partial_{\alpha_I^+}\partial_{\alpha_J^-}\mathcal{F} & \partial_{\alpha_I^+}\partial_{\beta_J^-}\mathcal{F} \\ \partial_{\beta_I^+}\partial_{h_J}\mathcal{F} & \partial_{\beta_I^+}\partial_{\alpha_J^+}\mathcal{F} & \partial_{\beta_I^+}\partial_{\beta_J^+}\mathcal{F} & \partial_{\beta_I^+}\partial_{\alpha_J^-}\mathcal{F} & \partial_{\beta_I^+}\partial_{\beta_J^-}\mathcal{F} \\ \partial_{\alpha_I^-}\partial_{h_J}\mathcal{F} & \partial_{\alpha_I^-}\partial_{\alpha_J^+}\mathcal{F} & \partial_{\alpha_I^-}\partial_{\beta_J^+}\mathcal{F} & \partial_{\alpha_I^-}\partial_{\alpha_J^-}\mathcal{F} & \partial_{\alpha_I^-}\partial_{\beta_J^-}\mathcal{F} \\ \partial_{\beta_I^-}\partial_{h_J}\mathcal{F} & \partial_{\beta_I^-}\partial_{\alpha_J^+}\mathcal{F} & \partial_{\beta_I^-}\partial_{\beta_J^+}\mathcal{F} & \partial_{\beta_I^-}\partial_{\alpha_J^-}\mathcal{F} & \partial_{\beta_I^-}\partial_{\beta_J^-}\mathcal{F} \end{pmatrix}, \tag{11.29}$$

and

$$\mathsf{D}_{IJ} = \begin{pmatrix} \partial_{h_I}\partial_{h_J}\mathcal{D} & \partial_{h_I}\partial_{\alpha_J^+}\mathcal{D} & \partial_{h_I}\partial_{\beta_J^+}\mathcal{D} & \partial_{h_I}\partial_{\alpha_J^-}\mathcal{D} & \partial_{h_I}\partial_{\beta_J^-}\mathcal{D} \\ \partial_{\alpha_I^+}\partial_{h_J}\mathcal{D} & \partial_{\alpha_I^+}\partial_{\alpha_J^+}\mathcal{D} & \partial_{\alpha_I^+}\partial_{\beta_J^+}\mathcal{D} & \partial_{\alpha_I^+}\partial_{\alpha_J^-}\mathcal{D} & \partial_{\alpha_I^+}\partial_{\beta_J^-}\mathcal{D} \\ \partial_{\beta_I^+}\partial_{h_J}\mathcal{D} & \partial_{\beta_I^+}\partial_{\alpha_J^+}\mathcal{D} & \partial_{\beta_I^+}\partial_{\beta_J^+}\mathcal{D} & \partial_{\beta_I^+}\partial_{\alpha_J^-}\mathcal{D} & \partial_{\beta_I^+}\partial_{\beta_J^-}\mathcal{D} \\ \partial_{\alpha_I^-}\partial_{h_J}\mathcal{D} & \partial_{\alpha_I^-}\partial_{\alpha_J^+}\mathcal{D} & \partial_{\alpha_I^-}\partial_{\beta_J^+}\mathcal{D} & \partial_{\alpha_I^-}\partial_{\alpha_J^-}\mathcal{D} & \partial_{\alpha_I^-}\partial_{\beta_J^-}\mathcal{D} \\ \partial_{\beta_I^-}\partial_{h_J}\mathcal{D} & \partial_{\beta_I^-}\partial_{\alpha_J^+}\mathcal{D} & \partial_{\beta_I^-}\partial_{\beta_J^+}\mathcal{D} & \partial_{\beta_I^-}\partial_{\alpha_J^-}\mathcal{D} & \partial_{\beta_I^-}\partial_{\beta_J^-}\mathcal{D} \end{pmatrix}, \tag{11.30}$$

where $\mathsf{D}$ is independent of $\mathsf{u}$ because the dissipation potential is a quadratic function of the rates of change of the system. Then, Newton's method results in the iterative algorithm

$$\mathsf{K}\left(\mathsf{u}^{(n)}\right)\left(\mathsf{u}^{(n+1)}-\mathsf{u}^{(n)}\right)=\mathsf{f}\left(\mathsf{u}^{(n)}\right), \tag{11.31}$$

where here we denote by $\mathsf{u}^{(n)}$ the $n$-th step in Newton's iterations, which should not be confused with $\mathsf{u}^n$, which contains the solution at the time-step $n$. We can rewrite Eq. (11.31) as

$$\boxed{\left(\frac{1}{\Delta t^n}\mathsf{H}\left(\mathsf{u}^{(n)}\right)+\mathsf{D}\right)\left(\mathsf{u}^{(n)}-\mathsf{u}^{(n+1)}\right)=\frac{1}{\Delta t^n}\mathsf{h}\left(\mathsf{u}^{(n)}\right)+\mathsf{d}\left(\mathsf{u}^{(n)}\right)+\mathsf{p}.} \tag{11.32}$$

The solution to this iterative process leads to $\mathsf{u}^{n+1}$.

## 11.4 Advection: Stabilized finite element formulation

Once we have solved the mechanical problem, we can now address the transport problem. Discretizing Eq. (11.3) we obtain

$$\sum_I \rho_I^{\pm} N_I = \left(\rho^{\pm}\right)^n \left[1+\Delta t^n \,\mathrm{tr}\boldsymbol{d}^{\pm}\right] + \Delta t^n \,\boldsymbol{c}^{\pm}\cdot\mathbf{grad}\rho^n, \tag{11.33}$$

To obtain the weak form, we multiply the previous expression by the test function

$$w_J = N_J, \tag{11.34}$$

following a usual Garlerkin method to solve the algebraic equation in a least-square sense. Then, the weak form is

$$\sum_I \int_{\tilde{\Gamma}} \rho_I^{\pm} N_I N_J = \int_{\tilde{\Gamma}} N_J \left\{\left(\rho^{\pm}\right)^n \left[1+\Delta t^n \,\mathrm{tr}\boldsymbol{d}^{\pm}\right] + \Delta t^n \,\boldsymbol{c}^{\pm}\cdot\mathbf{grad}\rho^n\right\}, \tag{11.35}$$

where, as in the previous Section, we have omitted the summation on $E$ for simplicity. Defining the solution vector for the transport problem

$$\mathsf{r}^{\pm} = \begin{pmatrix} \rho_1^{\pm} \\ \vdots \\ \rho_{N_n}^{\pm} \end{pmatrix}, \tag{11.36}$$

the system of equations can be formulated as a linear problem

$$\mathsf{M}^{\pm}\mathsf{r}^{\pm} = \mathsf{s}^{\pm}, \tag{11.37}$$

with

$$\mathsf{M}^{\pm}_{IJ} = \int_{\tilde{\Gamma}} N_I N_J J d\boldsymbol{\xi}, \tag{11.38}$$

the mass matrix and

$$\mathsf{s}^{\pm}_{J} = \int_{\tilde{\Gamma}} \left\{ (\rho^{\pm})^n \left[1 + \Delta t \, \mathrm{tr}\boldsymbol{d}^{\pm}\right] + \Delta t \, \boldsymbol{c}^{\pm} \cdot \mathbf{grad}\rho^n \right\} J d\boldsymbol{\xi}. \tag{11.39}$$

Alternative to Eq. (11.3), which uses a simple forward Euler integration, we could consider an implicit Euler scheme to discretize in time the process operator in the transport problem, which leads to

$$\frac{(\rho^{\pm})^{n+1} - (\rho^{\pm})^n}{\Delta t^n} + (\rho^{\pm})^{n+1} \, \mathrm{tr}\boldsymbol{d}^{\pm} + \boldsymbol{c}^{\pm} \cdot \mathbf{grad} \, (\rho^{\pm})^{n+1} = 0. \tag{11.40}$$

This is a reaction-convection problem in $(\rho^{\pm})^{n+1}$ and its discretization with finite elements has to be carefully considered, since Garlerkin methods cannot deal with large convective terms. Discretizing we obtain

$$\sum_I \rho^{\pm}_I \left[ N_I \left(1 + \Delta t^n \, \mathrm{tr}\boldsymbol{d}^{\pm}\right) + \Delta t^n \, \boldsymbol{c}^{\pm} \cdot \mathbf{grad} N_I \right] = (\rho^{\pm})^n . \tag{11.41}$$

To deal with the convective term appropriately, we use the test functions

$$w_J = N_J + \gamma_s \Delta t^n \, \boldsymbol{c}^{\pm} \cdot \mathbf{grad} N_J, \tag{11.42}$$

following a Petrov-Garlerkin method in which the weight functions do not coincide with the basis functions used in the approximation of the solution $(\rho^{\pm})^{n+1}$. This method is called *stream-upwind Petrov Garlerkin* (SUPG) [44], which is able to resolve the convective term of the transport problem by adding some numerical diffusion controlled by the SUPG parameter $\gamma_s$. Then, the weak form is

$$\sum_I \rho^{\pm}_I \int_{\tilde{\Gamma}} \left( N_J + \gamma_s \Delta t^n \, \boldsymbol{c}^{\pm} \cdot \mathbf{grad} N_J \right) \left[ N_I \left(1 + \Delta t^n \, \mathrm{tr}\boldsymbol{d}^{\pm}\right) + \Delta t^n \, \boldsymbol{c}^{\pm} \cdot \mathbf{grad} N_I \right] J d\boldsymbol{\xi}$$

$$= \int_{\tilde{\Gamma}} \left( N_J + \gamma_s \Delta t^n \, \boldsymbol{c}^{\pm} \cdot \mathbf{grad} N_J \right) \left( \rho^{\pm} \right)^n J d\boldsymbol{\xi}, \quad (11.43)$$

which can also be written as a linear system

$$\hat{\mathsf{M}}^{\pm} \mathsf{r}^{\pm} = \hat{\mathsf{s}}^{\pm}, \quad (11.44)$$

with

$$\hat{\mathsf{M}}^{\pm}_{IJ} = \int_{\tilde{\Gamma}} \left( N_J + \gamma_s \Delta t^n \, \boldsymbol{c}^{\pm} \cdot \mathbf{grad} N_J \right) \times \left[ N_I \left( 1 + \Delta t^n \, \mathrm{tr} \boldsymbol{d}^{\pm} \right) + \Delta t^n \, \boldsymbol{c}^{\pm} \cdot \mathbf{grad} N_I \right] J d\boldsymbol{\xi}, \quad (11.45)$$

and

$$\hat{\mathsf{s}}^{\pm}_J = \int_{\tilde{\Gamma}} \left( N_J + \gamma_s \Delta t^n \, \boldsymbol{c}^{\pm} \cdot \mathbf{grad} N_J \right) \left( \rho^{\pm} \right)^n J d\boldsymbol{\xi}. \quad (11.46)$$

We note that $\hat{\mathsf{M}}$ is not symmetric.

# Chapter 12

# Numerical examples

In this Chapter we examine a series of examples that illustrate the theoretical and computational framework for lipid bilayers developed in this Part of the Thesis. In particular, we examine two important processes in lipid bilayers, the relaxation of density disturbances and the mobility of proteins with spontaneous curvature.

## 12.1 Relaxation of density disturbances

### Introduction

Membranes in cells and organelles are often exposed to changes in their local density. For instance, proteins and other membrane inclusions, such as polymers, insert in the membrane and locally change the lipid packing [162, 184]. Chemical signals, such as pH disturbances [82, 54], can also alter the lipid density of the membrane. Furthermore, changes in the local density can occur asymmetrically, affecting only one of the two monolayers and mobilizing intermonolayer slippage. Local density perturbations lead to transient dynamics, where lipid flows and shape changes are tightly coupled, and in which the interplay between stretching, bending, shear and

intermonolayer friction is crucial. Thus, these processes constitute an excellent example of application of our theoretical and computational framework. Furthermore, these processes have been previously examined under the assumption of axisymmetry [139], which can be used as a reference to verify our numerical procedure.

### Simulation setting

Following [139], we examine deflated spheroidal prolate vesicles, initially at equilibrium, to which we apply a density disturbance. To prepare the initial state, we start with a sphere of radius $R$ and, fixing its volume $V$, we increase its surface area $S$ to obtain a given reduced volume $v$, which is defined as the ratio between $V$ and the volume of a sphere with surface area $S$

$$v = \frac{3\sqrt{4\pi}V}{S^{3/2}}. \tag{12.1}$$

For a sphere $v = 1$ and $v < 1$ otherwise. During the area increase, we solve the shape that minimizes the Helfrich energy. To break the initial symmetry of the sphere, we perturb the vesicle in the $z$ direction to force it to take a prolate shape with the longer axis aligned with this direction. Once the shape has been obtained, we initialize the lipid densities on each monolayer close to their equilibrium state for the given shape, i.e.

$$\rho^{\pm} = \rho_0(1 \mp dH). \tag{12.2}$$

To do this, we solve a least-squares problem for $\rho^{\pm}$ (note that since $H$ is discontinuous at irregular nodes, Eq. (12.2) cannot be imposed strongly at the control points in general). Then, we let the density and shape relax; this leads to the initial equilibrium state of the vesicle. To perturb the initial density profiles, we add a perturbation

$$\delta\rho^{\pm} = \delta\breve{\rho}^{\pm}(1 \mp dH), \tag{12.3}$$

where

$$\delta\breve{\rho}^{\pm} = \delta\breve{\rho}^{\pm}_m f(\theta, \phi), \tag{12.4}$$

is the perturbation of the densities at the neutral surfaces of each monolayer, $\delta\breve{\rho}_m^{\pm}$ is the maximum value of the perturbation at the outer and inner monolayers respectively, and $f(\theta,\phi)$ is a function with values from 0 to 1 of the angles $(\theta,\phi)$ of a set of spherical coordinates.

Following the common estimates for the model parameters [39, 139], we choose $\kappa = 10^{-19}\,\mathrm{J}$, $k_S = 5\times10^{-2}\,\mathrm{J\cdot m^{-2}}$, $b_I = 10^{9}\,\mathrm{J\cdot s\cdot m^{-4}}$, $\mu = 5\times10^{-10}\,\mathrm{J\cdot s\cdot m^{-2}}$, and $\lambda = 0$ (this parameter seems to play a minor role in the dynamics).

### Results

To compare with [139], we start by examining a small vesicle ($R = 200$ nm) with a reduced volume $v = 0.99$, to which we apply a disturbance of the 5% in the outer monolayer, $\delta\breve{\rho}_m^{+}/\rho_0 = 5\%$, with a distribution $f(\theta)$ given by

$$f(\theta) = \tanh\left(\frac{w-\theta}{\pi}\right), \tag{12.5}$$

where $w = \dfrac{\pi}{10}$ controls the width of the disturbance. We show some snapshots of the dynamics along with the time-evolution of the dissipation and the main energy contributions, see Fig. 12.1. First, we observe that the total energy $\mathcal{F}$ decays with time (Fig. 12.1A), as expected since $\mathcal{F}$ is a Lyapunov functional of the dynamics. Furthermore, from Fig. 12.1B we observe that the largest energetic component is $\mathcal{F}_{\mathrm{H}}$, the Helfrich energy. However, it does not play a significant role in this problem since its variation is very small. Instead, we observe that the relaxation of the stretching in the upper monolayer, and the response of stretching in the lower monolayer are the main drivers of the dynamics (see Fig. 12.1B). In snapshot III, we can observe how the local density asymmetry results in a small but noticeable shape change, whose signature can be seen in the curvature energy.

To better understand the dynamics, let us introduce a set of time-scales that are associated to our model, for which we follow the nomenclature in [139]. First, we note that gradients of the average density relax with a time-scale given by $t_4 = \dfrac{\mu}{k_S}$, as they are driven by stretching energy and dragged by

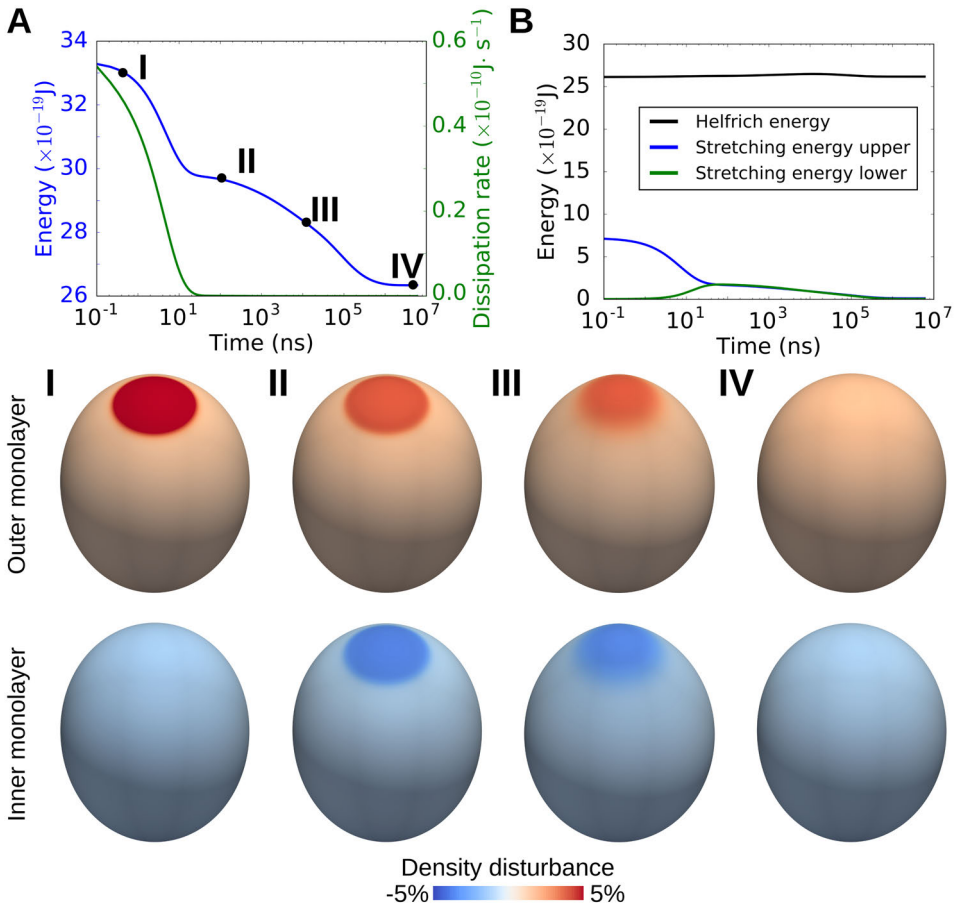


**Figure 12.1**: Relaxation dynamics of a density perturbation on the outer monolayer of a small vesicle of $R = 200\,\text{nm}$ with $\delta\breve{\rho}_m^+ = 5\%$. (A) Energy (blue) and dissipation (green) along the time-evolution of the system. Note that the $x-$axis is in log-scale to enhance the different time-scales in the problem. (B) Time-evolution of the different energies of the problem. (I-IV) show snapshots of the shape and the densities of outer and inner monolayers at different stages of the dynamics.

shear dissipation. This time-scale is size-independent, and usually very fast, $t_4 \approx 10\,\text{ns}$ for our choice of model parameters. This relaxation occurs without mobilizing intermonolayer slippage or bending energy. Gradients of density

differences between monolayers are also penalized by the stretching energy. However, at fixed shape, balancing these gradients requires intermonolayer slippage. Indeed, density differences have been shown to diffuse with a diffusivity $D = \frac{k_S}{b_I}$ [47], which results in a time-scale $t_1 = \frac{\bar{S}}{D} = \frac{\bar{S} b_I}{k_S}$, where $\bar{S}$ is the area of the density disturbance. However, density differences can also relax by curving the membrane, not mobilizing intermonolayer slippage, with a time-scale given by $t_2 = \frac{\sqrt{\bar{S}}\mu}{k_S d}$. It is clear that $t_1$ and $t_2$ characterize two alternative ways of relaxing density differences. Interestingly, $t_1$ scales linearly with the perturbed area $\bar{S}$ whereas $t_2$ scales with the square-root of $\bar{S}$. This suggests the existence of a given value $\bar{S}^*$ below which $t_1$ dominates and above which $t_2$ dominates. For our set of model parameters, $\bar{S}^* = 0.25\,\text{nm}$, which is smaller than the bilayer thickness. Thus, in the conditions of our simulations, density differences relax faster by changing shape rather than by diffusing laterally on the bilayer. This is the reason why the membrane of the previous example has a non-negligible shape change even if the initial density disturbance is small.

For the 200nm vesicle, we find that $t_1 \approx 0.151\,\text{ms}$ and $t_2 \approx 1\,\mu\text{s}$. These time-scales are clearly apparent from Fig. 12.1A. First, we observe an initial decay of the total energy associated with the rapid equilibration of the total density, in a time-scale comparable with $t_4$. We then observe a decay of the energy characterized by a shape deformation that accommodates the density difference in a time-scale comparable with $t_2$. Finally, this shape deformation and the density difference relax in a time-scale comparable with $t_1$. Consistent with this description, we observe an initial decay of the stretching energy of the outer monolayer, accompanied with an increase of the stretching energy of the lower monolayer, but with an almost negligible change in the bending energy (see Fig. 12.1B); given the initial disturbance of the total density, lipids in both monolayers are mobilized without creating curvature or intermonolayer slippage. Then, the total stretching energy partially relaxes due to the shape change, along with a small increase of the Helfrich energy. Finally, the stretching energy relaxes by lateral diffusion of the excess density through

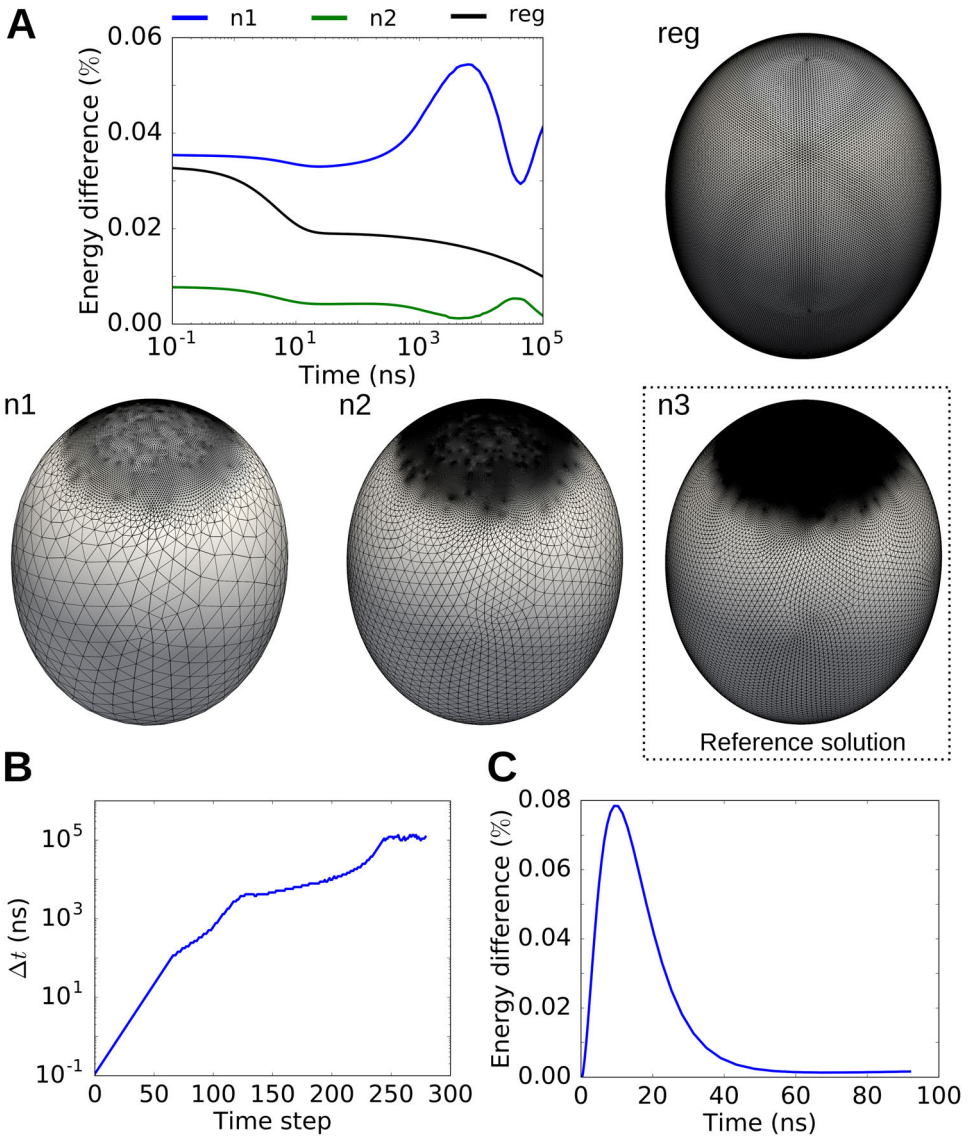


**Figure 12.2**: Convergence of the numerical method. (A) Difference between the energies obtained from the simulation of the meshes n1 (8,394 nodes),n2 (33,570) and reg (65,538) with respect to n3 (134,274). (B) Time-evolution of the time-step. (C) Comparison with a simulation with fixed time-step for the first 100 ns of dynamics.

intermonolayer slippage, the Helfrich energy decays almost to its original value, and the excess of energy due to the increase in the total mass of the upper monolayer is accommodated in the stretching energies of the outer and inner monolayers.

We note here two important aspects of the numerical simulation of the previous example. First, we have employed an unstructured mesh that has a larger resolution in the region where the density difference is applied (see Fig. 12.2 n1). A regular mesh with an equivalent resolution of the target zone requires many more nodes and degrees of freedom (see Fig. 12.2 reg), which leads to a much higher computational effort (with simulations 7 times longer under the same conditions). Thus, our general formulation on unstructured meshes allows us to focus on regions where density gradients and curvatures are higher to increase the computational efficiency. To examine the convergence of the numerical method, we compute the dynamics for two different levels of refinement of the previous unstructured mesh (Fig. 12.2 n2 and n3) and also for the regular mesh. In Fig. 12.2A we compute the difference in the total energy between the solution of mesh n3, taken as reference, and the others, which shows that the relative error between them is smaller than 0.1%. This analysis also shows that the difference between the meshes n1 and n3 is greater than that between n2 and n3, which is expected for a convergent method.

Second, given the dramatic difference between the time-scales of the problem, the time-step of the simulation has been adapted during the time-evolution, as we show in Fig. 12.2B. The simulation starts with a time-step of 0.1 ns to capture the initial fast dynamics associated to $t_4$ and progressively increases up to 0.1 ms. This is a difference of 6 orders of magnitude. To adapt the time-step we employ the following prescription: if Newton's method is solved less than $N_S$ steps, with $N_S$ given initially (usually a number between 4 and 6), we increase $\Delta t^{n+1} = f\Delta t^n$ with $f$ a scaling factor greater than 1, if however Newton's method does not converge in $N_S$ steps, we reduce $\Delta t^{n+1}$ as $\Delta t^{n+1} = \Delta t^n / f$. This adaptive time-stepping algorithm allows us to perform

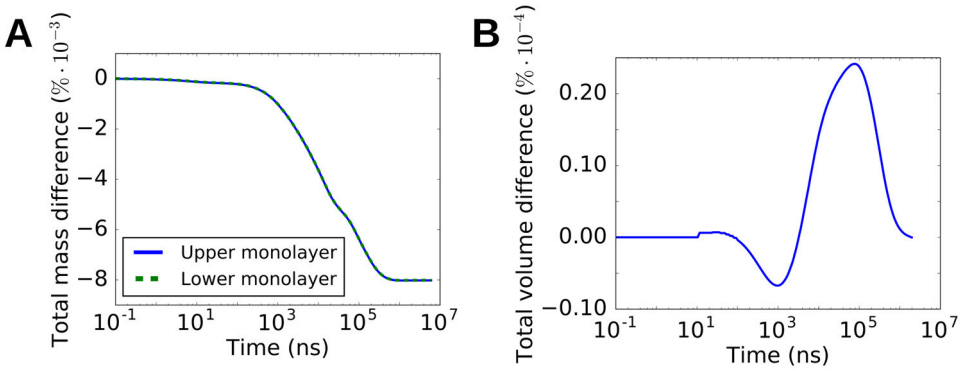


**Figure 12.3**: Time-evolution of the total mass difference (A) and the volume difference (B) with respect to their initial values.

the simulation in less than 300 time-steps, whereas a fixed time-step algorithm with the required initial resolution would need 10 million of time-steps. To show that, however, the dynamics is not affected by the adaptive time-stepping, we plot the difference in the total energy between a simulation with a fixed time-step and the simulation with the adaptability time-step for the first 100 ns of dynamics, which shows a difference smaller than 0.1% (Fig. 12.2C).

Another important aspect of the numerical method is the global conservation of mass and volume. Conservation of the total mass is not directly imposed in our numerical procedure, and we rely on the local mass conservation imposed weakly through the process operator. On the other hand, conservation of volume is imposed as a non-linear constraint at every time-step. We show the time-evolution of the total mass in the outer and inner monolayers and the total volume in Fig. 12.3, where we observe total mass differences smaller than $10^{-2}$% and volume differences smaller than $10^{-4}$%.

To further show the versatility of the numerical method, we examine the dynamics of a non-axisymmetric system, in which we have rotated the initial vesicle, and to which we apply a density disturbance pattern with $\delta\rho_m^+ = 25\%$ (see Fig. 12.4). We observe a similar dynamics, now with a larger bulge due to the larger density difference, and with an initial stretching energy 4-times

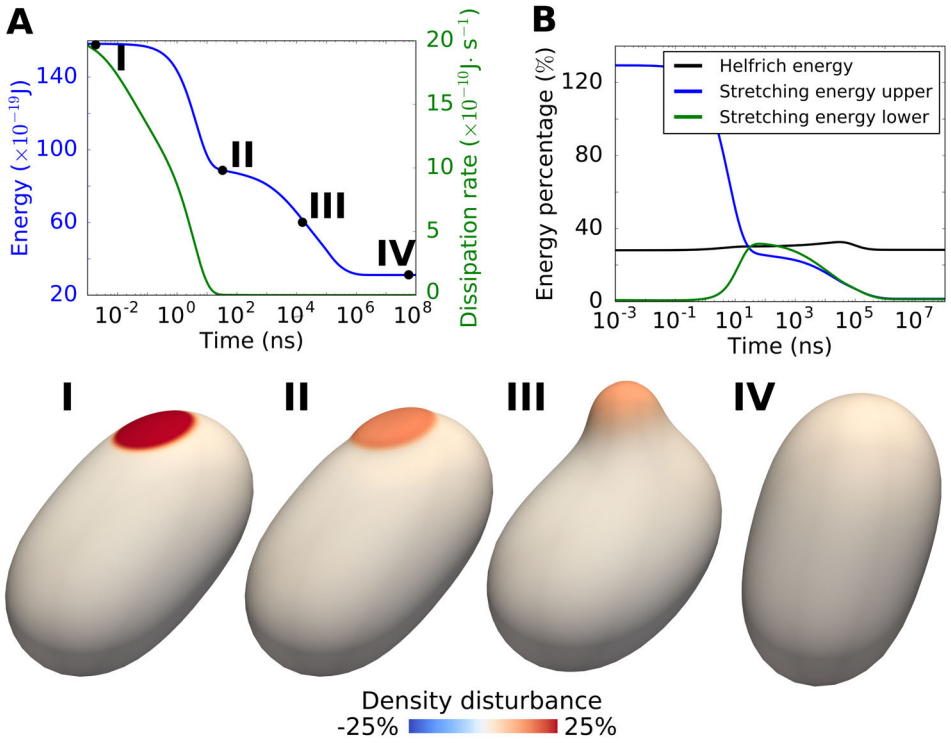


**Figure 12.4**: Relaxation dynamics of a density perturbation on the outer monolayer of a small vesicle of $R = 200\,\text{nm}$ with $\delta\breve{\rho}_m^+ = 25\%$ for a non-axisymmetric case. (A) Energy (blue) and dissipation (green) along the time-evolution of the system. (B) Time-evolution of the different energies of the problem. (I-IV) show snapshots of the shape and the density of outer monolayer at different stages of the dynamics.

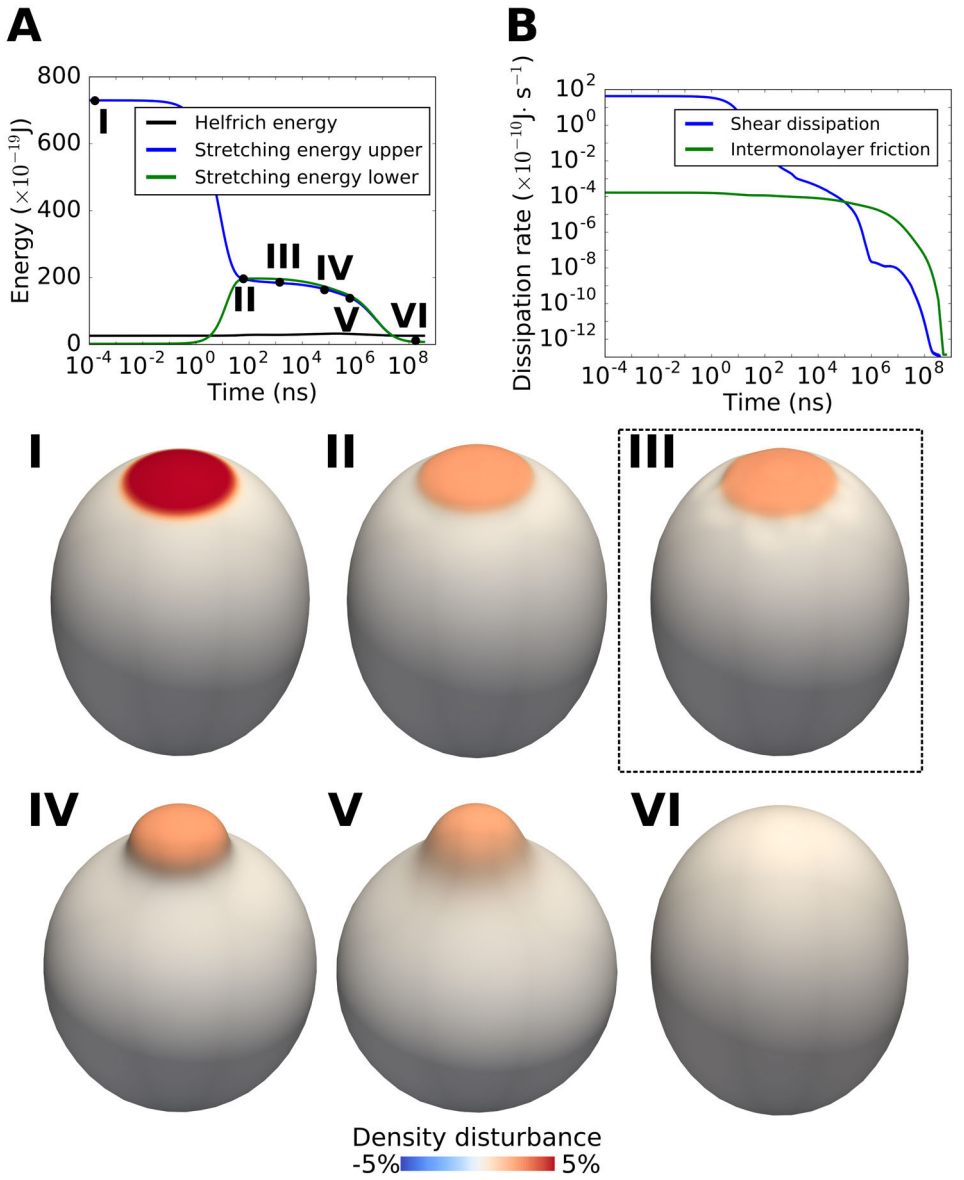


**Figure 12.5**: Relaxation dynamics of a density perturbation on the outer monolayer of a small vesicle of $R = 2\,\mu\text{m}$ with $\delta\check{\rho}_m^+ = 5\%$. (A) Time-evolution of the different energies of the problem. (B) Time-evolution of the different sources of dissipation of the problem. (I-IV) show snapshots of the shape and the density of outer monolayer at different stages of the dynamics.

larger than the bending energy.

Finally, we analyze a vesicle of $R = 2\,\mu\text{m}$ with $\delta\breve{\rho}_m^+/\rho_0 = 5\%$. For this size, the stretching energy becomes even more determinating than in the case of $R = 200\,\text{nm}$. Indeed, the relative influence between the different energetic components is highly size-dependent. Given two vesicles, say 1 and 2, related by a geometric scaling factor $X$, we have that $\mathcal{F}_\text{H}(2) = \mathcal{F}_\text{H}(1)$ (the Helfrich energy is size independent), whereas $\mathcal{F}_\text{S}(2) = X^2\mathcal{F}_\text{S}(1)$. In agreement with this, the dynamics for $R = 2\,\mu\text{m}$ show the formation of a large bulge that affects the shape of the whole vesicle and with a stretching energy 20-fold larger than the Helfrich energy (see Fig. 12.5). The time-scales associated to this problem are $t_1 \approx 15\,\text{ms}$ and $t_2 \approx 10\,\mu\text{s}$, with $t_4 = 20\,\text{ns}$ as before. In agreement with these time-scales, we observe again the initial peak of energy decrease in a scale comparable with $t_4$, and a total duration of the relaxation dynamics of 10 ms, similar to $t_1$. In Fig. 12.5B we plot the value of the different dissipation contributions, shear and intermonolayer friction, in a log-log plot. This plot shows that, during the initial equilibration of the total density and during the bulge formation, shear dissipation dominates. However, at the later stages of the dynamics, where the shape relaxes back to equilibrium, density differences relax due to intermonolayer slippage.

Surprisingly, in the initial stages of the bulge formation (Fig. 12.5III), we observe that a pattern resembling buckling forms at the edge of the bulge, presumably caused by a transient and local compression in a large enough region (compared to the Föppl-von Kármán length-scale $l_{FvK} = \sqrt{\dfrac{\kappa}{\sigma}} \approx 5\,\text{nm}$, where we have used the expression of the tension for the stretching energy $\sigma = k_S\left(\left(\dfrac{\rho^\pm}{\rho_0}\right)^2 - 1\right) \approx 10^{-2}\ \text{J}\cdot\text{m}^{-2}$ for $\rho^\pm = 1.05\rho_0$). This kind of buckling deformation is a three-dimensional phenomenon that could not develop in the axisymmetric simulations in [139]. To examine this phenomenon further, we zoom Fig. 12.5IV in the region where the pattern forms, see Fig. 12.6. First, we note that the formation of the pattern does not result from an increase of the total energy, which suggest that it is not caused by a numerical instability of our

method. In Figs. 12.6I and II, we show the velocity field of the outer monolayer near the bulge at two different instants during the pattern formation. After the pattern has formed, Figs. 12.6III and IV, the amplitude of the bulge continues to increase, and the oscillatory deformation pattern progressively dissapears, see Fig. 12.6V. The rest of the dynamics is similar to that obtained in [139], which suggest that the pattern forms due to an initial buckling instability that does not affect the final fate of the dynamics. Our model is lacking of the dissipative forces induced by the bulk medium, which provides a dynamical confinement that may attenuate or remove this buckling-induced pattern formation. Indeed, the size of the disturbance is close to the Saffman-Delbrück length, and therefore bulk dissipation could start playing a role. Thus, whether this phenomenon can be observed in experiments or is an artifact of the lack of bulk viscosity is an open question.

In summary, these examples provide a verification of our numerical approach in a fully non-linear and three-dimensional setting.

## 12.2 Rheology of inclusions in lipid membranes: beyond the Saffman-Delbrück theory

### Introduction

Proteins and other inclusions such as lipid or protein aggregates, populate biological membranes. Because the lipid membrane is fluid, these inclusions diffuse on the membrane as in a two-dimensional viscous fluid. This lateral mobility of proteins enables the dynamical lateral organization of biological membranes, for instance in cell-cell adhesion junctions.

As a first approach to understanding protein diffusion on lipid membranes, let us consider a simple model in which the membrane is represented as an inextensible viscous fluid of interfacial viscosity $\mu$. Computing the protein diffusion constant on the lipid membrane is equivalent to finding the mobility of a circular inclusion on a two-dimensional Stokes flow. In this fluid, we

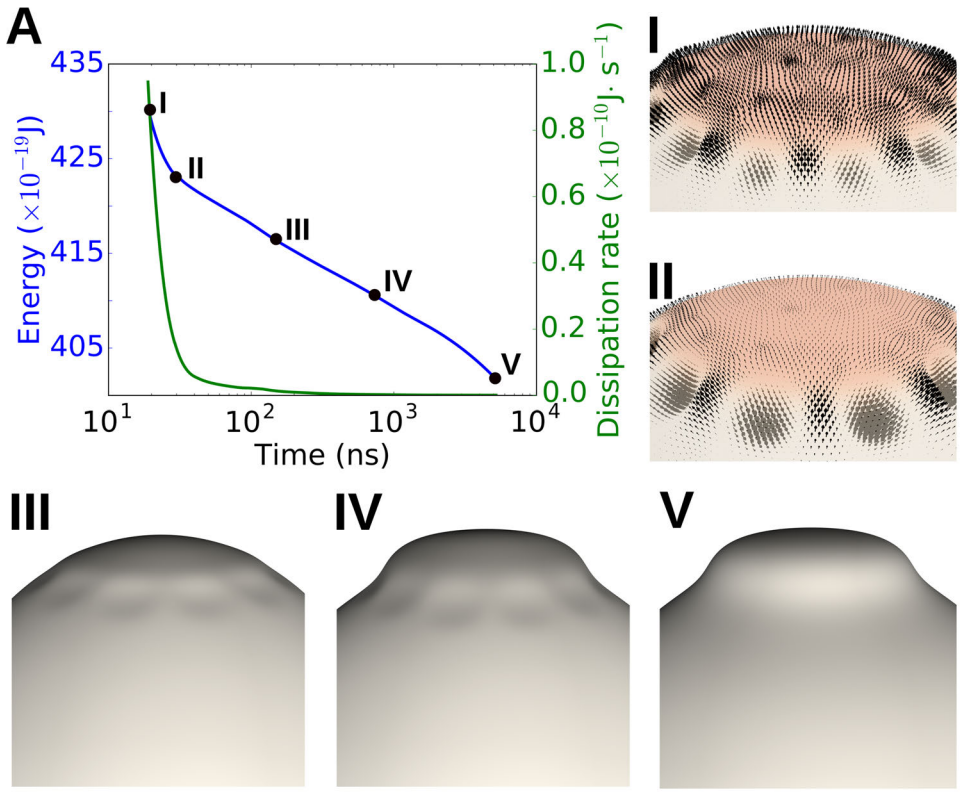


**Figure 12.6**: (A) Zoom of Fig. 12.5A in the region in which the pattern forms. (I) and (II) show the velocity field with arrows, which lead to the pattern formation. After the pattern has formed, the bulge continues growing (III) and (IV). Finally, once the bulge grows large enough, the wrinkles associated to the pattern smoothly dissappear.

consider a protein of cylindrical shape with a negligible spontaneous curvature. For simplicity, we consider a planar membrane (see Fig. 12.7A). The Stokes-Einstein relation states that the diffusion coefficient is the product of the thermal energy $k_BT$ and the hydrodynamic mobility $M$,

$$D = k_BTM. \tag{12.6}$$

For instance, in a three-dimensional viscous fluid of viscosity $\mu_b$, a sphere of

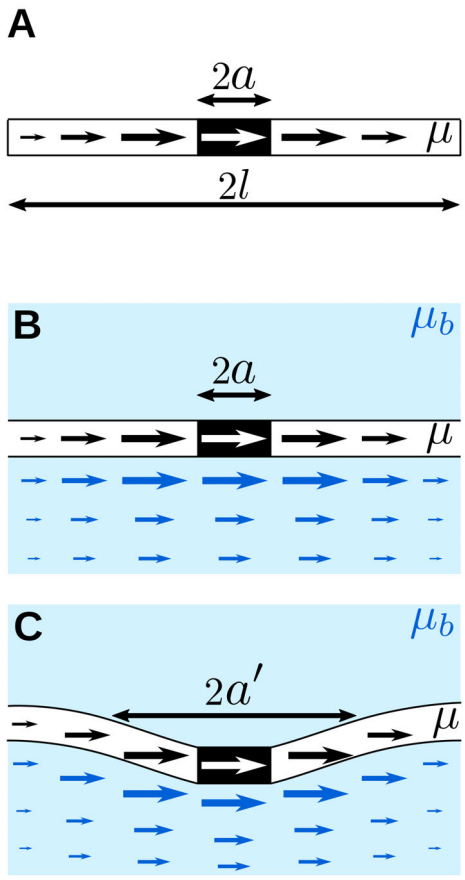


**Figure 12.7**: (A) Side view of a viscous layer of viscosity $\mu$ with an inclusion (black) moving on it. Velocity of the fluid is represented with black arrows. (B) Same system but now embedded in another viscous medium of viscosity $\mu_b$. (C) The inclusion now generates a spontaneous curvature that creates a dimple. Displacing the inclusion involves displacing the dimple (the velocity of the bidimensional fluid has non-tangential components that indicate the movement of the dimple).

radius $a$ moves with a mobility

$$M_{3D} = \frac{1}{6\pi\mu_b a}, \tag{12.7}$$

where the scaling $M \sim 1/(\mu_b a)$ can be explained from dimensional analysis, whereas the pre-factor $1/(6\pi)$ can only be obtained from the solution to a boundary value problem for the Stokes flow. A similar dimensional analysis for the mobility of a circular inclusion of size $a$ in a two-dimensional fluid of viscosity $\mu$ predicts a mobility $M \sim 1/\mu$, independent of $a$. However, by solving a boundary value problem in a circular patch of membrane of radius $l$, one obtains

$$D_{2D} = \frac{k_B T}{4\pi\mu}\left[\log\left(\frac{l}{a}\right) - \frac{1}{2}\right]. \tag{12.8}$$

We note that $D_{2D} \to \infty$ as $l \to \infty$. In other words, the drag force that the protein feels when moving in a viscous 2D fluid tends to zero as the size of the patch increases; this is the well-known *Stokes paradox*. There are different ways to overcome this paradox, depending on the context. In our setting, we note that the membrane inclusion is not moving in a bidimensional medium in vacuum. Instead, the membrane is surrounded by another viscous fluid of viscosity $\mu_b$ (see Fig. 12.7B). Although since $a \ll \mu/\mu_b$, a dimensional analysis argument would suggest that $\mu_b$ is irrelevant, the limit $\mu_b \to 0$ turns out to be a singular one. In a celebrated paper [152], Saffman and Delbrück showed that the diffusion constant of an inclusion in such a system has the form

$$D_{\mathrm{SD}} = \frac{k_B T}{4\pi\mu}\left[\log\left(\frac{l_{\mathrm{SD}}}{a}\right) - \gamma\right], \tag{12.9}$$

where $l_{\mathrm{SD}} = \mu/\mu_b$ is the so-called Saffman-Delbrück length, and $\gamma$ is Euler's constant. Thus, although the bulk viscosity of the membrane $\mu/d$ is much larger than the viscosity of the bulk $\mu_b$, the effect of the bulk fluid is needed in order to overcome the Stokes paradox. The main dragging mechanism acting on the protein is the interfacial viscous force generated by the protein-membrane interaction, but the bulk fluid imposes a constraint on the interfacial fluid in the far field that cannot be neglected. Yet, the dependence on $\mu_b$ is weak. Note also that in contrast to $D_{3D}$, the dependence on the inclusion size is also weak. Eq. (12.10) predicts a logarithmic scaling of the diffusion constant with respect to the protein size $a$, which has been confirmed in a number of experiments (see [141] and references therein). However, other

experiments [56, 137] present deviations of the Saffman-Delbrück theory for proteins that induce deformations of the lipid membrane, and in particular for proteins with intrinsic curvature. Indeed, a protein moving on a self-generated curved environment must not only displace the surrounding lipids as in a pure bidimensional medium, but must also displace the dimple generated by its own intrinsic curvature (see Fig. 12.7C). Following this interpretation, the protein would behave as if it had an apparent size $a'$ larger than $a$. From previous Chapters we have learned that the coupling between tangent flows and shape changes in the presence of curvature is not trivial, and thus the interplay between the motion of the dimple and the lipid flows may greatly affect the hydrodynamic mobility of the inclusion in unexpected ways. In particular, as shown in [140], non-uniform lipid flows in a curved environment generate out-of-plane viscous forces, that further deform the membrane and mobilize the bending rigidity. As a result, the protein will move as in a visco-elastic medium rather than on a purely viscous medium despite the Newtonian rheology of the membrane. The diffusion coeficient becomes frequency-dependent, as explained by the generalized Stokes-Einstein relations [169].

Recently, several works have tried to generalize the Saffman-Delbrück theory for proteins with intrinsic curvature. In [112], Naji et al. analyzed a membrane with Helfrich energy coupled to a curving protein following a Langevin dynamics, where hydrodynamics are included with an Oseen kernel accounting for the bulk medium and membrane viscosity is neglected. This study finds that the dimple caused by the curvature of the protein leads to a reduction of protein mobility. In agreement with this work, Quemeneur et al. [137] showed experimentally that the mobility of a protein with intrinsic curvature increases with tension; increasing tension would reduce the amplitude of the dimple, resulting in a larger mobility. To analyze their experiments, Quemeneur et al. followed an analytic approach similar to [145] also based on an Oseen kernel for the bulk viscosity that neglects or makes dramatic approximations of the interfacial elasto-hydrodynamics. As noted by Morris and Turner [109], the Oseen approximation cannot properly deal with lipid flows on the membrane, which are the main dragging force that membrane

inclusions sense. To overcome this issue, Morris and Turner analyzed the hydrodynamic force exerted on a protein moving on an inextensible lipid bilayer following a perturbation approach. The membrane is initially planar and deforms due to the presence of the protein, which imposes a contact angle with a given stiffness. A perturbation expansion is developed in terms of the protein angle with respect to the plane and, at zeroth order, they reproduce the Saffman-Delbrück expression Eq. (12.10). Following the expansion up to second order, they show that the tension-dependent mobility depends on the stiffness of the protein: for sufficiently soft proteins, the protein mobility increases with tension as the dimple becomes flatter with increasing tension. However, there is a technical issue in the boundary conditions used in this work, which are not consistent with the protein translating parallel to the $xy$-plane [181].

Here we use the theoretical and computational framework described in previous Chapters to investigate how the intrinsic curvature of a protein affects its mobility. Modeling a protein as a membrane domain with spontaneous curvature $H_G$, we investigate how tension $\sigma$ affects its mobility, as in [137, 109]. Following the same line of thought as in [152] and [109], we compute the interfacial flow around the protein in the absence of bulk fluid. For a membrane of finite size, we can then compute the difference in diffusivity of such curved protein with respect to a planar protein of same size $a$, allowing us to compute its tension-dependent apparent size $a'(\sigma)$. As curvature only affects the interfacial flow near the dimple, we assume that, in the far field, the solution is that of Saffman-Delbrück theory, which leads to a diffusivity

$$D_{\mathrm{SD}}(\sigma) = \frac{k_B T}{4\pi\mu}\left[\log\left(\frac{l_{\mathrm{SD}}}{a'(\sigma)}\right) - \gamma\right]. \tag{12.10}$$

To model the protein-membrane interaction, we modify the energy and dissipation potential as we explain next.

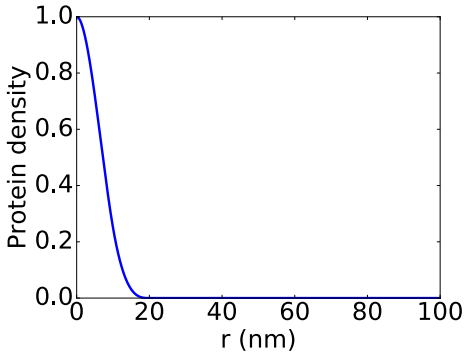


**Figure 12.8**: Protein density function $\rho_G(r)$ for a protein of radius 20 nm.

### Modeling protein-membrane interactions

To model the effect of the protein on the membrane, we follow an approach similar to that in [112], where the protein is considered as a field in the $xy$-plane that is characterized by a density $\rho_G(r)$, where $r = ||\mathbb{P}\boldsymbol{x} - \boldsymbol{x}_G||$ is the distance of $\boldsymbol{x}$ to $\boldsymbol{x}_G$ in the $xy$-plane, $\mathbb{P}$ stands for the projection operator onto the $xy$-plane, and $\boldsymbol{x}_G$ is the center of the protein (see Fig. 12.8). To model the bending rigidity of the protein we consider the following Helfrich-like energy functional

$$\mathcal{F}_{\mathrm{P}}[h] = \int_{\Gamma_t} \bar{\kappa}\rho_G(r)\,[H - H_G]^2\,dS, \tag{12.11}$$

where $\bar{\kappa}$ is the bending rigidity associated to the protein-membrane composite system, and $H_G$ stands for the spontaneous curvature of the protein. To penalize the slippage of the protein with respect to the surrounding lipid fluid, we add the dissipation potential

$$D_P[\partial_t h, \alpha^{\pm}, \beta^{\pm}] = \frac{1}{2}\int_{\Gamma_t} b_G\rho_G(r)||\mathbb{P}\boldsymbol{v}^{\pm} - \boldsymbol{v}_G||^2 dS, \tag{12.12}$$

where $b_G$ measures the strength of the frictional interaction between the bilayer and the protein. We simulate the system in a circular patch of membrane of radius $l$ with open boundary conditions, that is, we let fluid go in and out of the patch, but with a constraint on the total velocity $\boldsymbol{v}_B = \int_{\partial\Gamma_t} \boldsymbol{v} dl = \boldsymbol{0}$ so

that the patch does not have a net movement with respect to the far field. We impose a clamped boundary condition at the circular edge of the domain, so that it lies on the $xy$-plane with zero slope. We prescribe a tension $\sigma$ and the lipid density on the in-flow part of the boundary to

$$\rho_I = \rho_0 \sqrt{1 - \frac{\sigma}{k_S}}. \tag{12.13}$$

so that this density is at equilibrium with the prescribed tension. We note that, due to the translational invariance of the problem, it is equivalent to move the protein laterally with a velocity $\boldsymbol{v}_G$ with $\boldsymbol{v}_B = \mathbf{0}$ or to fix the velocity of the protein to $\mathbf{0}$ and set $\boldsymbol{v}_B = -\boldsymbol{v}_G$. From a numerical viewpoint, the former needs updating the position of the protein, and therefore updating the mesh if more resolution is needed near the protein. The latter approach allows us to fix the protein position and keep the mesh fixed. For this reason, we follow this approach, although we have checked that they are indeed equivalent.

### Results

We compute the tension-dependent hydrodynamic mobility (and hence the diffusion coefficient see Eq. (12.6)) for a protein of size $a = 20$ nm on a patch of $l = 100$ nm, with $\bar{\kappa} = 10\kappa$. The dynamics do not depend on $b_G$ if it is sufficiently large. We show the main results in Fig. 12.9. In Fig. 12.9A we show the difference in the shape of the dimple caused by the intrinsic curvature of the protein for two different tensions, along with the distribution of the density lipid in the upper monolayer. The basal levels of the density are different, because tension is related to lipid density in the model. Both density profiles depend on curvature, and therefore, they are not homogeneous at the dimple. In Fig. 12.9B we show the typical velocity profile around the inclusion, along with the density of the lower monolayer. This Figure shows how this largely inextensible fluid flow adapts not only to the obstacle but also to the curved geometry. Because of the coupling between interfacial hydrodynamics and shape dynamics in the presence of curvature. The velocity

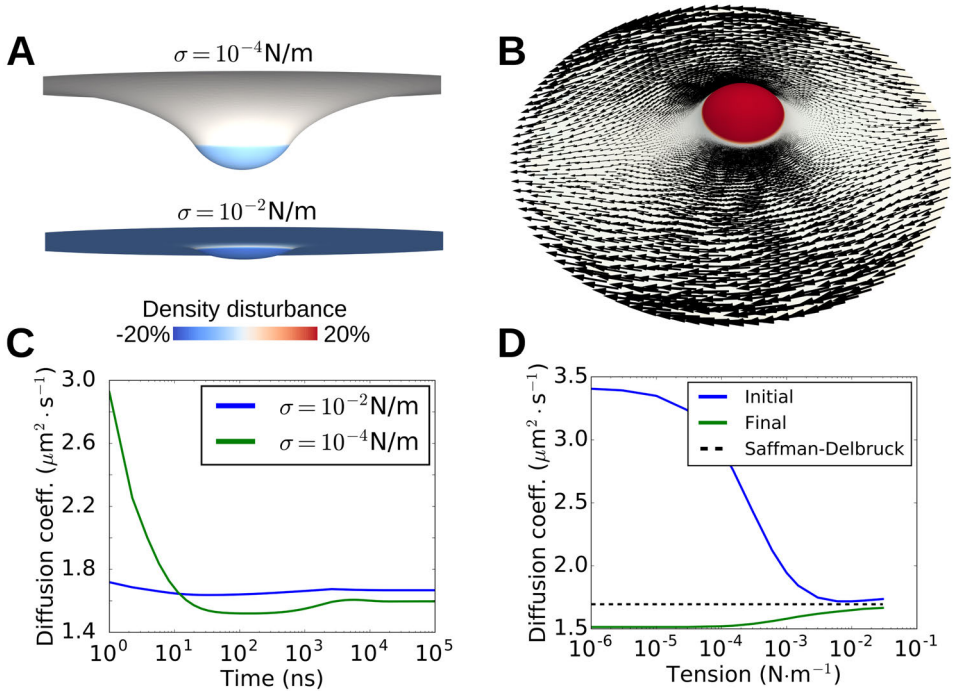


**Figure 12.9**: Mobility of a protein with intrinsic curvature as a function of tension. (A) Side view of the dimple caused by the intrinsic curvature for two different tensions with the density of the upper monolayer represented with colormap. (B) Velocity profile around the dimple and density of the lower monolayer. (C) Time-evolution of the mobility (diffusivity) for the two values of tension. (D) Diffusivity as a function of tension at the initial instant (blue) and for the steady state (green) along with the Saffman-Delbrück value.

field is time-dependent, which leads to a time-dependent mobility coefficient (see Fig. 12.9C). Because mobility (diffusivity) is time-dependent, for each tension we can keep track of the instantaneous and of the steady-state mobility. In Fig. 12.9D we show the dependence of the diffusion coefficient on tension at the fast and low time-scales. For higher tensions, the diffusivity is initially larger than for lower tensions, presumably due to the higher compliance of the more floppy system. However, the final diffusivity increases with tension, as expected for a smaller dimple. For higher tensions , the dimple is smaller

and the flow finds less resistance.

In summary, the diffusion of proteins on lipid bilayers is a central topic in membrane biophysics with a long history, dating back to the work of Saffman and Delbrück in 1975, which nevertheless is not fully settled. The study of the diffusion of proteins with intrinsic curvature has highlighted the need to account for the interaction between curvature and hydrodynamics, a subtle topic for which theoretical tools have been lacking. It has been examined with various models making drastic approximations about the elasto-hydrodynamics of lipid bilayers. In this work, we have shown that the frequency-dependence of the diffusion of proteins with intrinsic curvature is a significant effect. Our results indicate that the hydrodynamic mobility is dominated by the interfacial hydrodynamics of the membrane, where the bulk only enters through far field effects and intermonolayer slippage is a minor effect. However, slippage may become more important in proteins interacting only with one monolayer. A systematic study of the mobility of proteins and other membrane inclusions based on the approach presented here will be the subject of future work.

# Chapter 13

# Modeling and simulation of the actin cortex

## 13.1 Introduction

In this Chapter, we apply the tools developed for the modeling and simulation of lipid bilayers to another important fluid surface of the cell, the cell cortex. The cell cortex is a layer of cross-linked actin filaments lying just beneath the plasma membrane of animal cells [154]. The thickness of this layer is of hundreds of nanometers, while the typical size of an animal cell is of tens of microns. Thus, this layer can be considered as a quasi two-dimensional material. Apart from actin, this network is crowded with myosin motors, which bind to actin filaments. By consuming ATP, these molecular motors pull on actin filaments and generate an active tension. In turn, this active tension, if non-uniform, generates actin flows and drives shape changes. As another important property, the actin network undergoes a dynamic remodeling, with a continuous *turnover* of actin monomers, by polimerization and depolimerization in the filaments, and binding and unbinding of cross-linking proteins. This process is characterized by a time-scale in the order

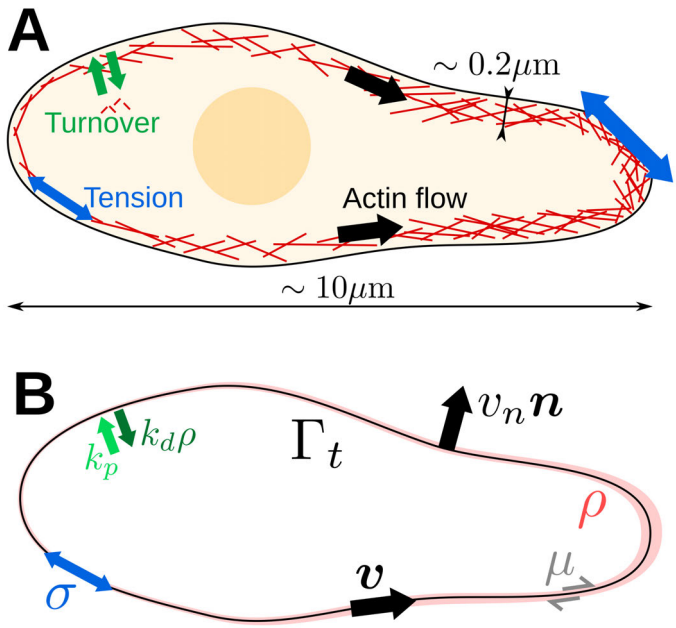


**Figure 13.1**: A viscous model for the cell cortex. (A) Schematic view of the different processes taking place in the cortex. (B) Schematic view of the main ingredients in our model.

of a few seconds. At time-scales smaller than the turnover time, the cortex behaves as an elastic network. On the other hand, at larger time-scales, the dynamic remodeling of the cortex leads to a fluid-like viscous behavior with active tension.

The theoretical and computational framework developed for lipid bilayers in this Part of the Thesis can be adapted to model the cell cortex. In the next Section we discuss the most basic ingredients needed to describe the cell cortex and in Section 3.12 we present a series of simulations that exemplify our approach.

## 13.2 Basic ingredients of the model

Following previous works [187], we model the cortex as an isotropic viscous material confined to a surface. This, and other previous works [24, 153], were restricted to axisymmetric or to two-dimensional flows, and derived the active gel equation from the stress tensor and the continuum statement of balance of linear momentum. Here, we develop a fully three-dimensional and geometrically non-linear model invoking Onsager's variational principle.

This modeling framework is based on two major approximations of the mechanical properties of the cortex. First, the elastic behavior at time-scales smaller than the turnover is neglected, since it plays a marginal role in processes happening at longer time-scales. Second, the model does not account for the orientational order of actin filaments; thus, we assume that the orientation of actin filaments is distributed randomly so that the effective response of the material is isotropic. This may not be the case in some important examples, such as during cytokinesis [147].

Mathematically, we characterize the cortex as a time-evolving surface $\Gamma_t$ with a space-varying thickness $\rho$. From the viewpoint of Onsager's variational principle, $\Gamma_t$ and $\rho$ are our state variables. The process variable in this problem is the velocity field $\boldsymbol{V}$ of actin, with a tangential component $\boldsymbol{v}$, characterizing the flow of actin on $\Gamma_t$, and a normal component $v_n\boldsymbol{n}$, describing the change of shape of the cell. The viscous rheology of the cortex is characterized by a dissipation potential, similar to that of lipid bilayers

$$\mathcal{D}[\rho;\boldsymbol{V}] = \int \rho \left[\mu||\boldsymbol{d}||^2 + \lambda(\mathrm{tr}\boldsymbol{d})^2\right] dS, \tag{13.1}$$

where here $\mu$ and $\lambda$ are the bulk shear and dilatational viscosities of the cortex, which we integrate along the cortex thickness $\rho$. Thus, this model neglects the viscous dissipation due to changes in cortex thickness. To characterize the active tension generated by the activity of myosin motors, we consider a power input

$$\mathcal{P}[\rho;\boldsymbol{V}] = \int \sigma \mathrm{tr}\boldsymbol{d}\, dS, \tag{13.2}$$

where $\sigma$ is an active tension proportional to the cortex thickness and to a measure of myosin activity $\xi$,

$$\sigma = \rho\xi, \tag{13.3}$$

where $\xi(\boldsymbol{x}, t)$ may be a function of space and time. A more detailed modeling would describe $\xi$ in terms of a chemical power supply linked to ATP hydrolysis. Instead, here we will write

$$\xi(\boldsymbol{x}, t) = \xi_0 + \delta\xi(\boldsymbol{x}, t), \tag{13.4}$$

where $\xi_0$ is a measure of the basal activity in the cortex, and $\delta\xi(\boldsymbol{x}, t)$ is a measure of the overactivity. Since tr$\boldsymbol{d}$ measures the rate at which local area expands (positive tr$\boldsymbol{d}$) or contracts (negative tr$\boldsymbol{d}$), for a positive $\sigma$ the previous term will try to contract the cortex area. As we neglect the elastic behavior of the cortex, there is no free energy associated to the problem. To relate the rate of change of $\rho$ and $\boldsymbol{V}$, we consider balance of cortex material

$$D_t\rho + \rho\,(\mathrm{div}\boldsymbol{v} - v_n H) = k_p - k_d\rho, \tag{13.5}$$

where the first term in the right hand side stands for the polimerization of actin, which we assume to happen at a constant rate $k_p$, independent of the thickness since it happens at the plasma membrane, and the second term stands for the depolimerization of actin, which is proportional to the amount of actin given by the local thickness, $k_d\rho$. The ratio $\rho_{eq} = k_p/k_d$ determines the thickness at equilibrium. Finally, we consider that the volume $V$ of the cell is constant, for which we impose a constraint with the pressure $P$ acting as a Lagrange multiplier.

Following [187], we choose the following set of model parameters, $\mu = 10^6$ Pa·s, $\lambda = 2\mu$, $k_d = 0.04\ \mathrm{s}^{-1}$, $k_p = 0.008\ \mu\mathrm{m}\cdot\mathrm{s}^{-1}$, and $\sigma_0 = 10^3$ Pa.

## 13.3 Results: measuring the rheology of the cortex

The elementary model introduced in the previous section exhibits a non-trivial phenomenology that can mimic the behavior of cells in different situations, as we show in this Section for three relevant examples.

We examine first a rheological essay to characterize the response of the cortex to compression, following the experimental setup in [50]. We place an initially spherical cell between two plates as we show in Fig. 13.2A, and we let it relax. To represent the confinement of the plates, we introduce a free energy

$$\mathcal{F}_c = \int_{\Gamma_t} V(z) dS, \tag{13.6}$$

where $z$ is a coordinate perpendicular to the plates, and $V(z)$ is a energy density characterizing the repulsion with respect to the plates,

$$V(z) = \begin{cases} 0 & \text{if } |z| < h/2, \\ \dfrac{k_c}{3}\left(\dfrac{|z| - h/2}{\delta_c}\right)^3 & \text{if } |z| \geq h/2. \end{cases} \tag{13.7}$$

with $k_c$ and $\delta_c$ characterizing the strength and the width of the repulsive interaction respectively. Since the volume of the cell is constant regardless of the compression, and since there is a basal tension given by $\rho_{eq}\xi_0$, the cell will exert a reaction force on the plates that confine it, which in general will depend on the separation between the plates. We now apply a sequence of compression events, characterized by the separation between the plates given in the green curve of Fig. 13.2B. These compression events produce a non-trivial time-dependent reaction force (blue curve); the reaction force increases during compression application, and then set-points higher than before compression. Peaks are a result of a non-equilibrium response of the cortex. To show it, we plot the density and velocity profiles at different stages of the dynamics during the first compression event (see Fig. 13.2I-IV). From these figures we can associate the density gradients in II to shape changes. Indeed, the part of the cortex that becomes in contact with the plates is transiently and locally compressed in the lateral direction, which leads to an increase in the local density because actin does not have time to flow out of this region or depolimerize. On the other hand, the free part of the cortex is expanding and, since there is not enough material coming by actin flows or polimerization, the density decreases. Thus, the magnitude of the peak and its relaxation

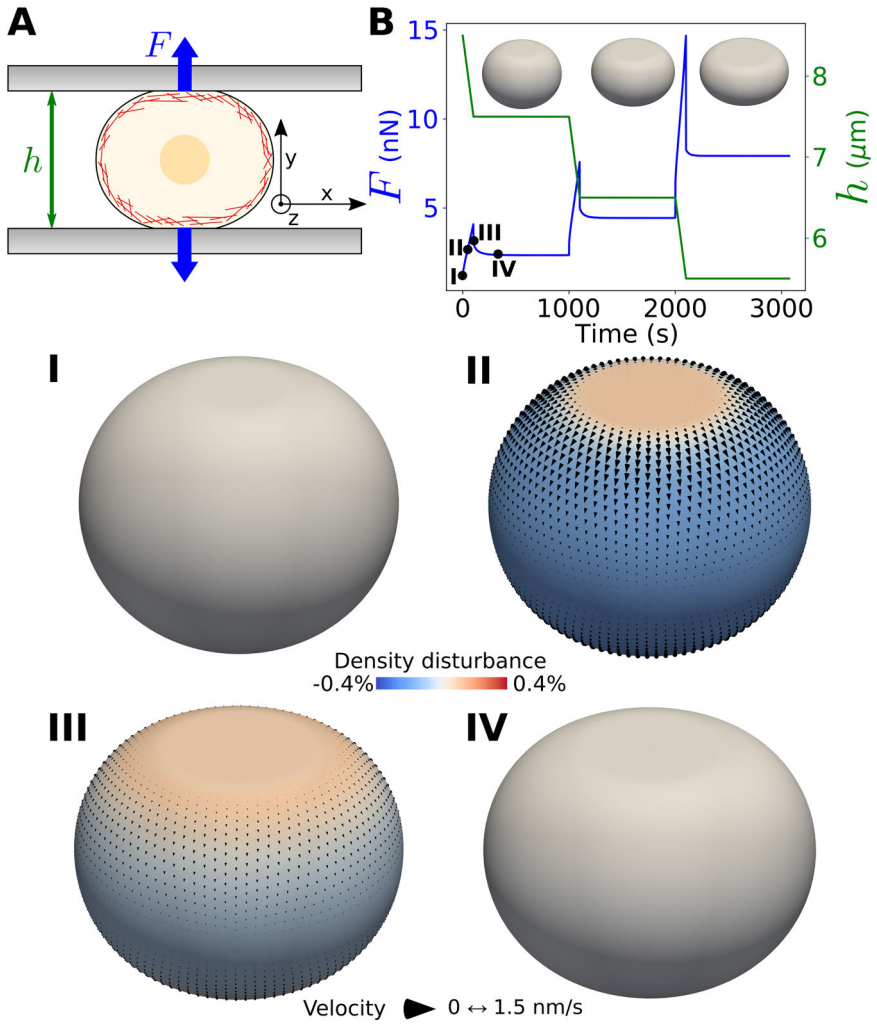


**Figure 13.2**: Rheological essay to examine the behavior of a cortical vesicle confinement between two plates. (A) Scheme of the setup. (B) Height (green) and reaction force (blue) of the cortex to a series of compression events. (I-IV) Different stages of the cell shape and the cortex density during the first compression event.

dynamics are dictated by the interplay between actin flows, shape changes, and turnover. The behavior predicted with our model is similar to that found

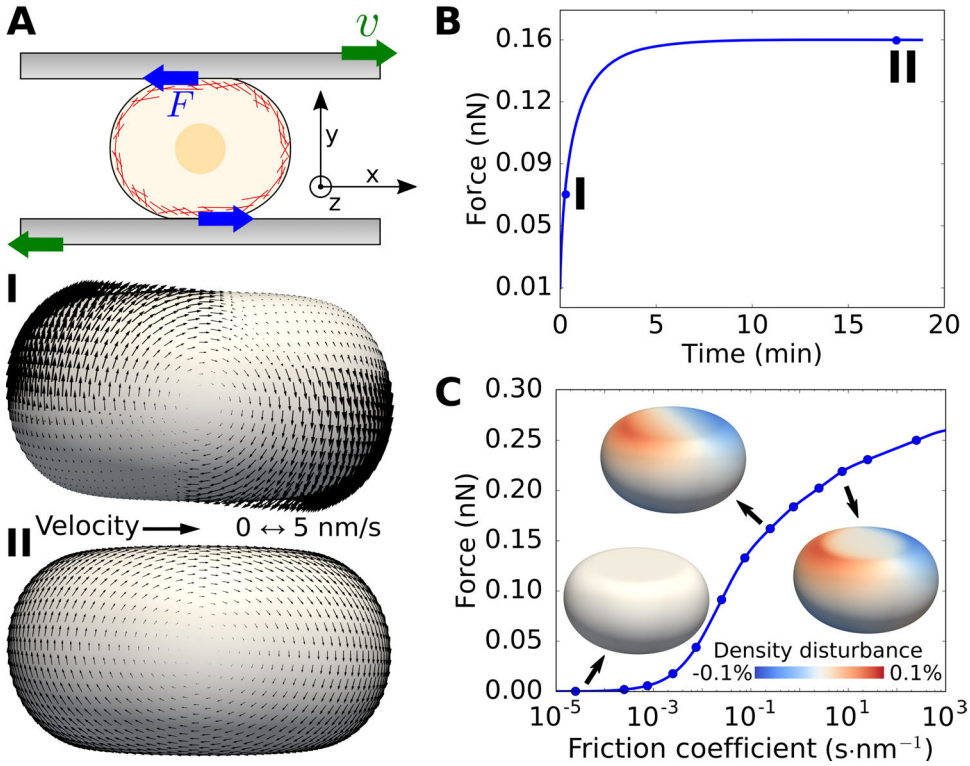


**Figure 13.3**: Rheological essay to examine the behavior of a cortical vesicle under shear. (A) Scheme of the setup. (B) Time-evolution of the reaction force. (C) Dependence of the force on the viscous friction with the plates (I-II) Different stages of cortex flows during equilibration.

experimentally in [50]. Thus, this example shows that our simple model captures this non-trivial phenomenology, and could be used to infer material parameters from these mechanical tests on rounded cells.

In a second rheological essay, we apply a shear test, in which, using the configuration obtained from the previous essay, we move the two plates confining the cortex in opposite directions with a velocity $v$ in the $x$ direction (see Fig. 13.3A). To characterize the frictional viscosity between the plate and

the cortex, we add a dissipation potential

$$\mathcal{D}_c = \int_{\Gamma_t} \frac{\mu_c V'(z)}{2} \left[ \left( v_x - v_x^{\text{plate}} \right)^2 + \left( v_y - v_y^{\text{plate}} \right)^2 \right] dS, \tag{13.8}$$

where $\boldsymbol{v}^{\text{plate}} = \pm v \boldsymbol{i}_1$ is the velocity of the upper and lower plates respectively, $\mu_c$ is a viscous friction coefficient, and the friction is proportional to the normal pressure exerted on the wall, $V'(z)$, in agreement with the framework of hydration lubrication [83]. In this case, we measure the lateral force exerted by the cortex on the plates due to this viscous interaction. As in the previous example, we observe a time-dependent response of the lateral force (see Fig. 13.3B). This time-dependence is caused by an initial accommodation of the cortex density and shape characterized by non-tangential velocity fields (see Fig. 13.3I). After some time, the system reaches a steady state in which the velocity field has only tangential velocities, i.e. shape is not changing (Fig. 13.3II). The density disturbance and the reaction force generated by shearing the plates depend dramatically on $\mu_c$, as we show in Fig. 13.3C. For $\mu_c < 10^{-3}$ s·nm$^{-1}$ the cortex is practically unaffected by the movement of the plates and shows a negligible density disturbance and velocity profile. For $10^{-3} < \mu_c < 1$ s·nm$^{-1}$ there is a continuous density gradient on the contact region that follows from the constant compression/expansion of the opposite edges of the contact region in the direction of the flow. For $\mu_c > 10^1$ s·nm$^{-1}$ the viscous friction with the wall is so high that gradients of the density cannot propagate along the contact region, where the cortex velocity is nearly $v$ everywhere. In turn, the ability of the cortical shell to maintain density gradients depends on turnover (characterized by $k_p$ and $k_d$). In summary, the reaction force is tightly controlled by shape changes, cortical flows, turnover, and the viscous drag with the plates. Therefore, this test in combination with the previous one could serve the purpose of material characterization.

Finally, we analyze another mechanical function of the cortex, namely its ability to generate cell migration in confined environments through nonspecific adhesion. For this experiment, we consider the cortex confined in a tube of radius $R$ parallel to the $x$ axis Fig. 13.4A. Thus, we introduce the confinement

potential

$$V(r) = \begin{cases} 0 & \text{if } r < R, \\ \dfrac{k_c}{3}\left(\dfrac{r-R}{\delta_c}\right)^3 & \text{if } r \geq R. \end{cases} \tag{13.9}$$

where $r = y^2 + z^2$, and the dissipation potential associated to the viscous interaction with the tube

$$\mathcal{D}_c = \int_{\Gamma_t} \frac{\mu_c V'(r)}{2} v_x^2 dS. \tag{13.10}$$

In confinement, the cell cortex self-polarizes and generates a gradient of active tension that drives the movement of the cell [24]. In a minimal model of polarization, we introduce a space-dependent activity

$$\delta\xi = \xi_0 \left(\frac{1}{2} + \frac{x - x_{cell}}{L}\right), \tag{13.11}$$

where $L$ is the total length of the confined cell along $x$ and $\boldsymbol{x}_{\text{cell}}$ is the geometric center of the cell. This gradient of activity will induce a directed cortical flow sustained by a net depolymerization in the contracting end and a net polimerization in the expanding end. Thanks to the frictional interaction with the wall, this flow will produce a propulsive force and cell motion along the tube. However, the cell motion will necessarily displace the fluid in the capillary, producing a hydrodynamic drag. The balance between the propulsive force and the drag force will set the cell velocity. The problem is subtle because the cortical flow itself will depend on the cell velocity. The effect of the fluid in the capillary can be introduced with a dissipation potential of the form

$$\mathcal{D}_d = \frac{\mu_d}{2} ||\boldsymbol{v}_{\text{cell}}||^2, \tag{13.12}$$

where $\boldsymbol{v}_{\text{cell}} = \dot{\boldsymbol{x}}_{\text{cell}}$ and $\mu_d$ can be computed from elementary hydrodynamics and involves the tube length. Following [24], we choose $\mu_d = 200$ kPa·s·m$^{-1}$. As we show in Fig. 13.4B, the net velocity of the cell (proportional to the drag hydrodynamic force $\boldsymbol{F}_d = -\mu_d \boldsymbol{v}_{\text{cell}}$ and hence to the frictional propulsive force by mechanical equilibrium on the cell) significantly depends on the viscous

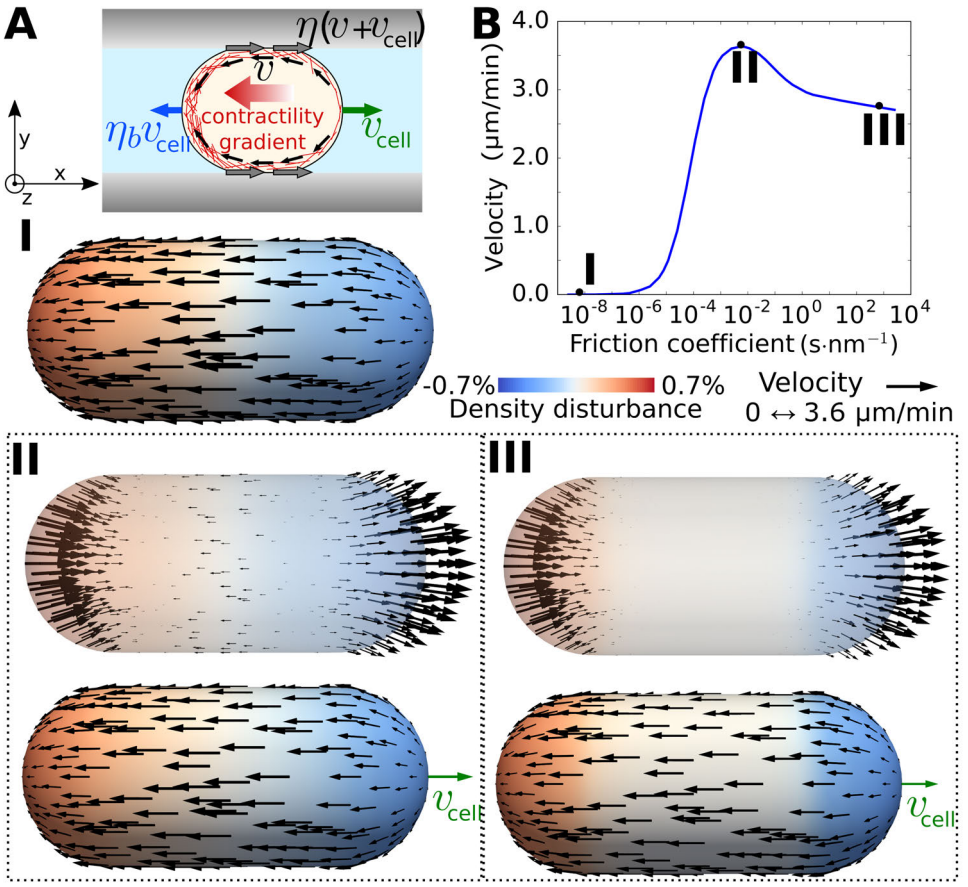


**Figure 13.4**: Actin flows regulate the migration of cells through non-specific adhesion. (A) Scheme of the system. (B) Net velocity of the cell as a function of the friction coefficient. (I-III) illustrate the density and velocity profiles of the cortex. In (I), there is no net velocity of the cell (velocity is tangent to the surface). In (II) and (III) the net velocities are not tangent to the cell surface and generate a constant contraction of the rear and expansion of the cell front (upper figures). To examine the velocity profile in detail for these cases (lower figures), we decompose the velocity into the velocity of the cell (green) and the relative velocity of the cortex with respect to the center.

interaction with the tube. For $\mu_c < 10^{-5}$ s·nm$^{-1}$, the polarization of the cell leads to a gradient of density and to a steady actin flow, which, however, does

not generate significant frictional forces with the wall and therefore is not affected by those forces. Accordingly, this cortical flow does not create a net movement of the cell (Fig. 13.4I). For $\mu_c > 10^{-5}$ s·nm$^{-1}$, the actin flow generated by the activity gradient generates a significantly larger propulsive frictional force to proper the cell forward. The sliding velocity with the wall becomes smaller as $\mu_c$ increases, but the frictional propulsive force increases up to a point ($\mu \sim 10^{-2}$ s·nm$^{-1}$, II). Beyond this point, the velocity of the adhered zone becomes very small, and the density nearly uniform in the contact region, and the cell velocity (or propulsing force) slightly decreases. The rate of turnover controls the ability of the system to sustain density gradients, and hence the steady state. The same behavior of the net velocity with respect to the friction coefficient was found in experimentally in [24], where it was explained with a simple model similar in spirit to ours. Thus, our modeling framework is able to reproduce cell migration through non-specific adhesion, which emerges in the presence of polarization as the interplay between shape changes leading to the contraction of the rear and expansion and the front of the cell, actin flows, and actin turnover, and the frictional interaction with the confining surface.

# Chapter 14

# Discussion and future work

We have developed a novel theoretical and computational framework to model and simulate the fully non-linear and three-dimensional dynamics of lipid membranes and other fluid surfaces, such as the cell cortex. More precisely,

- We have introduced a three-dimensional and non-linear formulation of the mechanics of lipid bilayers, generalizing the model by Seifert and Langer [160]. We have developed this formulation based on (1) Onsager's variational principle, a framework for modeling the dynamical behavior of dissipative systems, and (2) the differential geometry of fluid deformable surfaces.

- We have exercised the previous model in three-dimensional simulations, discretizing a system coupling an elliptic PDE for balance of linear momentum and a hyperbolic PDE for balance of mass. For the time-discretization, we have developed a novel variational time-integrator based on the discretization of Onsager's variational principle. Our spatial discretization is based on a combination of subdivision and linear finite elements, which allows us to account for the coupling between curvature and lipid flows.

- We have applied the previous theoretical and computational framework to another instance of fluid surface in the cell, the cortex. Our model is based on a viscous isotropic view of the cortex, which is able to reproduce a number of rheological experiments and could be employed to infer material parameters in conjunction with experiments.

Our formulation also sets the basis of future lines of work:

- The proposed framework opens new possibilities in the study of shape pattern formation under dynamical changes in lateral strain or osmotic conditions in supported membranes [172] beyond axisymmetry, relevant to cell membrane mechano-adaptation [84].
- Our method could also be useful to understand the effective rheology of a bilayer populated by transmembrane proteins, limiting inter-monolayer slippage in a heterogeneous manner, which could explain the unexpected and highly viscous behavior of complex biomembranes [29], or coupled to additional fields describing the concentration of membrane proteins to understand the dynamics of curvature sensing and generation (see [13, 19] and references therein).
- While interfacial hydrodynamics are dominant at length-scales smaller than the Saffman-Delbrück length, the bulk hydrodynamics may be a relevant ingredient in processes involving larger scales. Including the bulk hydrodynamics is straightforward conceptually, but requires specialized computational methods.
- While our model for the cortex can reproduce a number of rheological experiments, it is insufficient to reproduce phenomena where the transient elastic behavior of the cortex becomes important, such as in laser ablation [153], or situations in which the orientational order of actin filaments becomes relevant [147]. Furthermore, a more detailed mechano-chemical model of activity, the explicit treatment of the cytosol, and models capable of spontaneously producing polarization would provide a more complete understanding of the mechanics of the cortex.

- Finally, our models could allow us to investigate the complex interplay between the plasma membrane and the cortex/cytoskeleton.

In summary, our theoretical and computational framework provides a solid footing for the three-dimensional non-linear modeling and simulation of different processes involving lipid bilayers and the cell cortex.

# Appendix A

# Implementation of local stress calculations

## A.1 IKN stress

Here, we implement the IKN stress (GLD, CFD and cCFD) following Eqs. (3.6) and (3.7) . We discretize the simulation volume into a three-dimensional rectangular grid of cell size $\left(a_x, a_y, a_z\right)$, and compute the stress tensor in each node of the grid $\boldsymbol{x}_{(i,j,k)}$. To collect data at grid points we use trilinear weight functions of the form

$$w\left(\boldsymbol{y}, \boldsymbol{x}_{(i,j,k)}\right) = \begin{cases} \prod_I \frac{1}{a_I}\left(1 - \frac{\left|(\boldsymbol{y} - \boldsymbol{x}_{(i,j,k)})_I\right|}{a_I}\right) & \text{when } \left|(\boldsymbol{y} - \boldsymbol{x}_{(i,j,k)})_I\right| < a_I, \\ & I = x, y, z \\ 0 & \text{otherwise,} \end{cases} \tag{A.1}$$

which are centered at each $\boldsymbol{x}_{(i,j,k)}$ and whose support is given by the eight grid cells adjacent to it (see Fig. A.1 for an illustration in 2D). Then, the stress at a grid point is

$$\boldsymbol{\sigma}_{(i,j,k)} = \int_\Omega \boldsymbol{\sigma}(\boldsymbol{y}) w\left(\boldsymbol{y}, \boldsymbol{x}_{(i,j,k)}\right) d\boldsymbol{y} \tag{A.2}$$

This corresponds to a spatial filter aimed at collecting data at grid points but not mollifying the pointwise fields, in contrast with Eq. (B1). Common implementations of the IKN stress in MD simulations use constant weights within each cell [117, 201, 62], resulting in noisier and discontinuous stress fields at the edges of the cells. Broader and smoother weight functions such as higher order B-splines or long-range mollifying functions [110, 178] produce smoother stress fields, but can excessively smear local features and increase the computational cost. This issue is not minor, since the computational time required to calculate the local stress can be comparable to the time to simulate the system. We also note that the smaller the grid cells are, the longer the MD simulations need to be to adequately sample each local cell. In our experience, the trilinear weighting functions provide a good compromise of smoothness and efficiency. The weighted bond function $B_w\left(\boldsymbol{r}_i^\alpha, \boldsymbol{r}_i^\beta, \boldsymbol{x}_{(i,j,k)}\right)$ can be easily calculated analytically by integrating $w\left(\boldsymbol{x}_{(i,j,k)}; \boldsymbol{y}\right)$ along the interaction lines crossing the grid cell:

$$\begin{aligned} B_w\left(\boldsymbol{r}_i^\alpha, \boldsymbol{r}_i^\beta; \boldsymbol{x}_{(i,j,k)}\right) &= \int_\Omega w\left(\boldsymbol{y}, \boldsymbol{x}_{(i,j,k)}\right) B(\boldsymbol{r}^\alpha, \boldsymbol{r}^\beta; \boldsymbol{x}) d\boldsymbol{y} \\ &= \int_0^1 w\left[(1-s)\boldsymbol{r}^\alpha + s\boldsymbol{r}^\beta - \boldsymbol{x}; \boldsymbol{x}_{(i,j,k)}\right] ds, \end{aligned} \tag{A.3}$$

In addition to the spatial averaging, we must also decompose the forces resulting from multibody interactions, such as angle and dihedral potentials. For the GLD, Eq. (3.13) can be applied directly from the particle forces $\boldsymbol{F}^\alpha$ that the MD package provides. For the CFD, we solve the overdetermined system of equations Eq. (5.48) for each of the terms of the cluster expansion of the potential. Numerically, the system of equations can be solved by generic linear algebra algorithms, such as Gaussian elimination with partial pivoting, or by noting the special form of the equations as implemented in our code [190]. For underdetermined systems, such as those appearing for 5-body potentials for the CFD, we employ the DGELSD solver of LAPACK [7] based on the SVD decomposition that finds the solution with minimum norm. To compute the

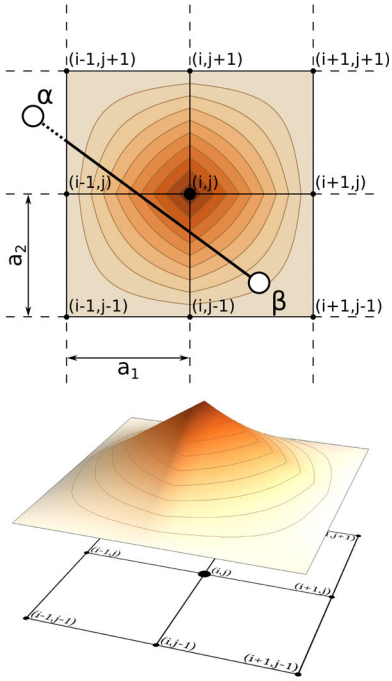


**Figure A.1**: Space discretization into a grid. The pointwise stress tensor is spatially averaged and distributed into regularly spaced grid points with a trilinear weighting function supported on the adjacent cells. The contour plot illustrates the weighting function in 2D. The contribution to the stress tensor at the grid point $(i, j)$ for two interacting particles $\alpha$ and $\beta$ is weighted by the bond function, $B\left(\boldsymbol{x}_{(i,j)}; \boldsymbol{r}_\alpha, \boldsymbol{r}_\beta\right)$, which is the integral of the weight function, $w\left(\boldsymbol{x}_{(i,j)}, \boldsymbol{y}\right)$, along the line segment connecting $\alpha$ and $\beta$. Because of the support of $w\left(\boldsymbol{x}_{(i,j)}, \boldsymbol{y}\right)$, only the solid part of the segment contributes to $B\left(\boldsymbol{x}_{(i,j)}; \boldsymbol{r}_\alpha, \boldsymbol{r}_\beta\right)$.

cCFD for 5-body interactions we apply Eq. (5.56) using the result from the previous solver.

It is worth noting that the SETTLE algorithm aggregates three bond constraints for a water molecule, and outputs the sum of the three constraint forces on each particle, but not the individual Lagrange multipliers. It is easy

to recover the three Lagrange multipliers [108], for instance performing a CFD on the SETTLE forces as if it was a three-body potential. We adopt this method to identify the Lagrange multipliers of SETTLE constraints both for CFD and GLD, and then follow the standard treatment of constraints described in the section 3.3.

Periodic boundary conditions are handled by considering always the closest periodic image of two interacting particles.

## A.2 Virial stress per atom

The virial stress per atom is computed from Eqs. (2.20) and (2.21) from the velocities and forces obtained directly from the MD package and assigned to each particle individually. To compute the volume of each particle, we use a Voronoi tessellation at the average configuration of the ensemble, similar to what it is proposed in [35].

# Appendix B

# MD simulations: Simulated systems and analysis

All simulations were conducted with the GROMACS 4.5.5 simulation package [74, 136] at the Barcelona Supercomputing Center.

## B.1 Graphene

The graphene sheet with the Stone-Wales defect was simulated with a Morse-potential modified version of the OPLS-AA FF [36] for 500 ns of data collection where the positions and velocities were stored every 5 ps. The system was simulated in the NVT ensemble and temperature was held at 300 K with a Nosé-Hoover thermostat. The infinitely periodic (in $x$ and $y$ directions) sheet contains 1500 atoms and was simulated in a box of size [6.369 nm, 6.131 nm, 3.0 nm]. Lennard-Jones forces were calculated with a plain cut-off of 1.0 nm, and all carbon atoms were uncharged.

## B.2 Lipid bilayers

Coarse-grained simulations were performed with the unmodified MARTINI [98, 99] force-field (FF) and a recently developed FF known as BMW-MARTINI [196], based on MARTINI and reparametrized for usage with the big multipole water (BMW) model [195]. All coarse-grained simulations are composed of 200 POPE lipids (1-palmitoyl-2-oleoyl-sn-glycero-3-phosphoethanolamine) and 3000 coarse-grained water molecules (equivalent to 12000 atomistic waters). Pressure was semi-isotropically coupled with a Parrinello-Rahman barostat [128] at 1 atm, and the temperature was held constant at 37 °C with a Nosé-Hoover thermostat [46]. MARTINI simulations were performed with a switched Lennard-Jones potential (the switch function is applied at a radius of 0.9 nm and the potential is zero at a radius of 1.2 nm), and a shifted Coulombic potential (cut-off radius of 1.2 nm) with a relative dielectric constant $\epsilon_r = 15$ for explicit screening. The integration time step for this model is 40 fs. The Lennard-Jones interactions for BMW-MARTINI systems were calculated in the same way as MARTINI, except for water-water interactions, where the switch function is applied at a radius of 1.2 nm and the potential is zero at a radius of 1.4 nm. Electrostatic interactions for this model were calculated using a reaction-field treatment [180] with a cut-off radius of 1.4 nm and a dielectric constant $\epsilon_{rf} = 74$. In BMW-MARTINI simulations, the time step was 2 fs for flexible water and 20 fs for rigid water.

Atomistic bilayers were simulated with the Gromos 43A1-S3 [32] FF. For simulations with the G43A1-S3 FF, Lennard-Jones forces where calculated using a twin-range cut-off scheme with interactions within 1.0 nm calculated at every time step and interactions between 1.0 and 1.6 nm only updated every 5 time steps. Long-range electrostatic interactions were computed using the particle-mesh Ewald (PME) method with a real-space cut-off of 1.0 nm and a Fourier grid spacing of 0.15 nm. Pressure was semi-isotropically coupled with a Parrinello-Rahman barostat at 1 atm, and the temperature was held constant at 37 °C for both POPE and POPC (1-palmitoyl-2-oleoyl-sn-glycero-3-phosphocholine), and at 50 °C for DPPC (1,2-dipalmitoyl-sn-glycero-

3-phosphocholine) with a Nosé-Hoover thermostat. All atomistic systems are composed of 200 lipids and 12000 water molecules (SPC/E [22]). The integration time step for the atomistic simulations was 2 fs.

All simulated systems were run for a 400 ns equilibration period, followed by a 100 ns data collection period where the positions and velocities were stored every 5 ps. The analysis for atomistic systems simulated with the PME method was carried out only considering Coulomb forces up to a cut-off radius of 2.2 nm. The accuracy of this common treatment is examined in [191].

## B.3 Coiled-coil

A synthetic coiled-coil protein was constructed from two identical parallel alpha-helices each with the amino-acid sequence $(IEALKAE)_{14}$. The protein was simulated as an infinitely long periodic molecule with a pitch of -3.673° per residue, so that the beginning and end residues of each chain would interact seamlessly across the periodic boundary. The positions of the backbone atoms were generated using the CCCP server [60, 61] and the sidechain positions were subsequently added with the molecular visualization package UCSF Chimera [132]. The amino-acid sequence was selected as it has been experimentally shown to be very stable even for short chains [176]. The protein was simulated with the CHARMM22/CMAP force field [95, 96]. Lennard-Jones forces where calculated using a cut-off scheme with a switching function between 1.0 nm and 1.2 nm. Long-range electrostatic interactions were computed using the particle-mesh Ewald (PME) method with a real-space cut-off of 1.2 nm and a Fourier grid spacing of 0.12 nm. Temperature was held constant at 298 K with a Nosé-Hoover thermostat. The system was composed of 196 protein residues (3,080 atoms) with 8,703 TIP3P [79] water molecules (26,109 atoms) and 28 $Na^+$ ions to neutralize the protein charge. Two alpha carbons of each protein chain were harmonically restrained with a force constant of 500 kJ/mol·nm$^2$ in order to prevent rotation of the molecule. The system was simulated under constant volume conditions, with the box size ([14.423 nm, 4.488 nm, 4.488 nm]) adjusted to produce global pressures close to 1 atm. The hydrated

protein system was first pre-equilibrated with harmonic position restraints on the protein backbone atoms for 250 ps. After the short pre-equilibration, the system was simulated for 300 ns where the first 100 ns were used for equilibration and the remaining 200 ns for data collection (storing position and velocities every 5 ps). The stress fields (cCFD, nCFD, and GLD) for the coiled-coil protein were calculated over the simulation period from 100 to 300 ns using a coulomb cut-off radius of 2.2 nm and a grid spacing of 0.1 nm. The computed stress fields were processed with a Gaussian filter (standard deviation of 0.8 nm) to remove high frequency fluctuations. The surface of the protein used to compute the traction was obtained as an iso-contour of the mass-density of the protein (also processed with a Gaussian filter with a standard deviation of 0.4 nm). Visualization of the traction was performed with the program ParaView.

# Appendix C

# Stress and traction for different mixtures of DPPC enantiomers

**Figure C.1**: Effect of chirality in the IKN-CFD stress and IKN-GLD stress. (A) IKN-CFD and IKN-GLD stresses for a bilayer composed of a monolayer of L-DPPC lipids and a monolayer of D-DPPC lipids (see inset on the left). While the IKN-CFD stress is diagonal, the IKN-GLD off-diagonal stress profiles are opposite to those in the membrane composed of two monolayers of L-DPPC lipids for the lower monolayer (see Fig. S3). (B) IKN-CFD and IKN-GLD stresses for a bilayer composed of a two monolayer with homogeneous mixture of L-DPPC lipids and D-DPPC lipids. The IKN-CFD stress remains diagonal regardless of the chirality of the lipids. In B, the IKN-GLD stress is also diagonal. From all these calculations we conclude that the torque densities generated in the IKN-GLD stresses stem from the internal chirality of the lipids.

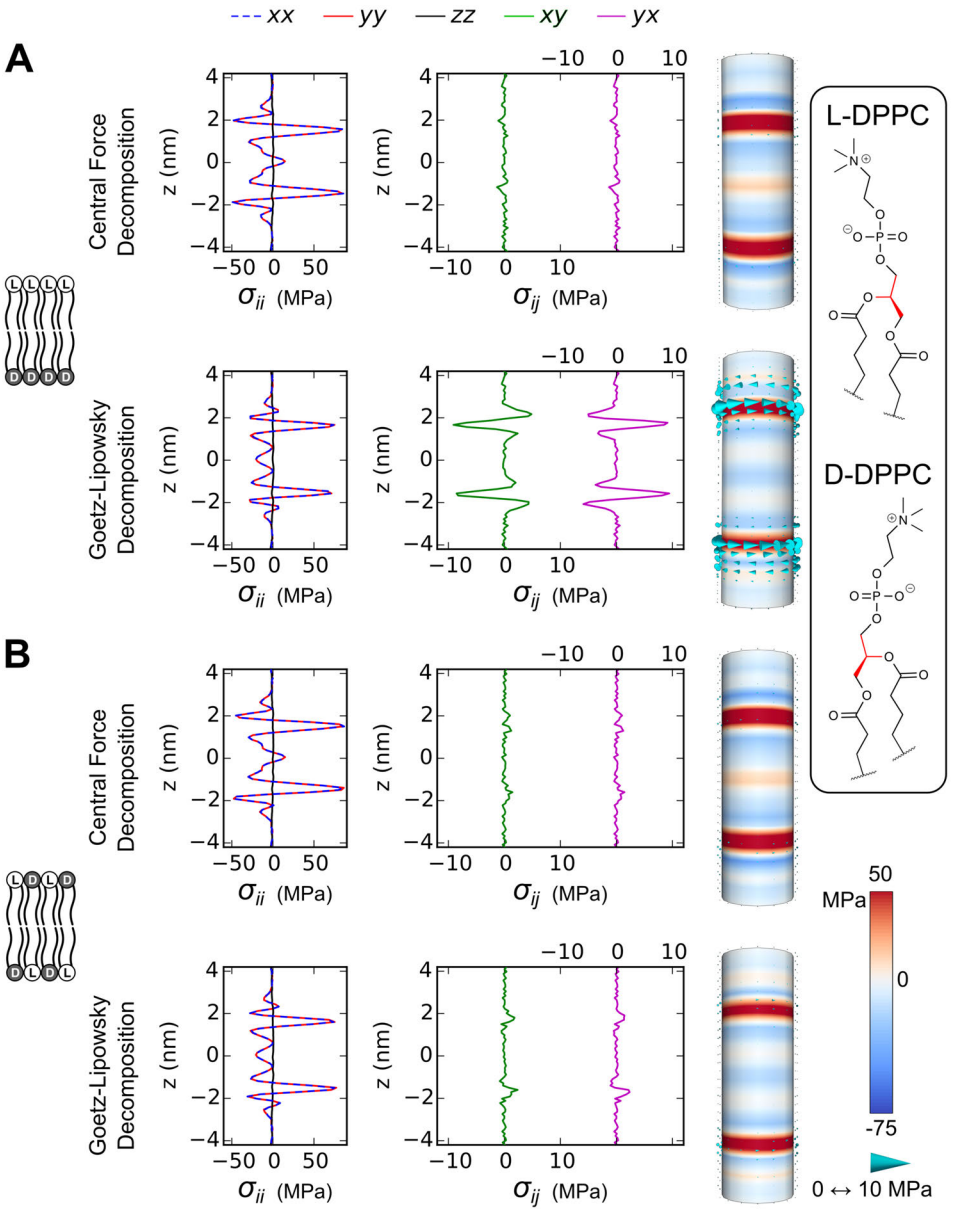
xx
yy
zz
xy
yx
A
Central Force Decomposition
Goetz-Lipowsky Decomposition
z (nm)
σii (MPa)
σij (MPa)
L-DPPC
D-DPPC
B
50
MPa
0
-75
0 ↔ 10 MPa

# Appendix D

# Differential geometry of surfaces

## D.1 Parametrization of the surface

In $\mathbb{R}^3$ we consider the cartesian coordinates $x_1, x_2, x_3$ and the orthonormal basis $\{\boldsymbol{i}_1, \boldsymbol{i}_2, \boldsymbol{i}_3\}$. We say that a subset $\Gamma \subset \mathbb{R}^3$ is a (regular) surface if for each $\boldsymbol{x} = (x_1, x_2, x_3) \in \Gamma$, there exists a neighborhood $V \in \mathbb{R}^3$ of $\boldsymbol{x}$ and a map, called a chart or parametrization, $\boldsymbol{\phi} = (\phi^1, \phi^2, \phi^3) : \bar{\Gamma} \to V \cap \Gamma$ with $\bar{\Gamma} \subset \mathbb{R}^2$ such that (i) $\boldsymbol{\phi}$ is a differentiable homeomorphism, i.e. a differentiable function with continuous inverse, and (ii) the differential of $\boldsymbol{\phi}$, $D\boldsymbol{\phi} : \mathbb{R}^2 \to \mathbb{R}^3$, has rank two everywhere. We consider in $\bar{\Gamma}$ a cartesian coordinate system characterized by coordinates $\bar{\xi}_1$ and $\bar{\xi}_2$ and the orthonormal basis $\left\{\bar{\boldsymbol{i}}_1, \bar{\boldsymbol{i}}_2\right\}$. In these coordinates, $D\boldsymbol{\phi}$ is represented by the matrix

$$D\boldsymbol{\phi} = \begin{pmatrix} \partial_1\phi^1 & \partial_2\phi^1 \\ \partial_1\phi^2 & \partial_2\phi^2 \\ \partial_1\phi^3 & \partial_2\phi^3 \end{pmatrix} \tag{D.1}$$

where $\partial_a \equiv \frac{\partial}{\partial \bar{\xi}_a}$. In components we write $D\boldsymbol{\phi}^\alpha{}_a = \partial_a \phi^\alpha$, where we use latin letters for indices running from 1 to 2 and greek letters for indices running

from 1 to 3. The parametrization $\phi$ is local, in the sense that it may not cover the entire surface, $V \cap \Gamma \neq \Gamma$, so that various parametrizations are required to describe $\Gamma$. A set of parametrizations describing a surface that are compatible with each other is called an atlas of charts of the surface.

## D.2 Tensor fields on a surface

A curve $\bar{\gamma} : \mathbb{R} \ni u \mapsto \bar{\boldsymbol{\xi}} \in \bar{\Gamma}$ in parametric space, with velocity $\frac{d\bar{\gamma}}{du}\Big|_{u=0} = v^a \boldsymbol{i}_a$, maps onto a curve $\gamma$ on $\Gamma$ by composition with $\phi$, $\gamma \equiv \phi \circ \bar{\gamma}$. The velocity of this curve

$$\boldsymbol{v}(u) = \left.\frac{d\boldsymbol{\gamma}}{du}\right|_{u=0} = [D\boldsymbol{\phi} \circ \bar{\gamma}] \left.\frac{d\bar{\boldsymbol{\gamma}}}{du}\right|_{u=0} = [\partial_a \boldsymbol{\phi} \circ \bar{\gamma}]\, v^a, \tag{D.2}$$

is a tangent vector to $\Gamma$ at the point $\boldsymbol{x} = \boldsymbol{\gamma}(0)$. The set of tangent vectors passing through a point $\boldsymbol{x} \in \Gamma$ forms the tangent space to $\Gamma$ at $\boldsymbol{x}$, denoted by $T_{\boldsymbol{x}}\Gamma$. A basis in $T_{\boldsymbol{x}}\Gamma$ is given by the pair of vectors

$$\boldsymbol{e}_a(\boldsymbol{x}) = \partial_a \boldsymbol{\phi} \circ \boldsymbol{\phi}^{-1}(\boldsymbol{x}), \tag{D.3}$$

which are tangent to the curves $\xi_a = \bar{\xi}_a \circ \boldsymbol{\phi}^{-1}$ and form a basis due to the regularity condition (ii), the so-called convected basis by $\boldsymbol{\phi}$. The velocity of $\boldsymbol{\gamma}(t)$ in this basis is $\boldsymbol{v} = v^a \boldsymbol{e}_a$; thus, the components of $\frac{d\boldsymbol{\gamma}}{dt}$ in $\boldsymbol{e}_a$ are equal to those of $\frac{d\bar{\gamma}}{dt}$ in $\boldsymbol{i}_a$. We now define the action of a vector $\boldsymbol{v} \in T_{\boldsymbol{x}}\Gamma$ on a scalar function $f \in \Gamma$, which computes the rate of change of $f$ along any curve $\boldsymbol{\gamma}(t)$ with tangent vector $\boldsymbol{v}$ at $\boldsymbol{x}$,

$$\boldsymbol{v}[f] \equiv \left.\frac{df(\boldsymbol{\gamma}(t))}{dt}\right|_{t=0} = \left.\frac{d\bar{f}(\bar{\gamma}(t))}{dt}\right|_{t=0} = \partial_a \bar{f} v^a = \partial_a f v^a, \tag{D.4}$$

where $\bar{f} = f \circ \boldsymbol{\phi}$, and we have defined $\partial_a f \equiv \partial_a \bar{f}$ for notational simplicity. The definition is independent of the choice of $\boldsymbol{\gamma}(t)$. We define the dual space to $T_{\boldsymbol{x}}\Gamma$ as the space of linear functionals, acting on tangent vectors, which we denote by $T^*_{\boldsymbol{x}}\Gamma$. Linear functionals are also called 1-forms or covectors. Given a scalar field $f : \Gamma \to \mathbb{R}$, we define an associated 1-form at $\boldsymbol{x}$, the differential of

$f$, $\boldsymbol{d}f$, through its action on the vectors $\boldsymbol{v} \in T_{\boldsymbol{x}}\Gamma$ as

$$\boldsymbol{d}f(\boldsymbol{v}) \equiv \boldsymbol{v}[f]. \tag{D.5}$$

A basis for $T^*_{\boldsymbol{x}}\Gamma$ is then given by the pair of forms

$$\boldsymbol{e}^a = \boldsymbol{d}\xi_a, \tag{D.6}$$

$a = 1, 2$, which satisfy the relation

$$\boldsymbol{e}^a(\boldsymbol{e}_b) = \delta^a{}_b. \tag{D.7}$$

Given a 1-form $\boldsymbol{\alpha}$ we write $\boldsymbol{\alpha} = \alpha_a \boldsymbol{e}^a$, with $\alpha_a$ are the components of $\boldsymbol{\alpha}$ in the basis $\left\{\boldsymbol{e}^1, \boldsymbol{e}^2\right\}$. In particular, $\boldsymbol{d}f = \partial_a f \boldsymbol{e}^a$. In general a $m$-contravariant $n$-covariant tensor, or $(m, n)$-tensor in short, is given by $\boldsymbol{T} = T^{a_1 \ldots a_m}{}_{b_1 \ldots b_n} \boldsymbol{e}_{a_1} \otimes \cdots \otimes \boldsymbol{e}_{a_m} \otimes \boldsymbol{e}^{b_1} \otimes \cdots \otimes \boldsymbol{e}^{b_n}$ and belongs to the product space $T^{(m,n)}_{\boldsymbol{x}}\Gamma = (T_{\boldsymbol{x}}\Gamma)^m \otimes (T_{\boldsymbol{x}}\Gamma)^n$. Upper indices indicate contravariant components whereas lower indices indicate covariant components. We define the $m$-tangent $n$-cotangent bundle as the union of all $m$-tangent $n$-cotangent spaces on the surface, $T^{(m,n)}\Gamma = \cup_{\boldsymbol{x}\in\Gamma} T^{(m,n)}_{\boldsymbol{x}}\Gamma$. A $(m, n)$-tensor field is a mapping $\boldsymbol{T} : \boldsymbol{x} \in \Gamma \to (\boldsymbol{x}, \boldsymbol{T}) \in (T\Gamma)^m \otimes (T\Gamma)^n$ that assigns a $(m, n)$-tensor to every point $\boldsymbol{x} \in \Gamma$. In the next section we introduce two important 2-covariant tensor fields on $\Gamma$, the first and second fundamental forms.

## D.3 Push-forward and pull-back

Although the push-forward and the pull-back operations are defined for maps between general manifolds, here we focus on the push-forward and the pull-back defined by the parametrization $\boldsymbol{\phi}$, which is a map between $\bar{\Gamma}$ and $\Gamma$. The push-forward is a linear operation that takes a tensor $\bar{\boldsymbol{t}}$ in $\bar{\Gamma}$ and transforms it onto a tensor $\boldsymbol{t} = \boldsymbol{\phi}_* \bar{\boldsymbol{t}}$ on $\Gamma$. For a scalar, it is simply defined as the composition

$$f = \boldsymbol{\phi}_* \bar{f} = \bar{f} \circ \boldsymbol{\phi}^{-1}. \tag{D.8}$$

For a vector $\bar{\boldsymbol{v}}$, $\boldsymbol{\phi}_*\bar{\boldsymbol{v}}$ is defined so that $\bar{\boldsymbol{v}}[\bar{f}]$ coincides with $(\boldsymbol{\phi}_*\bar{\boldsymbol{v}})\left[\boldsymbol{\phi}_*\bar{f}\right]$ for all $\bar{f}$, which leads to

$$\boldsymbol{v} = \boldsymbol{\phi}_*\bar{\boldsymbol{v}} = (D\boldsymbol{\phi}\,\bar{\boldsymbol{v}}) \circ \boldsymbol{\phi}^{-1}, \tag{D.9}$$

Similarly, for a 1-form $\bar{\boldsymbol{\alpha}}$, $\boldsymbol{\phi}_*\bar{\boldsymbol{\alpha}}$ is defined so that $\bar{\boldsymbol{\alpha}}[\bar{\boldsymbol{v}}]$ coincides with $(\boldsymbol{\phi}_*\bar{\boldsymbol{\alpha}})[\boldsymbol{\phi}_*\bar{\boldsymbol{v}}]$ for all $\bar{\boldsymbol{v}}$, which leads to

$$\boldsymbol{\alpha} = \boldsymbol{\phi}_*\bar{\boldsymbol{\alpha}} = \left(D\boldsymbol{\phi}^{-1}\,\bar{\boldsymbol{v}}\right) \circ \boldsymbol{\phi}^{-1}. \tag{D.10}$$

For a general $(m, n)$-tensor, we apply Eq. (D.9) to all contravariant components and Eq. (D.10) to all covariant components. On the other hand, the pull-back is a linear operation that takes a tensor $\boldsymbol{t}$ in $\Gamma$ and transforms it onto a tensor $\bar{\boldsymbol{t}} = \boldsymbol{\phi}^*\boldsymbol{t}$ on $\bar{\Gamma}$. Following the same line of thought as for the push-forward, we find

$$\bar{f} = \boldsymbol{\phi}^* f = f \circ \boldsymbol{\phi}, \tag{D.11}$$

$$\bar{\boldsymbol{v}} = \boldsymbol{\phi}^*\boldsymbol{v} = \left(D\boldsymbol{\phi}^{-1}\,\bar{\boldsymbol{v}}\right) \circ \boldsymbol{\phi}, \tag{D.12}$$

$$\bar{\boldsymbol{\alpha}} = \boldsymbol{\phi}^*\boldsymbol{\alpha} = (D\boldsymbol{\phi}\,\bar{\boldsymbol{v}}) \circ \boldsymbol{\phi}, \tag{D.13}$$

and for a general $(m, n)$-tensor, we apply Eq. (D.12) to all contravariant components and Eq. (D.13) to all covariant components. It is clear that the pull-back is the inverse of the push-forward (and vice versa),

$$\boldsymbol{\phi}^*\boldsymbol{\phi}_*\bar{\boldsymbol{t}} = \bar{\boldsymbol{t}}, \qquad \boldsymbol{\phi}_*\boldsymbol{\phi}^*\boldsymbol{t} = \boldsymbol{t}. \tag{D.14}$$

Finally, the components of a tensor on $\bar{\Gamma}$ and those of its push-forward on $\Gamma$ in the convected basis by $\boldsymbol{\phi}$ are the same. Equivalently, the components of a tensor on the convected basis on $\Gamma$ are the same that its pull-back.

## D.4 First and second fundamental forms, and the antisymmetric tensor

The inner product in $\mathbb{R}^3$, given by $\langle \boldsymbol{v}, \boldsymbol{w} \rangle = v^\alpha \delta_{\alpha\beta} v^\beta$ with $\delta_{\alpha\beta}$ the Kronecker delta, induces a natural inner product on the tangent space of $\Gamma$. More precisely,

we define the metric tensor or first fundamental form on $\Gamma$ as the 2-covariant tensor that satisfies

$$\boldsymbol{g}(\boldsymbol{v}, \boldsymbol{w}) = \langle \boldsymbol{v}, \boldsymbol{w} \rangle \tag{D.15}$$

for all $\boldsymbol{v}, \boldsymbol{w} \in T_{\boldsymbol{x}}\Gamma$. In components, we find

$$g_{ab} = \left( (D\phi)^{\alpha}{}_{a} \circ \boldsymbol{\phi}^{-1} \right) \delta_{\alpha\beta} \left( (D\phi)^{\beta}{}_{b} \circ \boldsymbol{\phi}^{-1} \right) = \langle \boldsymbol{e}_a, \boldsymbol{e}_b \rangle. \tag{D.16}$$

The inverse of the metric tensor, $\boldsymbol{g}^{-1}$ has components $g^{ab}$, i.e. $g^{ac} g_{cb} = \delta^{a}{}_{b}$. From the definition of the metric components,

$$\boldsymbol{e}^a(\boldsymbol{e}_b) = \delta^a_b = g^{ac} g_{cb} = g^{ac}(\boldsymbol{e}_c \cdot \boldsymbol{e}_b), \tag{D.17}$$

we can define the relations between the basis of the tangent and cotangent spaces

$$\boldsymbol{e}^a = g^{ac} \boldsymbol{e}_c, \quad \boldsymbol{e}_a = g_{ac} \boldsymbol{e}^c. \tag{D.18}$$

Thus, the application of the metric tensor to a vector leads to a form, in what is called lowering the index. Equivalently, the application of the inverse of the metric tensor to a form leads to a vector, in what is called raising the index. For instance, lowering the index of a vector $\boldsymbol{v} = v^a \boldsymbol{e}_a$ leads to the 1-form $v_a \boldsymbol{e}^a = g_{ab} v^b \boldsymbol{e}^a$ and raising the index of a 1-form $\boldsymbol{\alpha} = \alpha_a \boldsymbol{e}^a$ leads to the vector $\alpha^a \boldsymbol{e}_a = g^{ab} \alpha_b \boldsymbol{e}_a$. We write $\boldsymbol{T}^\sharp$ or $\boldsymbol{T}^\flat$ to identify the tensor obtained by raising or lowering all indices of a tensor. Upper and lower indices can be contracted by letting covariant components act on contravariant components. For instance, we define the trace of a $(1,1)$-tensor $\boldsymbol{T}$ as

$$\mathrm{tr}\boldsymbol{T} = T^a{}_a. \tag{D.19}$$

We define the scalar product of vectors as

$$\boldsymbol{v} \cdot \boldsymbol{w} = \boldsymbol{v}^\flat(\boldsymbol{w}) = \boldsymbol{w}^\flat(\boldsymbol{v}) = v_a w^a = g_{ab} v^a w^b, \tag{D.20}$$

and the norm

$$||\boldsymbol{v}|| = \sqrt{\boldsymbol{v} \cdot \boldsymbol{v}} = \sqrt{g_{ab} v^a v^b}. \tag{D.21}$$

It is clear from the definition of $\boldsymbol{v} \cdot \boldsymbol{w}$ and $||\boldsymbol{v}||$ that the metric tensor contains the information required to compute lengths and angles on $\Gamma$. We also define the scalar product of covariant 2-tensors as

$$\boldsymbol{p} : \boldsymbol{q} = \boldsymbol{p}^\sharp(\boldsymbol{q}) = \boldsymbol{q}^\flat(\boldsymbol{p}) = p_{ab} q_{ab} = g^{ac} p_{cd} g^{db} q_{ab}, \tag{D.22}$$

and the norm

$$||\boldsymbol{p}|| = \sqrt{\boldsymbol{p} : \boldsymbol{p}} = \sqrt{g^{ac} p_{cd} g^{db} p_{ab}}. \tag{D.23}$$

The determinant of the metric is $g = \varepsilon^{ab} g_{a1} g_{b2}$, where the $\varepsilon^{ab}$ are the Levi-Civita symbols, and $d\Gamma = \sqrt{g}\boldsymbol{d}\xi_1 \boldsymbol{d}\xi_2$ is the volume form of the surface. It is important to note that the Levi-Civita symbols do not form a tensor and should not be confused with the Levi-Civita (or antisymmetric) tensor field

$$\epsilon^{ab} = \varepsilon^{ab} / \sqrt{g}. \tag{D.24}$$

For surfaces embedded in Euclidean space, the surface normal can be obtained from the basis vectors

$$\boldsymbol{n} = \frac{\boldsymbol{e}_1 \times \boldsymbol{e}_2}{||\boldsymbol{e}_1 \times \boldsymbol{e}_2||}. \tag{D.25}$$

The surface curvature or second fundamental form is a $(0, 2)$-tensor field given by

$$k_{ab} = -\langle \partial_a (\boldsymbol{n} \circ \boldsymbol{\phi}^{-1}) \circ \boldsymbol{\phi}, \boldsymbol{e}_b \rangle = \langle \boldsymbol{n}, \partial_a \partial_b \boldsymbol{\phi} \circ \boldsymbol{\phi}^{-1} \rangle. \tag{D.26}$$

These components measure how the normal changes along the curve $\xi_a$ in the direction of $\boldsymbol{e}_b$, which is zero if the surface is planar but differs from zero for curved surfaces. The mean and Gaussian curvatures are the scalar fields

$$H = \mathrm{tr}\boldsymbol{k}, \qquad K = \det \boldsymbol{k}, \tag{D.27}$$

where $\det \boldsymbol{k} = \varepsilon^a{}_b \kappa_a{}^1 \kappa^b{}_2$.

## D.5 Covariant differentiation

We are interested in computing derivatives of tensor fields along the curves of $\Gamma$. For scalars, this notion was already introduced by $\boldsymbol{d}f$, which we will

also call the covarariant derivative of $f$ and denote it by $\nabla f$. This is a 1-form that, when applied to vectors $\boldsymbol{v}$, it gives the directional derivative of $f$ along $\boldsymbol{v}$. For a general tensor, these derivatives will contain an intrinsic part tangent to $\Gamma$ and a normal part. The intrinsic part introduces the notion of covariant differentiation, which generalizes to manifolds the gradient of a tensor and introduces important results such as the divergence theorem. Here we introduce covariant derivatives as the projections onto $\Gamma$ of partial derivatives on the surface; for a systematic way of introducing covariant derivatives without the notion of embedding space see [100, 41]. Let us first consider how the basis vectors $\boldsymbol{e}_b$ change along the curves $\xi_a$

$$\partial_a \boldsymbol{e}_b = \partial_a \partial_b \boldsymbol{\phi} \circ \boldsymbol{\phi}^{-1}. \tag{D.28}$$

Since the right-hand side of the previous equation is a vector in Euclidean space, it can be expressed in terms of the basis of $\mathbb{R}^3$ formed by the two tangent vectors $\boldsymbol{e}_1$ and $\boldsymbol{e}_2$, and the normal to the surface $\boldsymbol{n}$

$$\partial_a \boldsymbol{e}_b = \Gamma^c{}_{ab} \boldsymbol{e}_c + k_{ab} \boldsymbol{n}. \tag{D.29}$$

where the curvature tensor appears naturally from Eq. (D.26). The symbols $\Gamma^c{}_{ab}$ are called the Christoffel symbols. We note that from commutation of partial derivatives, we have $\Gamma^c{}_{ab} = \Gamma^c{}_{ba}$. Furthermore, by computing partial derivatives of the components of the metric tensor, we obtain

$$\begin{aligned} \partial_a g_{bd} = \left\langle \partial_a \partial_b \boldsymbol{\phi} \circ \boldsymbol{\phi}^{-1}, \boldsymbol{e}_d \right\rangle + \left\langle \boldsymbol{e}_b, \partial_a \partial_d \boldsymbol{\phi} \circ \boldsymbol{\phi}^{-1} \right\rangle &= \Gamma^c{}_{ab} g_{cd} + \Gamma^c{}_{ad} g_{cb}, \\ \partial_b g_{ad} &= \Gamma^c{}_{ab} g_{cd} + \Gamma^c{}_{bd} g_{ca}, \\ \partial_d g_{ba} &= \Gamma^c{}_{db} g_{ca} + \Gamma^c{}_{ad} g_{cb}, \end{aligned} \tag{D.30}$$

This system can be solved by summing the first two equations and substracting the last, to get

$$\Gamma^c{}_{ab} = \frac{1}{2} g^{cd} \left[ g_{bd,a} + g_{ad,b} - g_{ba,d} \right]. \tag{D.31}$$

For a general vector $\boldsymbol{v}$, applying the linearity of the partial derivative we find

$$\partial_a \boldsymbol{v} = \partial_a v^b \boldsymbol{e}_b + v^b \partial_a \boldsymbol{e}_b = \partial_a v^b \boldsymbol{e}_b + \Gamma^c{}_{ab} v^b \boldsymbol{e}_c + \kappa_{ab} \boldsymbol{n}, \tag{D.32}$$

The operator defined by

$$\partial \boldsymbol{v} \equiv \partial_a \boldsymbol{v} \otimes \boldsymbol{e}^a, \tag{D.33}$$

can be applied to tangent vectors $\boldsymbol{u}$ to give the change of $\boldsymbol{v}$ along the direction of $\boldsymbol{u}$

$$\partial_{\boldsymbol{u}} \boldsymbol{v} = \partial \boldsymbol{v}(\boldsymbol{u}) = \partial_a v^b u^a \boldsymbol{e}_b + \Gamma^c{}_{ab} v^b u^a \boldsymbol{e}_c + \kappa_{ab} v^b u^a \boldsymbol{n}, \tag{D.34}$$

The projection of $\partial_{\boldsymbol{u}} \boldsymbol{v}$ onto $T\Gamma$ is a vector called the covariant derivative of $\boldsymbol{v}$ in the direction of $\boldsymbol{u}$,

$$\nabla_{\boldsymbol{u}} \boldsymbol{v} = \nabla_a \boldsymbol{v} u^a = \partial_a v^b u^a \boldsymbol{e}_b + \Gamma^c{}_{ab} \boldsymbol{e}_c v^b u^a. \tag{D.35}$$

and generalizes the concept of directional derivative to surfaces. In particular, for the basis vectors we have

$$\nabla_b \boldsymbol{e}_a = \Gamma^c{}_{ab} \boldsymbol{e}_c. \tag{D.36}$$

The $(1,1)$-tensor,

$$\nabla \boldsymbol{v} = \nabla_a \boldsymbol{v} \otimes \boldsymbol{e}^a = \left( \partial_a v^b \boldsymbol{e}_b + \Gamma^c{}_{ab} \boldsymbol{e}_c v^b \right) \otimes \boldsymbol{e}^a, \tag{D.37}$$

is called the covariant derivative of the vector $\boldsymbol{v}$, in components,

$$\nabla_b v^a = \partial_a v^b + \Gamma^c{}_{ab} v^b. \tag{D.38}$$

The action of the operator $\nabla$ can be extended to general tensors by noting that

$$\begin{aligned} \partial_a \left( \left\langle \boldsymbol{e}^b, \boldsymbol{e}_c \right\rangle \right) = 0 \Rightarrow \left\langle \partial_a \boldsymbol{e}^b, \boldsymbol{e}_c \right\rangle &= - \left\langle \boldsymbol{e}^b, \partial_a \boldsymbol{e}_c \right\rangle \\ &= - \left\langle \boldsymbol{e}^b, -\Gamma^d{}_{ac} \boldsymbol{e}_d + \kappa_{ac} \boldsymbol{n} \right\rangle = -\Gamma^a{}_{bc} \\ \Rightarrow \nabla_b \boldsymbol{e}^a &= -\Gamma^a{}_{bc} \boldsymbol{e}^c \end{aligned} \tag{D.39}$$

Thus, we define the covariant derivative of a $(m,n)$-tensor as

$$\begin{aligned} \nabla_c T^{a_1 \ldots a_m}{}_{b_1 \ldots b_n} &= \partial_c T^{a_1 \ldots a_m}{}_{b_1 \ldots b_n} + \\ &+ \Gamma^{a_1}{}_{cd} T^{d \ldots a_m}{}_{b_1 \ldots b_n} + (\text{all upper indices}) \\ &- \Gamma^d{}_{cb_1} T^{a_1 \ldots a_m}{}_{d \ldots b_n} - (\text{all lower indices}), \end{aligned} \tag{D.40}$$

which is a $(m, n+1)$-tensor. As particular instances of the action of the covariant derivative we define the divergence operator

$$\mathrm{div}\boldsymbol{T} = \mathrm{tr}\,(\nabla \boldsymbol{T})\,, \tag{D.41}$$

and the gradient operator

$$\mathbf{grad} f = (\nabla f)^\sharp = (\boldsymbol{d} f)^\sharp\,. \tag{D.42}$$

## D.6 Flows and Lie derivatives

We introduce here the concept of Lie derivative, which measures the rate of change of a tensor field $\boldsymbol{T}(\boldsymbol{x})$ along the flow generated by a vector field $\boldsymbol{u}(\boldsymbol{x})$. For simplicity, we start with the concept of Lie derivative of a vector field $\boldsymbol{v}(\boldsymbol{x})$ along another vector field $\boldsymbol{u}(\boldsymbol{x})$. Let us employ a physical picture; we consider $\Gamma$ as a continuous material and $\boldsymbol{u}$ as the generator of a deformation, or flow, on $\Gamma$. We interpret $\boldsymbol{v}$ as a measure system on $\Gamma$; when applied to a function $f$, $\boldsymbol{v}[f]$ measures the derivative of $f$ in the direction of $\boldsymbol{v}$. For simplicity, we consider that $\boldsymbol{u}$ and $\boldsymbol{v}$ are independent of time. The time evolution of material particles follow integral curves of $\boldsymbol{u}(\boldsymbol{x})$, which are defined as the curves $\chi_t(\boldsymbol{x}) : \mathbb{R} \to \Gamma$ that satisfy $\frac{d\chi_t(\boldsymbol{x})}{dt} = \boldsymbol{u} \circ \gamma$ for all $t$ and $\chi_0(\boldsymbol{x}) = \boldsymbol{x}$. The collection of integral curves defines the deformation mapping $\chi_t(\boldsymbol{x})$. Let us now consider a scalar field $f(\boldsymbol{x}, t)$, such as the density of material or the local temperature, that is advected with the flow. The evolution of $f$ is then given by $f(\boldsymbol{x}, t) = f(\chi_t^{-1}(\boldsymbol{x}), 0) = \chi_{t*} f_0(\boldsymbol{x})$, where $f_0(\boldsymbol{x}) = f(\boldsymbol{x}, 0)$. We consider the time-evolution of the action $\boldsymbol{v}[f]$ along an integral curve $\chi_t(\boldsymbol{x})$, $\boldsymbol{v}(\chi_t(\boldsymbol{x}))[f($ $bmxi_t(\boldsymbol{x}), t)]$, which is a function of $t$ only. The rate of change of this measure at $t = 0$ is

$$\begin{aligned} \frac{d}{dt}\boldsymbol{v}(\chi_t(\boldsymbol{x}))\,[f(\chi_t(\boldsymbol{x}), t)]\Big|_{t=0} &= \frac{d}{dt}\boldsymbol{v}(\chi_t(\boldsymbol{x}))\,[\chi_{t*} f_0(\chi_t(\boldsymbol{x}))]\Big|_{t=0} \\ &= \frac{d}{dt}\chi_t^* \boldsymbol{v}(\boldsymbol{x})\Big|_{t=0}\,[f_0(\boldsymbol{x})]\,. \end{aligned} \tag{D.43}$$

Thus, the rate of change of $\boldsymbol{v}$ when applied to scalar fields that follow the deformation is given by the quantity

$$L_{\boldsymbol{u}}(\boldsymbol{v}) \equiv \left.\frac{d}{dt}\chi_t^*\boldsymbol{v}\right|_{t=0}. \tag{D.44}$$

This is the Lie derivative of the vector field $\boldsymbol{v}$ along the vector field $\boldsymbol{u}$. This definition can be generalized to any tensor

$$L_{\boldsymbol{u}}(\boldsymbol{T}) \equiv \left.\frac{d}{dt}\chi_t^*\boldsymbol{T}\right|_{t=0}. \tag{D.45}$$

In words, the Lie derivative measures the rate of change of a tensor field $\boldsymbol{T}$ when applied to tensor fields that are advected with the deformation generated by $\boldsymbol{u}$. Among the properties of the Lie derivative are (i) $L_{\boldsymbol{u}}(\boldsymbol{T}_1 \otimes \boldsymbol{T}_2) = L_{\boldsymbol{u}}(\boldsymbol{T}_1)\otimes\boldsymbol{T}_2 + \boldsymbol{T}_1 \otimes L_{\boldsymbol{u}}(\boldsymbol{T}_2)$, (ii) $L_{\boldsymbol{u}+\boldsymbol{w}}(\boldsymbol{T}) = L_{\boldsymbol{u}}(\boldsymbol{T}) + L_{\boldsymbol{w}}(\boldsymbol{T})$, and (iii) $L_{\boldsymbol{u}}(\boldsymbol{u}) = \boldsymbol{0}$.

An important Lie derivative for continuum mechanics is the Lie derivative of the metric tensor. Let us consider two material curves, parametrized with their respective arc-lengths, $\alpha(s) : \mathbb{R} \to \Gamma$ and $\beta(s) : \mathbb{R} \to \Gamma$, that pass by $\boldsymbol{x}$ at $s = 0$. We examine the advection of these curves, $\alpha_t(s) = \chi_t \circ \alpha(s)$ and $\beta_t(s) = \chi_t \circ \alpha(s)$; let us note that $s$ is not the arc-length of the curves $\alpha_t(s)$ and $\beta_t(s)$ for $t > 0$ since they may be deformed along the flow. The angle between both curves along the integral curve of the flow $\chi_t(\boldsymbol{x})$ is given by the scalar product

$$\left.\frac{d\alpha_t(s)}{ds}\cdot\frac{d\beta_t(s)}{ds}\right|_{s=0} = \boldsymbol{g}(\chi_t(\boldsymbol{x}))\left(\frac{d\alpha_t(s)}{ds},\frac{d\beta_t(s)}{ds}\right)\Bigg|_{s=0}, \tag{D.46}$$

and the rate of change of the angle at $t = 0$ is given by

$$\begin{aligned}\left.\frac{d}{dt}\frac{d\alpha_t(s)}{ds}\cdot\frac{d\beta_t(s)}{ds}\right|_{s=0,t=0} &= \left.\frac{d}{dt}\boldsymbol{g}(\chi_t(\boldsymbol{x}))\left(\frac{d\alpha_t(s)}{ds},\frac{d\beta_t(s)}{ds}\right)\right|_{s=0,t=0}\\ &= \left.\frac{d}{dt}\chi_t^*(\boldsymbol{x})\boldsymbol{g}\right|_{t=0}\left(\frac{d\alpha(s)}{ds},\frac{d\beta(s)}{ds}\right)\Bigg|_{s=0}\\ &= L_{\boldsymbol{u}}\boldsymbol{g}\left(\frac{d\alpha(s)}{ds},\frac{d\beta(s)}{ds}\right)\Bigg|_{s=0}.\end{aligned} \tag{D.47}$$

Equivalently, the time derivative along the flow of the arc-length of either of the curves is given by

$$\frac{d}{dt}\frac{d\alpha_t(s)}{ds}\cdot\frac{d\alpha_t(s)}{ds}\bigg|_{s=0,t=0} = L_{\boldsymbol{u}}\boldsymbol{g}\left(\frac{d\alpha(s)}{ds},\frac{d\alpha(s)}{ds}\right)\bigg|_{s=0}. \tag{D.48}$$

Thus, $L_{\boldsymbol{u}}\boldsymbol{g}$ measures the rate at which the material is deforming. The rate-of-deformation tensor for the flow $\chi_t$ is then defined as

$$\boldsymbol{d} = \frac{1}{2}L_{\boldsymbol{u}}\boldsymbol{g}. \tag{D.49}$$

Let us note that the action of the Lie derivative on a general tensor $\boldsymbol{T}$ can be expressed in terms of covariant derivatives

$$\begin{aligned}[L_{\boldsymbol{u}}(\boldsymbol{T})]^{a_1\ldots a_m}{}_{b_1\ldots b_n} &= T^{a_1\ldots a_m}{}_{b_1\ldots b_n|c}\,u^c \\ &- T^{c\ldots a_m}{}_{b_1\ldots b_n}\,u^{a_1}{}_{|c} - (\text{all upper indices}) \\ &- T^{a_1\ldots a_m}{}_{c\ldots b_n}\,u^{c}{}_{|b_1} - (\text{all lower indices}).\end{aligned} \tag{D.50}$$

In particular, this leads to the expression

$$\boldsymbol{d} = \frac{1}{2}\left(u_{a|b} + u_{b|a}\right). \tag{D.51}$$

We finally note that, for scalars,

$$\boldsymbol{d}f(\boldsymbol{u}) = \nabla_{\boldsymbol{u}}f = L_{\boldsymbol{u}}f. \tag{D.52}$$

## D.7 Divergence theorem

Let us finally introduce without proof the divergence theorem for surfaces. Given a domain $\Gamma \subset \Gamma$, with contour $\partial\Gamma$, and a vector field $\boldsymbol{v}$ on $\Gamma$,

$$\int_\Gamma \mathrm{div}\boldsymbol{v}\; d\Gamma = \int_{\partial\Gamma}\boldsymbol{v}\cdot\boldsymbol{\nu}dl, \tag{D.53}$$

where $\boldsymbol{\nu}$ is the unit outer normal vector to the contour $\partial\Gamma$ tangent to $\Gamma$, and $dl$ is the length element of the curve. If $\partial\Gamma$ is parametrized by $t$, $\partial\Gamma(t) : \mathbb{R} \to \Gamma$, $dl = \left\|\frac{d\partial\Gamma(t)}{dt}\right\| dt$.

# Appendix E

# Loop subdivision surfaces: Smooth surfaces with exact boundary control

## E.1 Definition

Subdivision surfaces extend spline-based smooth surfaces defined on shift-invariant meshes to irregular meshes. This paradigm hinges on the well-known refinement properties of B-splines –any B-spline can be expressed as the linear combination of B-splines on a refined mesh– and generalizes them to irregular meshes. Here we focus on Loop subdivision surfaces, which extend quartic box-splines in regular triangular meshes, with six incident edges to each node, to arbitrary connectivity triangular meshes [94].

In Loop subdivision surfaces, the starting point is a general triangulation, where fields are defined at the nodes through their control values. Following the isogeometric paradigm, these fields include the positions of the nodes of the triangulation. The triangulation can be subdivided iteratively following a 2-step procedure. First, the mesh is refined by adding new points at edge

midpoints. Each triangle in the existing triangulation is then replaced by four new triangles, obtained by connecting new and preexisting nodes. In the second stage, fields defined in the original mesh are mapped onto the new mesh by means of a *subdivision mask*. The subdivision mask is a linear application represented by $S^{(n)}_{i^{(n)}j^{(n-1)}}$, with $i^{(n)}$ being the label of a node at the $n$th subdivision level, and $j^{(n-1)}$ being the label of a node in the $(n-1)$th subdivision level. If the mask is well chosen, fields, including the surface geometry, obtained at the limit of an infinite number of subdivision steps are $C_2$ almost everywhere except at a finite number of points, whose positions correspond to those mapped from the irregular nodes in the control mesh, where they are $C_1$ [94]. The subdivision mask maps old nodes onto new nodes locally. In Loop subdivision if $i^{(n)}$ is a vertex in one of the triangles $E^{(n)}$ obtained by subdividing the triangle $G^{(n-1)}$, then $S^{(n)}_{i^{(n)}j^{(n-1)}}$ is only different from zero if $j^{(n-1)}$ is within the first ring of $G^{(n-1)}$, including the nodes in $G^{(n-1)}$ and all first neighbors to them.

Here we focus on a recent extension of Loop's original subdivision rules that provides an exact description of non-manifold features, such as creases, borders or corners [26]. This facilitates representing complex geometries and topologies as required for many realistic engineering applications [33]. Nodes are tagged as interior, crease or corner depending on their position at the control mesh and new nodes, with their corresponding tags, are created following the subdivision procedure. The subdivision matrix depends both on the valence (number of incident edges) of each node and their tags as shown in Fig. E.1.

Let us consider a parametrization of the control mesh $\boldsymbol{\psi} : \mathbb{R}^2 \to \Gamma^{(0)}$ so that given a point $\boldsymbol{x}$ in the control mesh $\boldsymbol{x} = \boldsymbol{\psi}(\boldsymbol{s})$ for some $\boldsymbol{s} \in \mathbb{R}^2$. Due to the linearity of the subdivision process, any field $\boldsymbol{u}(\boldsymbol{s})$ defined at the limit surface $\Gamma$ can be characterized through its values at the control mesh, $\{\boldsymbol{u}_a\}_{a=1,\dots,N}$, where $N$ is the number of nodes in the control mesh, and the set basis functions

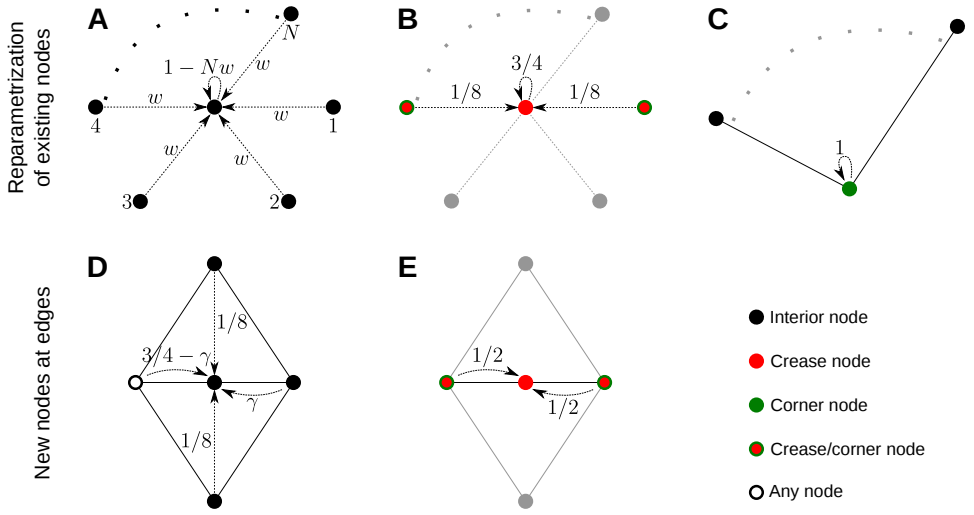


**Figure E.1**: Subdivision rules for interior and tagged patches. Each arrow indicates a term in the subdivision matrix. (A) Subdivision mask for an interior node in terms of its neighbors. The parameter $w$ depends on the valence of the node. (B) Subdivision mask for a crease node. In this case only the nodes that are at the border are taken into account. (C) Subdivision mask for a corner, in this case the corner is interpolated. (D) Creation of a node at an interior edge. The parameter $\gamma$ depends on the valence of the marked vertex as well as its nature (interior, crease or corner). (E) New node at the edge of the border.

$\{B_a(\boldsymbol{s})\}_{a=1,\dots,N}$,

$$\boldsymbol{u}(\boldsymbol{s}) = \sum_{a=1}^{N} B_a(\boldsymbol{s})\boldsymbol{u}_a. \tag{E.1}$$

The basis functions, $B_a(\boldsymbol{s})$, are obtained as the limit when $n \to \infty$ of

$$B_a^{(n)}(\boldsymbol{s}_b) = \sum_{c_{n-1}=1}^{N} S_{bc_{n-1}}^{(n)} \overset{(n-3)}{\cdots} \sum_{c_1=1}^{N} S_{c_2c_1}^{(2)} S_{c_1a}^{(1)}, \tag{E.2}$$

and

$$B(\boldsymbol{s}) = \lim_{n\to\infty} B_a^{(n)}(\boldsymbol{s}), \tag{E.3}$$

where $\boldsymbol{s}_b$ is the parametric position of node $b$ at the $n$th subdivision level.

## E.2 An efficient implementation

To practically compute the basis functions $B_a(\boldsymbol{s})$ we work element-wise. For each element, we define its *subdivision patch*, which is formed by its first ring of nearest nodes. These nodes are the only ones whose basis functions are different from zero at the given element. We then distinguish two cases. If the 3 nodes forming the element are regular, with 6 incident edges each, and the patch does not contain crease or corner tags, then the 12 basis functions at this element coincide with quartic box-splines and can therefore be directly computed without explicit subdivision [94, 170]. On the other hand, if the element contains one or several irregular nodes or has corner/crease tags, explicit subdivision is required.

Remarkably, no new irregular points are created at the subdivision procedure. Therefore, the number of irregular nodes remains constant and their density, and thus their area of influence, tends to zero as $n \to \infty$. We can then evaluate the basis functions at any interior point $\boldsymbol{s}$ different from the position of an irregular node at the control mesh with an algorithm consisting on two steps:

1. Given a point $\boldsymbol{s}$ on the control mesh, locally subdivide the mesh until reaching an interior regular patch in the absence of crease/corner tags, say in $n$ steps, and compute the matrix product $\sum_{c_{n-1}=1}^{N} S^{(n)}_{bc_{n-1}} \overset{(n-3)}{\cdots} \sum_{c_1=1}^{N} S^{(2)}_{c_2c_1} S^{(1)}_{c_1a}$.

2. Evaluate quartic box-splines for this regular patch $\tilde{B}_b(\boldsymbol{s})$. Then we can recover the basis function for the control node as

$$B_a(\boldsymbol{s}) = \sum_b \tilde{B}_b(\boldsymbol{s}) \sum_{c_{n-1}=1}^{N} S^{(n)}_{bc_{n-1}} \overset{(n-3)}{\cdots} \sum_{c_1=1}^{N} S^{(2)}_{c_2c_1} S^{(1)}_{c_1a} \tag{E.4}$$

   Equivalently, we compute the first and second derivatives of the basis function from

$$B_a(\boldsymbol{s}) = \sum_b \tilde{B}_{b,s_i}(\boldsymbol{s}) \sum_{c_{n-1}=1}^{N} S^{(n)}_{bc_{n-1}} \overset{(n-3)}{\cdots} \sum_{c_1=1}^{N} S^{(2)}_{c_2c_1} S^{(1)}_{c_1a} \tag{E.5}$$

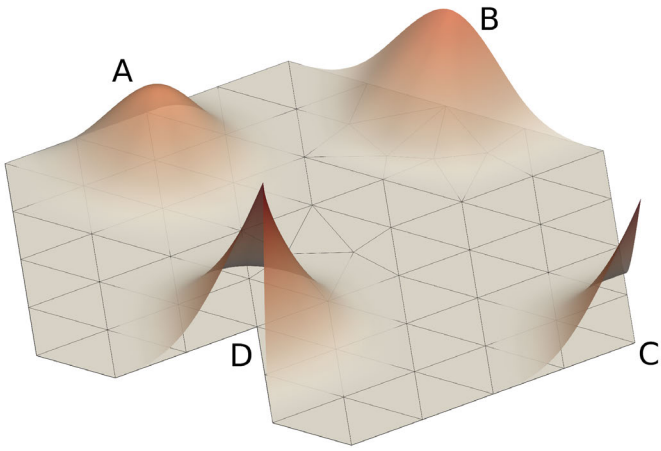


**Figure E.2**: Basis functions for irregular regular nodes. (A) Regular node at distance 1 to the border. In the interior elements, the basis function corresponds to a box-spline. In the element at the border, the basis functions are evaluated through explicit subdivision until reaching a regular patch without tags, where box-splines can be calculated and the basis function recovered. At the very border, the basis function is evaluated through the use of limit masks (see the main text). (B) Basis function for an irregular crease node. The basis function is $C_2$ everywhere except at the node, where it is $C_1$. (C) basis function for a convex corner. Here the function is $C_2$ everywhere except at the corner, where it is $C_1$. (D) Basis function for a concave corner. Here the basis function is $C_2$ everywhere except at the corner, where it is $C_0$.

$$B_a(\boldsymbol{s}) = \sum_b \tilde{B}_{b,s_1 s_2}(\boldsymbol{s}) \sum_{c_{n-1}=1}^{N} S^{(n)}_{bc_{n-1}} \overset{(n-3)}{\cdots} \sum_{c_1=1}^{N} S^{(2)}_{c_2 c_1} S^{(1)}_{c_1 a} \tag{E.6}$$

This algorithm cannot be applied to evaluate the basis functions at the borders or irregular nodes, since at these points it is impossible to reach a regular patch without crease/corner tags. Fortunately, in this case the problem can be posed in terms of limit masks, which can be obtained from an analysis of the eigenstructure of subdivision matrices as shown in [170, 26].

# Bibliography


[1] General discussion. *Faraday Discuss.*, 161:301, 2013.

[2] N. C. Admal. *Results on the interaction between atomistic and continuum models.* PhD thesis, the University of Minnesota, 2014.

[3] N. C. Admal and E. Tadmor. The non-uniqueness of the atomistic stress tensor and its relationship to the generalized beltrami representation. *J. Mech. Phys. Sol.*, 93:72 – 92, 2016. Special Issue in honor of Michael Ortiz.

[4] N. C. Admal and E. B. Tadmor. A Unified Interpretation of Stress in Molecular Systems. *J. Elast.*, 100(1-2):63–143, 2010.

[5] N. C. Admal and E. B. Tadmor. Stress and heat flux for arbitrary multibody potentials: A unified framework. *J. Chem. Phys.*, 134(18):184106, 2011.

[6] B. Alberts, A. Johnson, J. Lewis, D. Morgan, M. Raff, K. Roberts, and P. Walter. *Molecular Biology of the Cell*. Garland Science, 2014.

[7] E. Anderson, Z. Bai, C. Bischof, S. Blackford, J. Demmel, J. Dongarra, J. Du Croz, A. Greenbaum, S. Hammarling, A. McKenney, and D. Sorensen. *LAPACK Users' Guide*. Society for Industrial and Applied Mathematics, Philadelphia, PA, third edition, 1999.

[8] I. Arias and M. Arroyo. Size-dependent nonlinear elastic scaling of multiwalled carbon nanotubes. *Phys. Rev. Lett.*, 100:085503, 2008.

[9] R. Aris. *Vectors, Tensors, and the Basic Equations of Fluid Mechanics*. Prentice-Hall, 1962.

[10] M. Arroyo and A. DeSimone. Dynamics of fluid membranes. *Phys. Rev. E*, 79:031915, 2009.

[11] M. Arroyo, A. DeSimone, and L. Heltai. The role of membrane viscosity in the dynamics of fluid membranes. *arXiv*, (2007):1–21, 2010.

[12] M. Arroyo, L. Heltai, D. Millán, and A. DeSimone. Reverse engineering the euglenoid movement. *Proc. Nat. Acad. Sci. USA*, 109(44):17874–17879, 2012.

[13] M. Arroyo, N. Walani, A. Torres-Sánchez, and D. Kaurin. Continuum modeling of the dynamics of the interaction between proteins and fluid membranes. In *The role of mechanics in the study of lipid bilayers*. CISM, 2016.

[14] P. Aryal, V. Jarerattanachat, M. V. Clausen, M. Schewe, C. McClenaghan, L. Argent, L. J. Conrad, Y. Y. Dong, A. C. Pike, E. P. Carpenter, et al. Bilayer-mediated structural transitions control mechanosensitivity of the trek-2 k2p channel. *Structure*, 2017.

[15] K. Bacia, P. Schwille, and T. Kurzchalia. Sterol structure determines the separation of phases and the curvature of the liquid-ordered phase in model membranes. *Proc. Nat. Acad. Sci. USA*, 102(9):3272–3277, 2005.

[16] S. Baoukina, S. J. Marrink, and D. P. Tieleman. Lateral pressure profiles in lipid monolayers. *Faraday Discuss.*, 144:393–409, 2010.

[17] J. W. Barrett, H. Garcke, and R. Nürnberg. A stable numerical method for the dynamics of fluidic membranes. In *Numerische Mathematik*, volume 134, pages 1–40. Springer Berlin Heidelberg, 2016.

[18] D. Barthes-Biesel and H. Sgaier. Role of membrane viscosity in the orientation and deformation of a spherical capsule suspended in shear flow. *J. Fluid. Mech.*, 160:119, 1985.

[19] T. Baumgart, B. R. Capraro, C. Zhu, and S. L. Das. Thermodynamics and mechanics of membrane curvature generation and sensing by proteins and lipids. *Annu. Rev. Phys. Chem.*, 62:483–506, 2011.

[20] M. Baus and R. Lovett. Generalization of the stress tensor to nonuniform fluids and solids and its relation to Saint-Venant's strain compatibility conditions. *Phys. Rev. Lett.*, 65(14):1781–1783, 1990.

[21] M. Baus and R. Lovett. Stress-strain relations in nonuniform equilibrium fluids. *Phys. Rev. A*, 44(2):1211–1218, 1991.

[22] H. J. C. Berendsen, J. R. Grigera, and T. P. Straatsma. The missing term in effective pair potentials. *J. Phys. Chem.*, 91:6269–6271, 1987.

[23] M. Berger and D. Ebin. Some decompositions of the space of symmetric tensors on a Riemannian manifold. *J. Differ. Geom.*, 3(3-4):379–392, 1969.

[24] M. Bergert, A. Erzberger, R. A. Desai, I. M. Aspalter, A. C. Oates, G. Charras, G. Salbreux, and E. K. Paluch. Force transmission during adhesion-independent migration. *Nat. Cell Biol.*, 17(4):524–529, 2015.

[25] H. Bhatia, S. Member, and G. Norgard. The Helmholtz-Hodge decomposition – A survey. *IEEE Trans. Vis. Comp. Graph.*, 19(8):1386–1404, 2013.

[26] H. Biermann, A. Levin, and D. Zorin. Piecewise Smooth Subdivision Surfaces With Normal Control. *Proceedings of the 27th annual conference on Computer graphics and interactive techniques*, pages 113–120, 2000.

[27] F. Brochard-Wyart and P.-G. de Gennes. Adhesion induced by mobile binders: dynamics. *Proc. Nat. Acad. Sci. USA*, 99:7854–7859, 2002.

[28] D. S. Bruhn, M. A. Lomholt, and H. Khandelia. Quantifying the relationship between curvature and electric potential in lipid bilayers. *J. Phys. Chem. B*, 120(21):4812–4817, 2016.

[29] C. Campillo, P. Sens, D. Köster, L.-L. Pontani, D. Lévy, P. Bassereau, P. Nassoy, and C. Sykes. Unexpected membrane dynamics unveiled by membrane nanotube extrusion. *Biophys. J.*, 104(6):1248–1256, 2013.

[30] R. Capovilla and J. Guven. Stresses in lipid membranes. *J. Phys. A*, 35(30):6233–6247, 2002.

[31] P. Cermelli, E. Fried, and M. E. Gurtin. Transport relations for surface integrals arising in the formulation of balance laws for evolving fluid interfaces. *J. Fluid. Mech*, 544:339, 2005.

[32] S.-W. Chiu, S. A. Pandit, H. L. Scott, and E. Jakobsson. An Improved United Atom Force Field for Simulation of Mixed Lipid Bilayers. *J. Phys. Chem. B*, 113(9):2748–2763, 2009.

[33] F. Cirak and Q. Long. Subdivision shells with exact boundary control and non-manifold geometry. *Int. J. Num. Meth. Eng.*, 88(9):897–923, 2011.

[34] F. Cirak and M. Ortiz. Fully C1-conforming subdivision elements for finite deformation thin-shell analysis. *Int. J. Num. Meth. Eng.*, 51:813–833, 2001.

[35] S. Corporation. Compute stress/atom command. `http://lammps.sandia.gov/doc/compute_stress_atom.html`.

[36] B. I. Costescu, I. B. Baldus, and F. Gräter. Graphene mechanics: I. Efficient first principles based Morse potential. *Phys. Chem. Chem. Phys.*, 16:12591–12598, 2014.

[37] M. S. Daw and M. I. Baskes. Embedded-atom method: Derivation and application to impurities, surfaces, and other defects in metals. *Phys. Rev. B*, 29(12):6443–6453, 1984.

[38] G. De Fabritiis, M. Serrano, R. Delgado-Buscalioni, and P. V. Coveney. Fluctuating hydrodynamic modeling of fluids at the nanoscale. *Phys. Rev. E*, 75(2):15–18, 2007.

[39] R. Dimova, S. Aranda, N. Bezlyepkina, V. Nikolov, K. A. Riske, and R. Lipowsky. A practical guide to giant vesicles. Probing the membrane nanoregime via optical microscopy. *J. Phys.: Condens. Matter*, 18:1151–1176, 2006.

[40] M. P. do Carmo. *Differential geometry of curves and surfaces*. Prentice Hall, 1976.

[41] M. P. do Carmo. *Riemannian Geometry*. Birkhäuser, Boston, 1992.

[42] M. Doi. Onsager's variational principle in soft matter. *Journal of Physics-Condens. Matter*, 23(28):284118, 2011.

[43] M. Doi. *Soft matter physics*. Oxford University Press, 2013.

[44] J. Donea, A. Huerta, J.-P. Ponthot, and A. Rodríguez-Ferran. Arbitrary lagrangian-eulerian methods. In *Encyclopedia of Computational Mechanics*. John Wiley & Sons, Ltd, 2004.

[45] T. Doyle and J. Ericksen. Nonlinear Elasticity. In H.L. Dryden and Th. von Kármán, editor, *Advances in Applied Mechanics IV*, volume 4 of *Advances in Applied Mechanics*, pages 53–115. Elsevier, 1956.

[46] D. J. Evans and B. L. Holian. The nose–hoover thermostat. *J. Chem. Phys.*, 83(8):4069–4074, 1985.

[47] E. Evans and A. Yeung. Hidden dynamics in rapid changes of bilayer shape. *Chem. Phys. Lipids*, 73(1-2):39–56, 1994.

[48] B. Fábián, M. Sega, V. P. Voloshin, N. N. Medvedev, and P. Jedlovszky. Lateral pressure profile and free volume properties in phospholipid membranes containing anesthetics. *J. Phys. Chem. B*, 121(13):2814–2824, 2017.

[49] F. Feng and W. S. Klug. Finite element modeling of lipid bilayer membranes. *J. Comput. Phys.*, 220(1):394–408, 2006.

[50] E. Fischer-Friedrich, Y. Toyoda, C. J. Cattin, D. J. Müller, A. A. Hyman, and F. Jülicher. Rheology of the Active Cell Cortex in Mitosis. *Biophys. J.*, 111(3):589–600, 2016.

[51] M. Fisher. The free energy of a macroscopic system. *Arch. Ration. Mech. An.*, 17(5):377–410, 1964.

[52] T. R. Forester and W. Smith. SHAKE, rattle, and roll: Efficient constraint algorithms for linked rigid bodies. *J. Comput. Chem.*, 19(1):102–111, 1998.

[53] J. B. Fournier. On the hydrodynamics of bilayer membranes. *Int. J. Nonlin. Mech.*, 75:67–76, 2015.

[54] J.-B. Fournier, N. Khalifat, N. Puff, and M. I. Angelova. Chemically Triggered Ejection of Membrane Tubules Controlled by Intermonolayer Friction. *Phys. Rev. Lett.*, 102(1):018102, 2009.

[55] D. Frenkel and B. Smit. *Understanding Molecular Simulation*. Academic Press, Inc., 2nd edition, 2001.

[56] Y. Gambin, R. Lopez-Esparza, M. Reffay, E. Sierecki, N. S. Gov, M. Genest, R. S. Hodges, and W. Urbach. Lateral mobility of proteins in liquid membranes revisited. *Proc. Nat. Acad. Sci. USA*, 103(7):2098–2102, 2006.

[57] R. Goetz and R. Lipowsky. Computer simulations of bilayer membranes: Self-assembly and interfacial tension. *J. Chem. Phys.*, 108(17):7397–7409, 1998.

[58] H. Goldstein. *Classical mechanics*. World student series. Addison-Wesley, 1980.

[59] A. Goliaei, K. P. Santo, and M. L. Berkowitz. Local pressure changes in lipid bilayers due to adsorption of melittin and magainin-h2 antimicrobial peptides: Results from computer simulations. *J. Phys. Chem. B*, 118(44):12673–12679, 2014.

[60] G. Grigoryan. `http://www.grigoryanlab.org/cccp/index.gen.html`.

[61] G. Grigoryan and W. F. DeGrado. Probing designability via a generalized model of helical bundle geometry. *J. Mol. Biol.*, 405(4):1079 – 1100, 2011.

[62] J. Gullingsrud and K. Schulten. Lipid bilayer pressure profiles and mechanosensitive channel gating. *Biophys. J.*, 86(6):3496–3509, 2004.

[63] A. A. Gurtovenko and A. S. Lyulina. Electroporation of asymmetric phospholipid membranes. *J. Phys. Chem. B*, 118(33):9909–9918, 2014.

[64] M. Hamm and M. M. Kozlov. Tilt model of inverted amphiphilic mesophases. *The Eur. Phys. J. B*, 6(4):519–528, 1998.

[65] M. Hamm and M. M. Kozlov. Elastic energy of tilt and bending of fluid membranes. *The Eur. Phys. J. E*, 3(4):323–335, 2000.

[66] A. Harasima. Molecular Theory of Surface Tension. *Adv. Chem. Phys.*, 1:203–237, 1958.

[67] C. Hartmann, C. Schutte, and G. Ciccotti. On the linear response of mechanical systems with constraints. *J. Chem. Phys.*, 132(11):111103, 2010.

[68] H. W. Hatch and P. G. Debenedetti. Molecular modeling of mechanical stresses on proteins in glassy matrices : Formalism. *J. Chem. Phys.*, 137:035103, 2012.

[69] H. Heinz. Calculation of local and average pressure tensors in molecular simulations. *Molecular Simulation*, 33(9-10):747–758, 2007.

[70] W. Helfrich. Elastic properties of lipid bilayers: theory and possible experiments. *Z. Naturforsch.*, 28c:693–703, 1973.

[71] W. Helfrich. Lyotropic lamellar phases. *J Phys.-Condens. Mat.*, 6(23A):A79, 1994.

[72] M. L. Henle and A. J. Levine. Hydrodynamics in curved membranes: The effect of geometry on particulate mobility. *Phys. Rev. E*, 81(1):1–17, 2010.

[73] B. Hess, H. Bekker, H. J. C. Berendsen, and J. G. E. M. Fraaije. LINCS: a linear constraint solver for molecular simulations. *J. Comput. Chem.*, 18(12):1463–1472, 1997.

[74] B. Hess, C. Kutzner, D. van Der Spoel, and E. Lindahl. GROMACS 4: Algorithms for Highly Efficient, Load-Balanced, and Scalable Molecular Simulation. *J. Chem. Theory Comput.*, 4(3):435–447, 2008.

[75] M. Hu, D. H. de Jong, S. J. Marrink, and M. Deserno. Gaussian curvature elasticity determined from global shape transformations and local stress distributions: a comparative study using the martini model. *Faraday Discuss.*, 161:365–382, 2013.

[76] N. Ileri Ercan, P. Stroeve, J. W. Tringe, and R. Faller. Understanding the interaction of pluronics l61 and l64 with a dopc lipid bilayer: An atomistic molecular dynamics study. *Langmuir*, 32(39):10026–10033, 2016.

[77] J. H. Irving and J. G. Kirkwood. The Statistical Mechanical Theory of Transport Processes. IV. The Equations of Hydrodynamics. *J. Chem. Phys.*, 18(6):817–829, 1950.

[78] R. Jordan, D. Kinderlehrer, and F. Otto. The Variational Formulation of the Fokker–Planck Equation. *SIAM J. Math. Anal.*, 29(1):1–17, 1998.

[79] W. L. Jorgensen, J. Chandrasekhar, J. D. Madura, R. W. Impey, and M. L. Klein. Comparison of simple potential functions for simulating liquid water. *J. Chem. Phys.*, 79(2):926–935, 1983.

[80] F. Jülicher and R. Lipowsky. Domain-induced budding of vesicles. *Phys. Rev. Lett.*, 70(19):2964–2967, 1993.

[81] B. Jüttler, A. Mantzaflaris, R. Perl, and M. Rumpf. On numerical integration in isogeometric subdivision methods for PDEs on surfaces. *Comput. Method. Applied M.*, 302:131–146, 2016.

[82] N. Khalifat, N. Puff, S. Bonneau, J.-B. Fournier, and M. I. Angelova. Membrane deformation under local ph gradient: mimicking mitochondrial cristae dynamics. *Biophys. J.*, 95(10):4924–4933, 2008.

[83] J. Klein. Hydration lubrication. *Friction*, 1(1):1–23, 2013.

[84] A. J. Kosmalska, L. Casares, A. Elosegui-Artola, J. J. Thottacherry, R. Moreno-Vicente, V. González-Tarragó, M. Á. del Pozo, S. Mayor, M. Arroyo, D. Navajas, X. Trepat, N. C. Gauthier, and P. Roca-Cusachs. Physical principles of membrane remodelling during cell mechanoadaptation. *Nat. Comm.*, 6:7292, 2015.

[85] J. Kruczek, S.-W. Chiu, E. Jakobsson, and S. A. Pandit. Effects of lithium and other monovalent ions on palmitoyl oleoyl phosphatidylcholine bilayer. *Langmuir*, 33(4):1105–1115, 2017.

[86] A. J. Levine, T. B. Liverpool, and F. C. MacKintosh. Dynamics of rigid and flexible extended bodies in viscous films and membranes. *Phys. Rev. Lett.*, 93(3):038102–1, 2004.

[87] A. Lew, J. E. Marsden, M. Ortiz, and M. West. Variational time integrators. *Int. J. Num. Meth. Eng.*, 60(1):153–212, 2004.

[88] J. Li, K. J. Van Vliet, T. Zhu, S. Yip, and S. Suresh. Atomistic mechanisms governing elastic limit and incipient plasticity in crystals. *Nature*, 418(6895):307–310, 2002.

[89] Y. Li, R. Lipowsky, and R. Dimova. Membrane nanotubes induced by aqueous phase separation and stabilized by spontaneous curvature. *Proc. Nat. Acad. Sci. USA*, 108(12):4731–4736, 2011.

[90] X. Lin, S. Zhang, H. Ding, I. Levental, and A. A. Gorfe. The aliphatic chain of cholesterol modulates bilayer interleaflet coupling and domain registration. *FEBS Lett.*, 590(19):3368–3374, 2016.

[91] E. Lindahl and O. Edholm. Spatial and energetic-entropic decomposition of surface tension in lipid bilayers from molecular dynamics simulations. *J. Chem. Phys.*, 113(9):3882–3893, 2000.

[92] R. Lipowsky. The conformation of membranes. *Nature*, 349(6309):475–481, 1991.

[93] R. G. Littlejohn and M. Reinsch. Gauge fields in the separation of rotations and internal motions in the n-body problem. *Rev. Mod. Phys.*, 69(1):213–275, 1997.

[94] C. Loop. *Smooth subdivision surfaces based on triangles*. PhD thesis, University of Utah, 1987.

[95] A. MacKerell and D. Bashford. All-atom empirical potential for molecular modeling and dynamics studies of proteins. *J. Phys. Chem. B*, 102(18):3586–3616, 1998.

[96] A. D. Mackerell, M. Feig, and C. L. Brooks. Extending the treatment of backbone energetics in protein force fields: Limitations of gas-phase quantum mechanics in reproducing protein conformational distributions in molecular dynamics simulation. *J. Comput. Chem.*, 25:1400–1415, 2004.

[97] S. J. Marrink. 3D pressure field. `http://md.chem.rug.nl/cgmartini/index.php/3d`.

[98] S. J. Marrink, A. H. de Vries, and A. E. Mark. Coarse Grained Model for Semiquantitative Lipid Simulations. *J. Phys. Chem. B*, 108(2):750–760, 2004.

[99] S. J. Marrink, H. J. Risselada, S. Yefimov, D. P. Tieleman, and A. H. de Vries. The MARTINI force field: coarse grained model for biomolecular simulations. *J. Phys. Chem. B*, 111(27):7812–7824, 2007.

[100] J. Marsden and T. J. R. Hughes. *Mathematical foundations of elasticity*. Dover Publications, Inc., 1983.

[101] D. Marsh. Elastic curvature constants of lipid monolayers and bilayers. *Chem. Phys. Lipids*, 144(2):146–159, 2006.

[102] J. W. Martin. Many-body forces in metals and the brugger elastic constants. *J. Phys. C*, 8(18):2837, 1975.

[103] A. Mielke. On thermodynamically consistent models and gradient structures for thermoplasticity. *GAMM-Mitteilungen*, 34(1):51–58, 2011.

[104] A. Mielke. Thermomechanical modeling of energy-reaction-diffusion systems, including bulk-interface interactions. *Discrete and Continuous Dynamical Systems - Series S*, 6(2):479–499, 2012.

[105] D. Millán, B. Li, A. Torres-Sánchez, and M. Arroyo. A higher–order phase–field model for fracture in geometrically nonlinear Kirchhoff–Love shells. *In preparation*.

[106] D. Millán, A. Rosolen, and M. Arroyo. Thin shell analysis from scattered points with maximum-entropy approximants. *Int. J. Num. Meth. Eng.*, 85(6):723–751, 2011.

[107] L. Mistura. The definition of the pressure tensor in the statistical mechanics of nonuniform classical fluids. *Int. J. Thermophys.*, 8(3):397–403, 1987.

[108] S. Miyamoto and P. A. Kollman. SETTLE : An Analytical Version of the SHAKE and RATTLE Algorithm for Rigid Water Models. *J. Comput. Chem.*, 13(8):952–962, 1992.

[109] R. G. Morris and M. S. Turner. Mobility Measurements Probe Conformational Changes in Membrane Proteins due to Tension. *Phys. Rev. Lett.*, 115(19):1–5, 2015.

[110] A. I. Murdoch. A critique of atomistic definitions of the stress tensor. *J. Elast.*, 88(2):113–140, 2007.

[111] A. I. Murdoch. *Physical foundations of continuum mechanics*. Cambridge University Press, 1st edition, 2012.

[112] A. Naji, P. J. Atzberger, and F. L. H. Brown. Hybrid elastic and discrete-particle approach to biomembrane dynamics with application to the mobility of curved integral membrane proteins. *Phys. Rev. Lett.*, 102(13):1–4, 2009.

[113] V. A. Ngo, R. K. Kalia, A. Nakano, and P. Vashishta. Molecular mechanism of flip-flop in triple-layer oleic-acid membrane: correlation between oleic acid and water. *J. Phys. Chem. B*, 116(45):13416–13423, 2012.

[114] I. Nitschke, a. Voigt, and J. Wensch. A finite element approach to incompressible two-phase flow on manifolds. *J. Fluid Mech.*, 708(2012):418–438, 2012.

[115] W. Noll. Die Herleitung der Grundgleichungen der Thermomechanik der Kontinua aus der statistischen Mechanik. *J. Natural Mech. and Anal.*, 4:627–646, 1955.

[116] O. H. S. Ollila, M. Louhivuori, S. J. Marrink, and I. Vattulainen. Protein shape change has a major effect on the gating energy of a mechanosensitive channel. *Biophys. J.*, 100(7):1651–1659, 2011.

[117] O. H. S. Ollila, H. Risselada, M. Louhivuori, E. Lindahl, I. Vattulainen, and S. Marrink. 3D Pressure Field in Lipid Membranes and Membrane-Protein Complexes. *Phys. Rev. Lett.*, 102(7):1–4, 2009.

[118] O. S. Ollila. Lateral pressure profile calculations of lipid membranes from atomic scale molecular dynamics simulations. Master's thesis, Helsinki University of Technology, 2006.

[119] O. S. Ollila. *Lateral pressure in lipid membranes and its role in function of membrane proteins*. PhD thesis, Tampere University of Technology, 2010.

[120] L. Onsager. Irreversible processes. *Phys. Rev.*, 37:237–241, 1931.

[121] L. Onsager. Reciprocal relations in irreversible processes. I. *Phys. Rev.*, 37(4):405–426, 1931.

[122] M. Orsi and J. W. Essex. Physical properties of mixed bilayers containing lamellar and nonlamellar lipids: insights from coarse-grain molecular dynamics simulations. *Faraday Discuss.*, 161:249–272, 2013.

[123] M. Orsi, J. Michel, and J. W. Essex. Coarse-grain modelling of DMPC and DOPC lipid bilayers. *J. Phys.: Condens. Matter*, 22(15):155106–155121, 2010.

[124] M. Ortiz and E. Repetto. Nonconvex energy minimization and dislocation structures in ductile single crystals. *J. Mech. Phys. Solids*, 47(2):397–462, 1999.

[125] H. C. Öttinger. *Beyond Equilibrium Thermodynamics*. John Wiley & Sons, Inc., 2005.

[126] F. Otto. The geometry of dissipative evolution equations: The porous medium equation. *Communications in Partial Differential Equations*, 26(1-2):101–174, 2001.

[127] C.-W. Pao, S. M. Foiles, E. B. Webb, D. J. Srolovitz, and J. A. Floro. Atomistic simulations of stress and microstructure evolution during polycrystalline Ni film growth. *Phys. Rev. B*, 79(22):224113, 2009.

[128] M. Parrinello and A. Rahman. Polymorphic transitions in single crystals: A new molecular dynamics method. *J. Appl. Phys.*, 52(12):7182–7190, 1981.

[129] M. Patra. Lateral pressure profiles in cholesterol-DPPC bilayers. *Eur. Biophys. J.*, 35(1):79–88, 2005.

[130] C. Peco, A. Rosolen, and M. Arroyo. An adaptive meshfree method for phase-field models of biomembranes. Part II: A Lagrangian approach for membranes in viscous fluids. *J. Comput. Phys.*, 249:320–336, 2013.

[131] M. A. Peletier. Variational modelling: Energies, gradient flows, and large deviations. *arXiv preprint arXiv:1402.1990*, 2014.

[132] E. F. Pettersen, T. D. Goddard, C. C. Huang, G. S. Couch, D. M. Greenblatt, E. C. Meng, and T. E. Ferrin. UCSF Chimera–a visualization system for exploratory research and analysis. *J. Comput. Chem.*, 25(13):1605–1612, 2004.

[133] L. Piegl and W. Tiller. *The NURBS Book*. Monographs in Visual Communication. Springer Berlin Heidelberg, 1996.

[134] J. Porta, L. Ros, F. Thomas, and C. Torras. A branch-and-prune solver for distance constraints. *IEEE T. Robot.*, 21(2):176–187, 2005.

[135] I. Prigogine. *Introduction to thermodynamics of irreversible processes*. Interscience Publishers, 1967.

[136] S. Pronk, S. Páll, R. Schulz, P. Larsson, P. Bjelkmar, R. Apostolov, M. R. Shirts, J. C. Smith, P. M. Kasson, D. van der Spoel, B. Hess, and E. Lindahl. GROMACS 4.5: a high-throughput and highly parallel open source molecular simulation toolkit. *Bioinformatics*, 29(7):845–854, 2013.

[137] F. Quemeneur, J. K. Sigurdsson, M. Renner, P. J. Atzberger, P. Bassereau, and D. Lacoste. Shape matters in protein mobility within membranes. *Proc. Nat. Acad. Sci. USA*, 111(14):5083–5087, 2014.

[138] M. Rahimi. *Shape dynamics and lipid hydrodynamics of bilayer membranes : modeling , simulation and experiments*. PhD thesis, Universitat Politècnica de Catalunya - BarcelonaTech, 2013.

[139] M. Rahimi and M. Arroyo. Shape dynamics, lipid hydrodynamics, and the complex viscoelasticity of bilayer membranes. *Phys. Rev. E*, 86(1):011932, 2012.

[140] M. Rahimi, A. DeSimone, and M. Arroyo. Curved fluid membranes behave laterally as effective viscoelastic media. *Soft Matter*, 9(46):11033, 2013.

[141] S. Ramadurai, A. Holt, V. Krasnikov, G. van den Bogaart, J. A. Killian, and B. Poolman. Lateral diffusion of membrane proteins. *J. Am. Chem. Soc.*, 131(35):12650–12656, 2009.

[142] R. Rangarajan and H. Gao. A finite element method to compute three-dimensional equilibrium configurations of fluid membranes: Optimal parameterization, variational formulation and applications. *J. Comput. Phys.*, 297:266–294, 2015.

[143] W. Rawicz, K. Olbrich, and T. McIntosh. Effect of chain length and unsaturation on elasticity of lipid bilayers. *Biophys. J.*, 79:328–339, 2000.

[144] Rayleigh. *Proc. Math. Soc. London*, 363:357, 1873.

[145] E. Reister-Gottfried, S. M. Leitenberger, and U. Seifert. Diffusing proteins on a fluctuating membrane: Analytical theory and simulations. *Phys. Rev. E*, 81(3), 2010.

[146] S. Reuther and A. Voigt. Incompressible two-phase flows with an inextensible Newtonian fluid interface. *J. Comput. Phys.*, 322:850–858, 2016.

[147] A. C. Reymann, F. Staniscia, A. Erzberger, G. Salbreux, and S. W. Grill. Cortical flow aligns actin filaments to form a furrow. *eLife*, 5:1–25, 2016.

[148] D. S. Rodrigues, R. F. Ausas, F. Mut, and G. C. Buscaglia. A semi-implicit finite element method for viscous lipid membranes. *J. Comput. Phys.*, 298:565–584, 2015.

[149] G. C. Rossi and M. Testa. The stress tensor in thermodynamics and statistical mechanics. *J. Chem. Phys.*, 132(7):074902, 2010.

[150] A. Roux, G. Cappello, J. Cartaud, J. Prost, B. Goud, and P. Bassereau. A minimal system allowing tubulation with molecular motors pulling on giant liposomes. *Proc. Nat. Acad. Sci. USA*, 99(8):5394–5399, 2002.

[151] A. Rustom, R. Saffrich, I. Markovic, P. Walther, and H.-H. Gerdes. Nanotubular highways for intercellular organelle transport. *Science (New York, N.Y.)*, 303(5660):1007–1010, 2004.

[152] P. Saffman and M. Delbrück. Brownian motion in biological membranes. *Proc. Natl. Acad. Sci.*, 72(8):3111–3113, 1975.

[153] A. Saha, M. Nishikawa, M. Behrndt, C. P. Heisenberg, F. Jülicher, and S. W. Grill. Determining Physical Properties of the Cell Cortex. *Biophys. J.*, 110(6):1421–1429, 2016.

[154] G. Salbreux, G. Charras, and E. Paluch. Actin cortex mechanics and cellular morphogenesis. *Trends Cell. Biol.*, 22(10):536–45, 2012.

[155] R. A. Sauer, T. X. Duong, K. Mandadapu, and D. Steigmann. A stabilized finite element formulation for liquid shells and its application to lipid bilayers Summary of liquid shell theory. *J. Comput. Phys.*, 330:1–19, 2017.

[156] P. Schofield and J. Henderson. Statistical mechanics of inhomogeneous fluids. *Proc. R. Soc. Lond. A*, 379:231–246, 1982.

[157] L. Scriven. Dynamics of a fluid interface Equation of motion for Newtonian surface fluids. *Chem. Eng. Sci.*, 12(2):98–108, 1960.

[158] B. Seguin and E. Fried. Statistical foundations of liquid crystal theory: II Macroscopic balance laws. *Arch. Ration. Mech. Anal.*, 207(1):1–37, 2013.

[159] U. Seifert. *Advances in Physics Configurations of fluid membranes and vesicles*. Number July 2011. 1997.

[160] U. Seifert and S. A. Langer. Viscous Modes of Fluid Bilayer Membranes. *Europhys. Lett.*, 23(1):71–76, 1993.

[161] P. Sens, L. Johannes, and P. Bassereau. Biophysical approaches to protein-induced membrane deformations in trafficking. *Curr. Opin. Cell Biol.*, 20(4):476–482, 2008.

[162] Y. Shibata, J. Hu, M. M. Kozlov, and T. A. Rapoport. Mechanisms shaping the membranes of cellular organelles. *Annu. Rev. Cell Dev. Biol.*, 25:329–354, 2009.

[163] J. K. Sigurdsson and P. J. Atzberger. Hydrodynamic coupling of particle inclusions embedded in curved lipid bilayer membranes. *Soft Matter*, 12(32):6685–6707, 2016.

[164] R. Skalak and T. W. Secomb. Surface Flow of Viscoelastic. *Q. J. Mech. Appl. Math.*, XXXV:233, 1982.

[165] A. J. Sodt and T. Head-Gordon. An implicit solvent coarse-grained lipid model with correct stress profile. *J. Chem. Phys.*, 132(20):205103–205111, 2010.

[166] Z. Song, V. I. Artyukhov, B. I. Yakobson, and Z. Xu. Pseudo hall–petch strength reduction in polycrystalline graphene. *Nano Lett.*, 13(4):1829–1833, 2013.

[167] J. Sonne, F. Y. Hansen, and G. H. Peters. Methodological problems in pressure profile calculations for lipid bilayers. *J. Chem. Phys.*, 122(12):124903–124912, 2005.

[168] H. Sprong, P. van der Sluijs, and G. van Meer. How proteins move lipids and lipids move proteins. *Nat. Rev. Mol. Cell Biol.*, 2(7):504–513, 2001.

[169] T. M. Squires and T. G. Mason. Fluid mechanics of microrheology. *Annu. Rev. Fluid Mech.*, 42:413–438, 2010.

[170] J. Stam. Evaluation of Loop subdivision surfaces. In *SIGGRAPH'99 Course notes*, 1999.

[171] G. Staneva, M. I. Angelova, and K. Koumanov. Phospholipase A2 promotes raft budding and fission from giant liposomes. *Chem. Phys. Lipids*, 129(1):53–62, 2004.

[172] M. Staykova, M. Arroyo, M. Rahimi, and H. A. Stone. Confined bilayers passively regulate shape and stress. *Phys. Rev. Lett.*, 110:028101, 2013.

[173] D. J. Steigmann. Fluid Films with Curvature Elasticity. *Arch. Ration. Mech. Anal.*, 150(2):127–152, 1999.

[174] D. J. Steigmann and R. W. Ogden. Elastic surface—substrate interactions. *P. Roy Soc. A-Math Phy.*, 455(1982):437–474, 1999.

[175] H. A. Stone and A. Ajdari. Hydrodynamics of particles embedded in a flat surfactant layer overlying a subphase of finite depth. *J. Fluid Mech.*, 369(1998):151–173, 1998.

[176] J. Y. Su, R. S. Hodges, and C. M. Kay. Effect of chain length on the formation and stability of synthetic alpha-helical coiled coils. *Biochemistry*, 33(51):15501–15510, 1994.

[177] I. Szleifer, D. Kramer, A. Benshaul, W. M. Gelbart, S. A. Safran, and A. Sen-shaul. Molecular theory of curvature elasticity in surfactant films Molecular theory of curvature elasticity in surfactant films. *J. Chem. Phys.*, 92:6800, 1990.

[178] E. B. Tadmor and R. E. Miller. *Modeling Materials: Continuum, Atomistic and Multiscale Techniques*. Cambridge University Press, 2011.

[179] A. P. Thompson, S. J. Plimpton, and W. Mattson. General formulation of pressure and stress tensor for arbitrary many-body interaction potentials under periodic boundary conditions. *J. Chem. Phys.*, 131(15):–, 2009.

[180] I. G. Tironi, R. Sperb, P. E. Smith, and W. F. van Gunsteren. A generalized reaction field method for molecular dynamics simulations. *J. Chem. Phys.*, 102(13):5451–5459, 1995.

[181] A. Torres-Sánchez and M. Arroyo. Rheology of membrane inclusions generating intrinsic curvature. *In preparation*.

[182] A. Torres-Sánchez, J. M. Vanegas, and M. Arroyo. Examining the mechanical equilibrium of microscopic stresses in molecular simulations. *Phys. Rev. Lett.*, 114:258102, 2015.

[183] A. Torres-Sánchez, J. M. Vanegas, and M. Arroyo. Geometric derivation of the microscopic stress: A covariant central force decomposition. *J. Mech. Phys. Solids*, 93:224–239, 2016.

[184] I. Tsafrir, Y. Caspi, M.-A. Guedeau-Boudeville, T. Arzi, and J. Stavans. Budding and tubulation in highly oblate vesicles by anchored amphiphilic molecules. *Phys. Rev. Lett.*, 91:138102, 2003.

[185] D. H. Tsai. The virial theorem and stress calculation in molecular dynamics. *J. Chem. Phys.*, 70(3):1375–1382, 1979.

[186] Z. C. Tu and Z. C. Ou-Yang. A geometric theory on the elasticity of bio-membranes. *J. Phys. A*, 37(47):11407–11429, 2004.

[187] H. Turlier, B. Audoly, J. Prost, and J. F. Joanny. Furrow constriction in animal cell cytokinesis. *Biophys. J.*, 106(1):114–123, 2014.

[188] J. M. Vanegas and M. Arroyo. Force transduction and lipid binding in MscL: A continuum-molecular approach. *PLoS ONE*, 9(12):e113947, 2014.

[189] J. M. Vanegas, M. L. Longo, and R. Faller. Crystalline, Ordered and Disordered Lipid Membranes: Convergence of Stress Profiles due to Ergosterol. *J. Am. Chem. Soc.*, 133(11):3720–3723, 2011.

[190] J. M. Vanegas, A. Torres-Sánchez, and M. Arroyo. Computing the Local Stress Tensor in MD Simulations. `http://www.lacan.upc.edu/LocalStressFromMD`.

[191] J. M. Vanegas, A. Torres-Sánchez, and M. Arroyo. Importance of force decomposition for local stress calculations in biomembrane molecular simulations. *J. Chem. Theory Comput.*, 10:691–702, 2014.

[192] N. K. Voulgarakis and J. W. Chu. Bridging fluctuating hydrodynamics and molecular dynamics simulations of fluids. *J. Chem. Phys.*, 130(13), 2009.

[193] H. Wagner. The microscopic stress tensor field in particle systems with many-body interactions. *J. Stat. Phys.*, 55:1293–1302, 1989.

[194] Y. Wei, J. Wu, H. Yin, X. Shi, R. Yang, and M. Dresselhaus. The nature of strength enhancement and weakening by pentagon–heptagon defects in graphene. *Nat. Mater.*, 11(9):759–763, 2012.

[195] Z. Wu, Q. Cui, and A. Yethiraj. A new coarse-grained model for water: the importance of electrostatic interactions. *J. Phys. Chem. B*, 114(32):10524–10529, 2010.

[196] Z. Wu, Q. Cui, and A. Yethiraj. A New Coarse-Grained Force Field for Membrane-Peptide Simulations. *J. Chem. Theory Comput.*, pages 3793–3802, 2011.

[197] B. I. Yakobson, C. J. Brabec, and J. Bernholc. Nanomechanics of carbon tubes: Instabilities beyond linear response. *Phys. Rev. Lett.*, 76:2511–2514, 1996.

[198] N. Yamaguchi, T. Mizutani, K. Kawabata, and H. Haga. Leader cells regulate collective cell migration via Rac activation in the downstream signaling of integrin $\beta$1 and PI3K. *Sci. Rep–UK*, 5:7656, 2015.

[199] A. Yavari and J. E. Marsden. Covariantization of nonlinear elasticity. *Zeitschrift für angewandte Mathematik und Physik*, 63(5):921–927, 2012.

[200] A. Yavari, J. E. Marsden, and M. Ortiz. On spatial and material covariant balance laws in elasticity. *Journal of Mathematical Physics*, 47(4):–, 2006.

[201] J. Yoo and Q. Cui. Curvature generation and pressure profile modulation in membrane by lysolipids: insights from coarse-grained simulations. *Biophys. J.*, 97(8):2267–2276, 2009.

[202] J. Yoo and Q. Cui. Three-Dimensional Stress Field around a Membrane Protein: Atomistic and Coarse-Grained Simulation Analysis of Gramicidin A. *Biophys. J.*, 104(1):117–127, 2013.

[203] Y. Zhou and D. Yan. Real-Time Membrane Fission of Giant Polymer Vesicles. *Angewandte Chemie International Edition*, 44(21):3223–3226, 2005.

[204] L. Zhu, J. Wu, L. Liu, Y. Liu, Y. Yan, Q. Cui, and X. Chen. Gating mechanism of mechanosensitive channel of large conductance: a coupled continuum mechanical-continuum solvation approach. *Biomech. Model. Mechan.*, 15(6):1557–1576, 2016.